Optical fibres : analysis, numerical modelling and optimisation

Document status and date:

Published: 01/01/2009

Document Version:

Publisher's PDF, also known as Version of Record (includes final page, issue and volume numbers)

Please check the document version of this publication:

• A submitted manuscript is the version of the article upon submission and before peer-review. There can be important differences between the submitted version and the official published version of record. People interested in the research are advised to contact the author for the final version of the publication, or visit the DOI to the publisher's website.
• The final author version and the galley proof are versions of the publication after peer review.
• The final published version features the final layout of the paper including the volume, issue and page numbers.

[Link to publication](#)

Optical fibres

Analysis, numerical modelling and optimisation

Optical fibres

Analysis, numerical modelling and optimisation

PROEFSCHRIFT

ter verkrijging van de graad van doctor aan de
Technische Universiteit Eindhoven, op gezag van de
Rector Magnificus, prof.dr.ir. C.J. van Duijn, voor een
commissie aangewezen door het College voor
Promoties in het openbaar te verdedigen
op woensdag 20 mei 2009 om 16.00 uur

door

Rutger Wilhelmus Smink

geboren te Wijnandsrade

Dit proefschrift is goedgekeurd door de promotoren:

prof.dr. A.G. Tijhuis
en
prof.dr. H.J.S. Dorren

Copromotor:
dr.ir. B.P. de Hon

Cover design: Almer Smink and Con Tonnaer

In memory of my mother.
To my father, brother and wife.

Summary

For several decades silica-based optical fibres have been used for telecommunication and sensor purposes. The single-mode fibre is frequently employed in long-distance networks, whereas the multi-mode fibre is the preferred means of signal transport in campus and in-building networks. Because of the huge bandwidth of optical fibres in comparison to its electrical wireless and copper-based counterparts, the demand for optical fibres keeps increasing. In a competitive market, fibre manufacturers aim to produce ever better fibres that are as cheap and easy to employ as possible.

As fibre research, development and manufacturing is a mature discipline, improvements in fibre design can only be achieved through the construction of robust, accurate and efficient numerical fibre models for the computation of those quantities that determine the behaviour of the fibre. We have developed a modular software code, based on Maxwell's equations, to compute these quantities in a vectorial full-wave way for both single-mode and multi-mode optical fibres. Key is the refractive-index profile, or, more specifically, the dopant profile, as it defines the propagation, splicing and bending-loss characteristics of the fibre. For the single-mode fibre, the fibre quantities that we have concentrated on are dispersion, dispersion slope, mode-field diameter, effective area, bending loss, effective and theoretical cut-off wavelength and MAC-value.

We highlight one fibre quantity in particular, viz. the computation of the bending loss in a single-mode fibre. Many approximate modelling techniques have been developed to estimate this loss in a fast way. Our numerical scheme, however, is the first rigorous one, as we have performed a vectorial full-wave analysis of the bent optical fibre. In this context, triple integrals involving products of Bessel functions with large, complex order and argument appear. Due to cancellations in the pertaining computation, a high relative accuracy is needed for the computation of each product. As a result, it takes weeks on a contemporary computer to compute the bending loss as a function of the radius of curvature. We have used the vectorial full-wave bending-loss results to determine the most appropriate approximate method. Subsequently, we have extended that approximate method to compute the bending losses of higher-order modes, since the required effective cut-off wavelength depends on the bending loss of the first higher-order mode. The selected

approximate method has been used in the ensuing bending-loss calculations.

Since the fibre properties are often conflicting, it is a challenging task to adapt the radial dopant profile to meet a set of predefined design goals. A design goal is a combination of desired values for (some of) the aforementioned fibre quantities, and can mathematically be translated into a cost function. The minimisation of this cost function provides us with the optimal dopant profile for that specific set. For the single-mode fibre, we have performed this minimisation for piecewise-linear profiles, by employing various global and gradient-based local optimisation strategies to speed up the design step considerably. Frequently, these optimisation strategies lead to counter-intuitive dopant profile designs that could not have been contrived otherwise. We have selected a deliberate mix of several optimisation routines and have compared their performances. Perhaps the most important conclusion is that there still appears to be room for improvement in the design of the radial dopant profile of commercially available fibres.

For the multi-mode fibre, vectorial full-wave optimisation is not feasible yet because of the long computation times for the large number of propagating modes. Still, our numerical scheme allows for a manual fine-tuning of the popular power-law profile to minimise differential mode delay. Further, we have included mode coupling and differential mode attenuation in our model to obtain intensity patterns that match closely with measurements. We have also analysed the influence of profile variations, e.g. on-axis dips and kinks, on the intensity pattern.

A selective excitation of different mode groups in a multi-mode fibre, offers the possibility to create several independent transmission channels, and thus a higher information capacity. Recently, the feasibility of this so-called mode group diversity multiplexing technique has been demonstrated. Simulations provide us with a means to better understand its operation and possibly increase its efficiency. The channel separation may be enhanced by employing a lens between the fibre and the detector, which is called mode-selective spatial filtering. Our numerical simulations of a mode group diversity multiplexing link, with and without mode-selective spatial filtering, are in agreement with the measurements.

The above discussion makes clear that the developed software code has a wide range of applicability. Moreover, it is built in a modular way and thus extensions, like the inclusion of more fibre quantities or different profile dopants, are straightforward.

Contents

Chapter 1

Introduction

1.1   The field of fibre optics

High-definition television, the internet, dike surveillance, and endoscopy. Just a short selection out of the numerous applications in which optical fibres can fulfill key roles. Of course, all these applications are subject to the ever increasing demands of the end-consumers, which often comes down to words like better, faster and cheaper. As a result, the field of fibre optics, which is the branch of research that deals with the design and utilisation of optical fibres, has become a major field of applied research over the past decades.

Fibre-optic telecommunication systems and sensor systems form two important application categories in the field of fibre optics. For telecommunication, optical fibres are especially designed to achieve large bandwidths, while keeping the transmission losses at bay. For sensor systems, small parameter changes in the fibre properties can be a measure for, for example, ruptures or temperature changes in the surrounding material. Obviously, all these applications put different constraints on the specifications of the employed optical fibre. An optical fibre is made of glass and/or plastic. By adding dopants to these base components, a refractive-index profile is created that is characteristic for the fibre, and allows light to be guided along its core.

In the design and manufacturing process of an optical fibre, the computer has become an indispensable tool. As a consequence of improved control over the production process, the match between a given design of the optical fibre and the actual fabricated product has improved considerably. As fibre optics is a mature field of research and current fibres are already quite good, improvements can only be achieved through the construction of fibre models and an efficient and meticulous computation of those quantities that specify the fibre.

1.2   Computational electromagnetics

In the late 1960s, the optical fibre has first been considered as a practical medium for communication, as difficulties regarding its attenuation proved bridgeable. Soon, several methods were developed to analyse the propagation of electromagnetic waves along these inhomogeneous cylindrical open waveguides. Initially, the main challenge was to treat the inhomogeneities in the radial direction, under the assumption that this inhomogeneous region was surrounded by a homogeneous medium and that the waveguide was circularly symmetric.

Mathematically, this problem can be described by Maxwell's equations, which form a system of coupled first-order partial differential equations. By a careful elimination of field components, one can arrive at a system of four first-order differential equations, or equivalently a pair of coupled second-order differential equations, or a single fourth-order ordinary differential equation. However, because of limited computer resources, initially one had to resort to approximate techniques for the evaluation of the propagation characteristics. Accurate numerical schemes to solve the differential equations were first introduced by Dil and Blok [19] in 1973, and have been expanded upon by Vassell [110] a year later.

With the advent of fast digital computers, universal software packages that, for example, are based on the finite-element method [81, 85], the finite-difference method [84, 119], or an integral-equation method [5] have become popular. Also approximate solution methods for Maxwell's equations, like ray asymptotics [91] and the weak-guidance approximation [33, 109], are frequently used to simplify and speed up the computations. Unfortunately, approximations are limited by inaccuracies and restricted to a certain albeit wide class of problems. Chiang [11] has written a review paper covering frequently used methods that are used for the analysis of optical fibres.

In view of the number of different and often conflicting specifications that the optical fibre should meet, the employed numerical method should be accurate, efficient and flexible. In particular one would like to employ a method that can be extended in a modular way, such that fibre specifications can easily be augmented. Further, the numerical scheme should be powerful enough to explain and predict experimentally observed wave phenomena. Additionally, it should lend itself to preventing any undesirable behaviour through a proper design of the refractive-index profile.

Nevertheless, the design process remains a cumbersome task as the odds for directly finding a feasible refractive-index profile that meets all set requirements turn out to be negligible. As a result, the parameters that define the profile should be carefully chosen and tuned, a task that has therefore often been assigned to an experienced (expensive) designer. Optimisation routines may offer a solution, as they search for the best parameter

settings to meet a set of pre-defined specifications. It is desirable that these routines are as time-efficient as possible. Thus far, genuine optimisation methods have hardly ever been applied to the design of optical fibres. The article by Bingle et al. [9] shows an initial impetus for our profile optimisation. A few other articles describe optimisation results in the field of fibre optics [26, 49, 51], but those are concerned with fibre Bragg gratings and photonic-crystal fibres.

While optimisation schemes can be applied for the design of the next generation of optical fibres, other techniques exist to achieve an increase in bandwidth of existing fibres. In particular, this is an issue for the multi-mode fibre, which primarily suffers from bandwidth limitations introduced by differential mode delay, i.e. a pulse spreads due to (small) differences in the group velocity of the propagating modes [36]. This is the main reason why these fibres are only used in short-range networks [53]. Diversity multiplexing techniques, like, for example, wavelength division multiplexing and time division multiplexing [48], are efficient methods to increase the information capacity of fibres.

Another promising multiplexing technique concerning the multi-mode fibre is called mode group diversity multiplexing [53]. Here, the idea is that for the right launching conditions, clusters of modes may be excited that are effectively confined spatially to annuli in the cross-sectional plane, and thus may be regarded as separate channels. By combining this technique with mode-selective spatial filtering, which consists of placing a properly designed lens at the fibre's end, up to five stable channels can be attained [102].

1.2.1   Selected research topics

From the discussion above, we have extracted several important contemporary problems on which this thesis will focus. For these problems, an adequate model of the optical fibre, and a robust numerical scheme to analyse the pertaining model are essential. Maxwell's equations form the basis for this scheme. Cast into the more convenient Marcuvitz-Schwinger equations [60], which consist of a coupled system of four differential equations, Dil and Blok [19] were the first to perform a numerical integration of this system in the radial direction. Along the lines of their work, we have implemented a vectorial full-wave modelling code. This code forms the cornerstone for the subsequent numerical computation of some typical fibre quantities.

In our numerical scheme, we distinguish between the single-mode fibre and the multi-mode fibre, for which different fibre quantities are of importance. For the former, we concentrate on the following quantities: dispersion, dispersion slope, mode-field diameter, effective area, bending loss, effective and theoretical cut-off wavelength and the MAC-value [69, 105]. For the multi-mode fibre, differential mode delay, differential mode attenuation, and mode coupling are considered as the most important quantities [36, 118].

We highlight one quantity in more detail, viz. the bending loss in a single-mode fibre. Many approximate modelling techniques have been developed to estimate the bending loss as a function of radius of curvature [22, 58, 108, 115]. Our numerical scheme, however, is the first rigorous one, and is intended to select the most appropriate approximate method. Subsequently, that approximate method has been extended to compute the bending losses of higher-order modes. Since the effective cut-off wavelength and indirectly the MAC-value are related to the bending loss of the first higher-order mode, these quantities are evaluated in approximate form as well.

On the basis of our inventory of fibre quantities, we have performed a refractive-index profile optimisation. Since the computation of the fibre quantities of a multi-mode fibre simply takes too long on contemporary computers, the full profile optimisation is limited to single-mode fibres. For the multi-mode power-law profile [89] only the optimum value of the power-law exponent g has been determined. For the single-mode fibre, we have chosen to discretise the profile in piecewise-linear segments. The endpoints of the line segments serve as the free optimisation parameters, which are key in any optimisation scheme. Although many different schemes are available, by and large, they can be subdivided into two categories, viz. statistically oriented optimisers and deterministic methods based on gradient information. For both methods, the cost function is pivotal, as it is the means to cast pre-set design goals in terms of the fibre quantities into a mathematical formula. The minimisation of the cost function, possibly with the aid of gradient information, is the aim of all these schemes.

As a last challenge, we have investigated certain wave phenomena that typically occur in multi-mode fibres. Differential mode delay, differential mode attenuation, and mode coupling are such phenomena. Not only do they affect the intensity pattern at the fibre's end, they also determine the bandwidth of the fibre. The differential mode delay has been computed for all modes, following the work by Bingle and de Hon [8]. The model allows for optimisation of the refractive index power-law profile to minimise differential mode delay and thus to maximise the bandwidth. Differential mode attenuation and mode coupling are introduced by an empirical formula [118] and via a set of coupled power equations, respectively [59]. In addition, we demonstrate the influence of an offset and/or tilted launching (position) on the intensity pattern at the fibre's end. Also, the effects of possible manufacturing defects in the fibre's refractive-index profile on the intensity pattern, based on the "108-fiber model" [40, 114], are shown.

Lastly, the mode group diversity multiplexing technique is discussed and experimentally obtained near-field patterns are compared with simulated ones. The launching conditions are optimised, and mode-selective spatial filtering is simulated to achieve a maximum number of separate channels.

1.3 Outline of the thesis

In Chapter 2, we introduce our optical waveguide model. On the basis of this model, we derive expressions for the electromagnetic fields. To this end, Maxwell's equations, which form the basis for all subsequent computations, are cast in the form of the Marcuvitz-Schwinger equations, which involve transverse field components only. By enforcing proper boundary conditions, the propagation coefficients of the modes propagating along the optical fibre are obtained. Next to this exact vectorial full-wave approach, we briefly touch upon the more popular but approximate weak-guidance approximation.

Once the foundation of our numerical scheme is laid, we introduce important fibre quantities, which typically characterise the optical fibre. Chapter 3 deals with their numerical computation. To keep the discussion tractable, we have subdivided this chapter in two parts, namely the numerical computation of the characteristics for the single-mode fibre and the one for the multi-mode fibre, respectively.

In Chapter 4, we focus on one of the fibre quantities in particular, viz. the bending loss. However, before we analyse the bent optical fibre, we derive electromagnetic field expressions for the bent slab waveguide, which is its two-dimensional equivalent. As an intermediate step, we compute the electromagnetic fields inside a perfectly conducting curved pipe. Through the use of the Lorentz' reciprocity theorem, we compute the vectorial full-wave bending losses in the bent fibre. These are compared with the bending losses that result from two frequently used scalar approximations. Subsequently, the best scalar approximation is extended to deal with higher-order modes, which is used in the computation of the effective cut-off wavelength and the MAC-value.

The refractive-index profile optimisation for the single-mode fibre is performed in Chapter 5. We compare globally oriented optimisation schemes with gradient-based deterministic ones. Further, we elaborate on the numerical computation of the pertaining gradients and demonstrate the difference between exact and (finite-difference) approximate gradient computations. Also the influence of the initial profile, the choice of the optimisation parameters and an optimised profile sensitivity analysis are treated in detail.

Chapter 6 deals with wave propagation along multi-mode fibre transmission links. We show the influence of an excitation with a radial offset and/or angular tilt on the intensity pattern at the fibre's end and produce patterns for the worst profile defects out of the "108-fiber model". Further, we simulate intensity patterns for the mode group diversity multiplexing technique and demonstrate the effect of mode-selective spatial filtering.

In the final chapter of this thesis, Chapter 7, the main conclusions are presented. Further research topics and recommendations for future development areas are addressed as well.

Chapter 2

Formulation of the problem

To analyse the propagation of light along the optical fibre, we have chosen to derive expressions for the electromagnetic fields by following early work of Dil and Blok [19]. Starting from Maxwell's equations, we arrive at a smaller system of coupled partial differential equations eliminating the longitudinal field components, i.e. the components along the waveguide. This system is referred to as the Marcuvitz-Schwinger equations [60]. We shall derive the Marcuvitz-Schwinger equations for a general system of orthogonal curvilinear coordinates, thus allowing for the analysis of both straight cylindrical waveguide structures and bent toroidal waveguide structures. Subsequently, we will discuss the numerical implementation and the limitations of the thus acquired numerical scheme.

As a last step, we briefly touch upon a widely used approximation, i.e. the weak-guidance approximation [33, 91]. This approximation will be compared with our exact reference method to compute the bending loss in Chapter 4. Further, it will serve as a basis for those occasions were full-wave methods prove too complex and as a means to provide physical interpretations.

2.1 The optical fibre model

The optical fibre is treated as a cylindrical open waveguide structure. A model is shown in Figure 2.1, where we have assumed circular symmetry. Hence, we neglect imperfections such as longitudinally varying ellipticity or corrugation. Such imperfections will be accounted for in Section 3.2 through a mode-coupling model. There, we will also address the influence of possible loss mechanisms, which are neglected elsewhere, by introducing a heuristic loss model. The shaded cross-sectional areas denote, from dark to light, the core, cladding and coating region(s). The coating may be surrounded by a jacket, although that is of no interest in our field analysis, as no power reaches this interface. Moreover, as long as sharp bends are absent in geometry of the fibre, we may omit the coating as
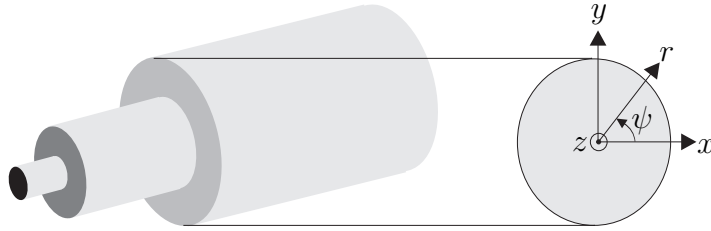
Figure 2.1: *Model of the optical fibre. From dark to light, the shaded cross-sectional areas denote the core, cladding and coating region, respectively.*

well from our model for the same reason. Therefore, we shall assume that the cladding is homogeneous and of infinite extent.

The core region, on the other hand, is considered to be radially inhomogeneous. Hence, the so-called refractive-index profile $n(r)$ may vary arbitrarily with respect to the radial coordinate r. By way of illustration, let us briefly consider two frequently encountered profiles in optics, namely the step-index profile and the power-law profile. The step-index profile consists, as the name already indicates, of a homogeneous core region, i.e. $n(r) = n_{\mathrm{co}}$, whereas the refractive-index profile of the power-law profile is given by [27]

$$n(r) = n_{\mathrm{co}} \sqrt{1 - 2\Delta(r/a)^g}, \tag{2.1}$$

where a denotes the core radius and typically the power-law exponent $g \geq 1$. The relative refractive-index difference Δ is given by [42]

$$\Delta = \left(n_{\mathrm{co}}^2 - n_{\mathrm{cl}}^2\right) / 2n_{\mathrm{co}}^2, \tag{2.2}$$

where n_{cl} denotes the refractive index of the (innermost) cladding. To allow for wave guidance, $n_{\mathrm{co}} = \max[n(r)] > n_{\mathrm{cl}}$. For the power-law profile defined by Eq. (2.1), this implies that $n_{\mathrm{co}} = n(0)$.

As we will explain in more detail in Section 3.1.2, the refractive index is also a function of wavelength λ. As a consequence, the Kramers-Kronig relations [54] apply, and the refractive index $n \in \mathbb{C}$, where the imaginary part corresponds to the absorption loss in the optical fibre. In [4] it is shown that for all optical fibre wavelengths this imaginary part may safely be neglected.

To measure the refractive-index profile, many measurement techniques have been introduced and implemented in commercial instruments [21, 27]. However, these instruments may use different wavelengths, and unfortunately, many articles fail to state the wavelength at which their profile has been defined.

To avoid confusion, we adhere to the standard measurement methods set by the ITU [42] in G.650–G.652. For multi-mode fibres, the reference test method for the numerical

aperture (NA), defined through $\text{NA} = \sqrt{n_{\text{co}}^2 - n_{\text{cl}}^2}$, is the far-field light distribution. The NA is to be measured at a wavelength of $850\,\text{nm}$, and therefore we assume that the refractive-index difference Δ in Eq. (2.2) is defined at this wavelength as well.

The refracted near-field technique [27], a frequently employed alternative certified test method, is commonly used to measure the refractive-index profile of single-mode fibres. The employed light source is typically a laser with a wavelength ranging from $630\,\text{nm}$ to $850\,\text{nm}$ [32, 80, 116]. Since a He–Ne laser with a wavelength of $632.8\,\text{nm}$ is often used, we assume that for single-mode fibres Δ is defined at that wavelength, unless explicitly stated otherwise.

For both the step-index profile and the (infinite) parabolic one, which is a power-law profile with power-law exponent $g = 2$, Maxwell's equations can be solved in closed form [73, 89]. It is therefore not surprising that the first approach to tackle an arbitrary refractive-index profile appearing in the literature consists of a composition of successive step-index profiles, the so-called *staircase approximation* [13, 64]. Examples of other discretisation methods to tackle the Maxwell's equations for a fibre with an arbitrary profile include the *perturbation method* [89] and the *finite-element method* [72]. The extension to a numerical scheme that follows the exact shape of the arbitrary profile was first introduced by Dil and Blok, and is known as the *direct integration method* [19]. In this method, Maxwell's equations are first transformed into a matrix-type system of differential equations, the so-called Marcuvitz-Schwinger equations. Subsequently, these equations are solved numerically by a direct integration along the radial coordinate, while taking the non-uniform profile into account. It is this method that we have employed to compute the propagation characteristics of the electromagnetic fields along the optical fibre.

2.2   The Marcuvitz-Schwinger equations

To derive the Marcuvitz-Schwinger equations for a general curvilinear coordinate system, we start from Maxwell's equations. In the space-time domain, they are given by

$$\nabla \times \boldsymbol{\mathcal{E}}(\mathbf{r}, t) + \partial_t \boldsymbol{\mathcal{B}}(\mathbf{r}, t) = -\boldsymbol{\mathcal{K}}(\mathbf{r}, t), \tag{2.3a}$$

$$-\nabla \times \boldsymbol{\mathcal{H}}(\mathbf{r}, t) + \partial_t \boldsymbol{\mathcal{D}}(\mathbf{r}, t) = -\boldsymbol{\mathcal{J}}(\mathbf{r}, t), \tag{2.3b}$$

where the script indicates an arbitrary time dependence and the boldface denotes the vectorial nature of the field quantities

$\boldsymbol{\mathcal{E}}$ electric field strength $\left[\text{Vm}^{-1}\right]$, $\boldsymbol{\mathcal{H}}$ magnetic field strength $\left[\text{Am}^{-1}\right]$,
$\boldsymbol{\mathcal{B}}$ magnetic flux density $\left[\text{Vsm}^{-2}\right]$, $\boldsymbol{\mathcal{D}}$ electric flux density $\left[\text{Asm}^{-2}\right]$,
$\boldsymbol{\mathcal{K}}$ magnetic current density $\left[\text{Vm}^{-2}\right]$, $\boldsymbol{\mathcal{J}}$ electric current density $\left[\text{Am}^{-2}\right]$.

The position in space is denoted by the position vector $\mathbf{r}$ with respect to a fixed reference frame, and t is the time coordinate.

We consider time harmonic fields with an $\exp(j\omega t)$ time factor, where the angular frequency ω is real and positive. Maxwell's equations in the frequency domain read

$$\nabla \times \mathbf{E}(\mathbf{r}, \omega) + j\omega \mathbf{B}(\mathbf{r}, \omega) = -\mathbf{K}(\mathbf{r}, \omega), \tag{2.4a}$$

$$-\nabla \times \mathbf{H}(\mathbf{r}, \omega) + j\omega \mathbf{D}(\mathbf{r}, \omega) = -\mathbf{J}(\mathbf{r}, \omega). \tag{2.4b}$$

Keeping the optical fibre configuration in the back of our mind, we assume that the material inside the waveguide is linear, time-invariant, isotropic, and inhomogeneous in the radial direction. Then, the constitutive relations are given by

$$\mathbf{D} = \varepsilon(r, \omega)\mathbf{E} = \varepsilon_0 \varepsilon_r(r, \omega)\mathbf{E}, \tag{2.5a}$$

$$\mathbf{B} = \mu(r, \omega)\mathbf{H} = \mu_0 \mu_r(r, \omega)\mathbf{H} = \mu_0 \mathbf{H}, \tag{2.5b}$$

where the scalar functions μ and ε denote the permeability and permittivity of the medium, respectively. Further, $\mu_0 = 4\pi 10^{-7}\,\mathrm{VsA^{-1}m^{-1}}$ and $\varepsilon_0 = (\mu_0 c_0^2)^{-1}\,\mathrm{AsV^{-1}m^{-1}}$, with c_0 denoting the speed of light in vacuum. The substitution of the constitutive relations in Eq. (2.4) yields

$$\nabla \times \mathbf{E}(\mathbf{r}, \omega) + j\omega\mu\mathbf{H}(\mathbf{r}, \omega) = -\mathbf{K}(\mathbf{r}, \omega), \tag{2.6a}$$

$$-\nabla \times \mathbf{H}(\mathbf{r}, \omega) + j\omega\varepsilon\mathbf{E}(\mathbf{r}, \omega) = -\mathbf{J}(\mathbf{r}, \omega). \tag{2.6b}$$

Next, let us eliminate the longitudinal components of the field. To keep the derivation as general as possible, we introduce general curvilinear coordinates. Although the coordinate systems which we will encounter are orthogonal, the derivation is given, for transparency, in tensor notation, and is therefore also valid for non-orthogonal coordinate systems. For those, unfamiliar with tensor calculus, the Marcuvitz-Schwinger equations have been derived for orthogonal coordinate systems by employing the well-known scale factors h_i [3], where $i = \{1, 2, 3\}$, in Appendix B.

In our tensor notation, we introduce a convention in which lowercase Roman subscripts and superscripts take the values $1, 2, 3$, and Greek subscripts and superscripts take the values $1, 2$. Consequently, the curl of a vector $\mathbf{v}$ is written as [96]

$$\nabla \times \mathbf{v} = \left(\partial_i v_j - v_k \Gamma_{ji}^k\right) \eta^{ijk} \mathbf{c}_k = (\partial_i v_j)\eta^{ijk}\mathbf{c}_k, \tag{2.7}$$

where $\{\mathbf{c}_k\}$ defines a set of covariant basis vectors. The associated set of contravariant basis vectors is denoted as $\{\mathbf{c}^k\}$. These sets of basis vectors are related through $\mathbf{c}_p \cdot \mathbf{c}^q = \delta_p^q$, where δ_p^q denotes the Kronecker delta . The contravariant components of the fully asymmetric permutation tensor are given by

$$\eta^{ijk} = g^{-\frac{1}{2}}\epsilon^{ijk}, \tag{2.8}$$

where ϵ^{ijk} denotes the Levi-Civita symbol. Further, $g = \det(g_{pq})$, where the metric tensor is defined through an inner product

$$g_{pq} = g_{qp} = \langle \mathbf{c}_p, \mathbf{c}_q \rangle. \tag{2.9}$$

The symmetry in the Christoffel symbol $\Gamma^k_{ji} = \Gamma^k_{ij}$ has been used to eliminate the symbol in the second step in Eq. (2.7). Hence, Maxwell's equations of Eq. (2.6) may be written, by raising and lowering indices, as

$$(\partial_i E_j)\,\eta^{ijk}\mathbf{c}_k + j\omega\mu H^k \mathbf{c}_k = -K^k \mathbf{c}_k, \tag{2.10a}$$

$$-(\partial_i H_j)\,\eta^{ijk}\mathbf{c}_k + j\omega\varepsilon E^k \mathbf{c}_k = -J^k \mathbf{c}_k. \tag{2.10b}$$

The longitudinal constituent of the electric field, which we will denote by the index 3, is obtained upon dot-multiplying both sides of Eq. (2.10b) by $g_{3m}\mathbf{c}^m$, i.e.

$$E_3 = (j\omega\varepsilon)^{-1}\, g_{3m} \left(\eta^{ijm}\partial_i H_j - J^m \right). \tag{2.11}$$

The transverse constituents, on the other hand, are obtained by dot-multiplying Eq. (2.10a) by $(\mathbf{c}_3 \times \mathbf{c}_n) = \eta_{3n\lambda}\mathbf{c}^\lambda$, which yields

$$\partial_3 E_n - \partial_n E_3 + j\omega\mu\eta_{3n\lambda}H^\lambda = -\eta_{3n\lambda}K^\lambda, \tag{2.12}$$

where we have used $\eta^{ij\lambda}\eta_{3n\lambda} = \delta^i_3\delta^j_n - \delta^i_n\delta^j_3$. To eliminate the longitudinal constituent, we substitute Eq (2.11) in Eq (2.12). Since $n = 3$ leads to the trivial identity $(0 = 0)$, we replace the index n by κ, which gives us

$$\partial_3 E_\kappa - \partial_\kappa \left[(j\omega\varepsilon)^{-1} \left(g_{3m}\eta^{ijm}\partial_i H_j - J_3 \right) \right] + j\omega\mu\eta_{3\kappa\lambda}H^\lambda = -\eta_{3\kappa\lambda}K^\lambda. \tag{2.13}$$

After using standard tensor arithmetic, we arrive at

$$-\partial_3 E_\kappa = j\omega\mu \left[\mathcal{V}^\sigma_{\kappa\mu} + k^{-2}\varepsilon\partial_\kappa\varepsilon^{-1} \left(g_{33}\eta^{\mu\sigma3} + g_{3\iota}\eta^{\mu\sigma\iota} \right) \partial_\mu \right] H_\sigma + \mathcal{V}^\sigma_{\kappa\mu}K^{\text{eff}}_\sigma, \tag{2.14}$$

where $k = \omega\sqrt{\mu\varepsilon}$ denotes the wavenumber of the pertaining medium and

$$K^{\text{eff}}_\sigma = \left[K_\sigma - (j\omega)^{-1}\eta^{\alpha\kappa3}g_{\sigma\alpha}\partial_\kappa\varepsilon^{-1}J_3 \right] \quad \text{and} \quad \mathcal{V}^\sigma_{\kappa\mu} = g_{33}g_{\kappa\mu}\eta^{\mu\sigma3}. \tag{2.15}$$

By duality, we may replace $\{E_k, H_k, \varepsilon, \mu, J_k, K_k\}$ by $\{H_k, -E_k, \mu, \varepsilon, K_k, -J_k\}$, which leads to

$$-\partial_3 H_\lambda = -j\omega\varepsilon \left[\mathcal{W}^\tau_{\lambda\nu} + k^{-2}\mu\partial_\lambda\mu^{-1} \left(g_{33}\eta^{\nu\tau3} + g_{3\varsigma}\eta^{\nu\tau\varsigma} \right) \partial_\nu \right] E_\tau - \mathcal{W}^\tau_{\lambda\nu}J^{\text{eff}}_\tau, \tag{2.16}$$

where

$$J^{\text{eff}}_\tau = \left[J_\tau + (j\omega)^{-1}\eta^{\beta\lambda3}g_{\tau\beta}\partial_\lambda\mu^{-1}K_3 \right] \quad \text{and} \quad \mathcal{W}^\tau_{\lambda\nu} = g_{33}g_{\lambda\nu}\eta^{\nu\tau3}. \tag{2.17}$$

Next, we cast the differential equations of Eq. (2.14) and Eq. (2.16) in matrix form and impose that $\mathbf{c}_3$ is orthogonal to $\mathbf{c}_1$ and $\mathbf{c}_2$, i.e. $g_{\varsigma 3} = g_{3\varsigma} = 0$. As a result, we obtain the following elegant form [75]

$$-\partial_3 \begin{pmatrix} E_\kappa \\ H_\lambda \end{pmatrix} = \begin{pmatrix} 0 & j\omega\mu\left[\mathcal{U}_{\kappa\mu} + \mathcal{T}_{\kappa\mu}\left(\varepsilon\right)\right] \\ j\omega\varepsilon\left[\mathcal{U}_{\lambda\nu} + \mathcal{T}_{\lambda\nu}\left(\mu\right)\right] & 0 \end{pmatrix} \begin{pmatrix} \epsilon^{\nu 3\tau} E_\tau \\ \epsilon^{\mu\sigma 3} H_\sigma \end{pmatrix}$$
$$+ \begin{pmatrix} \mathcal{U}_{\kappa\mu}\epsilon^{\mu\sigma 3} K_\sigma^{\mathrm{eff}} \\ \mathcal{U}_{\lambda\nu}\epsilon^{\nu 3\tau} J_\tau^{\mathrm{eff}} \end{pmatrix}, \tag{2.18}$$

where

$$\mathcal{U}_{\kappa\mu} = g^{-\frac{1}{2}} g_{33} g_{\kappa\mu} \quad \text{and} \quad \mathcal{T}_{\kappa\mu}(x) = k^{-2} x \partial_\kappa x^{-1} g^{-\frac{1}{2}} g_{33} \partial_\mu. \tag{2.19}$$

The longitudinal components E_3 and H_3 follow from Eq. (2.11) and are given by

$$E_3 = (j\omega\varepsilon)^{-1} g_{33} \left(\eta^{\mu\nu 3}\partial_\mu H_\nu - J^3\right),$$
$$H_3 = (j\omega\mu)^{-1} g_{33} \left(\eta^{\mu 3\nu}\partial_\mu E_\nu - K^3\right). \tag{2.20}$$

The differential equations of Eq. (2.18), which are expressed in terms of field components transverse to the longitudinal direction, are referred to as the Marcuvitz-Schwinger equations. Further, note that the right-hand side of both Eqs. (2.18) and (2.20) only contain operators that are independent of the longitudinal direction.

The Marcuvitz-Schwinger equations are not yet related to any waveguide structure, as they have to be supplemented with appropriate boundary conditions.

2.2.1 Boundary conditions

At the interface between two media, say 1 and 2, with different material properties, the following general boundary conditions hold, for a normal $\mathbf{n}$ pointing into medium 2 [83]

$$\mathbf{n} \times (\mathbf{E}_2 - \mathbf{E}_1) = -\mathbf{K}_s, \qquad \mathbf{n} \cdot (\mathbf{B}_2 - \mathbf{B}_1) = \rho_{s,k},$$
$$\mathbf{n} \times (\mathbf{H}_2 - \mathbf{H}_1) = \mathbf{J}_s, \qquad \mathbf{n} \cdot (\mathbf{D}_2 - \mathbf{D}_1) = \rho_{s,j}. \tag{2.21}$$

The subscripts 1 and 2 denote the limits of the fields on opposite sides of the interface in region 1 and 2, respectively. Further, $\mathbf{K}_s$ and $\mathbf{J}_s$ are the respective magnetic and electric surface current densities flowing along and tangential to the interface. Similarly, $\rho_{s,j}$ and $\rho_{s,k}$ denote the electric and magnetic surface charge densities. The presence of surface current and charge densities cause the pertaining electromagnetic field components to be discontinuous across the interface.

At any interface of the optical fibre in Figure 2.1, the boundary conditions simplify as surface charges and currents are absent throughout. Focusing on the core/cladding

interface, we impose that the tangential electric and magnetic field components must be continuous there.

Further, from energy considerations, we require that the electromagnetic fields remain bounded throughout. This implies that the fields must decay in the cladding of the optical fibre, while remaining finite at the core centre. All boundary conditions have to be satisfied to obtain physically meaningful results.

2.3   Electromagnetic field solutions

In the preceding sections, we set the basis for the computation of the electromagnetic fields in circularly cylindrical waveguides. Now, we will carry out the modal analysis for the straight optical fibre. On the basis of the model discussed in Section 2.1, and with an eye towards the constitutive relations of Eq. (2.5), we distinguish between the inhomogeneous core and homogeneous cladding region, i.e.

$$\mu(r,\omega) = \mu_0 \quad \text{and} \quad \varepsilon(r,\omega) = \varepsilon_0 \varepsilon_r(r,\omega) = \begin{cases} \varepsilon_0 \varepsilon_r(r,\omega) & \text{for} \quad r < a, \\ \varepsilon_0 \varepsilon_{r,\text{cl}}(\omega) & \text{for} \quad r \geq a, \end{cases} \tag{2.22}$$

where a is the core radius. The relative permittivity ε_r is related to the refractive-index profile of Eq. (2.1) by

$$\varepsilon_r(r,\omega) = n^2(r,\omega). \tag{2.23}$$

Upon imposing boundary conditions at the core/cladding interface at $r = a$, we obtain a characteristic equation for modal, i.e. source-free, field solutions, which provides the criterion for matching the electromagnetic field in the core to that in the cladding.

The Marcuvitz-Schwinger equations, which are given by Eq. (2.18) and Eq. (2.20), are especially well-suited for computing the field solutions in the core region. For the cladding region, on the other hand, field solutions can be derived analytically, and the use of the Marcuvitz-Schwinger equations is not essential. Since we are interested in the modal field solutions, we have to omit the source terms in the Marcuvitz-Schwinger equations.

In view of the geometry of the fibre, it is convenient to use cylindrical coordinates and regard the radial coordinate as the longitudinal constituent. Therefore, we introduce (covariant) basis vectors $\{\mathbf{c}_1, \mathbf{c}_2, \mathbf{c}_3\} = \{r\mathbf{u}_\psi, \mathbf{u}_z, \mathbf{u}_r\}$ with the corresponding (contravariant) coordinates $\{x^1, x^2, x^3\} = \{\psi, z, r\}$. As a consequence, the metric tensor of Eq. (2.9) reads $g_{pq} = \text{diag}(r^2, 1, 1)$, and hence the (covariant) electric and magnetic field components are given by $\{E_1, E_2, E_3\} = \{rE_\psi, E_z, E_r\}$ and $\{H_1, H_2, H_3\} = \{rH_\psi, H_z, H_r\}$, respectively.

Owing to the invariance in the ψ- and z-directions of the refractive-index profile, we

consider electromagnetic fields of the following form

$$\begin{pmatrix} E_k(\psi, z, \rho) \\ H_k(\psi, z, \rho) \end{pmatrix} = \sum_{m=-\infty}^{\infty} \begin{pmatrix} e_{k,m}(\rho) \\ h_{k,m}(\rho) \end{pmatrix} \exp\left(jm\psi\right) \exp\left(-j\hat{\omega}\zeta a^{-1}z\right), \qquad (2.24)$$

where $k = \{1, 2, 3\}$. Further, we have introduced a normalised frequency and a normalised radial coordinate, i.e.

$$\hat{\omega} = \omega a c_0^{-1} \quad \text{and} \quad \rho = r a^{-1}, \qquad (2.25)$$

respectively. Note that this wave propagates in the positive z-direction, as we have assumed an $\exp(j\omega t)$ time factor. To exploit the periodicity in the ψ-direction, we have employed a Fourier series with azimuthal index m, where $m \in \mathbb{Z}$. The computation of the unknown normalised propagation coefficient ζ forms the main challenge of the subsequent sections. As soon as all modal propagation coefficients are determined, the modal field amplitudes associated with a specific excitation can be computed, which renders full knowledge of the electromagnetic field inside the optical fibre.

For lossless straight fibres, the modal propagation coefficients are real and positive. However, we will demonstrate that in the case of a bent fibre ζ becomes complex with $\text{Re}(\zeta) > n_{\text{cl}}$.

2.3.1   The core region

To obtain electromagnetic field solutions in the core region, and more specifically at the core/cladding interface, we substitute Eq. (2.24) in the source-free Marcuvitz-Schwinger equations given by Eq. (2.18). We extract a single azimuthal component by multiplying both sides of the equation by $\exp(-j\ell\psi)$ and subsequently integrating over a period of length 2π. This yields a coupled system of differential equations for the radial dependence of the fields, which can be solved separately, owing to the Kronecker delta $\delta_{\ell,m}$, for each azimuthal index ℓ [18], i.e.

$$-d_\rho \hat{\mathbf{f}} = \rho^{-1} \begin{pmatrix} \mathbf{0} & jZ_0\varepsilon_r^{-1}\mathsf{M}\mathsf{J} \\ -jZ_0^{-1}\mathsf{M}\mathsf{J} & \mathbf{0} \end{pmatrix} \hat{\mathbf{f}}, \qquad (2.26)$$

with $\hat{\mathbf{f}} = (\rho e_\psi, e_z, \rho h_\psi, h_z)^T$, where T indicates transposition, and $Z_0 = \sqrt{\mu_0/\varepsilon_0}$ denotes the free-space plane-wave impedance. The matrices, written in Sans serif style, are given by

$$\mathsf{M} = \begin{pmatrix} \hat{\omega}\varepsilon_r\rho^2 - m^2/\hat{\omega} & m\zeta \\ m\zeta & -\hat{\omega}(\zeta^2 - \varepsilon_r) \end{pmatrix}, \quad \mathsf{J} = \begin{pmatrix} 0 & 1 \\ -1 & 0 \end{pmatrix}, \qquad (2.27)$$

where m denotes the azimuthal index. To arrive at Eq. (2.26), we have used the metric tensor for a cylindrical coordinate system. Note that the transverse operator $\mathcal{T}_{\kappa\mu}(\varepsilon)$ in

Eq. (2.19) only contains derivatives of ε with respect to the transverse coordinates z and ψ. Since ε_r is independent of these coordinates, the choice $x^3 = r$ implies that the transverse derivatives are absent.

The next step is to determine an initial field vector to commence with the numerical integration of Eq. (2.26). As we wish to incorporate an inhomogeneous core region in our numerical scheme, it seems logical to define the initial field vector at the core centre. However, we infer from Eq. (2.26) that $\rho = 0$ is a singular point of the differential equation. To circumvent this difficulty, we would have to start the integration at some point $\rho = \rho_0$ bounded away from zero. To this end, we first scale the electromagnetic field components of $\hat{\mathbf{f}}$ in a convenient way, i.e.

$$\hat{\mathbf{f}} = (\rho e_\psi, e_z, \rho h_\psi, h_z)^T = \rho^{|m|} (-jZ_0 p_1, -jZ_0 p_2, q_1, q_2)^T. \tag{2.28}$$

Consequently, we may rewrite Eq. (2.26) as follows

$$d_\rho \mathbf{f} = \rho^{-1} \mathsf{A}(\rho) \mathbf{f}, \tag{2.29}$$

where the field vector is given by $\mathbf{f} = (p_2, q_1, q_2, p_1)^T$, and

$$\mathsf{A}(\rho) = \begin{pmatrix} -|m| & \hat{\omega}(\zeta^2 - \varepsilon_r)/\varepsilon_r & m\zeta/\varepsilon_r & 0 \\ \hat{\omega}\rho^2 \varepsilon_r - m^2/\hat{\omega} & -|m| & 0 & -m\zeta \\ m\zeta & 0 & -|m| & \hat{\omega}(\zeta^2 - \varepsilon_r) \\ 0 & -m\zeta/\varepsilon_r & \hat{\omega}\rho^2 - m^2/\hat{\omega}\varepsilon_r & -|m| \end{pmatrix}. \tag{2.30}$$

We demand that the electromagnetic energy remains finite. An asymptotic analysis shows that the corresponding field vector $\mathbf{f}$ must remain regular for $\rho \downarrow 0$, and that its amplitude is bounded away from zero there. Hence, we may write a Taylor expansion about $\rho = 0$

$$\begin{align} \mathbf{f}(\rho) &= \mathbf{f}(0) + \rho \mathbf{f}'(0) + O(\rho^2), \tag{2.31a} \\ \mathsf{A}(\rho) &= \mathsf{A}(0) + \rho \mathsf{A}'(0) + O(\rho^2), \tag{2.31b} \end{align}$$

where the prime indicates differentiation to ρ. Upon substitution of Eq. (2.31) in Eq. (2.29), we readily obtain

$$\mathbf{f}'(0) + O(\rho) = \rho^{-1} \mathsf{A}(0)\mathbf{f}(0) + \mathsf{A}(0)\mathbf{f}'(0) + \mathsf{A}'(0)\mathbf{f}(0) + O(\rho), \tag{2.32}$$

from which we infer that

$$\begin{align} \mathsf{A}(0)\mathbf{f}(0) &= 0, \tag{2.33a} \\ \mathbf{f}'(0) &= [\mathsf{I} - \mathsf{A}(0)]^{-1}\mathsf{A}'(0)\mathbf{f}(0), \tag{2.33b} \end{align}$$

where I denotes the 4 by 4 identity matrix. The existence of the inverse of $[\mathsf{I} - \mathsf{A}(0)]$ in Eq. (2.33b) can be proven through construction. Further, note that the rank$[\mathsf{A}(0)] = 2$.

As a consequence, Eq. (2.33a) has two independent solutions, which we will denote as
$\mathbf{f}_1$ and $\mathbf{f}_2$, respectively. The corresponding derivatives are given by $\mathbf{f}_1'$ and $\mathbf{f}_2'$. Evidently,
the two-dimensional orthogonal complement of the null-space of $\mathsf{A}(0)$ is the span of the
solutions of Eq. (2.29) that are singular at $\rho = 0$. A complete set of solutions to Eq. (2.33)
is given by

$$(\mathbf{f}_1, \mathbf{f}_2) = \begin{pmatrix} 1 & \zeta \\ -m\hat{\omega}^{-1} & 0 \\ \zeta & \varepsilon_{r,0} \\ 0 & -m\hat{\omega}^{-1} \end{pmatrix}, \quad (\mathbf{f}_1', \mathbf{f}_2') = D \begin{pmatrix} 0 & \zeta \\ 0 & 0 \\ 0 & -\varepsilon_{r,0} \\ 0 & -m\hat{\omega}^{-1} \end{pmatrix}, \quad (2.34)$$

where

$$D = -\frac{m\partial_\rho\varepsilon_{r,0}}{(1+2m)\varepsilon_{r,0}}, \quad (2.35)$$

in which $\varepsilon_{r,0} = \varepsilon_r(0,\omega)$ denotes the permittivity at the fibre axis and $\partial_\rho\varepsilon_{r,0}$ its derivative.

Consequently, two independent field vector solutions $\mathbf{f}_1(\rho_i)$ and $\mathbf{f}_2(\rho_i)$ at $\rho = \rho_i$ in the
waveguide core are determined by a numerical integration of Eq. (2.29) from $\rho = \rho_0$ to
$\rho = \rho_i$, with ρ_0 small, starting from the initial field vectors $\mathbf{f}_1(\rho_0) = \mathbf{f}_1 + \rho_0\mathbf{f}_1'$ and $\mathbf{f}_2(\rho_0) = \mathbf{f}_2 + \rho_0\mathbf{f}_2'$. As we wish to impose the boundary conditions at the core/cladding interface, we
take $\rho_i = 1$. An adaptive Adams method has been used to perform the actual numerical
integration of this initial-value problem [37, 78].

2.3.2 The cladding region

In our model, the cladding region is considered to be of infinite extent, consisting of a
homogeneous medium $\varepsilon_{r,\text{cl}}$, as defined by Eq. (2.22). Owing to this homogeneity, the
electromagnetic field solutions can be derived analytically in terms of modified Bessel
functions from Eq. (2.26). Since the electromagnetic fields should carry finite energy, the
fields have to decay and/or radiate away from the fibre. Hence, the solutions can be
expressed in terms of modified Bessel functions of the second kind. Upon introducing the
variable

$$w = \hat{\omega}(\zeta^2 - \varepsilon_{r,\text{cl}})^{1/2}, \quad (2.36)$$

and a similar scaling as in Eq. (2.28)

$$\hat{\mathbf{f}} = (\rho e_\psi, e_z, \rho h_\psi, h_z)^T = K_{|m|}(-jZ_0 p_1, -jZ_0 p_2, q_1, q_2)^T, \quad (2.37)$$

the pertaining two independent field vector solutions are given by

$$[\mathbf{f}_3(\rho), \mathbf{f}_4(\rho)] = -jZ_0^{-1} \begin{pmatrix} 1 & 0 \\ v_1\varepsilon_{r,\text{cl}} & v_2 \\ 0 & 1 \\ v_2 & v_1 \end{pmatrix}, \quad \text{with} \quad \begin{cases} v_1 = \dfrac{\hat{\omega}\rho}{w}\dfrac{K_{|m|}'}{K_{|m|}}, \\ v_2 = -\dfrac{m\hat{\omega}\zeta}{w^2}, \end{cases} \quad (2.38)$$

where $\mathbf{f} = (p_2, q_1, q_2, p_1)^T$, and $K_{|m|} = K_{|m|}(w\rho)$ and $K'_{|m|} = K'_{|m|}(w\rho)$ denotes the modified Bessel function of the second kind and its derivative with respect to its argument, respectively.

For the sake of completeness, we note that the radial electromagnetic field components follow from Eq. (2.20) and throughout may be expressed in terms of the transverse field constituents, i.e.

$$
\begin{aligned}
E_r &= (\hat{\omega}\varepsilon_r)^{-1} Z_0 \left(\rho^{-1} m H_z + \hat{\omega}\zeta H_\psi \right), \\
H_r &= -(\hat{\omega}Z_0)^{-1} \left(\rho^{-1} m E_z + \hat{\omega}\zeta E_\psi \right).
\end{aligned}
\tag{2.39}
$$

2.3.3   The characteristic equation

The total field vector in the core region is a linear combination of the field vectors $\mathbf{f}_1$ and $\mathbf{f}_2$. In the cladding, the total field vector is a linear combination of $\mathbf{f}_3$ and $\mathbf{f}_4$. Mathematically, this implies that

$$
\mathbf{f}(\rho) = C_1 \mathbf{f}_1(\rho) + C_2 \mathbf{f}_2(\rho) \quad \text{for } \rho < 1, \tag{2.40a}
$$

$$
\mathbf{f}(\rho) = C_3 \mathbf{f}_3(\rho) + C_4 \mathbf{f}_4(\rho) \quad \text{for } \rho > 1, \tag{2.40b}
$$

where C_i, with $i = 1, \ldots, 4$, are arbitrary constant coefficients. Upon applying the boundary conditions at the core/cladding interface at $\rho = 1$, i.e. the transverse (to the boundary) electromagnetic field components must be continuous, we arrive at the following equality

$$
[\mathbf{f}_1(\rho)\ \mathbf{f}_2(\rho)\ \mathbf{f}_3(\rho)\ \mathbf{f}_4(\rho)]
\begin{pmatrix}
\rho^{|m|} C_1 \\
\rho^{|m|} C_2 \\
-K_{|m|} C_3 \\
-K_{|m|} C_4
\end{pmatrix}
\Bigg|_{\rho=1}
= \mathbf{0}.
\tag{2.41}
$$

Non-trivial solutions are obtained by solving the characteristic equation

$$
\mathsf{C}(\zeta) = \det [\mathbf{f}_1(\rho)\ \mathbf{f}_2(\rho)\ \mathbf{f}_3(\rho)\ \mathbf{f}_4(\rho)]|_{\rho=1} = 0, \tag{2.42}
$$

which yields the desired normalised modal propagation coefficients ζ_{mn}, where m denotes the azimuthal index and n the radial index. A Van Wijngaarden–Dekker–Brent root-finding scheme [78] is employed to find all propagation coefficients in a fast and highly accurate way. The corresponding eigenvector follows from Eq. (2.41). The subsequent substitution in Eq. (2.40) gives us the total transverse field vector for all values of ρ. Then, the modal electromagnetic field components are determined from Eqs. (2.24), (2.28) and (2.39). As a last step, each mode is normalised such that it carries unit power (e.g. see Eq. (3.14)).

In Figure 2.2, the propagation coefficients for step-index profiles and parabolic-index profiles, with a small refractive-index difference $\Delta = 0.3\,\%$ (upper), a moderate one of $\Delta = 2\,\%$ (middle) and an extremely large one of $\Delta = 15\,\%$ (lower), are set against the frequently used normalised frequency [89]

$$V = \hat{\omega} \left(\varepsilon_{r,0} - \varepsilon_{r,\mathrm{cl}} \right)^{1/2} . \tag{2.43}$$

Since V is a non-linear function of wavelength through the permittivity (see Eq. (3.8)) and $\hat{\omega} = 2\pi a \lambda^{-1}$, we have chosen a fixed $\lambda = 1550\,\mathrm{nm}$. To vary V, we have gradually increased the core radius a of the fibre. The refractive index differences are defined at $\lambda = 632.8\,\mathrm{nm}$.

Observe that for small contrasts, some modes are (nearly) degenerate. This degeneracy forms the basis of the so-called *weak-guidance approximation*, which we will discuss in Section 2.5. Further, we would like to point out that a refractive-index profile difference of $\Delta = 15\,\%$ is unusual among the available fibres nowadays, which have typical differences up to about $\Delta = 2\,\%$.

For all of the figures in Figure 2.2, the fundamental mode, HE_{11}, is described by the leftmost dispersion curves. Despite the fact that these curves all appear to approach the V-axis, the fundamental mode is never really cut off. The designation HE_{mn} stands for a hybrid mode for which H_z is dominant compared to E_z [36]. Hybrid modes EH_{mn}, on the other hand, have complementary properties and can propagate along the optical fibre as well. Further, we distinguish between transverse electric (TE) and transverse magnetic (TM) modes, for which $E_z = 0$, $H_z \neq 0$ and $H_z = 0$, $E_z \neq 0$, respectively. Both modes only exist for $m = 0$, since then Eq. (2.26) decouples into two sets of differential equations for which either $H_z = 0$ or $E_z = 0$. As a consequence, $m \geq 1$ holds for hybrid modes. For completeness, we mention that transverse electromagnetic (TEM) modes, for which both $H_z = 0$ and $E_z = 0$, do not occur in optical fibres.

2.4 Numerical considerations for short wavelengths

A pivotal aspect in the proposed computation of the electromagnetic fields in an optical fibre is formed by the numerical integration of a system of differential equations for the core region. However, at each integration step, inevitably, round-off errors are introduced due to the finite precision arithmetic of the computer [37]. To attain a high accuracy, a small adaptive step size is required. Due to the large number of integration steps, the total round-off error gradually increases. Especially for multi-mode fibres with large core radii, or conversely for short wavelengths, this error eventually imposes a limit on the accuracy of the numerical integration.
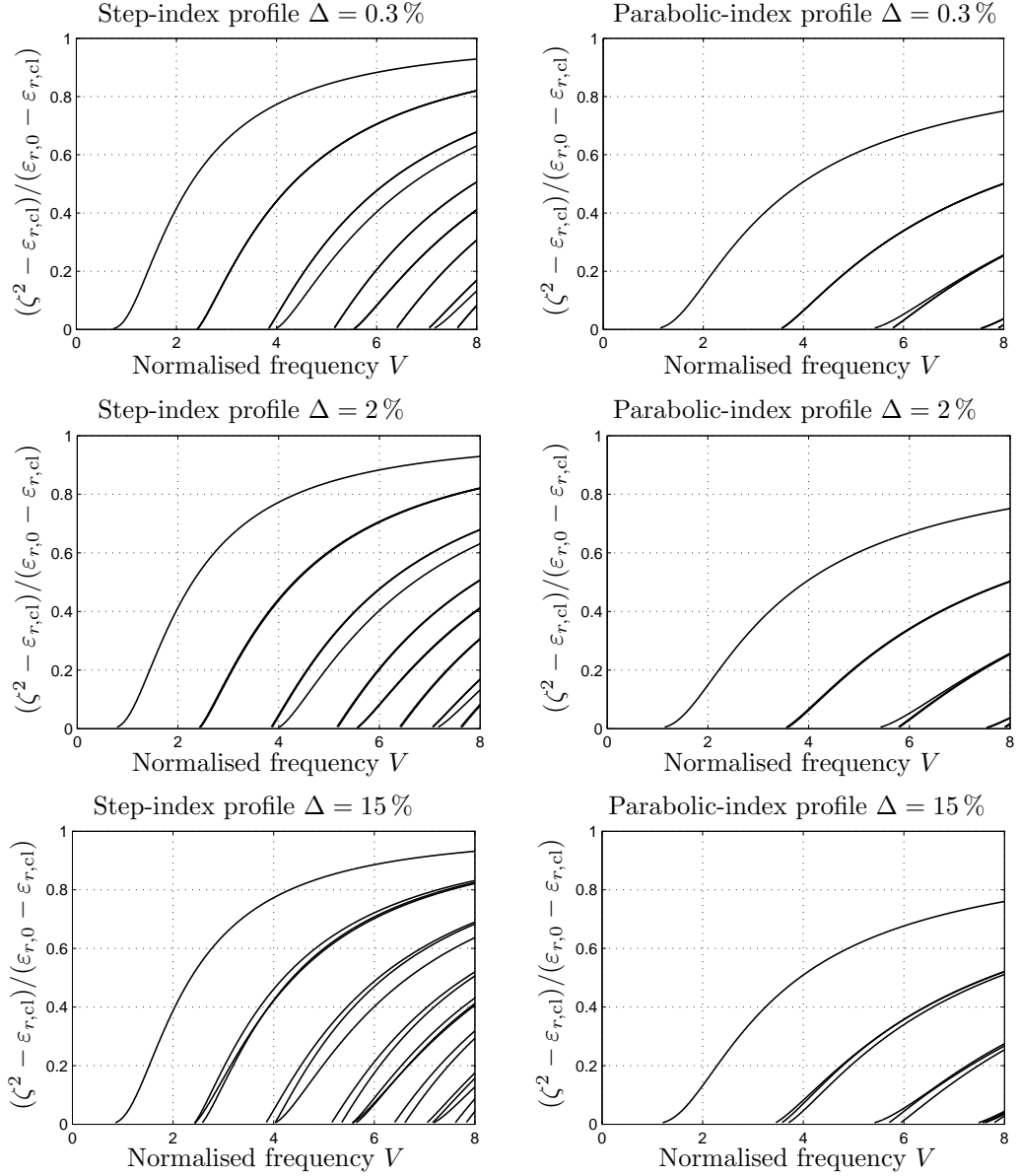
Figure 2.2: *Normalised propagation coefficients $(\zeta^2 - \varepsilon_{r,cl})/(\varepsilon_{r,0} - \varepsilon_{r,cl})$ of the modes propagating in a fibre with a step-index profile (left) and a parabolic-index profile (right), set against the normalised frequency V of Eq. (2.43). The upper figures are the results for a refractive-index difference of $\Delta = 0.3\%$, the middle ones correspond to $\Delta = 2\%$, whereas the lower ones are generated with $\Delta = 15\%$.*

It turns out that integration with an adaptive Adams method from the fibre axis towards the core/cladding transition is limited to core radii up to about 30λ with double precision arithmetic. To stretch this range, we have added the second-order derivative of the field vectors at the fibre axis in Eq. (2.33), i.e.

$$\mathbf{f}''(0) = [\mathsf{I} - 1/2\mathsf{A}(0)]^{-1} \left[1/2\mathsf{A}''(0) + \mathsf{A}'(0)[\mathsf{I} - \mathsf{A}(0)]^{-1}\mathsf{A}'(0) \right] \mathbf{f}(0), \qquad (2.44)$$

to Eq. (2.31), which reads

$$\mathbf{f}(\rho) = \mathbf{f}(0) + \rho\mathbf{f}'(0) + 1/2\rho^2\mathbf{f}''(0) + O(\rho^3). \tag{2.45}$$

The second-order derivatives of the initial vectors are given by

$$(\mathbf{f}_1'', \mathbf{f}_2'') = G \begin{pmatrix} -u^2 & -\zeta H \\ 2\hat{\omega}\varepsilon_{r,0} + mu^2\hat{\omega}^{-1} & 2\hat{\omega}\zeta\varepsilon_{r,0} \\ -u^2\zeta & m\left(\partial_\rho^2\varepsilon_{r,0} + D\partial_\rho\varepsilon_{r,0}\right) - u^2\varepsilon_{r,0} \\ 2\hat{\omega}\zeta & mH\hat{\omega}^{-1} + 2\hat{\omega}\varepsilon_{r,0} \end{pmatrix}, \tag{2.46}$$

where

$$G = (2m+2)^{-1} \quad \text{and} \quad H = u^2 + m\varepsilon_{r,0}^{-1}\partial_\rho^2\varepsilon_{r,0} + D\varepsilon_{r,0}^{-1}(2+3m)\partial_\rho\varepsilon_{r,0}, \tag{2.47}$$

with D given by Eq. (2.35), $u = \hat{\omega}(\varepsilon_{r,0} - \zeta^2)^{1/2}$, and $\partial_\rho^2\varepsilon_{r,0}$ denotes the second-order derivative with respect to ρ at the fibre axis. This reduces the number of integration steps since the starting point of integration, $\rho = \rho_0$, may be increased. In combination with an integration of the field solutions from both the fibre axis and the core/cladding transition towards half the core radius, we arrive at a maximal core radius of about 36λ.

Inspired by an article of Sung [95], we have employed extended precision arithmetic, with which we can increase the range of accurate results to core radii of up to 49λ. Since the system of differential equations tends to become slightly stiff for higher-order modes propagating close to the core/cladding transition, the backward differentiation formula (BDF) [78] is used for numerical integration at those intervals where the Adams method fails. A drawback of extended precision arithmetic forms the computation time, which may increase drastically depending on the used compiler and computer.

2.5   Weak-guidance approximation

The concept behind the weak-guidance approximation (WGA) was first introduced by Snyder in 1969 [91], and shortly thereafter, named as such by Gloge [33]. A complete overview and a further generalisation to arbitrary refractive-index profiles was given in the late 1970s by Snyder and Young [90]. The approximation consists of two simultaneous assumptions for the refractive-index difference Δ and the normalised frequency V, i.e.

$$\begin{cases} \Delta = \left(n_{\text{co}}^2 - n_{\text{cl}}^2\right)/2n_{\text{co}}^2 \ll 1, \\ V = \hat{\omega}\left(\varepsilon_{r,0} - \varepsilon_{r,\text{cl}}\right)^{1/2} \sim 1 \text{ or more.} \end{cases} \tag{2.48}$$

Under these assumptions, the longitudinal z-components of the electromagnetic field become negligible, and consequently, the cumbersome exact vectorial calculations can be replaced by scalar ones [109].

We employ the Cartesian field components E_x and E_y that are transverse with respect to the fibre axis. Similar to Eq. (2.24), these components are expanded into modes, e.g.

$$E_x = \sum_{\ell=-\infty}^{\infty} \Phi_\ell(\rho) \exp\left(j\ell\psi\right) \exp\left(-j\hat{\omega}\zeta a^{-1}z\right). \tag{2.49}$$

A similar expression holds for E_y. Under the assumption of weak guidance, the transverse field $\mathbf{E}_t$ satisfies the following scalar wave equation

$$\nabla_{t,n}^2 \mathbf{E}_t + \hat{\omega}^2 \left[\varepsilon_r(\rho) - \zeta^2\right] \mathbf{E}_t = 0, \tag{2.50}$$

where $\nabla_{t,n} = a\nabla_t$ denotes a normalised Laplacian with respect to the transverse coordinates. Note that we have replaced the azimuthal index m of Eq. (2.24) by ℓ. Obviously, these indices correspond to different modes, as Cartesian transverse components $\{E_x, E_y\}$ are different from cylindrical polar coordinates $\{E_r, E_\psi\}$. The modes in a weakly guiding fibre are known as linearly polarised $(\mathrm{LP}_{\ell n})$ modes, where n denotes the radial index [33].

Upon substituting Eq. (2.49) in Eq. (2.50), we obtain a second-order differential equation for the scalar $\Phi_\ell(\rho)$, i.e.

$$\left\{\rho\partial_\rho\rho\partial_\rho + \hat{\omega}^2\rho^2\left[\varepsilon_r(\rho) - \zeta^2\right] - \ell^2\right\}\Phi_\ell(\rho) = 0. \tag{2.51}$$

This equation can be solved analytically for piecewise-constant refractive-index profiles in terms of (modified) Bessel functions, analogous to the exact vectorial calculations. For non-uniform index profiles, again, one could resort to approximate methods, like the staircase approximation [13, 64] or the finite-element method [72]. But also here we have opted for an exact method, similar to the one outlined in the previous section. More specifically, we solve the second-order differential equation of Eq. (2.51) in the core region numerically and in the cladding region analytically. Next, we connect the pertaining field vectors at the core/cladding interface by employing boundary conditions, and obtain a characteristic equation, which may be solved to yield the desired propagation coefficient.

Let us start with the numerical scheme for the core region. We rewrite the second-order differential equation of Eq. (2.51) into a system of two first-order differential equations by introducing $\chi = \rho\partial_\rho\Phi$. In view of Eq. (2.28), we employ $\{\Phi, \chi\} = \rho^{|\ell|}\{g_\alpha, g_\beta\} = \rho^{|\ell|}\mathbf{g}$, which results in

$$d_\rho\mathbf{g} = \rho^{-1}\mathsf{B}(\rho)\mathbf{g}, \quad \text{where} \quad \mathsf{B}(\rho) = \begin{pmatrix} -|\ell| & 1 \\ \ell^2 - \hat{\omega}^2\rho^2\left[\varepsilon_r(\rho) - \zeta^2\right] & -|\ell| \end{pmatrix}. \tag{2.52}$$

This is the 2 by 2 system counterpart of Eq. (2.29). The initial field vector at $\rho = \rho_0$, with ρ_0 small, which is the starting point of the numerical integration of the differential

equations follows from a Taylor expansion about $\rho = 0$. By equating equal orders of ρ, we obtain

$$\mathbf{g}_1 = \begin{pmatrix} 1 \\ |\ell| \end{pmatrix}, \quad \mathbf{g}_1' = \mathbf{0}, \tag{2.53}$$

so that $\mathbf{g}_1(\rho_0) = \mathbf{g}_1 + \rho_0 \mathbf{g}_1'$.

Bounded analytical field solutions for the homogeneous cladding region $\varepsilon_{r,\mathrm{cl}}$ follow directly from Eq. (2.51), i.e.

$$\mathbf{g}_2 = \rho^{-|\ell|} \begin{pmatrix} K_{|\ell|}(w\rho) \\ w\rho K_{|\ell|}'(w\rho) \end{pmatrix}, \tag{2.54}$$

where w is defined by Eq. (2.36). Consequently, the core and cladding field vectors can now be represented by

$$\begin{aligned} \mathbf{g}(\rho) &= C_1 \mathbf{g}_1(\rho) \quad \text{for } \rho < 1, \\ \mathbf{g}(\rho) &= C_2 \mathbf{g}_2(\rho) \quad \text{for } \rho > 1, \end{aligned} \tag{2.55}$$

where C_i, with $i = 1, 2$, denote arbitrary constant coefficients. Since the field vector solutions must be continuous at the core/cladding interface, we arrive at the equality

$$[\mathbf{g}_1(\rho) \; \mathbf{g}_2(\rho)] \begin{pmatrix} C_1 \\ C_2 \end{pmatrix} \bigg|_{\rho=1} = \mathbf{0}, \tag{2.56}$$

and consequently, the characteristic equation for a weakly guiding fibre is given by

$$\mathsf{C}_{\mathrm{wga}}(\zeta) = \det \left[\mathbf{g}_1(\rho) \; \mathbf{g}_2(\rho) \right]\big|_{\rho=1} = 0. \tag{2.57}$$

The propagation coefficient $\zeta_{\ell n}$ for which this equation holds corresponds to an $\mathrm{LP}_{\ell n}$ mode, where ℓ is the azimuthal index and n the radial index. In Figure 2.3, the propagation coefficients for a step-index profile and a parabolic-index profile, with a small (weakly guiding) contrast $\Delta = 0.3\,\%$, are set against the normalised frequency V of Eq. (2.43). The refractive-index difference is defined at $\lambda = 632.8\,\mathrm{nm}$, whereas the simulations are performed at the wavelength $\lambda = 1550\,\mathrm{nm}$. To vary V, we gradually increase the core radius a of the fibre.

Note that these propagation coefficients are similar to the ones in the two upper graphs in Figure 2.2, i.e. the weak-guidance case. The number of degenerate vectorial modes is readily obtained if we relate the LP modes with indices $\{\ell, n\}$ to the vectorial modes with indices $\{m, n\}$, i.e.

$$\ell = \begin{cases} 1 & \text{for TE and TM modes } (m = 0), \\ m + 1 & \text{for EH modes } (m \geq 1), \\ m - 1 & \text{for HE modes } (m \geq 1). \end{cases} \tag{2.58}$$
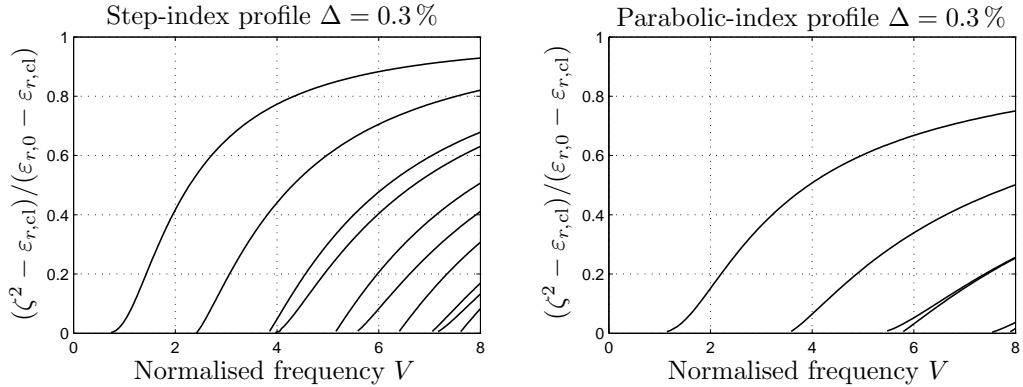
Figure 2.3: *Normalised propagation coefficients $(\zeta^2 - \varepsilon_{r,cl})/(\varepsilon_{r,0} - \varepsilon_{r,cl})$ of the modes propagating along a weakly-guiding step-index fibre (left) and weakly-guiding parabolic-index fibre (right) as a function of the normalised frequency V of Eq. (2.43).*

In comparison with the vectorial full-wave approach of the previous section the computation of the LP modes is less time consuming, as the system consists of 2 by 2 matrices instead of 4 by 4 ones. In Appendix E, we have performed a computation time and accuracy analysis of both approaches. There, it is demonstrated that the relative accuracy of the propagation coefficient is fair, namely of $O(10^{-6})$, with respect to the exact one for a weakly guiding fibre in the WGA, and therefore one often decides in favour of this simpler approach. On the other hand, the difference in computation time between both approaches is only a factor of 1.5. Hence, as we would like the field solutions to satisfy Maxwell's equations, all computations are performed by the vectorial full-wave approach, unless stated otherwise.

In the following, the WGA is used to compute the macrobending losses and the results are compared with the ones determined using a vectorial full-wave approach. Further, we employ the WGA to perform those computations for which full-wave computations become too complex, e.g. the computation of the effective cut-off wavelength and differential mode attenuation.

Chapter 3

Fibre characteristics

We will discuss the most significant quantities that characterise the optical fibre. We distinguish between the single-mode fibre (SMF) and the multi-mode fibre (MMF), for which alternative sets of quantities are considered to be of importance. For the single-mode fibre, we discuss the following fibre quantities:

- dispersion,

- dispersion slope,

- mode-field diameter and effective area,

- macro- and microbending losses,

- MAC-value[1], theoretical and effective cut-off wavelength.

For the multi-mode fibre, the dominant quantities are

- differential mode delay,

- inter- and intra-group coupling,

- differential mode attenuation.

For all quantities, we will discuss the underlying numerical computations. The foundation for these computations has been laid in Chapter 2.

---

[1]The MAC-value was first introduced by Chung [12] without commenting on the designation "MAC".

3.1   Single-mode fibre characteristics

For single-mode fibres, the fundamental properties of the fibre quantities are demonstrated on the basis of three frequently used step-index single-mode fibres, i.e. a conventional single-mode fibre (CSF), a dispersion-shifted fibre (DSF), and a dispersion compensating fibre (DCF). As the names already indicate, these fibres differ by their dispersion characteristics. In particular, the dispersion characteristic of the DCF is shifted downward in frequency with respect to that of the DSF, while the characteristic of the CSF is shifted upward. Obviously, we could have opted for single-mode fibres with more refined refractive-index profiles. However, the elementary step-index profile serves our purposes equally well.

The computed values of the fibre quantities will be used in our optimisation scheme in Chapter 5 to attain an optimised refractive-index profile.

3.1.1   Dispersion

As an electromagnetic pulse propagates along a single-mode optical fibre, generally, its shape will be distorted [2]. From an optimal transmission point of view, a distorted pulse is undesirable since it could lead to an increase of the bit-error rate. For example, pulse broadening may be such that the overlap with adjacent pulses renders the signal meaningless.

To control pulse distortion, we aim at a model which includes all types of dispersion, starting with one of the most tangible, i.e. the *chromatic dispersion*. This distortion effect is caused by the finite, albeit small spectral width $\Delta\omega$ of the light source, e.g. a laser or an LED, which illuminates the fibre. Since the propagation coefficient $\beta(\hat{\omega}) = \hat{\omega}\zeta a^{-1}$ (see Eq. (2.24)) of the propagating mode depends on the wavelength, it will endure a similar small variation $\Delta\beta$ as well. This variation can be made explicit, if we expand $\beta(\omega)$ in a Taylor series about the centre frequency of the light source ω_0, i.e.

$$\beta(\omega) = \sum_{n=0}^{\infty} \frac{d^n\beta(\omega_0)}{d\omega^n}(\omega - \omega_0)^n. \tag{3.1}$$

The first-order term ($n = 1$) is known as the group delay time per unit length, which is the reciprocal of the group velocity v_g, i.e.

$$v_g^{-1} \triangleq \frac{d\beta}{d\omega} = \frac{1}{c_0}\left(\zeta + \hat{\omega}\frac{d\zeta}{d\hat{\omega}}\right), \tag{3.2}$$

where c_0 denotes the speed of light in vacuum. The light pulse propagates at the group velocity along the fibre. The second-order term, which is the actual chromatic dispersion, is responsible for pulse spreading, and thus a distortion of the pulse. Although chromatic

dispersion occurs in both SMFs and MMFs, it is the dominant effect in SMFs, whereas it is mostly regarded as a side effect in MMFs. Mathematically, it is defined as

$$D \triangleq -\frac{2\pi c_0}{\lambda}\frac{d^2\beta}{d\omega^2} = -\frac{\hat{\omega}^2}{2\pi a c_0}\left(2\frac{d\zeta}{d\hat{\omega}} + \hat{\omega}\frac{d^2\zeta}{d\hat{\omega}^2}\right), \qquad (3.3)$$

where $\lambda = 2\pi a/\hat{\omega}$. Chromatic dispersion is a combination of two dispersion effects, namely material and waveguide dispersion [89]. The first encompasses the wavelength dependence of the material medium, as defined by Eq. (2.22). The second one refers to the effect that the propagation coefficient is wavelength dependent even in the absence of material dispersion. Material dispersion is included in Eq. (3.3) via the so-called Sellmeier equation, which will be discussed in Section 3.1.2. The total chromatic dispersion follows from repeated direct differentiation of ζ with respect to frequency.

Typical chromatic dispersion plots of three distinct step-index single-mode fibres, the conventional single-mode fibre (CSF), the dispersion-shifted fibre (DSF) and the dispersion compensating fibre (DCF), are shown in Figure 3.1. In Table 3.1, the specifications
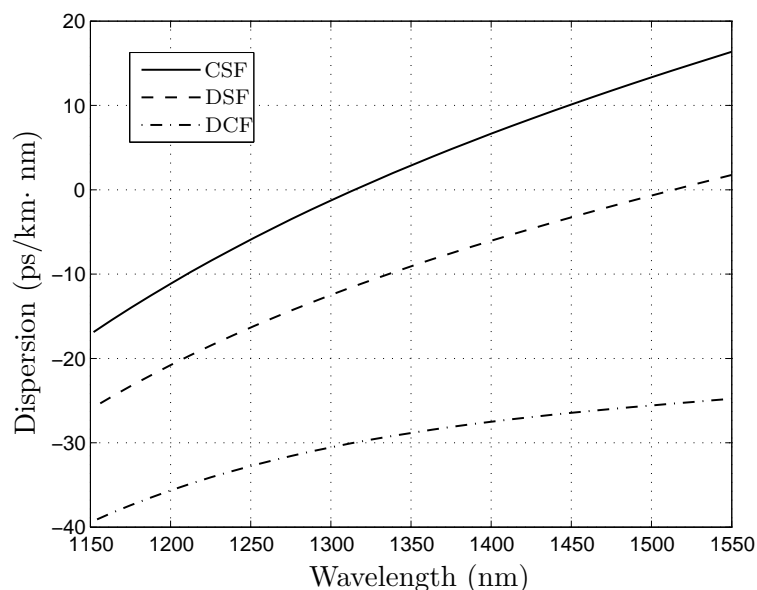
Figure 3.1: *Chromatic dispersion of a CSF, DSF and DCF where waveguide dispersion is included via the Sellmeier equation of Eq. (3.8), with $X^F = 0$ in Eq. (3.9).*

for these fibres are listed explicitly. The refractive-index difference Δ is defined at a wavelength of 632.8 nm, as discussed in Section 2.1. Observe that a decrease in the core radius and a simultaneous increase of the refractive-index difference lower the dispersion over the entire wavelength range.

The wavelength, λ_D, at which $D(\lambda_D) = 0$ is called the zero-dispersion wavelength. The CSF has a typical λ_D of about 1310 nm, which corresponds to the optical telecommuni-

Table 3.1: *Specifications for the CSF, DSF and DCF.*

	CSF	DSF	DCF
Core radius $a(\mu m)$	4.1	2.3	1.5
Refractive-index difference $\Delta(\%)$	0.27	0.75	2.0
Zero-dispersion wavelength λ_D (nm)	1315	1514	-

cation window. The DSF, on the other hand, which owes its name to the shift in λ_D, has by definition a λ_D close to 1550 nm [42]. However, zero dispersion is not always a desirable effect. For example, to transmit ultrashort pulses, near-zero dispersion is often not recommended as it enhances non-linear phenomena (see Section 3.1.3). In that case, a link of CSFs and DCFs, where the first have a positive and the last a negative dispersion at $\lambda = 1550$ nm, can be used to let the dispersion effects cancel, without introducing unwanted non-linear effects [27].

Further, we mention *polarisation-mode dispersion* (PMD) as a limiting factor for the transmission capacity of the single-mode fibre, as it distorts a pulse as well. As an example, let us consider the fundamental mode, which consist of two degenerate modes of propagation, distinguishable by their polarisation. Due to random birefringence in the fibre, for example induced by external stresses or by the manufacturing process, the propagation coefficients of these modes will fluctuate along the fibre in different ways. As a consequence, the pulse will be distorted [35].

Numerical computation

Mathematical expressions for the group velocity and the dispersion have been given in Eq. (3.2) and Eq. (3.3), respectively. Key quantities are the derivatives of the normalised propagation coefficient ζ with respect to $\hat{\omega}$. To compute these derivatives, let us recall the characteristic function $\mathsf{C}(\zeta)$ of Eq. (2.42). Since $\mathsf{C}(\zeta) = 0$ holds for all $\hat{\omega}$, its derivative with respect to $\hat{\omega}$ results in

$$\frac{d\mathsf{C}(\zeta)}{d\hat{\omega}} = 0 \quad \Rightarrow \quad \frac{d\zeta}{d\hat{\omega}} = -\frac{\partial_{\hat{\omega}}\mathsf{C}}{\partial_{\zeta}\mathsf{C}}, \tag{3.4}$$

where

$$\partial_{\alpha}\mathsf{C} = \det\left[\partial_{\alpha}\mathbf{f}_1(\rho)\ \mathbf{f}_2(\rho)\ \mathbf{f}_3(\rho)\ \mathbf{f}_4(\rho)\right]\big|_{\rho=1} + \det\left[\mathbf{f}_1(\rho)\ \partial_{\alpha}\mathbf{f}_2(\rho)\ \mathbf{f}_3(\rho)\ \mathbf{f}_4(\rho)\right]\big|_{\rho=1}$$
$$+ \det\left[\mathbf{f}_1(\rho)\ \mathbf{f}_2(\rho)\ \partial_{\alpha}\mathbf{f}_3(\rho)\ \mathbf{f}_4(\rho)\right]\big|_{\rho=1} + \det\left[\mathbf{f}_1(\rho)\ \mathbf{f}_2(\rho)\ \mathbf{f}_3(\rho)\ \partial_{\alpha}\mathbf{f}_4(\rho)\right]\big|_{\rho=1}, \tag{3.5}$$

in which α is either ζ or $\hat{\omega}$. To determine $\partial_{\alpha}\mathbf{f}_1$ and $\partial_{\alpha}\mathbf{f}_2$ at the core/cladding interface ($\rho = 1$), we differentiate the system of first-order differential equations in Eq. (2.29) with

respect to α. As a result, we arrive at the following expanded system

$$
d_\rho \begin{pmatrix} \mathbf{f} \\ \partial_{\hat{\omega}} \mathbf{f} \\ \partial_\zeta \mathbf{f} \end{pmatrix} = \rho^{-1} \begin{pmatrix} \mathsf{A} & 0 & 0 \\ \partial_{\hat{\omega}} \mathsf{A} & \mathsf{A} & 0 \\ \partial_\zeta \mathsf{A} & 0 & \mathsf{A} \end{pmatrix} \begin{pmatrix} \mathbf{f} \\ \partial_{\hat{\omega}} \mathbf{f} \\ \partial_\zeta \mathbf{f} \end{pmatrix}. \tag{3.6}
$$

The partial derivatives of the matrix A and of the initial vectors $\mathbf{f}_1(\rho_0)$ and $\mathbf{f}_2(\rho_0)$ are readily determined from Eqs. (2.30) and (2.34). Numerical integration of this coupled system yields two independent field vectors at $\rho = 1$, which provides two of the elements required for the computation of Eq. (3.5). Further, note that the matrix $\partial_{\hat{\omega}} \mathsf{A}$ contains the derivative $\partial_{\hat{\omega}} \varepsilon_r$, as the material is dispersive. This derivative is computed from the Sellmeier equation, which we will discuss in Section 3.1.2. The derivatives of the cladding field vectors $\partial_\alpha \mathbf{f}_3$ and $\partial_\alpha \mathbf{f}_4$ at $\rho = 1$ are obtained from a direct differentiation with respect to α of the field vectors in Eq. (2.38). This completes the calculation of $\partial_\alpha \mathsf{C}$, and as a result of $d\zeta/d\hat{\omega}$ in Eq. (3.4).

An extension to higher-order derivatives of ζ with respect to $\hat{\omega}$ follows directly from Eq. (3.4) by repeated differentiations. To compute the chromatic dispersion in Eq. (3.3), the second-order derivative is required, which is in terms of the characteristic function $\mathsf{C}(\zeta)$ given by

$$
\frac{d^2\zeta}{d\hat{\omega}^2} = -\frac{(\partial_{\hat{\omega}} \mathsf{C})^2 \, \partial_\zeta^2 \mathsf{C} - 2\partial_{\hat{\omega}\zeta}^2 \mathsf{C} \partial_{\hat{\omega}} \mathsf{C} \partial_\zeta \mathsf{C} + (\partial_\zeta \mathsf{C})^2 \, \partial_{\hat{\omega}}^2 \mathsf{C}}{(\partial_\zeta \mathsf{C})^3}. \tag{3.7}
$$

The pertaining second-order derivatives of $\mathsf{C}(\zeta)$ are obtained by expanding Eq. (3.5) accordingly, which yields second-order derivatives of the field vectors as well, in particular $\partial_{\hat{\omega}}^2 \mathbf{f}$, $\partial_\zeta^2 \mathbf{f}$ and $\partial_{\hat{\omega}\zeta}^2 \mathbf{f}$. For the core region, these vectors are obtained by expanding the system of Eq. (3.6). For the cladding region, the derivatives of the field vectors are again derived analytically.

The same derivation holds for the case of a weakly guiding fibre, with the characteristic equation given by Eq. (2.57). An accuracy comparison of the chromatic dispersion between the exact method and the weak-guidance approximation is discussed in Appendix E.

3.1.2   The Sellmeier equation

To model the dispersion properties of the media in the optical fibre, a lot of dispersion formulae exist that incorporate the wavelength dependence of the refractive index [4]. In general, these empirical equations are only valid in the spectral range of glass where material absorption is negligible, i.e. $0.4\,\mu\mathrm{m} < \lambda < 2.3\,\mu\mathrm{m}$, and have varying degrees of precision. We employ the so-called Sellmeier equation, which is favourable for its excellent data fitting properties of measured refractive indices. As a result, it has an overall accuracy

of $\pm 6 \cdot 10^{-5}$ over the spectral range of interest. The Sellmeier equation reads

$$\varepsilon_r(\rho, \omega) = n^2(\rho, \omega) = 1 + \sum_{i=1}^{3} b_i \lambda^2 \left(\lambda^2 - \lambda_i^2\right)^{-1} = 1 + \sum_{i=1}^{3} b_i \hat{\omega}_i^2 \upsilon^{-1}, \qquad (3.8)$$

where $\upsilon = \hat{\omega}_i^2 - \hat{\omega}^2$. Further, b_i and λ_i denote the Sellmeier parameters, which are functions of dopant concentrations, and $\lambda_i = 2\pi a / \hat{\omega}_i$.

Since the available dopants are numerous, a proportional number of Sellmeier parameters exist [48]. To have enough degrees of freedom to alter the refractive-index profile over a wide range, we have opted for ternary $GeO_2/F/SiO_2$ doped PCVD (Plasma-Activated Chemical Vapour Deposition)-silica fibres. For these dopants the Sellmeier parameters are given by [38]

$$b_i(X^{\mathrm{Ge}}, X^{\mathrm{F}}) = b_i^0 + X^{\mathrm{Ge}} db_i^{\mathrm{Ge}} + X^{\mathrm{F}} db_i^{\mathrm{F}}, \qquad (3.9a)$$

$$\lambda_i(X^{\mathrm{Ge}}, X^{\mathrm{F}}) = \lambda_i^0 + X^{\mathrm{Ge}} d\lambda_i^{\mathrm{Ge}} + X^{\mathrm{F}} d\lambda_i^{\mathrm{F}}, \qquad (3.9b)$$

where b_i^0 and λ_i^0 denote the zero-order Sellmeier coefficients for pure silica, and where db_i^{Ge}, $d\lambda_i^{\mathrm{Ge}}$, db_i^{F}, $d\lambda_i^{\mathrm{F}}$ are the material specific first-order variation terms. Their values are listed in Table 3.2. The advantage of this approach lies in the possibility to alter specific doping

Table 3.2: *The Sellmeier parameters for Germanium and Fluor.*

i	b_i^0	db_i^{Ge}	db_i^{F}	λ_i^0	$d\lambda_i^{\mathrm{Ge}}$	$d\lambda_i^{\mathrm{F}}$
1	0.697668	0.031510	-3.234366	0.070861	0.001677	-1.108703
2	0.407339	0.267302	0.164911	0.113600	0.032138	0.752919
3	0.889883	-0.012950	1.369490	9.784231	0.318034	2.906858

concentrations, viz. the Fluorine (F) mole fraction X^{F} and the Germanium (GeO_2) mole fraction X^{Ge}, independently. An increase in GeO_2 increases the refractive index, whereas an increase in Fluorine decreases it, as is shown in Figure 3.2. Moreover, Fluorine does not introduce absorption bands near operating optical wavelengths, and suppresses unwanted water content.

In our model, we have assumed that X^{F} is piecewise constant in the core and cladding region, while $X^{\mathrm{Ge}}(\rho)$ may vary arbitrarily in the core region, but must be constant in the cladding. If one wishes to use different dopants than the ones we have chosen, only the Sellmeier parameters of Eq. (3.9), with their corresponding coefficients, need to be changed, as Eq. (3.8) remains valid.

First-order derivatives of the permittivity profile with respect to ρ and $\hat{\omega}$, which occur
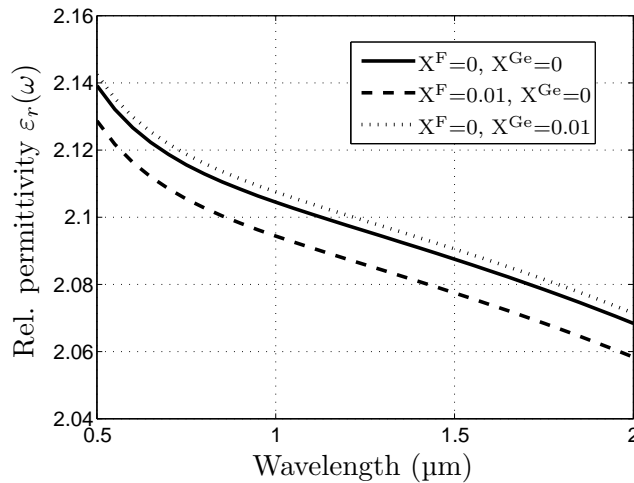
Figure 3.2: *The relative permittivity as a function of the wavelength computed by the Sellmeier equation for different dopant concentrations.*

in Eq. (2.35), Eq. (2.47) and Eq. (3.6), are now, with the aid of Eq. (3.8), easily derived

$$\partial_\rho \varepsilon_r = \sum_{i=1}^{3} \hat{\omega}_i v^{-1} \left[\hat{\omega}_i d_\rho b_i - 2v^{-1} b_i \hat{\omega}^2 d_\rho \hat{\omega}_i \right], \quad \partial_{\hat{\omega}} \varepsilon_r = \sum_{i=1}^{3} 2b_i \hat{\omega}_i^2 \hat{\omega} v^{-2}. \tag{3.10}$$

To validate the implementation of the Sellmeier equation for PCVD fibres in our numerical code, we have computed the dispersion via Eq. (3.3) for a depressed cladding PCVD single-mode fibre specified by Hermann and Wiechert [38], and have compared our results with their measured data and computed values. The refractive-index difference profile at $\lambda = 632.8$ nm for this fibre is plotted in Figure 3.3. The corresponding amounts of Germanium and Fluorine mole fractions are shown in Figure 3.4. In the core region
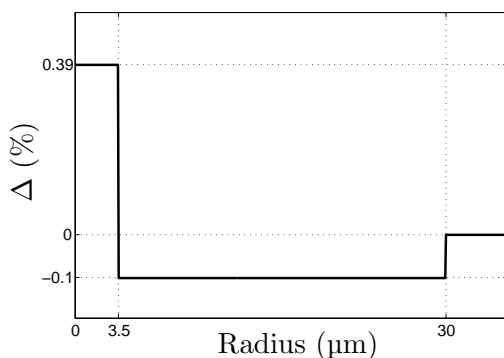
Figure 3.3: *Refractive-index difference profile given at $\lambda = 632.8$ nm.*
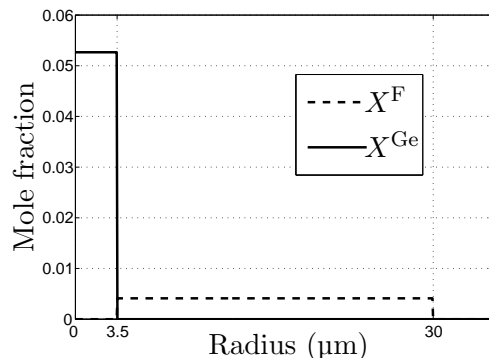
Figure 3.4: *Fluorine (X^F) and Germanium (X^{Ge}) concentrations as a function of radius.*

($r < 3.5$ μm), $X^{Ge} \neq 0$ and $X^F = 0$, in the cladding region up to $r = 30$ μm, $X^{Ge} = 0$ and

$X^F \neq 0$, and in the remainder of the cladding $X^{Ge} = X^F = 0$. In comparison to a step-index single-mode fibre without depression, the depressed cladding fibre is favourable for its enhanced mode confinement, and, as a result, for its high bend tolerance.

Recall that it was stated in Section 2.1 that the cladding region has to be homogeneous throughout to limit the numerical integration of the system in Eq. (2.29). Since the profile is not homogeneous until $r = 30\,\mu m$, we have to integrate the system fibre up to this boundary, instead of up to the actual core/cladding interface at $r = 3.5\,\mu m$. At the employed wavelengths, this does not pose problems for our numerical integration scheme. Therefore, we have not included the depressed cladding fibre as a separate case in our program. However, if one wishes to avoid the additional numerical integration over the region $3.5\,\mu m < r < 30\,\mu m$, one can make use of the *piecewise* homogeneity of this region, as it yields solutions in terms of Bessel functions with known arguments. These solutions have to be connected to the fields at both interfaces such that the continuity conditions hold, resulting in an eigenvalue problem with zero eigenvalues, similar to the approach discussed for the staircase approximation [13, 64].

The dispersion results are shown in Figure 3.5. The computed values obtained by Eq. (3.3) and [38] coincide, while the dispersion measurements are somewhat off. According to Hermann and Wiechert, this difference may be due to insufficient measurement resolution in the preform characterisation step. Although the use of the Sellmeier model seems fully justified, the Sellmeier parameters may be replaced by more accurate ones in the future.
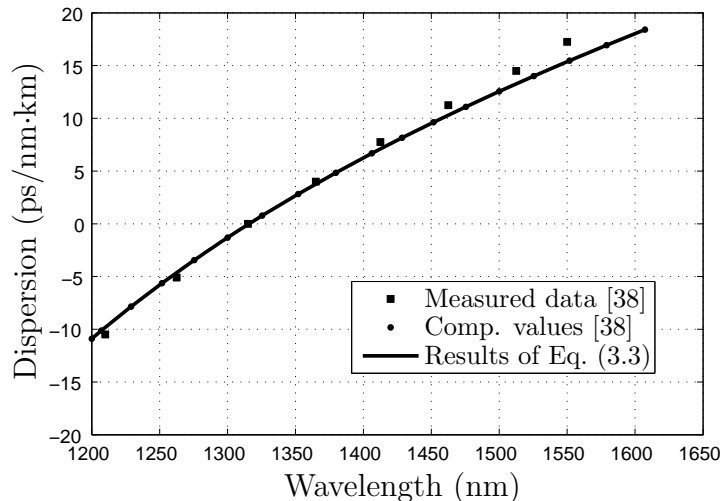
Figure 3.5: *Dispersion plot for the depressed cladding fibre of Figure 3.3. Squares and dots, respectively, correspond to measured and computed values in [38]. The solid line shows our results.*

3.1.3   Dispersion slope

The dispersion slope, which corresponds to the third-order term in the series in Eq. (3.1), is defined as [59]

$$S \triangleq \frac{d^2 D}{d\lambda^2} = \frac{\hat{\omega}^3}{(2\pi a)^2 c_0} \left(4\frac{d\zeta}{d\hat{\omega}} + 5\hat{\omega}\frac{d^2\zeta}{d\hat{\omega}^2} + \hat{\omega}^2\frac{d^3\zeta}{d\hat{\omega}^3} \right). \tag{3.11}$$

For frequencies near the zero-dispersion wavelength λ_D, the inclusion of the third-order term is necessary, as the second-order term in the series vanishes ($D \approx 0$). For an ultrashort pulse, which has a large spectral width, the third-order term has to be taken into account as well even when $D \neq 0$, since the term $(\omega - \omega_0)^3$ in the expansion in Eq. (3.1) is not yet negligible.

In [2], it has been proven that a large value of the dispersion slope introduces rapid undesirable fluctuations in the trailing edge of the transmitted electromagnetic pulse, and should therefore be avoided as well. In Figure 3.6, the dispersion slopes for the three fibres in Table 3.1 are shown.
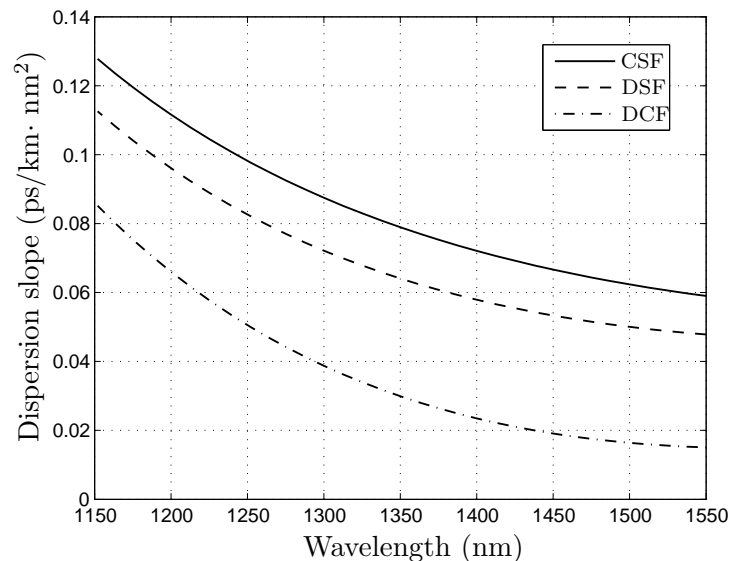
Figure 3.6: *Dispersion slope of the CSF, DSF and DCF specified in Table 3.1.*

Numerical computation

The dispersion slope S, given by Eq. (3.11), is obtained by a straightforward extension of the method introduced in Section 3.1.1. There, we have discussed the computation of the first-order and second-order derivatives of the normalised propagation coefficient

with respect to $\hat{\omega}$. To compute the dispersion slope, the computation of the third-order derivative remains, i.e.

$$
\frac{d^3\zeta}{d\hat{\omega}^3} = -\left(\partial_\zeta \mathsf{C}\right)^{-1} \left[\partial_{\hat{\omega}}^3 \mathsf{C} + \left(\frac{d\zeta}{d\hat{\omega}}\right)^3 \partial_\zeta^3 \mathsf{C} + 3 \left(\frac{d\zeta}{d\hat{\omega}}\right)^2 \partial_{\hat{\omega}\zeta^2}^3 \mathsf{C} \right.
$$
$$
\left. + 3 \left(\frac{d\zeta}{d\hat{\omega}}\right) \partial_{\hat{\omega}^2\zeta}^3 \mathsf{C} + 3 \left(\frac{d\zeta}{d\hat{\omega}}\right) \left(\frac{d^2\zeta}{d\hat{\omega}^2}\right) \partial_\zeta^2 \mathsf{C} + 3 \left(\frac{d^2\zeta}{d\hat{\omega}^2}\right) \partial_{\hat{\omega}\zeta}^2 \mathsf{C} \right]. \quad (3.12)
$$

As a consequence, Eq. (3.5) has to be extended accordingly. This, in turn, implies that the system of differential equations of Eq. (3.6) becomes larger and third-order derivatives of the matrix A, and the initial and cladding field vectors have to be derived.

In Appendix E, we have performed an accuracy comparison of the dispersion slope between the exact method and the weak-guidance approximation.

3.1.4 Mode-field diameter and effective area

In single-mode fibres, the mode-field diameter (MFD) is of greater importance than the core diameter [69]. This quantity essentially specifies the transverse extent of the fundamental mode field, corresponding to what one might think of as the spot size. A mismatch in MFD between two connected fibres affects the splice loss. Further, also estimates for cut-off wavelength, backscattering characteristics, microbending and macrobending losses can be obtained from the MFD. Usually, the MFD is given at the optical operating wavelengths of 1310 nm and 1550 nm. As there are several definitions of the MFD, we limit ourselves to the two that are most commonly used, i.e. the near-field rms MFD d_I and the far-field rms MFD d_{II}, which are given by

$$
d_I^2 = 8a^2 \frac{\displaystyle\int_{A_\infty} S(\rho)\rho^3 d\rho d\psi}{\displaystyle\int_{A_\infty} S(\rho)\rho d\rho d\psi}, \quad d_{II}^2 = 32a^2 \frac{\displaystyle\int_{A_\infty} S(\rho)\rho d\rho d\psi}{\displaystyle\int_{A_\infty} \frac{[d_\rho S(\rho)]^2}{S(\rho)}\rho d\rho d\psi}, \quad (3.13)
$$

where A_∞ denotes the infinite cross-section of the fibre and

$$
S(\rho) = \frac{1}{2} \left[\mathbf{E}(\rho,\omega) \times \mathbf{H}^*(\rho,\omega) \right] \cdot \mathbf{u}_z, \quad (3.14)
$$

is the z-component of the complex Poynting vector, where the asterisk denotes complex conjugation. The Petermann-1 (w_I) and the Petermann-2 (w_{II}) spot sizes are related to Eq. (3.13) by $d_I = 2w_I$ and $d_{II} = 2w_{II}$, respectively.

The evaluation of the electromagnetic field components needed to compute the Poynting vector has been discussed in Section 2.3. The subsequent integration over the core

region is performed numerically by a Gauss-Legendre quadrature rule in the radial direction. The integration over the cladding region, on the other hand, is performed analytically, with the exception of the denominator of the MFD d_{II}, for which we employ a Gauss-Laguerre quadrature rule. The analytic solutions to the pertaining integrations are given in Appendix F.3.

Further, we point out that the computation of $[d_\rho S(\rho)]^2$ in the denominator of the MFD d_{II} can cause numerical difficulties as this definition is designed for analytical refractive-index profiles. For continuous piecewise-linear profiles, the Poynting vector $S(\rho)$ contains kinks, and, hence, its derivative with respect to ρ is discontinuous. Furthermore, for discontinuous profiles, e.g. the step-index profile, squares of delta functions occur, which makes the subsequent integration over A_∞ impossible. Since the MFD d_{II} is prescribed in the specifications of an optical fibre, we have computed this quantity by neglecting the presence of any delta functions. Fortunately, for small-contrast fibres, the amplitudes of the pertaining discontinuities, and, as a result, of the delta functions are very small. From a mathematical point of view, the MFD d_I is better suited since delta functions are absent.

The effective (cross-sectional) area A_{eff} of an optical single-mode fibre is defined as

$$A_{\text{eff}} = a^2 \frac{\left(\displaystyle\int_{A_\infty} S(\rho)\rho\,d\rho\,d\psi\right)^2}{\displaystyle\int_{A_\infty} S^2(\rho)\rho\,d\rho\,d\psi}, \tag{3.15}$$

and is, via a correction factor, directly related to the MFD d_{II} [68]. It is key in system designs that are prone to exhibit the non-linear Kerr effect [48], since the pertaining refractive index n is related to A_{eff} by

$$n = n_0 + n_2 P/A_{\text{eff}}, \tag{3.16}$$

where n_0 corresponds to the regular refractive index of the material, defined by Eq. (2.1), n_2 is a non-linear refractive index coefficient, and P denotes the modal power. For silica single-mode fibres n_2 varies from 2.2 to $3.4 \times 10^{-8}\,\mu\text{m}^2/\text{W}$. The non-linear Kerr effect gives rise to so-called self-phase modulation [48]. The change in the refractive index seems very small. However, for very long interaction lengths, high signal powers, or a small A_{eff}, the accumulated effects become significant. Moreover, non-linear Raman and Brillouin scattering increases for decreasing A_{eff} [2]. Large-effective-area fibres (LEAF) are especially designed to reduce these non-linear effects.

In Table 3.3, we compare the MFDs d_I and d_{II}, and the effective area for the three fibres of Table 3.1. For completeness, we have added the normalised power of the fundamental mode in the core and cladding region. Although all values are computed at an operating wavelength of $\lambda = 1550\,\text{nm}$, keep in mind that Δ is still defined at $\lambda = 632.8\,\text{nm}$.

Table 3.3: *The MFDs d_I and d_{II}, the effective area A_{eff}, and the normalised power of the fundamental mode for the three fibres of Table 3.1 at an operating wavelength of $\lambda = 1550\,nm$.*

	CSF	DSF	DCF
MFD d_I (µm)	12.4	7.6	4.5
MFD d_{II}(µm)	11.6	7.0	4.2
A_{eff} (µm^2)	101	36	13
Normalised P_{core}	0.66	0.61	0.66
Normalised P_{clad}	0.34	0.39	0.34

3.1.5   Macro- and microbending losses

Bending losses (or radiative losses) occur whenever a fibre is bent with a locally finite radius of curvature R. We distinguish between two bending regimes, i.e. macroscopic bends for which $R \gg a$, where a denotes the core radius, and random microscopic bends. The first loss mechanism is mostly encountered during the (in-house) deployment and installation process of the optical fibre, whereas the second one arises primarily during the manufacturing process.

Macrobending losses, or simply bending losses, increase faster than exponentially as the radius of curvature decreases [58]. In particular, higher-order modes that propagate close to the core/cladding interface lose their power rapidly as they fail to take even the slightest bends. Bending losses are reduced if we employ a large refractive-index difference Δ with a small core radius, which ensures that the modes are well confined. However, in that case the dispersion and MFD characteristics alter, as has been shown in the Sections 3.1.1 and 3.1.4, respectively. In the fibre design process, one has to balance these factors to obtain an optimal refractive-index profile to achieve a given objective, e.g. long-distance communication. An optimisation procedure for the refractive-index profile is discussed in Chapter 5.

The power attenuation coefficient, which is the measure for the bending loss, is directly related to the imaginary part of the normalised propagation coefficient ζ. For example, if we consider wave propagation along the z-direction, the z-dependence of the electromagnetic fields can, in accordance with Eq. (2.24), be written as

$$\{E_k, H_k\} \sim \exp(-j\hat{\omega}\zeta' a^{-1}z)\exp(-\hat{\omega}\zeta'' a^{-1}z) = \exp(-j\beta z)\exp(-\alpha z), \qquad (3.17)$$

where $\zeta = \zeta' - j\zeta''$, with $\alpha \geq 0$ and $\beta > 0$. The power attenuation (or bending-loss) coefficient per unit length reads 2α, accordingly. To keep the values for α tractable, we will employ a logarithmic scale and express the bending losses in dB/m. In Chapter 4, we introduce a full-wave approach to compute these bending losses exactly.

Microbending losses are due to small-scale fluctuations in the radius of curvature of the fibre axis. They can be caused, for instance, by minor irregularities in the drum on which the fibre is wound under tension. Further, nonuniform lateral stresses during the cabling of the fibre or the deployment in the ground can introduce microbends. As possible higher-order modes are prone to leakage radiation, the slightest perturbations already cause significant power losses.

3.1.6 MAC-value

To characterise the macro- and microbending sensitivity of a single mode optical fibre, the MAC-value turns out to be a proper measure [12, 105]. This dimensionless quantity is defined as

$$\text{MAC} = d_{II}/\lambda_{ce}, \tag{3.18}$$

where the MFD d_{II} is given by Eq. (3.13) at a wavelength of $\lambda = 1550\,\text{nm}$, and λ_{ce} is the so-called effective fibre cut-off wavelength of the first higher-order mode. This wavelength terminates the region for which the fibre is "effectively" in single-mode operation. In comparison with the theoretical cut-off wavelength λ_c, below which ideally the first higher-order mode exists, the effective one is always smaller even up to values of 100 to 200 nm. This is caused by the fact that the electromagnetic field of the first higher-order mode, near cut off, extends far into the cladding region. Consequently, due to macro- and microbends, as well as the presence of (absorbing) coatings, it will attenuate rapidly. As a consequence, the transmission system can be operated at λ_{ce}, thus enhancing fundamental mode confinement.

For modelling purposes, the computation of the effective cut-off wavelength is far more complicated than computing the theoretical one. However, the theoretical cut-off wavelength is impossible to measure, and no simple ratio factor between practical and theoretical values can be applied. Therefore, we will discuss the numerical computation of both cut-off wavelengths briefly in the following sections.

Theoretical cut-off wavelength

The theoretical cut-off wavelength λ_c of the first higher-order mode is an important transmission parameter, as it separates the single-mode regime from the multi-mode regime. It is defined as the first wavelength at which the propagation coefficient ζ equals the minimum refractive-index value of the pertaining profile. For a step-index single-mode fibre, the normalised cut-off frequency is given by $\hat{\omega}_c \approx 1.7/(n_{\text{co}}\sqrt{\Delta})$ [69], and, consequently,

$$\lambda_c = 2\pi a/\hat{\omega}_c \approx 3.7 a n_{\text{co}}\sqrt{\Delta}. \tag{3.19}$$

Again, we assume that the refractive-index profile is defined at $\lambda = 632.8\,\mathrm{nm}$ (see Section 2.1). Since $n(\lambda)$, the specification of the refractive-index profile at a different wavelength results in a different value for λ_c.

In practice, the change from multi-mode to single-mode operation does not occur at a single wavelength, but is a gradual transition. Moreover, for wavelengths just below λ_c, one can not really speak of mode propagation for the first higher-order mode, since still most of its power is present in the cladding, and therefore the mode already attenuates rapidly for the slightest bend or imperfection in the fibre. Hence, the effective cut-off wavelength is a more appropriate design parameter.

Effective cut-off wavelength

The International Telecommunication Union (ITU), the former CCITT, defines the effective (fibre) cut-off wavelength (λ_{ce}) as follows [42] : "The effective cut-off wavelength is the wavelength greater than which the ratio between the total power and the fundamental mode power has decreased to less than $0.1\,\mathrm{dB}$ in a quasi straight two metre fibre with one single loop with a radius of curvature $R = 14\,\mathrm{cm}$." The configuration is shown in Figure 3.7.

Figure 3.7: *Configuration of a two metre fibre with one single loop of $R = 14$ cm to obtain λ_{ce}.*

Depending on the refractive-index profile, the first-higher order mode is not necessarily the TE_{01} or TM_{01} mode, as in the case of the step-index or parabolic-index profile (see Figure 2.2). To overcome this difficulty, and to simplify matters, we resort to the LP modes introduced in Section 2.5, which together with the HE_{21} mode are combined into the LP_{11} mode. Although its has not been proven that this is always the first higher-order LP mode, the author is not aware of a profile for which it is not. However, to be safe, we first compute the theoretical cut-off wavelengths of the lowest higher-order modes, and we then check to which LP mode the first higher-order mode belongs. Finally, we compute the differences between these theoretical cut-off wavelengths to determine whether there exists an LP mode close to the first higher-order one, which then evidently has to be taken into account as well.

For the moment, let us assume that the first higher-order mode is indeed the LP_{11} mode as suggested in [69]. Next, the launching conditions of the fibre are utilised in such

a way that both the fundamental mode (LP_{01}) and the first higher-order mode (LP_{11}) are excited with comparable power. This can be achieved in practice, for example, by splicing a single-mode fibre with a multi-mode fibre [66]. Under this restriction, the input power of the second-order mode is twice as large as that of the fundamental one, since we excite four and two degenerate modes, respectively, i.e. $P_{11}(0) = 2P_{01}(0)$. Hence, the level difference at the input is

$$10 \log \left(\frac{P_{01}(0)}{P_{11}(0)} \right) \approx -3.0 \,\text{dB}. \tag{3.20}$$

At the fibre end, the LP_{11} mode is considered to be fully attenuated due to the introduction of an additional loop of $R = 3 \,\text{cm}$, whereas the fundamental mode attenuation is negligible since this mode is confined, i.e. $P_{01}(L) = P_{01}(0)$. Then, according to the definition above, we obtain the following level difference at $L = 2 \,\text{m}$

$$10 \log \left(\frac{P_{01}(L) + P_{11}(L)}{P_{01}(L)} \right) = 0.1 \,\text{dB}, \quad \Rightarrow \quad 10 \log \left(\frac{P_{01}(L)}{P_{11}(L)} \right) \approx 16.3 \,\text{dB}. \tag{3.21}$$

With the aid of Eq. (3.20), the attenuation of the LP_{11} mode is given by

$$\alpha_{LP_{11}} = 10 \log \left(\frac{P_{11}(0)}{P_{11}(L)} \right) \approx 19.3 \,\text{dB/turn} \approx 22 \,\text{dB/m}. \tag{3.22}$$

Hence, the wavelength at which the bending loss of the LP_{11} mode equals $22 \,\text{dB/m}$ is the desired λ_{ce}. A Van Wijngaarden–Dekker–Brent root-finding scheme [78] is used to obtain this wavelength, by decreasing λ steadily from the theoretical cut-off wavelength onwards. It takes about ten seconds to determine the effective cut-off wavelength to a relative accuracy of 10^{-5}. Note that if unexpectedly the LP_{02} mode is the first higher-order mode instead of the LP_{11} mode, then $P_{02}(0) = P_{01}(0)$, and, consequently, $\alpha_{LP_{02}} \approx 18.6 \,\text{dB/m}$. In Section 4.2, we describe an accurate procedure for computing the bending losses of all LP modes with arbitrary refractive-index profiles.

In Table 3.4, we compare the theoretical and effective wavelength for the three fibres of Table 3.1. With the aid of Eq. (3.18) and Table 3.3, we have computed the corresponding MAC-values at a wavelength of $1550 \,\text{nm}$ as well.

According to the definition of λ_{ce} set by the ITU, the loop has a radius of curvature of $R = 14 \,\text{cm}$. However, as soon as the fibre is bent, stress causes the refractive index of the fibre to change. These stress-induced changes in the refractive index are taken into account by introducing an effective radius of curvature R_{eff}. It has been found experimentally that $1.28R < R_{\text{eff}} < 1.325R$ [22, 67, 82]. For an intermediate effective radius of curvature $R_{\text{eff}} = 1.3R = 18.2 \,\text{cm}$, the effective cut-off wavelength and the corresponding MAC-value have been added to Table 3.4 as well. Note that the MAC-value is rather insensitive to a change in the radius of curvature.

Table 3.4: *Theoretical and effective cut-off wavelengths and the corresponding MAC-values for the fibres specified in Table 3.1.*

	CSF	DSF	DCF
λ_c (nm) (Eq. (3.19))	1152	1081	1166
λ_{ce} (nm) (R=14 cm)	1023	1019	1121
λ_{ce} (nm) (R_{eff}=18.2 cm)	1036	1024	1142
MAC-value (R=14 cm)	11.4	6.9	3.7
MAC-value (R_{eff}=18.2 cm)	11.2	6.8	3.7

To measure λ_{ce}, ITU recommends two transmitted-power techniques as reference test methods, i.e. the bending method and the power step method. In [94], a complete overview of these methods is discussed. The derivation above holds for the bending method, but can be used as a stepping stone for the power-step method as well. A validation of the computed values of λ_{ce} with existing literature, and the forthcoming MAC-value, is performed in Section 4.6. The details of the pertaining computation are discussed there as well.

3.2   Multi-mode fibre characteristics

Primarily, the multi-mode fibre is employed within short distance communication networks, e.g. within premises or local area networks (LANs). Typical operating wavelengths are 850 nm and 1300 nm. Owing to its large core diameter, low loss connections and simple fibre–to–fibre or fibre–to–transceiver alignments are possible. Therefore, installation costs can be kept low in comparison with the critical alignment required for single-mode fibres. On the other hand, the large core diameter allows for many modes to propagate along the optical fibre. This introduces some undesirable effects that limit the capacity to transmit information at a high speed. Some of these effects can be computed accurately, others can only be approximated. We will discuss the most important effects and their numerical computation for the special case of a frequently employed multi-mode refractive-index profile, viz. the graded-index power-law profile (see Eq. (2.1)). This is a power-law profile with a finite power-law exponent g.

3.2.1   Differential mode delay

When a multi-mode fibre (MMF) is excited by a light source or a single-mode fibre, many modes will propagate along the fibre. Each mode has a distinct propagation coefficient

$\beta(\hat{\omega})$, and, consequently, its own group velocity v_g, given by Eq. (3.2), at which it transfers power. As a result, power arrives at the receiver end at (slightly) different times, which causes an input pulse to spread. The effect is known as *differential mode delay* (DMD) and also as *intermodal dispersion*, since, in essence, it is a dispersion effect. Fortunately, by choosing a proper value for the power-law exponent g in the power-law profile in Eq. (2.1), DMD can be reduced considerably.

To show the effect of the refractive-index profile on the DMD, we employ a step-index single-mode fibre pigtail to excite the multi-mode fibre at a given radial offset. In Figure 3.8, the DMD measurement procedure, as described in the standard [97], is shown schematically for several radial offset positions of the pigtail. Depending on these
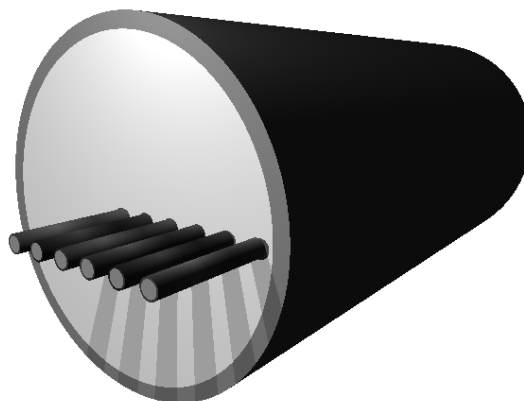
Figure 3.8: *The DMD measurement set-up, where a Gaussian time pulse is launched into an SMF pigtail. Possible SMF pigtail positions at the end-face of an MMF are shown. In turn, subsets of modes are excited in the MMF. At the fibre end the total instantaneous output power is measured as a function of time.*

positions, various subsets of modes are excited in the MMF. The modal power at the launch spot in combination with the group velocity v_g of each mode, determines the DMD plot at the fibre end ($z = L$).

For the moment, let us assume that there is neither power transfer among modes nor power absorption. These subjects will be covered in the upcoming sections. For the excitation of the SMF pigtail, we consider a time pulse $\Phi(t)$, with a Gaussian power distribution, of the following form [36]

$$\Phi(t) = \Phi(t_0) \exp\left[-8\ln(2)\left(t - t_0\right)^2 / t_w^2\right] \tag{3.23}$$

where t_w is the full width of the pulse at 25% of the maximum power amplitude and $t_0 = z/v_g$ denotes the mean arrival time of the pulse. According to [97], the MFD d_{II} of the SMF pigtail must be in the range

$$8.7\,\lambda - 2.89 \leq d_{II} \leq 8.7\,\lambda - 1.89, \tag{3.24}$$

where λ is given in micrometres. Further, we have opted for a pulse of $t_w = 56.6\,\text{ps}$ and an MMF with length $L = 500\,\text{m}$. At optical wavelengths, we may neglect the influence of the chromatic dispersion D since [27]

$$D \ll \pi c_0 t_w^2 / \left[2\ln(4)\lambda^2 L \right] . \tag{3.25}$$

In Figure 3.9, the DMD simulations for an MMF with various power-law profiles are plotted. The employed MMF has a core radius $a = 31.25\,\mu\text{m}$, an $\text{NA} = 0.275$, and is operated at $\lambda = 850\,\text{nm}$. The employed SMF pigtail has a core radius $a = 1.9\,\mu\text{m}$ and an $\text{NA} = 0.133$, to achieve an MFD $d_{II} = 5\,\mu\text{m}$ within the range in Eq. (3.24) at the operating wavelength. The power-law exponents g of the pertaining power profiles read from left to right $g = 1.98$,
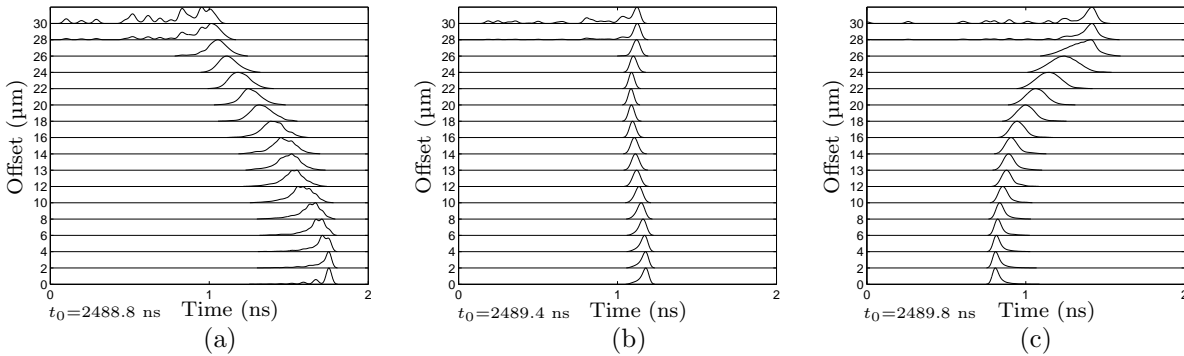
Figure 3.9: *DMD simulations for a power-law profile with power-law exponents g=1.98 (a), g=2.06 (b), and g=2.14 (c).*

$g = 2.06$, and $g = 2.14$, respectively. The azimuthal index ranges from $m = 0$ to $m = 33$.

From Figure 3.9, we observe that there exists an optimal g which minimises the travel-time drift for various probe offsets. For the MMF under consideration, the optimum is obviously about $g = 2.06$. Hence, the travel time of each pulse, propagated by a group of modes, will be nearly the same. This condition translates into a smaller bit-error rate and a higher transmission rate.

Further, note that for radial offsets near the core/cladding interface the pulse spreads considerably. This pulse spreading is a result of the slope discontinuity in the refractive-index profile at the core/cladding interface, which especially affects the delay times of the higher-order modes [74]. Fortunately, in practice, these modes are attenuated due to macro- and microbending losses.

To perform the numerical DMD simulation, it suffices to compute the excited modal amplitudes and the corresponding modal group velocities. The latter are obtained from Eq. (3.2), which implies that we have to solve the characteristic equation of Eq. (2.42) to obtain all propagation coefficients ζ for each azimuthal index m. The excited modal amplitudes, on the other hand, are computed via overlap integrals [69]. To facilitate

computations, we normalise the modal fields, which are orthogonal, such that the power carried by each mode, integrated over an infinite cross-section of the fibre A_∞, equals one, i.e.

$$\frac{1}{2} \int_{A_\infty} \mathrm{Re}\left[\mathbf{E}_{m'n'}(\rho,\psi) \times \mathbf{H}^*_{mn}(\rho,\psi)\right] \cdot \mathbf{u}_z \; dA = \delta_{m',m}\,\delta_{n',n}, \qquad (3.26)$$

where dA denotes an area element, $\delta_{m',m}$ is the Kronecker delta, and where m,n are the azimuthal and radial index, respectively, in accordance with the definitions given in Section 2.3. Consequently, the modal amplitudes are determined via an overlap integral at the plane $z=0$, i.e. [69]

$$A_{mn} = \frac{1}{2} \int_{A_\infty} \mathrm{Re}\left[\mathbf{E}_i(\rho'',\psi'') \times \mathbf{H}^*_{mn}(\rho,\psi)\right] \cdot \mathbf{u}_z \; dA, \qquad (3.27)$$

where the label i corresponds to the electric field of the SMF pigtail at the interface with the MMF. The configuration is shown schematically in Figure 3.10. For the DMD
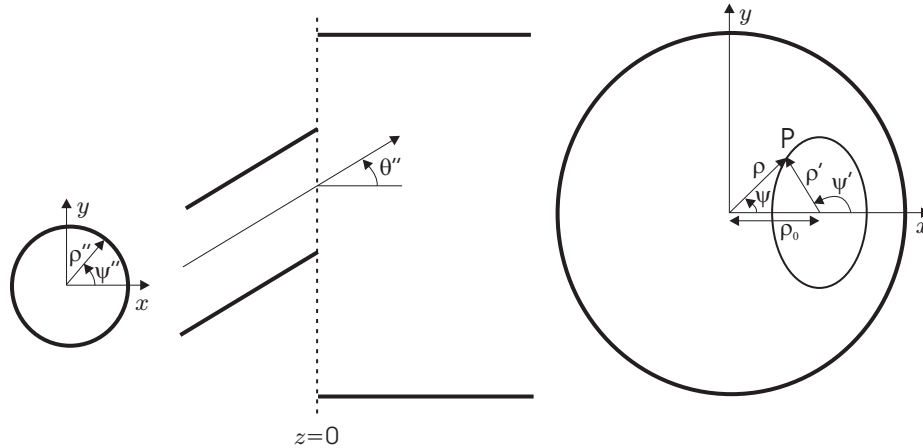
Figure 3.10: *Coordinate systems for the computation of the overlap integral in Eq. (3.27).*

simulations the angular tilt of the pigtail with respect to the MMF is $\theta''=0$. Non-zero angular tilts are encountered in Chapter 6 to excite several mode groups more selectively. The computation of Eq. (3.27) is discussed extensively in Appendix F.2 for both angular tilt and radial offset excitations.

As we have assumed that there is neither power loss nor power coupling among the modes propagating along the MMF, a modal amplitude and its corresponding modal group velocity enters into Eq. (3.23) as $\Phi(t_0)$ and $t_0 = L/v_g$, respectively. Addition of all Gaussian power distributions yields the DMD results at $z=L$.

As a last remark, we mention that, in principle, one would have to solve a scattering problem at the interface $z=0$ to determine the modal amplitudes. To complicate matters, the actual interface is seldom perfect and varies from case to case. However, the refractive-index difference between both fibres (and possible index matching gel) is so small that

scattering is negligible. Hence, it is justified to project the SMF field onto the modal fields of the MMF [69].

3.2.2 Inter- and intra-group coupling

Fibre deformations, like microbends and deformations due to externally exerted traction on the fibre, will cause a power exchange between propagating modes with similar propagation coefficients. We distinguish between power mixing among degenerate modes, i.e. intra-group coupling, and among non-degenerate modes, i.e. inter-group coupling [47].

At distances up to several kilometres, intra-group coupling is dominant due to the degeneracy of the modes. For very short distances, say up to several decimetres, we may assume that no form of coupling is relevant. Since, in practice, MMFs are typically employed in premises and LAN applications, long distances do not frequently occur. Therefore, we have opted for a model in which we can simulate the effect of either full intra-group coupling or no coupling at all. The latter case has already been discussed in the previous section.

To simulate intra-group coupling, we employ a set of coupled power equations, which describe the power exchange among the modes [59]

$$\frac{dP_\mu}{dz} = -2\alpha_\mu P_\mu + \sum_\nu h_{\mu\nu}(P_\nu - P_\mu), \qquad (3.28)$$

where P_μ and $2\alpha_\mu$ are the power and the attenuation coefficient, defined in Eq. (3.17), of the corresponding mode μ, respectively. The elements in the coupling matrix $h_{\mu\nu}$ are a measure of the probability per unit length of a transition occurring between modes μ and ν. In the absence of inter-group coupling, a proper choice of degenerate mode groups exists to diagonalise the matrix $h_{\mu\nu}$, which renders a thorough investigation of the pertaining elements unnecessary [59].

As argued in [47], we may assume that degenerate modes have equal power for fibre lengths of $L > V^2/(600H_1)$, where V is given by Eq. (2.43) and $H_1 = 0.015 \sim 0.02(m^{-1})$. In Section 2.5, we have already encountered degenerate modes for the case of a weakly guiding fibre, namely the $\text{LP}_{\ell n}$ modes. Among the LP modes, the modes with principal mode number $M = 2n + \ell - 1$, with M integer, form a so-called principal mode group (PMG), since they are nearly degenerate [36]. For the MMF of Figure 3.9(b), the first five PMGs, which are denoted by their principal mode number M, and the corresponding propagation coefficients ζ are given in Table 3.5.

Upon regarding ζ, the degeneracy of the modes in each PMG becomes evident. However, it turns out that this degeneracy only occurs for power-law refractive-index profiles. When we introduce a dip at the fibre centre, and a kink at $r = a/2$, as will be discussed in Chapter 6, the propagation coefficients ζ_p apply in Table 3.5.

Table 3.5: *Propagation coefficients ζ of the modes for various PMGs with corresponding principal mode numbers M for a power-law refractive-index profile. The propagation coefficients ζ_p correspond to the same power-law profile, albeit supplemented with a dip at the fibre centre and a kink at $r = a/2$.*

M	LP mode $\{\ell, n\}$	Waveguide mode $\{m, n\}$	ζ	ζ_p
1	LP_{01}	HE_{11}	1.4787513	1.4749222
2	LP_{11}	TE_{01}	1.4779648	1.4743078
		TM_{01}	1.4779648	1.4743069
		HE_{21}	1.4779644	1.4743075
3	LP_{02}	HE_{12}	1.4771657	1.4733463
	LP_{21}	EH_{11}	1.4771720	1.4735630
		HE_{31}	1.4771712	1.4735624
4	LP_{12}	TE_{02}	1.4763665	1.4726986
		TM_{02}	1.4763665	1.4726976
		HE_{22}	1.4763661	1.4726980
	LP_{31}	HE_{41}	1.4763736	1.4743770
		EH_{21}	1.4763749	1.4743782
5	LP_{03}	HE_{13}	1.4755605	1.4717625
	LP_{22}	HE_{32}	1.4755640	1.4719786
		EH_{12}	1.4755649	1.4719538
	LP_{41}	HE_{51}	1.4755726	1.4735824
		EH_{31}	1.4755744	1.4735841

We observe that we can no longer speak of any form of degeneracy in a PMG, and, hence, the power may no longer be equalised among its modes to simulate intra-group coupling. The degeneracy within the individual LP modes, however, seems to remain valid. Unfortunately, for larger values of M, this degeneracy starts to break. Therefore, we introduce a maximum relative difference between the propagation coefficients $\zeta_{\max}$ to decide whether modes are degenerate, and subsequently mix the power uniformly among them. With reference to Table 3.5, we take $\zeta_{\max} = 7 \cdot 10^{-5}$. For the sake of simplicity, we dub these mode groups DMGs, where the capital D refers to the degeneracy of the modes in such a mode group.

Since the modal amplitudes A_{mn} at $z = 0$ are known from Eq. (3.27), the average

amplitude of each mode in a DMG reads

$$\left|A_{mn}^{DMG}\right|_{ave} = \sqrt{\frac{\sum_{m,n}\left|A_{mn}^{DMG}\right|^2}{N^{DMG}}}, \tag{3.29}$$

where N^{DMG} denotes the number of modes in a DMG. The phase of $A_{m,n}^{DMG}$ is chosen randomly, with a uniform distribution within $[0, 2\pi)$, as it couples in a random fashion with the other modes within the group [36].

If we regard the indices μ and ν of the coupling matrix $h_{\mu\nu}$ in Eq. (3.28) in terms of DMGs, the matrix diagonalises for the case of intra-group coupling (in the absence of inter-group coupling), and hence $P_\mu(z) = P_\mu(0)\exp(-2\alpha_\mu z)$. In Chapter 6, we will show the effects of intra-group coupling and we will compare simulations of the intensity pattern at various distances $z = L$ with measurements. The reader should keep in mind that the full coupling as described by Eq. (3.29) only holds for fibre lengths $L > V^2/(600H_1)$. For the MMF in Figure 3.9(b) this implies that $L > 73\,\mathrm{m}$.

3.2.3   Differential mode attenuation

In a multi-mode optical fibre, conventional loss mechanisms like material absorption, Rayleigh scattering and loss on reflection at the core/cladding interface cause the propagating modes to attenuate [89]. Since this attenuation is different for each mode, the effect is known as *differential mode attenuation* (DMA). For example, the loss, due to a nonuniform fibre boundary, influences the modes near cut-off more than the lower-order modes as they extend further into the cladding. In general, lower-order modes do not necessarily have the lowest attenuation, although as long as the numerical aperture is small enough or the wavelength is long, scattering is weak and the DMA gradually increases as a function of the mode order [118].

To derive a loss model that incorporates all these conventional loss mechanisms is by no means a trivial task. Especially, since such a model will inevitably involve some parameters that are difficult to measure. Since multi-mode fibres are used at long wavelengths in the $850\,\mathrm{nm}$ and $1300\,\mathrm{nm}$ telecommunication windows, the DMA should be increasing as a function of mode order, as stated above. Therefore, we have opted for an empirically matched formula to compute the DMA that can be easily matched to a measured DMA of a (silica) fibre. The DMA is incorporated in the power attenuation coefficient 2α introduced in Eq (3.17), and is for a individual PMG κ given by [118]

$$2\alpha_\kappa(\lambda) = 2\alpha_{\kappa,0}(\lambda) + 2\alpha_{\kappa,0}(\lambda)I_\rho\left[\eta\left(\frac{\kappa-1}{M_{PMG}}\right)^{2g/(g+2)}\right], \tag{3.30}$$

where $\rho = 9$, $\eta = 7.35$, I_ρ denotes the modified Bessel function of order ρ, and $2\alpha_{\kappa,0}$ is the intrinsic fibre attenuation at a specific wavelength λ, which is assumed to be equal for all

propagating modes. Further, M_{PMG} denotes the total number of PMGs, while g is the
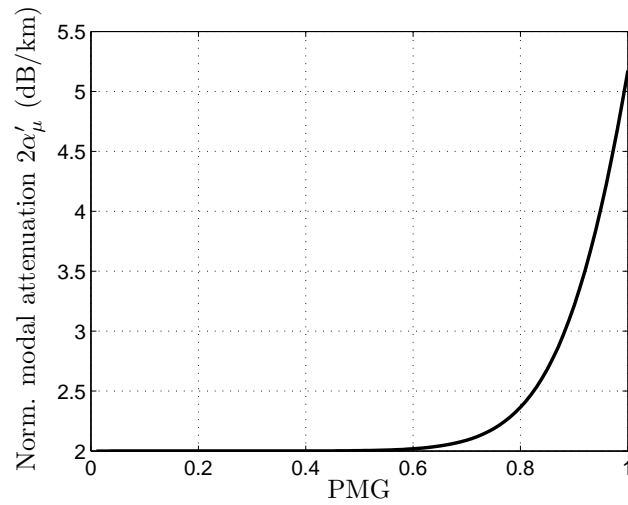
Figure 3.11: *Normalised modal attenuation coefficient according to Eq. (3.30) as a function of the normalised principal mode group (PMG) with $\alpha_{\kappa,0} = 2.0$ dB/km.*

power-law exponent of the power-law profile. In Figure 3.11, we have plotted the DMA as a function of the normalised PMG. Although this formula is given for PMGs, we do not expect considerable differences in its form if we employ the DMGs (with or without employing intra-group mode coupling) instead. Also, the values for ρ and η apply, strictly speaking, only to power-law fibres, but also here we do not expect significant differences in the values for small deviations of the exact power-law profile, e.g. a kink or a dip. Observe that indeed the higher-order mode groups are attenuated more than the lower-order ones.

Chapter 4

Macrobending loss

It is well known that radiation (bending) losses occur whenever an optical fibre is bent. As a consequence, the propagating modes attenuate, which is an undesirable effect in many telecommunication applications, e.g. fiber-to-the-home [55]. Therefore, it is important to be able to design fibres in such a way that they are relatively insensitive to bending.

Several authors have derived theoretical expressions of the attenuation coefficient for weakly guiding fibres. The methods presented in [22, 82, 108] are based on the scalar wave equation of the equivalent straight waveguide. In [89], an electric-current contrast source is introduced to compute the bending losses. All these methods rely on the assumption that the radius of curvature of the bend is very large with respect to the core radius of the fibre. However, in practice, it appears that these approximate expressions are not always accurate enough.

Owing to the significant increase in the speed of computers, a vectorial full-wave analysis of the bent fibre can now be performed. However, since this analysis is quite complex, we begin, for tutorial reasons, with the equivalent 2-D problem first, i.e. the bent slab waveguide. Next, we gradually change the geometry, while addressing the occurring problems in each configuration, to make the final analysis of the bent optical fibre geometry more tractable. Further, we will give a succinct derivation of the available approximations to derive the bending loss in the bent fibre. These serve as a reference to compare our full-wave results with.

4.1   The bent slab waveguide: full-wave analysis

Before we analyse the bent optical fibre, we first compute the bending losses for a bent slab waveguide, which is the fibre's 2-D equivalent. This, to introduce the Bessel function of complex order and argument, which is a pivotal aspect that occurs in radiation problems with open bent configurations. In the literature, both exact and approximate methods

exist to compute the bending losses of a slab waveguide [18, 39, 57, 109]. We adopt an exact method, based on the approach outlined in Section 2.3, to obtain the electromagnetic field components. We compare the computed bending loss values with [18], as there 10 digits of accuracy are given.

The bent slab configuration is shown in Figure 4.1. The radius of curvature is denoted by R and the slab thickness equals a. We adopt a cylindrical coordinate system $\{x^1, x^2, x^3\} = \{\phi, z, r\}$ in which we distinguish between three regions. In regions 1 and
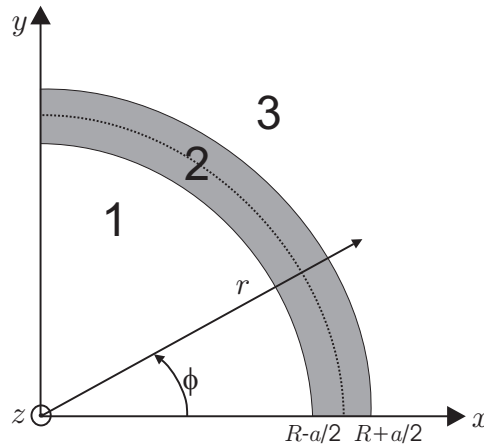
Figure 4.1: *Configuration of the bent slab. Region 2 has an arbitrary index profile.*

3, the refractive index $n_1 = n_3 = n_{\mathrm{cl}}$ is considered to be constant, whereas it may vary arbitrarily in the radial direction in region 2, i.e. $n_2 = n(r)$. Since the structure still has to serve as a waveguide, we demand that $\max(n_2) > n_{\mathrm{cl}}$ somewhere in the interval $R - a/2 > r > R + a/2$. Further, we consider all media to be lossless. The configuration is invariant in the z-direction. We will consider field solutions that are independent of z, i.e. $\partial_z = 0$. We introduce (covariant) basis vectors $\{\mathbf{c}_1, \mathbf{c}_2, \mathbf{c}_3\} = \{r\mathbf{u}_\phi, \mathbf{u}_z, \mathbf{u}_r\}$, consistent with our cylindrical coordinate system, and corresponding (covariant) electromagnetic field components $\{E_1, E_2, E_3\} = \{rE_\phi, E_z, E_r\}$ and $\{H_1, H_2, H_3\} = \{rH_\phi, H_z, H_r\}$. With reference to Eq. (2.24) and [57], we cast the electromagnetic field components in the following form

$$\begin{pmatrix} E_k(\rho, \phi) \\ H_k(\rho, \phi) \end{pmatrix} = \begin{pmatrix} e_k(\rho) \\ h_k(\rho) \end{pmatrix} \exp\left(-j\hat{\omega}\zeta\rho_c\phi\right), \qquad (4.1)$$

where the normalised frequency $\hat{\omega}$ and the normalised radial coordinate ρ are given by Eq. (2.25), and where $\rho_c = R/a$ denotes a normalised radius of curvature. It is important to note that the propagation coefficient $\zeta \in \mathbb{C}$, and that its imaginary part accounts for the loss (see Eq. (3.17)).

To obtain the propagation coefficients of the propagating modes, we substitute the expressions of Eq. (4.1) in the Marcuvitz-Schwinger equations of Eq. (2.18), and define a

favourable rescaling of the fields, viz. $\{e_1, e_2\} = jZ_0\{\rho_c a p_1, p_2\}$ and $\{h_1, h_2\} = \{\rho_c a q_1, q_2\}$. Owing to the z-independence, this yields two independent systems of differential equations, viz.

$$d_\rho \begin{pmatrix} p_1 \\ q_2 \end{pmatrix} = \hat{\omega}\rho^{-1} \begin{pmatrix} 0 & \rho_c^{-1}\left[(\zeta\rho_c/n)^2 - \rho^2\right] \\ \rho_c n^2 & 0 \end{pmatrix} \begin{pmatrix} p_1 \\ q_2 \end{pmatrix}, \tag{4.2}$$

and

$$d_\rho \begin{pmatrix} p_2 \\ q_1 \end{pmatrix} = \hat{\omega}\rho^{-1} \begin{pmatrix} 0 & \rho_c \\ \rho_c^{-1}n^2\left[(\zeta\rho_c/n)^2 - \rho^2\right] & 0 \end{pmatrix} \begin{pmatrix} p_2 \\ q_1 \end{pmatrix}, \tag{4.3}$$

which correspond to transverse magnetic (TM) and transverse electric (TE) modes with respect to the radial direction, respectively. The radial field components readily follow from Eq. (2.20)

$$\{e_3, h_3\} = \rho^{-1}\rho_c\zeta\{-Z_0 n^{-2} q_2, Z_0^{-1} p_2\}. \tag{4.4}$$

Since the media are homogeneous in the regions 1 and 3, both systems may be solved analytically there. However, for region 2, where $n_2 = n(\rho)$, we perform a numerical integration either simply from $\rho = \rho_c - 1/2$ to $\rho = \rho_c + 1/2$, or from both boundaries towards an arbitrary intermediate point ρ_i. The integration is performed by an adaptive Adams method [37].

For convenience, we restrict ourselves to the TE-case, as the TM-case is analogous. Therefore, we substitute the second first-order differential equation in Eq. (4.3) in the first one, which eliminates q_1. Upon introducing the variable $z = \hat{\omega}n\rho$, we arrive at Bessel's differential equation

$$\left[z\partial_z z\partial_z + z^2 - (\hat{\omega}\zeta\rho_c)^2\right] p_2 = 0. \tag{4.5}$$

After imposing boundary conditions at $\rho = 0$ and infinity, we obtain the following transverse field components for regions 1 and 3,

$$p_2 = \begin{cases} A J_{\hat{\omega}\zeta\rho_c}(z) & \text{in region 1,} \\ B H_{\hat{\omega}\zeta\rho_c}^{(2)}(z) & \text{in region 3,} \end{cases} \qquad q_1 = \rho_c^{-1}\rho n \begin{cases} A J'_{\hat{\omega}\zeta\rho_c}(z) & \text{in region 1,} \\ B H_{\hat{\omega}\zeta\rho_c}^{\prime(2)}(z) & \text{in region 3,} \end{cases} \tag{4.6}$$

where q_1 is determined through the substitution of p_2 in Eq. (4.3). The functions $J_\nu(z)$ and $H_\nu^{(2)}(z)$ denote Bessel functions of the first and third kind, respectively. Their arguments, $z = \hat{\omega}n_{\text{cl}}\rho$, are real-valued, while their orders, $\nu = \hat{\omega}\zeta\rho_c$, are complex. The prime indicates a derivative with respect to the argument of the pertaining Bessel function.

These expressions serve as the boundary field solutions for our numerical integration scheme. By imposing the continuity of the transverse electromagnetic field components at the common interface ρ_i (see Section 2.2.1), we end up with the following linear equation

$$\begin{pmatrix} p_2^-(\rho_i) & p_2^+(\rho_i) \\ q_1^-(\rho_i) & q_1^+(\rho_i) \end{pmatrix} \begin{pmatrix} A \\ B \end{pmatrix} = \mathbf{0}, \tag{4.7}$$

where the – and + signs correspond to the value of the pertaining field components approaching ρ_i from below or from above, respectively. Non-trivial solutions of Eq. (4.7) only exist if the determinant vanishes, which leads to a characteristic equation for the normalised complex propagation coefficient ζ. The search for ζ in the complex plane is performed using Muller's method [78], which requires a proper initial value of ζ to initiate the search. Therefore, we start the search from the propagation coefficient for the straight slab waveguide, for which $\zeta \in \mathbb{R}$, and trace out the locus of the propagation coefficients through the complex plane while gradually decreasing the radius of curvature.

Note that for large radii of curvature, the ratio between the imaginary and the real part of the propagation coefficient is very small, since there is little loss. However, this loss accumulates for increasing propagation distances $\rho_c\phi$. Therefore, a highly accurate computation of ζ is essential. Moreover, the radius of curvature is very large with respect to the wavelength, i.e. $\rho_c \gg 1$. As a consequence, we need to compute Bessel functions of large complex order and argument. This computation is anything but straightforward, and is treated in Appendix C. There it is shown that we can compute the Bessel functions to a relative accuracy of at least 10^{-11}, and, therefore, the integration with the adaptive Adams method of the systems in Eqs. (4.2) and (4.3) has been performed to the same relative accuracy.

To verify our code, and in particular our Bessel function subroutines, we have computed the bending loss of a propagating TE mode as a function of R and compared our results with the ones of de Hon and Bingle [18] and Vassallo [109]. The results are shown in Figure 4.2 for a bent slab with a 90° bend, where $\lambda = 1\,\mu\text{m}$, $a = 4\,\mu\text{m}$ $n_{\text{cl}} = 1.500$ and $n_2 = 1.503$. In [18], reference values of the bending loss, which are based on a modal angle-formulism, are given up to 10 digits of accuracy, which are met with our method as well. In Figures 4.3(a) and 4.3(b), we have plotted the magnitude of the Poynting vector and the electric field component E_z for the pertaining TE-polarised wave at $R = 5\,\text{mm}$. The radiation loss is clearly observable as power is leaking away into the outer region.

4.2   The bent optical fibre: scalar analysis

As an intermediate step towards the vectorial full-wave analysis of the bent optical fibre, we first consider its scalar counterpart, which will be used as a reference to compare our full-wave results with. For the scalar analysis of a bent dielectric waveguide, the concept of an equivalent straight waveguide is often used. The basic idea consists in converting Maxwell's equations within a local curvilinear coordinate system $\{\phi, \psi, r\}$ to equivalent equations in a rectified Cartesian coordinate system $\{\phi, z, x\}$ by introducing an equivalent permittivity profile, as shown in Figure 4.4. We introduce a radial distance from the fibre
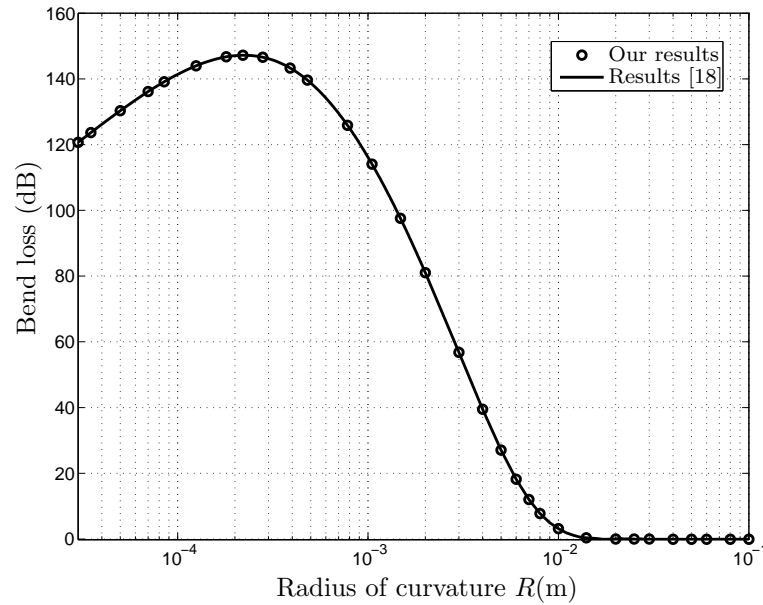
Figure 4.2: *Bending loss [-10π Im($\hat{\omega}\zeta\rho_c$)/log10] in dB of the TE-mode with $a = 4\,\mu m$, $\lambda = 1\,\mu m$, $n_{cl}=1.500$ and $n_2 = 1.503$ along a 90° bend of a bent slab.*
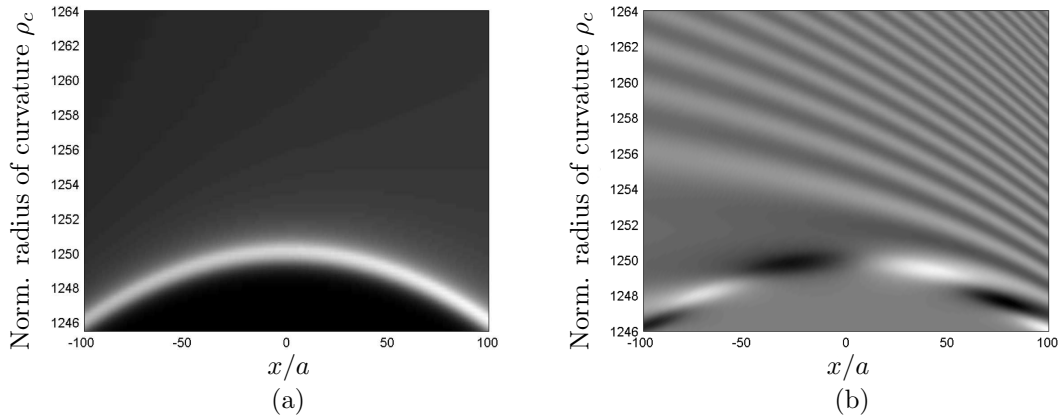
Figure 4.3: *Magnitude of the Poynting vector (a) and the field component E_z (b) for $R = 5\,mm$.*

axis, $r = \rho a = (x^2 + z^2)^{1/2}$, where again a denotes the core radius. Since modes propagate along the ϕ-direction, we assume that the fields have an $\exp(-j\hat{\omega}\zeta\rho_c\phi)$ dependence, where $\zeta = (\beta - j\alpha')/R$ denotes an as yet unknown complex normalised propagation coefficient, with an imaginary part that accounts for the loss.

Under the assumption of weak guidance, the transverse field components in the rectified waveguide obey a two-dimensional scalar wave equation [109], which follows directly from Eq. (2.50) by the substitution of an equivalent permittivity profile $\varepsilon_r(r) \to \varepsilon_r(r)(1+2X/\rho_c)$,
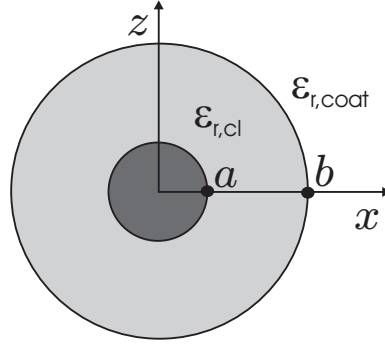
Figure 4.4: *Coordinate system for the equivalent straight waveguide.*

i.e.

$$\left\{\partial_X^2 + \partial_Z^2 + \hat{\omega}^2 \left[\varepsilon_r \left(1 + 2X/\rho_c\right) - \zeta_{\text{str}}^2\right]\right\} \psi(X, Z) = 0, \tag{4.8}$$

where $X = x/a$ and $Z = z/a$ denote normalised coordinates and ζ_{str} is a known normalised propagation coefficient corresponding to an LP$_{\ell n}$ mode of the straight fibre (see Section 2.5).

First, let us consider the case of an infinite cladding, i.e. $b \to \infty$. Then the half space $x > a$ corresponds to the homogeneous circularly cylindrical region enclosing the waveguide with $\varepsilon_r = \varepsilon_{r,\text{cl}}$. For this region, Eq. (4.8) can be solved by using a Fourier representation for the z-dependence of the fields

$$\tilde{\psi}(X, \xi) = a \int_{Z=-\infty}^{\infty} \psi(X, Z) \exp\left(j\hat{\omega}\xi Z\right) dZ, \tag{4.9a}$$

$$\psi(X, Z) = \frac{\hat{\omega}}{2\pi a} \int_{\xi=-\infty}^{\infty} \tilde{\psi}(X, \xi) \exp(-j\hat{\omega}\xi Z) d\xi. \tag{4.9b}$$

The solution is given in terms of Airy functions [1, 22]

$$\tilde{\psi}(X, \xi) = G(\xi)\text{Bi}(\chi) + H(\xi)\text{Ai}(\chi), \tag{4.10}$$

where ξ denotes the wavenumber corresponding to the normalised variable Z, $G(\xi)$ and $H(\xi)$ are yet unknown amplitude functions, and where

$$\chi(X, \xi) = \left(\frac{\hat{\omega}\rho_c\sqrt{\varepsilon_{r,\text{cl}}}}{2}\right)^{2/3} \left(\frac{\gamma^2}{\varepsilon_{r,\text{cl}}} - \frac{2X}{\rho_c}\right), \tag{4.11}$$

with $\gamma^2 = \zeta_{\text{str}}^2 - \varepsilon_{r,\text{cl}} + \xi^2$. To ensure that the fields satisfy the radiation condition in the infinite cladding, we choose $H(\xi) = -jG(\xi)$.

To determine $G(\xi)$ for the individual LP$_{\ell n}$ modes, one demands that $\tilde{\psi}(1, \xi)$ is equal to the unperturbed LP$_{\ell n}$ cladding field $K_\ell(w\rho)\cos(\ell\theta)$ at $X = 1$, where K_ℓ denotes an ℓ-th

order modified Bessel function of the second kind and $w = \hat{\omega} \left(\zeta_{\text{str}}^2 - \varepsilon_{r,\text{cl}} \right)^{1/2}$, i.e. [108]

$$
\begin{aligned}
\tilde{\psi}(1,\xi) &= G(\xi) \left\{ \text{Bi} \left[\chi \left(1, \xi \right) \right] - j \text{Ai} \left[\chi \left(1, \xi \right) \right] \right\} \\
&= a \int_{Z=-\infty}^{\infty} K_\ell \left[w(1+Z^2)^{1/2} \right] \cos(\ell\theta) \exp\left(j\hat{\omega}\xi Z \right) dZ \\
&= S_\ell(\xi),
\end{aligned}
\tag{4.12}
$$

where

$$
S_\ell(\xi) = a\pi \left(\hat{\omega}\gamma \right)^{-1} \cosh(\ell\phi) \exp\left(-\hat{\omega}\gamma \right),
\tag{4.13}
$$

with $\cosh\phi = \hat{\omega}\gamma/w$. Upon imposing the condition $\rho_c \gg 1$, we observe that the argument χ of the Airy functions in Eq. (4.11) is large and positive. By employing their large-argument expansions [1], we can distinguish between forward and backward evanescent fields in the cladding region before the caustic is reached. This leads to

$$
\begin{aligned}
\text{Bi}(\chi) &\simeq \pi^{-1/2} \chi^{-1/4} \exp\left(\frac{2}{3}\chi^{3/2} \right), \\
\text{Ai}(\chi) &\simeq \frac{1}{2}\pi^{-1/2} \chi^{-1/4} \exp\left(-\frac{2}{3}\chi^{3/2} \right),
\end{aligned}
\tag{4.14}
$$

respectively. This is schematically shown in Figure 4.5, where we have plotted the behaviour of the Airy functions as a function of X near the caustic X_{ct}. The caustic, which
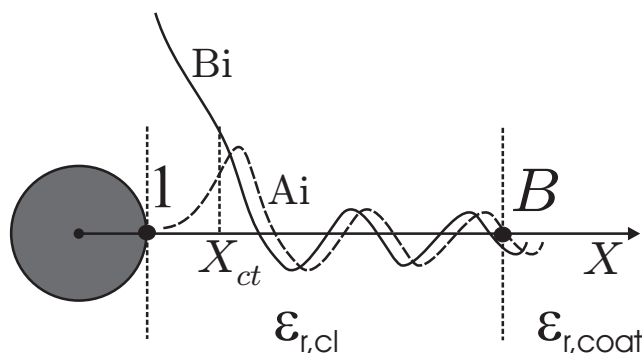
Figure 4.5: *Schematic plot of the behaviour of the Airy functions as a function of X before and after the caustic X_{ct}, where $X = B = b/a$ denotes a possible cladding/coating transition*

corresponds to $\chi \left(X_{ct}, 0 \right) = 0$, is readily given by [82]

$$
X_{ct} = \frac{\rho_c \left(\zeta_{\text{str}}^2 - \varepsilon_{r,\text{cl}} \right)}{2\zeta_{\text{str}}^2}.
\tag{4.15}
$$

In this region, $\text{Ai}(\chi)$ is negligible with respect to $\text{Bi}(\chi)$, and therefore it follows from Eq. (4.12) that

$$
G(\xi) \simeq \frac{S_\ell(\xi)}{\text{Bi} \left[\chi \left(1, \xi \right) \right]}.
\tag{4.16}
$$

Vassallo [107] has formulated the induced perturbation, $\delta\zeta$, on the (unperturbed) propagation coefficient ζ_{str} for large radii of curvature in terms of the amplitude of the perturbed backward field on the fibre axis $\psi_{BW}(0,0)$, i.e.

$$\zeta_{\text{str}}\delta\zeta = \frac{\pi\partial_X^\ell\psi_{BW}(0,0)}{P_\ell w^\ell(\hat{\omega}\rho_c)^2}, \tag{4.17}$$

where P_ℓ denotes the modal power of a propagating $\text{LP}_{\ell n}$ mode throughout a cross-sectional plane of the straight fibre, and ∂_X^ℓ is the ℓ-th derivative of ψ_{BW} with respect to X. As the field has to be continuous at $\rho = 1$, we adopt the following real-valued form of the LP fields

$$\psi_\ell(\rho,\theta) = \begin{cases} \dfrac{\psi(\rho)}{\psi(1)}K_\ell(w)\cos(\ell\theta) & \text{for } \rho < 1, \\ K_\ell(w\rho)\cos(\ell\theta) & \text{for } \rho > 1, \end{cases} \tag{4.18}$$

where $\psi(\rho)$ is determined via the procedure discussed in Section 2.5. As a result

$$P_\ell = \eta_\ell a^2\pi\left\{K_\ell^2(w)\int\limits_{\rho=0}^{1}\left[\frac{\psi(\rho)}{\psi(1)}\right]^2\rho d\rho + \frac{1}{2}\left[K_{\ell+1}(w)K_{\ell-1}(w) - K_\ell^2(w)\right]\right\}, \tag{4.19}$$

where $\eta_\ell = 2$ for $\ell = 0$ and $\eta_\ell = 1$ for $\ell \neq 0$. The perturbed backward evanescent field follows from Eq. (4.12) and Eq. (4.16) as

$$\psi_{BW}(X,Z) = \frac{\hat{\omega}}{\pi ja}\int\limits_{\xi=0}^{\infty}S_\ell(\xi)\frac{\text{Ai}\left[\chi\left(X,\xi\right)\right]}{\text{Bi}\left[\chi\left(1,\xi\right)\right]}\exp(-j\hat{\omega}\xi Z)d\xi. \tag{4.20}$$

Substituting Eq. (4.19) and Eq. (4.20) in Eq. (4.17), results in an expression for the induced perturbation on the normalised propagation coefficient ζ_{str}. With reference to Section 3.1.5, the power attenuation (bending-loss) coefficient per unit length is $\alpha = 2\hat{\omega}\alpha'/a$. Hence, the bending loss per unit length for an $\text{LP}_{\ell n}$ mode may be approximated by

$$\alpha = -2\,\text{Im}\left[\frac{a\pi\partial_X^\ell\psi_{BW}(0,0)}{P_\ell w^\ell\hat{\omega}\zeta_{str}}\right] = \frac{2\left(-w\right)^{-\ell}}{P_\ell\zeta_{str}}\left(\frac{2\hat{\omega}^2\zeta_{str}^2}{\rho_c}\right)^{\ell/3}\int\limits_{\xi=0}^{\infty}S_\ell(\xi)\frac{\text{Ai}^{(\ell)}\left[\chi\left(0,\xi\right)\right]}{\text{Bi}\left[\chi\left(1,\xi\right)\right]}d\xi, \tag{4.21}$$

where $\text{Ai}^{(\ell)}(\chi)$ is the ℓ-th derivative with respect to χ. For a step-index profile with $\ell = 0$, Eq. (4.21) reduces to [22]

$$\alpha = \frac{2u^2}{\hat{\omega}a\zeta_{str}V^2K_1^2(w)}\int\limits_{\xi=0}^{\infty}\gamma^{-1}\exp\left(-\hat{\omega}\gamma\right)\frac{\text{Ai}\left[\chi\left(0,\xi\right)\right]}{\text{Bi}\left[\chi\left(1,\xi\right)\right]}d\xi, \tag{4.22}$$

where $u = \hat{\omega}\left(\varepsilon_{r,\text{co}} - \zeta_{\text{str}}^2\right)^{1/2}$ and $V = \hat{\omega}\left(\varepsilon_{r,\text{co}} - \varepsilon_{r,\text{cl}}\right)^{1/2}$. When the Airy functions are replaced by their leading-order asymptotic expansions for large arguments of Eq. (4.14),

and under the hypothesis that $\xi^2 \ll \zeta_{\text{str}}^2 - \varepsilon_{r,\text{cl}}$, which is automatically satisfied if $\rho_c \gg 1$ [108], the integration over ξ can be performed analytically. This results in the following simplified bending-loss formula

$$\alpha = \frac{u^2}{2aV^2K_1^2(w)}\sqrt{\frac{\pi}{w^3\rho_c}}\exp\left(-\frac{2w^3\rho_c}{3\hat{\omega}^2n_{\text{cl}}^2}\right). \tag{4.23}$$

Other authors, who developed various approaches to deriving bending-loss formulae, ultimately arrived for a step-index profile at Eq. (4.23) [57, 82, 89, 108, 115]. In Section 4.5, the approximate expressions of Eqs. (4.21) through (4.23) are compared with vectorial full-wave (VFW) results. Further, we have used Eq. (4.21), i.e. the most accurate albeit the most complicated of the approximate expressions, to compute the effective cut-off wavelength, discussed in Section 3.1.6.

Next, let us include additional cladding and coating layers in the derivation above [22, 112]. For one added coating layer at $X = b/a = B$, see Figure 4.4, Eq. (4.21) can be generalised to

$$\alpha = \frac{2}{P_\ell\zeta_{str}}\left(-w\right)^{-\ell}\left(\frac{2\hat{\omega}^2\zeta_{str}^2}{\rho_c}\right)^{\ell/3}\int_{\xi=0}^{\infty}S_\ell(\xi)\frac{\text{Ai}^{(\ell)}\left[\chi\left(0,\xi\right)\right]}{\text{Bi}\left[\chi\left(1,\xi\right)\right]}R_{23}d\xi, \tag{4.24}$$

where

$$R_{23} = -\frac{\left(\text{Bi}\left[\chi\right]\text{Ai}'\left[\chi\right] - \text{Ai}\left[\chi\right]\text{Bi}'\left[\chi\right]\right)\left(\text{Bi}'\left[\chi_3\right]\text{Ai}\left[\chi_3\right] - \text{Ai}'\left[\chi_3\right]\text{Bi}\left[\chi_3\right]\right)}{\left(\text{Ai}'\left[\chi\right]\text{Bi}\left[\chi_3\right] - \text{Bi}'\left[\chi_3\right]\text{Ai}\left[\chi\right]\right)^2 + \left(\text{Ai}'\left[\chi_3\right]\text{Ai}\left[\chi\right] - \text{Ai}'\left[\chi\right]\text{Ai}\left[\chi_3\right]\right)^2}, \tag{4.25}$$

with $\chi = \chi\left(B,\xi\right)$. Further, $\chi_3 = \chi\left(B,\xi\right)$ with $\gamma^2 = \zeta_{\text{str}}^2 - \varepsilon_{r,coat} + \xi^2$.

This allows for simulations by which reflections at the cladding/coating interface are taken into account as well, which causes oscillations in the bending loss. For large radii of curvature, i.e. those ρ_c for which [82]

$$\rho_c > 2B\zeta^2/\left(\zeta_{\text{str}}^2 - \varepsilon_{r,\text{cl}}\right), \tag{4.26}$$

which corresponds to $\chi(B,0) = 0$, the field that is reflected at the pertaining interface is evanescent, and consequently, these oscillations are absent. This implies that for the evaluation of the effective cut-off wavelength, which involves a large radius of curvature, $R_{\text{eff}} = 18.2\,\text{cm}$, the additional layers do not have to be taken into account as long as Eq. (4.26) holds. For very small radii of curvature, the amplitude of the oscillations decreases, as the caustic moves away from the cladding/coating interface towards the core/cladding interface.

4.3   The idealised curved pipe: full-wave analysis

As a next step towards performing the full-wave analysis of the bent optical fibre, we derive field solutions for an idealised curved pipe. This provides us with a computational scheme to tackle the core region of the fibre later on, while avoiding the difficulty of radiation. We assume that the pipe is perfectly conducting (idealised), and hence attenuation due to leakage of conduction currents in the guide walls is absent. With the bent fibre in mind, we assume that the pipe is filled with a radially inhomogeneous medium. To obtain field solutions within the pipe, we follow the approach outlined in Section 2.3 for the core region. Hence, we employ a numerical integration of the pertaining Marcuvitz-Schwinger equations from bounded regular solutions at the core centre towards the waveguide wall.

We employ a toroidal coordinate system $\{x^1, x^2, x^3\} = \{\phi, \psi, r\}$ as it conforms nicely to the curved shape of the geometry. The configuration is shown in Figure 4.6. The cor-
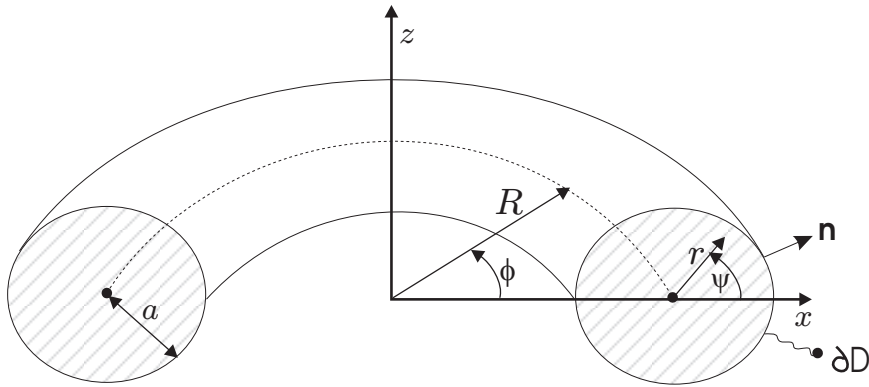
Figure 4.6: *Toroidal coordinate system conforming to the bent pipe as well as the bent fibre.*

responding (covariant) basis vectors are given by $\{\mathbf{c}_1, \mathbf{c}_2, \mathbf{c}_3\} = \{(R + r\cos\psi)\,\mathbf{u}_\phi, r\mathbf{u}_\psi, \mathbf{u}_r\}$. As a consequence, the metric tensor of Eq. (2.9) reads $g_{pq} = \mathrm{diag}\left[(R + r\cos\psi)^2, r^2, 1\right]$, and hence the (covariant) electric and magnetic field components are defined as $\{E_1, E_2, E_3\} = \{(R + r\cos\psi)\,E_\phi, rE_\psi, E_r\}$ and $\{H_1, H_2, H_3\} = \{(R + r\cos\psi)\,H_\phi, rH_\psi, H_r\}$, respectively. In accordance with Eq. (2.24) and Eq. (4.1), we assume electromagnetic field components of the following form

$$\begin{pmatrix} E_k(\phi, \psi, \rho) \\ H_k(\phi, \psi, \rho) \end{pmatrix} = \sum_{m=-\infty}^{\infty} \begin{pmatrix} e_{k,m}(\rho) \\ h_{k,m}(\rho) \end{pmatrix} \exp\left(-j\hat{\omega}\zeta\rho_c\phi\right)\exp(-jm\psi), \qquad (4.27)$$

where $k \in \{1, 2, 3\}$, and where the normalised frequency $\hat{\omega}$ and the normalised radial coordinate ρ are given by Eq. (2.25). These components are substituted in the Marcuvitz-Schwinger equations of Eq. (2.18). The resulting equation is multiplied on both sides of the equality sign by $\exp(j\ell\psi)$ and subsequently integrated over a single period of ψ. As

a consequence, we lose the summation on the left-hand side, owing to appearance of the Kronecker delta $\delta_{\ell,m}$. The integrals that occur on the right-hand side are evaluated in closed form in Appendix F.1. We arrive at the following coupled system of differential equations

$$-d_\rho \begin{pmatrix} e_{\kappa;\ell} \\ h_{\lambda;\ell} \end{pmatrix} = \rho^{-1} \sum_{m=-\infty}^{\infty} \begin{pmatrix} 0 & j\hat{\omega}Z_0 B_{\kappa\lambda} \\ -j\hat{\omega}Z_0^{-1}\varepsilon_r B_{\lambda\kappa} & 0 \end{pmatrix} \begin{pmatrix} e_{\kappa;m} \\ h_{\lambda;m} \end{pmatrix}, \tag{4.28}$$

where B is a tensor with elements

$$\begin{aligned}
B_{11} &= \frac{m\zeta\rho_c}{\hat{\omega}n^2}G, & B_{12} &= \rho_c\delta_{\ell,m} + \frac{\rho}{2}(\delta_{\ell+1,m} + \delta_{\ell,m+1}) - \left(\frac{\rho_c\zeta}{n}\right)^2 G, \\
B_{21} &= \frac{m\ell - (\hat{\omega}n\rho)^2}{(\hat{\omega}n)^2}G, & B_{22} &= -\frac{\ell\zeta\rho_c}{\hat{\omega}n^2}G,
\end{aligned} \tag{4.29}$$

with

$$G = (\rho_c^2 - \rho^2)^{-1/2} \xi_+^{|\ell - m|}, \quad \xi_+ = -\rho\left(\rho_c + \sqrt{\rho_c^2 - \rho^2}\right)^{-1}. \tag{4.30}$$

To account for the boundary conditions at $\rho = 0$, where the field must remain finite, we first scale the electromagnetic field components, i.e.

$$\{e_1, e_2\} = jZ_0\rho^{|\ell|}\{\hat{\omega}\rho_c p_2, -p_1\}, \quad \{h_1, h_2\} = \rho^{|\ell|}\{\hat{\omega}\rho_c q_1, q_2\}. \tag{4.31}$$

Subsequent substitution in Eq. (4.28) gives

$$d_\rho \mathbf{f}_\ell = -\rho^{-1}\left(|\ell|\mathbf{f}_\ell + \sum_{m=-\infty}^{\infty} \rho^{|m|-|\ell|}\mathsf{A}_{\ell,m}\mathbf{f}_m\right). \tag{4.32}$$

where $\mathbf{f} = \{p_1, p_2, q_1, q_2\}$,

$$\mathsf{A}_{\ell,m} = \begin{pmatrix} \mathbf{0} & \hat{\omega}\mathsf{S} \\ \hat{\omega}n^2\mathsf{JSJ} & \mathbf{0} \end{pmatrix}, \quad \mathsf{S} = \begin{pmatrix} -\hat{\omega}\rho_c B_{21} & -B_{22} \\ B_{11} & B_{12}/\hat{\omega}\rho_c \end{pmatrix}, \tag{4.33}$$

and J is given by Eq. (2.27). Due to the toroidal coordinate system, this system of differential equations is no longer separable for each azimuthal index m, i.e. all Fourier constituents are coupled. If we truncate the pertaining Fourier series at $m = M$, the general solution of Eq. (4.32) may be expressed as a linear combination of $4(2M + 1)$ independent solutions. To obtain the solutions that remain bounded at the core centre, which will be the initial vectors for the numerical integration, we expand the vectors $\mathbf{f}_\ell$, $\mathbf{f}_m$ and the dyad $\mathsf{A}_{\ell,m}$ about $\rho = 0$ in terms of a Taylor series. Consequently, Eq. (4.32) is written in the form

$$d_\rho\left[\rho^\alpha\mathbf{f}_\ell^{(\alpha)}(0)\right] = -\rho^{\alpha-1}|\ell|\mathbf{f}_\ell^{(\alpha)}(0) - \sum_{m=-M}^{M} \rho^{\gamma+\beta+|m|-|\ell|-1}\frac{\alpha!}{\gamma!\beta!}\mathsf{A}_{\ell,m}^{(\gamma)}(0)\mathbf{f}_m^{(\beta)}(0), \tag{4.34}$$

where $\{\alpha, \beta, \gamma\}$ are non-negative integers. The superscript indices between parentheses denote the order of the derivative with respect to ρ.

To simplify the derivation below, we assume that $d_\rho n(0) = 0$. The independent initial field vectors are found by equating equal orders of ρ in Eq. (4.34). Through construction, it turns out that there are $2(2M + 1)$ independent solutions that remain bounded at the core centre. These solutions occur in pairs for each ℓ, i.e.

$$\left(\mathbf{f}_{\ell,1}(0), \mathbf{f}_{\ell,2}(0)\right) = \delta_{\ell,m} \begin{pmatrix} 0 & 0 \\ 0 & -1 \\ 1 & 0 \\ 0 & 0 \end{pmatrix} \text{ for } m = 0, \tag{4.35}$$

and

$$\left(\mathbf{f}_{\ell,1}(0), \mathbf{f}_{\ell,2}(0)\right) = \delta_{\ell,m} \begin{pmatrix} -|m| & 0 \\ 0 & -1 \\ \zeta^2 - n^2 & \frac{m\zeta}{|m|} \\ m\zeta & |m| \end{pmatrix} + \frac{\delta_{|m|,m\ell-m^2}}{2\rho_c|m|} \begin{pmatrix} 0 & 0 \\ \frac{m\zeta}{|m|} & 1 \\ n^2 & 0 \\ 0 & 0 \end{pmatrix} \text{ for } m \neq 0. \tag{4.36}$$

These initial vectors are used as the starting values for the numerical integration of Eq. (4.32) to $\rho = 1$. This gives us $2(2M + 1)$ independent field solutions at the guide walls. Note that the contribution of the second term on the right-hand side in Eq. (4.36) vanishes as $\rho_c \to \infty$, which results in a set of uncoupled initial vectors, similar to the ones for the straight fibre.

Next, we invoke the boundary conditions at the perfectly conducting waveguide wall, which state that the tangential electric field components to the surface must be zero. With reference to Eq. (4.31), we deduce that $p_1 = p_2 = 0$ for each m and ℓ. As a consequence, the characteristic equation is that the determinant of a $2(2M + 1) \times 2(2M + 1)$ matrix has to vanish, which provides the conditions for the propagation coefficients.

To test the numerical integration in the core region, we compare our normalised propagation coefficients ζ with the ones obtained via a first-order approximation [57] for various radii of curvature R of an empty circularly cylindrical waveguide. As noted before, the system of differential equations decouples as $R \to \infty$, and consequently the modes present in the straight circular pipe must appear. The normalised propagation coefficients of the propagating modes are shown in Figure 4.7.

In a straight pipe, the modes under consideration are TE_{01} and TM_{11}. The former is frequently used for long-distance communications at high frequency owing to its low attenuation. As expected, the first-order approximation improves as the radius of curvature increases.
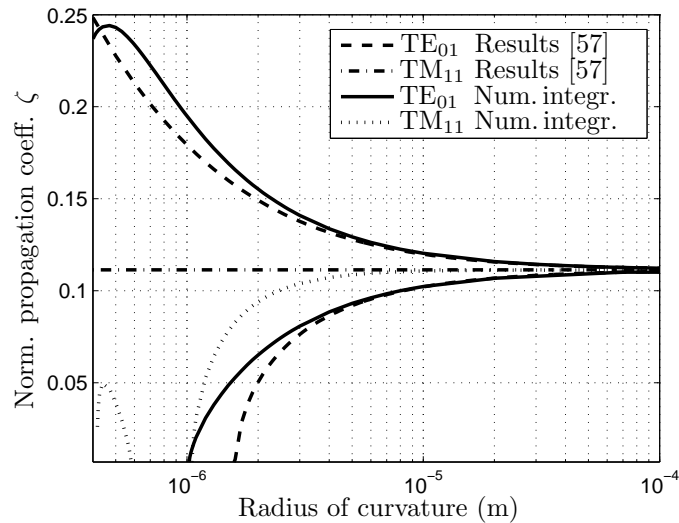
Figure 4.7: *Normalised propagation coefficients ζ of the propagating modes in a bent pipe with $\lambda = 1.0\,\mu m$, $a = 0.4\,\mu m$, and $n^2 = 1.5$. The numerical integration of Eq. (4.35) is compared with a first-order approximation given by Lewin et al. [57]. In a straight pipe, the modes under consideration are TE_{01} and TM_{11}.*

4.4 The bent optical fibre: full-wave analysis

We perform the vectorial full-wave (VFW) analysis of the bent fibre, which is valid for all radii of curvature. Similar to the curved pipe, it is convenient to employ the toroidal coordinate system $\{\phi, \psi, r\}$ of Figure 4.6, since it properly conforms to the shape of the fibre. As the bent fibre is an open waveguide structure, in contrast to the perfectly conducting pipe, we distinguish an interior and an exterior region of the fibre. Field solutions for the former region are determined by the numerical scheme derived for the bent pipe, i.e. by the numerical integration of a system of ordinary differential equations from the core centre towards the interface $\partial \mathcal{D}$. This implies that the interior region is allowed to be radially inhomogeneous. However, the numerical integration of an initial-value problem eventually encounters accuracy and stability limitations. It turns out that a stable integration all the way up to the cladding/coating interface cannot be guaranteed with double precision arithmetic. This concurs with the discussion in Section 2.4. Therefore, we regard the core/cladding interface as the upper limit of our numerical integration. As a result, the homogeneous cladding region, which is assumed to be of infinite extent, corresponds to the exterior region, whereas the radially inhomogeneous core region corresponds to the interior one.

We have to keep in mind that the inclusion of a coating may introduce significant oscillations in the bending loss versus wavelength or radius of curvature. Fortunately,

these effects can be studied in an *ad hoc* fashion [82]. Further, in our full-wave model, we neglect the effects of imperfections in the fibre itself as well as the induced stress and strain.

4.4.1   Interaction integral at the fibre surface

Having described the formulism for the interior region on the basis of the curved pipe, the next step is to determine $2(2M+1)$ independent field solutions in the exterior region, which have to be matched at the core/cladding interface to the interior ones. The matching is complicated by the fact that the electromagnetic fields propagating along the bent fibre are non-periodic in the ϕ-direction due to radiation. Therefore, it is necessary to view the ϕ-direction as a complex Riemann surface, having an infinite number of sheets [23]. However, for most of our observations we may restrict ϕ to the finite interval $-\pi < \phi \leq \pi$.

To achieve the matching at the core/cladding interface, we consider two electromagnetic states, viz. state A and state B. State B is the actual state in a configuration consisting of the fibre core surrounded by a homogeneous cladding, as shown in Figure 4.6. It is in this state that we perform the numerical integration of the system of differential equations in the interior region. To obtain field solutions in the exterior region that satisfy the radiation condition, we introduce an auxiliary state A. For this state, we consider a homogeneous configuration with a refractive index equal to that of the homogeneous cladding $n(\rho) = n_{\text{cl}}$. To generate the auxiliary wavefield, we introduce ring sources on an imaginary torus within the interior region, as is shown in Figure 4.8. In the next sections, we will elaborate on this choice and will determine the wavefield generated by a single ring source and an array of them.
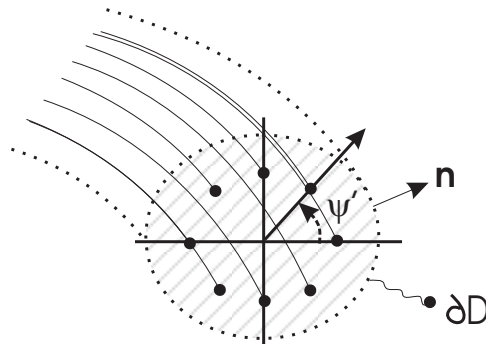
Figure 4.8: *Electromagnetic state A in which ring sources are deployed in a homogeneous background medium of $n(\rho) = n_{cl}$.*

To connect the states, we apply the reciprocity theorem to the exterior region. Since the states A and B are both source-free in their exterior regions, we arrive at a vanishing

interaction integral at the interface $\partial \mathcal{D}$, i.e.

$$\int_{\partial \mathcal{D}} \left(\mathbf{E}^B \times \mathbf{H}^A - \mathbf{E}^A \times \mathbf{H}^B \right) \cdot \mathbf{n} \, \mathrm{d}A = 0, \tag{4.37}$$

where the normal unit vector $\mathbf{n} = \mathbf{u}_r$. In accordance with Eq. (4.27), we assume that states A and B depend on ϕ through $\exp(\pm j\hat{\omega}\zeta\rho_c\phi)$, respectively, i.e. they correspond to waves that propagate in opposite ϕ-directions [18, 56]. As a result, the integrand in Eq. (4.37) no longer depends on ϕ, and hence, only an integral with respect to the ψ-coordinate remains.

We employ Muller's method [78] in the search for a complex propagation coefficient ζ such that Eq. (4.37) holds. At this value of ζ, the field mismatch between the states should vanish, since any field mismatch would indicate the presence of equivalent boundary surface sources, which for a genuine modal field solution should be absent. As this search is quite cumbersome, especially if one wishes to find several propagation coefficients, the initial guess should be as good as possible, otherwise Muller's method will fail. Similar to the discussion for the bent slab waveguide in Section 4.1, we start our search from the known propagation coefficients of the straight fibre. Subsequently, we trace out the locus of the propagation coefficients in the complex plane step by step, while decreasing the radius of curvature in a gradual way. The approximate bending-loss formulae of Eqs. (4.21) and (4.23) can provide us with proper initial values of ζ as well. It will be demonstrated that a gradual change in radius of curvature results in a gradual change in the value of the complex propagation coefficient.

4.4.2 Wavefield excitation by an array of modulated ring sources

To generate $2(2M+1)$ independent field solutions in the exterior region of state A, we place ring sources, like the one of Figure 4.9, parallel to the fibre axis in a ring-like fashion, as shown in Figure 4.8. These ring sources are either all electric or magnetic and are located
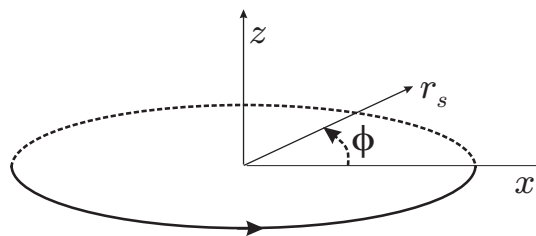

Figure 4.9: *Electric or magnetic ring source located in a homogeneous medium with $n(\rho)=n_{cl}$.*

in a homogenous background medium with $n(\rho) = n_{\mathrm{cl}}$. Since Maxwell's equations decouple in cylindrical coordinates, closed-form integral representations for the fields, generated by

the ϕ-directed sources can readily be constructed. Owing to the duality between the two types of sources, the respective field solutions are linearly independent. Hence, each type of source must provide us with $2M + 1$ independent field solutions. To achieve this, we place an equal number of ring sources and modulate them with an azimuthal $\exp(jm'\psi')$ dependence [45]. Here, ψ' denotes the angle with respect to the horizontal in the transverse plane at which the current loop is located, and $m' = \{-M, ..., M\}$. Further, we assume that the sources have an exponential phase factor of $\exp(j\hat{\omega}\zeta\rho_c\phi)$ along the ϕ-direction, to generate a wavefield with the same behaviour.

The introduction of ring sources directed along the ϕ-direction is based on an analysis of the straight fibre, whose coordinate system is shown in Figure 2.1. Inspired by the multifilament current model introduced by Leviatan and Boag [56], we have employed magnetic and electric line sources along the z-direction, the equivalent of ϕ-directed sources in the bent fibre case, to obtain $2M + 1$ independent field solutions for each type of source. These line sources are placed in an equally-spaced ring-like fashion in the azimuthal ψ-direction within the interior region. They generate the wavefield in the exterior region in the equivalent state A of the straight fibre configuration, which we denote A^{str}. The electromagnetic fields generated in the equivalent state B of the straight fibre, B^{str}, are derived by the procedure outlined in Section 2.3.1

The interaction integral in Eq. (4.37) is applied to connect the fields of both equivalent states of the straight fibre at the core/cladding interface $\partial\mathcal{D}$, where we have assumed that the states A^{str} and B^{str} depend on z through $\exp(\pm j\hat{\omega}\zeta a^{-1}z)$, respectively. As a result, only an integral with respect to ψ remains, which we have solved with a Gauss-Legendre quadrature rule. We have compared the accuracy of the obtained propagation coefficients with the corresponding exact values for a multi-mode fibre and proven that differences are marginal (10^{-9}) as long as sufficient line sources are employed. The number of used line sources $2M + 1$ is related to the highest azimuthal index m, i.e. at least $M \geq m$. The radial position of the line sources, which we have varied between $0.3 < \rho < 0.7$, does neither influence the accuracy of the computed propagation coefficients nor the convergence to this value [56]. As the results for the straight fibre configuration with z-directed line sources look promising, we have chosen for the equivalent ϕ-directed sources in the bent fibre case.

For the bent fibre configuration, it turns out that the radial position of the ring sources is much more critical from a convergence point of view than that for the straight fibre case. If the various ring sources are placed too close to the fibre axis, the fields excited by a full spread of angular harmonics ($-M \leq m \leq M$) become nearly dependent at $\partial\mathcal{D}$. As a consequence, instability looms and computation times increase considerably. On the other hand, if we move the rings toward $\partial\mathcal{D}$, aliasing of higher-order angular harmonics

may only be avoided through finer sampling. Although $2M + 1$ independent ring sources would suffice to compute the unknown independent field solutions, the use of additional sources helps to reduce aliasing. For a chosen balance between robustness, suppression of aliasing and the number of auxiliary sources, there exists an "optimal" $\rho = \rho_s$ for the position of the ring sources. In Appendix D, we present a more in-depth analysis of these counteracting phenomena for a scalar-wave straight open-waveguide scenario.

4.4.3 Field solutions for a single ring source

To derive a closed-form expression for the field generated by a single ring source, it is convenient to employ a cylindrical coordinate system $\{x^1, x^2, x^3\} = \{\phi, z, r_s\}$, with corresponding (covariant) basis vectors $\{\mathbf{c}_1, \mathbf{c}_2, \mathbf{c}_3\} = \{r_s \mathbf{u}_\phi, \mathbf{u}_z, \mathbf{u}_{r_s}\}$, as shown in Figure 4.9. The conversion into the toroidal coordinate system is performed in a subsequent stage. Since the derivation is similar for both types of ring sources, we will limit ourselves to the case of an electric ring source. Its electric current distribution is given by

$$J_1 = A(\psi') \exp(j\hat{\omega}\zeta\rho_c\phi)\delta(\rho_s - \rho_s')\delta(Z - Z')r_s, \tag{4.38}$$

where $\rho_s = r_s/R$, $Z = z/a$ are normalised coordinates, and ρ_s' and Z' denote the source location in the ρ_s and Z-direction, respectively. For convenience, we have included the azimuthal $\exp(jm'\psi')$ modulation in the amplitude factor $A(\psi')$. To exploit the invariance of the source-free auxiliary configuration in the z-direction, we employ a Fourier integral representation with respect to the Z-direction. In view of Eq. (4.9), the electromagnetic field components may be written as

$$\begin{pmatrix} E_k(\phi, Z, \rho_s) \\ H_k(\phi, Z, \rho_s) \end{pmatrix} = \frac{\hat{\omega}}{2\pi a} \exp(j\hat{\omega}\zeta\rho_c\phi) \int_{\xi=-\infty}^{\infty} \begin{pmatrix} \tilde{e}_k(\xi, \rho_s) \\ \tilde{h}_k(\xi, \rho_s) \end{pmatrix} \exp(-j\hat{\omega}\xi Z)d\xi, \tag{4.39}$$

where the tilde indicates that the specific quantity is a spectral domain term, and where $k \in \{1, 2, 3\}$. Consequently, for the partial derivatives, we have $\partial_Z \to -j\hat{\omega}\xi$ and $\partial_\phi \to j\hat{\omega}\zeta\rho_c$. Again, the Marcuvitz-Schwinger equations given by Eq. (2.18), in their curvilinear form, provide us with a system of first-order differential equations. A more convenient form is obtained by introducing new variables according to $\{\tilde{e}_1, \tilde{e}_2\} = jZ_0\{\rho_c a\tilde{p}_2, -\tilde{p}_1\}$ and $\{\tilde{h}_1, \tilde{h}_2\} = \{\rho_c a\tilde{q}_1, \tilde{q}_2\}$, which yields

$$\partial_{\rho_s}\tilde{\mathbf{f}} = \rho_c\rho_s^{-1}\left[\begin{pmatrix} \mathbf{0} & \hat{\omega}n_{\text{cl}}^{-2}\mathsf{S} \\ \hat{\omega}\mathsf{JSJ} & \mathbf{0} \end{pmatrix}\tilde{\mathbf{f}} + \begin{pmatrix} \mathbf{0} \\ \tilde{\mathbf{m}} \end{pmatrix}\right], \tag{4.40}$$

where $\tilde{\mathbf{f}} = (\tilde{p}_1, \tilde{p}_2, \tilde{q}_1, \tilde{q}_2) = (\tilde{\mathbf{p}}, \tilde{\mathbf{q}})$. The matrix S is given by

$$\mathsf{S} = \begin{pmatrix} \xi^2 - n_{\text{cl}}^2 & \zeta\xi \\ \zeta\xi & \zeta^2 - (\rho_s n_{\text{cl}})^2 \end{pmatrix}, \tag{4.41}$$

and

$$\tilde{\mathbf{m}} = \begin{pmatrix} 0 \\ -A(\psi') \exp(j\hat{\omega}\xi Z')\delta(\rho_s - \rho_s')\rho_s a \end{pmatrix}. \tag{4.42}$$

For convenience, Eq. (4.40) is rewritten as

$$\partial_{\rho_s}\tilde{\mathbf{f}} = \rho_c \rho_s^{-1} \left(\mathsf{A}\tilde{\mathbf{f}} + \tilde{\mathbf{u}} \right). \tag{4.43}$$

There exists a pair of independent interior field solutions ($\rho_s < 1$) for which $\tilde{\mathbf{p}}$ and $\tilde{\mathbf{q}}$ remain bounded as $\rho_r \downarrow 0$, denoted by $\tilde{\mathbf{p}}^i$ and $\tilde{\mathbf{q}}^i$. Likewise, there is a pair of independent exterior field solutions ($\rho_s > 1$) for which both $\tilde{\mathbf{p}}$ and $\tilde{\mathbf{q}}$ decay exponentially or algebraically depending on the value of ξ. These solutions are denoted by $\tilde{\mathbf{p}}^e$ and $\tilde{\mathbf{q}}^e$. Hence, we may regard these source-free regions separately and connect the corresponding field vectors at the ring source's location ($\rho_s = 1$).

Field vectors in the source-free regions

Let us start with the computation of the exterior field solutions, viz. solutions outside the ring source with $\rho_s > 1$. In view of the cylindrical geometry, we know that the solution will involve Bessel functions [18]. Therefore, we rewrite Eq. (4.40) in Bessel's (modified) differential equation for both $\tilde{\mathbf{p}}^e$ and $\tilde{\mathbf{q}}^e$ in the following way

$$[\rho_s\partial_{\rho_s}\rho_s\partial_{\rho_s} - (x^2 + \nu^2)]\,\tilde{\mathbf{p}}_1^e = 0, \quad \text{if} \quad \tilde{\mathbf{q}}_e = \{\tilde{q}_{1,1}^e, 0\}, \tag{4.44a}$$

$$[\rho_s\partial_{\rho_s}\rho_s\partial_{\rho_s} - (x^2 + \nu^2)]\,\tilde{\mathbf{q}}_2^e = 0, \quad \text{if} \quad \tilde{\mathbf{p}}_e = \{0, \tilde{p}_{2,2}^e\}, \tag{4.44b}$$

where $\nu = \hat{\omega}\zeta\rho_c$ and $x = \hat{\omega}\rho_s\rho_c\gamma$ with

$$\gamma = \sqrt{\xi^2 - n_{\text{cl}}^2}, \quad \text{with} \begin{cases} \text{Im}(\gamma) < 0, \\ \text{Re}(\gamma) > 0 \ \text{if} \ \text{Im}(\gamma) = 0. \end{cases} \tag{4.45}$$

Both second-order differential equations give us independent exterior field vectors. In matrix form, they are given by

$$\left(\tilde{\mathbf{f}}_1^e, \tilde{\mathbf{f}}_2^e\right) = \begin{pmatrix} K_\nu(x) & 0 \\ \zeta\xi\gamma^{-2}K_\nu(x) & -\rho_s\gamma^{-1}K_\nu'(x) \\ \rho_s n^2\gamma^{-1}K_\nu'(x) & -\zeta\xi\gamma^{-2}K_\nu(x) \\ 0 & K_\nu(x) \end{pmatrix} \begin{pmatrix} C_1^e & 0 \\ 0 & C_2^e \end{pmatrix}, \tag{4.46}$$

where $\tilde{\mathbf{f}}^e = \{\tilde{\mathbf{p}}^e, \tilde{\mathbf{q}}^e\}$, and C_1^e, C_2^e are constants that remain to be determined. Further, $K_\nu(x)$ denotes the modified Bessel function of the second kind and the prime indicates a derivative with respect to its argument. For convenience, we introduce an exterior

radial impedance matrix $\tilde{\mathsf{Z}}^e(\rho)$, which is defined by $\tilde{\mathsf{P}}^e = \tilde{\mathsf{Z}}^e \tilde{\mathsf{Q}}^e$, where $\tilde{\mathsf{P}}^e = \{\tilde{\mathbf{p}}_1^e, \tilde{\mathbf{p}}_2^e\}$ and $\tilde{\mathsf{Q}}^e = \{\tilde{\mathbf{q}}_1^e, \tilde{\mathbf{q}}_2^e\}$ follow from Eq (4.46). As a result, the impedance matrix reads

$$\tilde{\mathsf{Z}}^e = \frac{1}{L_\nu^e n^2} \begin{pmatrix} -\gamma^2 & -\zeta\xi \\ -\zeta\xi & \gamma^{-2}(L_\nu^{e2}n^2 - \zeta^2\xi^2) \end{pmatrix}, \quad \text{where} \quad L_\nu^e = -\rho_s\gamma\frac{K_\nu'(x)}{K_\nu(x)}. \tag{4.47}$$

In a similar way, we obtain an interior impedance $\tilde{\mathsf{Z}}^i$ matrix for the region inside the ring source. Replacing the modified Bessel functions of the second kind $K_\nu(x)$ by those of the first kind $I_\nu(x)$ in Eq. (4.46) results in the interior counterpart $\{\tilde{\mathbf{f}}_1^i, \tilde{\mathbf{f}}_2^i\}$. As a consequence, the interior impedance $\tilde{\mathsf{Z}}^i$ matrix for the region inside the ring source is, with the introduction of the variables $\tilde{\mathsf{P}}^i = \tilde{\mathsf{Z}}^i\tilde{\mathsf{Q}}^i$, where $\tilde{\mathsf{P}}^i = \{\tilde{\mathbf{p}}_1^i, \tilde{\mathbf{p}}_2^i\}$ and $\tilde{\mathsf{Q}}^i = \{\tilde{\mathbf{q}}_1^i, \tilde{\mathbf{q}}_2^i\}$, directly found as

$$\tilde{\mathsf{Z}}^i = \frac{1}{L_\nu^i n^2} \begin{pmatrix} -\gamma^2 & -\zeta\xi \\ -\zeta\xi & \gamma^{-2}(L_\nu^{i2}n^2 - \zeta^2\xi^2) \end{pmatrix}, \quad \text{where} \quad L_\nu^i = -\rho_s\gamma\frac{I_\nu'(x)}{I_\nu(x)}. \tag{4.48}$$

As a result, the total interior and exterior field vectors are given by

$$\tilde{\mathbf{f}}^i(\rho_s) = \left[C_1^i\tilde{\mathbf{f}}_1^i(\rho_s) + C_2^i\tilde{\mathbf{f}}_2^i(\rho_s)\right] \quad \text{for} \quad \rho_s < 1, \tag{4.49a}$$

$$\tilde{\mathbf{f}}^e(\rho_s) = \left[C_1^e\tilde{\mathbf{f}}_1^e(\rho_s) + C_2^e\tilde{\mathbf{f}}_2^e(\rho_s)\right] \quad \text{for} \quad \rho_s > 1. \tag{4.49b}$$

The next step is to connect these field vectors at $\rho_s = 1$, where the ring source is located.

Field matching at the ring source

So far, we have obtained two pairs of independent (interior and exterior) solutions, which have been added in Eq. (4.49). In terms of the impedance matrices, they can be written as follows

$$\tilde{\mathbf{f}}^i = \begin{pmatrix} \tilde{\mathsf{Z}}^i\tilde{\mathsf{Q}}^i \\ \tilde{\mathsf{Q}}^i \end{pmatrix} \mathbf{c}^i, \quad \tilde{\mathbf{f}}^e = \begin{pmatrix} \tilde{\mathsf{Z}}^e\tilde{\mathsf{Q}}^e \\ \tilde{\mathsf{Q}}^e \end{pmatrix} \mathbf{c}^e, \tag{4.50}$$

where $(\mathbf{c}^i)^T = (C_1^i, C_2^i)$ and $(\mathbf{c}^e)^T = (C_1^e, C_2^e)$. To determine the unknown amplitude vectors $\mathbf{c}^i$ and $\mathbf{c}^e$, we integrate the differential equation of Eq. (4.43) across the ring source radius and take the limit of approaching the ring source radius from both the interior and exterior regions. As a result, we integrate the delta function in the source distribution $\tilde{\mathbf{u}}$ to a finite result, i.e.

$$\tilde{\mathbf{f}}^e(\rho_s') - \tilde{\mathbf{f}}^i(\rho_s') = \lim_{h\to 0} \int_{\rho_s=\rho_s'-h}^{\rho_s'+h} \rho_c\rho_s^{-1}\tilde{\mathbf{u}}d\rho_s = \begin{pmatrix} \tilde{\mathbf{u}}_K \\ \tilde{\mathbf{u}}_J \end{pmatrix}, \tag{4.51}$$

where $\tilde{\mathbf{u}}_K$ and $\tilde{\mathbf{u}}_J$ correspond to a magnetic and electric source distribution, respectively. By substituting Eq. (4.42), the source distributions can be made explicit

$$\tilde{\mathbf{u}}_K = \begin{pmatrix} 0 \\ 0 \end{pmatrix}, \quad \tilde{\mathbf{u}}_J = \begin{pmatrix} 0 \\ -A(\psi')\exp(j\hat{\omega}\xi Z')\rho_c a \end{pmatrix}, \tag{4.52}$$

which indicates how the discontinuity at $\rho_s = 1$ of the interior and exterior field vectors is matched to the source strength. With the aid of Eq. (4.50), the left-hand side of Eq. (4.51) can be rewritten as follows

$$\tilde{\mathbf{f}}^e(\rho_s') - \tilde{\mathbf{f}}^i(\rho_s') = \begin{pmatrix} -\tilde{\mathsf{Z}}^i(\rho_s') & \tilde{\mathsf{Z}}^e(\rho_s') \\ -\mathsf{I} & \mathsf{I} \end{pmatrix} \begin{pmatrix} \tilde{\mathsf{Q}}^i(\rho_s') & 0 \\ 0 & \tilde{\mathsf{Q}}^e(\rho_s') \end{pmatrix} \begin{pmatrix} \mathbf{c}^i \\ \mathbf{c}^e \end{pmatrix}, \tag{4.53}$$

where I denotes the 2×2 identity matrix. Consequently, the amplitude vectors $\mathbf{c}^i$ and $\mathbf{c}^e$ can be expressed in terms of the electric and magnetic source distributions, i.e.

$$\begin{pmatrix} \mathbf{c}^i \\ \mathbf{c}^e \end{pmatrix} = \begin{pmatrix} \left[\tilde{\mathsf{Q}}^i(\rho_s')\right]^{-1} \left[\tilde{\mathsf{Z}}^e(\rho_s') - \tilde{\mathsf{Z}}^i(\rho_s')\right]^{-1} \left[\tilde{\mathbf{u}}_K - \tilde{\mathsf{Z}}^e(\rho_s')\tilde{\mathbf{u}}_J\right] \\ \left[\tilde{\mathsf{Q}}^e(\rho_s')\right]^{-1} \left[\tilde{\mathsf{Z}}^e(\rho_s') - \tilde{\mathsf{Z}}^i(\rho_s')\right]^{-1} \left[\tilde{\mathbf{u}}_K - \tilde{\mathsf{Z}}_i(\rho_s')\tilde{\mathbf{u}}_J\right] \end{pmatrix}, \tag{4.54}$$

which are next substituted in Eq. (4.50). This yields the following exterior field solution

$$\tilde{\mathbf{f}}^e(\rho_s) = \begin{pmatrix} \tilde{\mathsf{A}}^e \tilde{\mathbf{u}}_K + \tilde{\mathsf{C}}^e \tilde{\mathbf{u}}_J \\ \tilde{\mathsf{B}}^e \tilde{\mathbf{u}}_K + \tilde{\mathsf{D}}^e \tilde{\mathbf{u}}_J \end{pmatrix}, \tag{4.55}$$

with

$$\tilde{\mathsf{A}}^e = \begin{pmatrix} x' K_\nu(x) I_\nu'(x') & 0 \\ \zeta \xi \gamma^{-2} \left(x K_\nu'(x) I_\nu(x') + x' K_\nu(x) I_\nu'(x') \right) & -x K_\nu'(x) I_\nu(x') \end{pmatrix},$$

$$\tilde{\mathsf{B}}^e = \begin{pmatrix} \dfrac{1}{\hat{\omega}\rho_c\gamma^2} \left(x x' n_{\mathrm{cl}}^2 K_\nu'(x) I_\nu'(x') + (\nu\xi)^2 K_\nu(x) I_\nu(x') \right) & -\nu\xi K_\nu(x) I_\nu(x') \\ -\nu\xi K_\nu(x) I_\nu(x') & \hat{\omega}\rho_c\gamma^2 K_\nu(x) I_\nu(x') \end{pmatrix},$$

$$\tilde{\mathsf{C}}^e = n_{\mathrm{cl}}^{-2} \mathsf{J}\tilde{\mathsf{B}}^e \mathsf{J}, \quad \tilde{\mathsf{D}}^e = -\mathsf{J}\tilde{\mathsf{A}}^e \mathsf{J}, \tag{4.56}$$

where $x' = \hat{\omega}\rho_s'\rho_c\gamma$. In deriving Eq. (4.56), we have used the Wronskian relation [1]

$$K_\nu(x') I_\nu'(x') - K_\nu'(x') I_\nu(x') = K_\nu(x') I_{\nu+1}(x') + K_{\nu+1}(x') I_\nu(x') = (x')^{-1}. \tag{4.57}$$

The substitution of the electric and magnetic source distribution vectors $\tilde{\mathbf{u}}$ of Eq. (4.52) gives

$$\tilde{\mathbf{f}}^e(\xi, \rho_s) = A(\psi') \hat{\omega}\rho_c^2 a \begin{pmatrix} \zeta\xi n_{\mathrm{cl}}^{-2} K_\nu(x) I_\nu(x') \\ \rho_s\rho_s' K_\nu'(x) I_\nu'(x') + (\zeta\xi/\gamma n_{\mathrm{cl}})^2 K_\nu(x) I_\nu(x') \\ \zeta\xi\gamma^{-1} \left[\rho_s K_\nu'(x) I_\nu(x') + \rho_s' K_\nu(x) I_\nu'(x') \right] \\ -\rho_s'\gamma K_\nu(x) I_\nu'(x') \end{pmatrix} \exp(j\hat{\omega}\xi Z'). \tag{4.58}$$

Similarly, we obtain the interior field solution as

$$\tilde{\mathbf{f}}^i(\rho_s) = \begin{pmatrix} \tilde{\mathsf{A}}^i \tilde{\mathbf{u}}_K + \tilde{\mathsf{C}}^i \tilde{\mathbf{u}}_J \\ \tilde{\mathsf{B}}^i \tilde{\mathbf{u}}_K + \tilde{\mathsf{D}}^i \tilde{\mathbf{u}}_J \end{pmatrix}, \tag{4.59}$$

with

$$\tilde{\mathsf{A}}^i = \begin{pmatrix} x' I_\nu(x) K_\nu'(x') & 0 \\ \zeta\xi\gamma^{-2}\left(xI_\nu'(x)K_\nu(x') + x'I_\nu(x)K_\nu'(x')\right) & -xI_\nu'(x)K_\nu(x') \end{pmatrix},$$

$$\tilde{\mathsf{B}}^i = \begin{pmatrix} \dfrac{1}{\hat{\omega}\rho_c\gamma^2}\left(xx'n_{\mathrm{cl}}^2 I_\nu'(x)K_\nu'(x') + (\nu\xi)^2 I_\nu(x)K_\nu(x')\right) & -\nu\xi I_\nu(x)K_\nu(x') \\ -\nu\xi I_\nu(x)K_\nu(x') & \hat{\omega}\rho_c\gamma^2 I_\nu(x)K_\nu(x') \end{pmatrix},$$

$$\tilde{\mathsf{C}}^i = n_{\mathrm{cl}}^{-2}\mathsf{J}\tilde{\mathsf{B}}^i\mathsf{J}, \quad \tilde{\mathsf{D}}^i = -\mathsf{J}\tilde{\mathsf{A}}^i\mathsf{J}, \tag{4.60}$$

which, after substituting the electric and magnetic distribution vectors $\tilde{\mathbf{u}}$ of Eq. (4.52), results in

$$\tilde{\mathbf{f}}^i(\xi,\rho_s) = A(\psi')\hat{\omega}\rho_c^2 a \begin{pmatrix} \zeta\xi n_{\mathrm{cl}}^{-2} I_\nu(x)K_\nu(x') \\ \rho_s\rho_s' I_\nu'(x)K_\nu'(x') + (\zeta\xi/\gamma n_{\mathrm{cl}})^2 I_\nu(x)K_\nu(x') \\ \zeta\xi\gamma^{-1}\left[\rho_s I_\nu'(x)K_\nu(x') + \rho_s' I_\nu(x)K_\nu'(x')\right] \\ -\rho_s'\gamma I_\nu(x)K_\nu'(x') \end{pmatrix} \exp(j\hat{\omega}\xi Z'). \tag{4.61}$$

To obtain the field vectors in the spatial domain, expressed in normalised cylindrical coordinates $\{\phi, Z, \rho_s\}$, we apply the inverse Fourier transformation of Eq. (4.39).

Transformation from the cylindrical to the toroidal coordinate system

In conformity with the geometry of the fibre, we translate our problem from the cylindrical (cyl) to the toroidal (tor) coordinate system $\{\phi, \psi, \rho\}$ (see Figure 4.6) via

$$\begin{aligned} \rho_s &= \rho_c^{-1}\left(\rho_c + \rho\cos\psi\right), \quad Z = \rho\sin\psi, \\ \rho_s' &= \rho_c^{-1}\left(\rho_c + \rho'\cos\psi'\right), \quad Z' = \rho'\sin\psi'. \end{aligned} \tag{4.62}$$

In particular, the field vectors are transformed by the following matrix

$$\begin{pmatrix} p_1 \\ p_2 \\ q_1 \\ q_2 \end{pmatrix}^{\mathrm{tor}} = a \begin{pmatrix} \rho\cos\psi & 0 & -j\xi Z\rho_s^{-1}n_{\mathrm{cl}}^{-2} & -j\zeta Z\rho_s^{-1}n_{\mathrm{cl}}^{-2} \\ 0 & a^{-1} & 0 & 0 \\ 0 & 0 & a^{-1} & 0 \\ -j\zeta Z\rho_s^{-1} & j\xi Z\rho_s^{-1} & 0 & \rho\cos\psi \end{pmatrix} \begin{pmatrix} p_1 \\ p_2 \\ q_1 \\ q_2 \end{pmatrix}^{\mathrm{cyl}}, \tag{4.63}$$

where we have used the fact that $J_3 = M_3 = 0$, and where we have employed the same conversion of the electromagnetic field components as stated above Eq. (4.40). This results in the following respective exterior $(\rho_s > \rho_s')$ and interior $(\rho_s < \rho_s')$ field solution vectors

generated by an electric ring source excitation:

$$
\mathbf{F}^e(\phi, \psi, \rho) = \frac{A(\psi')\hat{\omega}^2 \rho_c^2}{2\pi} \exp(j\hat{\omega}\zeta\rho_c\phi) \int\limits_{\xi=-\infty}^{\infty} \exp\left[-j\hat{\omega}\xi\left(\rho\sin\psi - \rho'\sin\psi'\right)\right]
$$

$$
\times \begin{pmatrix} \zeta a \gamma^{-1}\left[\xi n_{\mathrm{cl}}^{-2} L^e I_\nu(x') - jZ\rho_s'\rho_s^{-1} K_\nu(x)I_\nu'(x')\right] \\ \rho_s\rho_s' K_\nu'(x)I_\nu'(x') + (\zeta\xi/\gamma n_{\mathrm{cl}})^2 K_\nu(x)I_\nu(x') \\ \zeta\xi\gamma^{-1}\left[\rho_s K_\nu'(x)I_\nu(x') + \rho_s' K_\nu(x)I_\nu'(x')\right] \\ j\zeta^2\xi Z a\gamma^{-2}\rho_s^{-1} K_\nu(x)I_\nu(x') - \rho_s' a L^e I_\nu'(x') \end{pmatrix} d\xi, \quad (4.64)
$$

$$
\mathbf{F}^i(\phi, \psi, \rho) = \frac{A(\psi')\hat{\omega}^2 \rho_c^2}{2\pi} \exp(j\hat{\omega}\zeta\rho_c\phi) \int\limits_{\xi=-\infty}^{\infty} \exp\left[-j\hat{\omega}\xi\left(\rho\sin\psi - \rho'\sin\psi'\right)\right]
$$

$$
\times \begin{pmatrix} \zeta a \gamma^{-1}\left[\xi n_{\mathrm{cl}}^{-2} L^i K_\nu(x') - jZ\rho_s'\rho_s^{-1} I_\nu(x)K_\nu'(x')\right] \\ \rho_s\rho_s' I_\nu'(x)K_\nu'(x') + (\zeta\xi/\gamma n_{\mathrm{cl}})^2 I_\nu(x)K_\nu(x') \\ \zeta\xi\gamma^{-1}\left[\rho_s I_\nu'(x)K_\nu(x') + \rho_s' I_\nu(x)K_\nu'(x')\right] \\ j\zeta^2\xi Z a\gamma^{-2}\rho_s^{-1} I_\nu(x)K_\nu(x') - \rho_s' a L^i K_\nu'(x') \end{pmatrix} d\xi, \quad (4.65)
$$

where

$$
L^i = \gamma\rho\cos\psi I_\nu(x) - j\xi Z I_\nu'(x), \quad \text{and} \quad L^e = \gamma\rho\cos\psi K_\nu(x) - j\xi Z K_\nu'(x). \qquad (4.66)
$$

To connect the electromagnetic field vectors of both states at either side of the fibre surface $\partial\mathcal{D}$ via the interaction integral of Eq. (4.37), the form of the field representation for this state should be similar to the one of state B in Eq. (4.27), i.e.

$$
\mathbf{F}(\phi, \psi, \rho) = \sum_{m=-M}^{M} \mathbf{f}_m(\rho) \exp(j\hat{\omega}\zeta\rho_c\phi) \exp(jm\psi), \qquad (4.67)
$$

where we have already truncated the angular Fourier series, and included the ϕ-dependence corresponding to state A. We multiply these vectors with $\exp\left(-j\ell\psi\right)$, and integrate over a single period of ψ, which introduces the Kronecker delta $\delta_{\ell,m}$ on the left-hand side. The ρ-dependence of the field vectors is then found as

$$
\mathbf{f}_\ell(\rho) = A(\psi')\left(\frac{\hat{\omega}\rho_c}{2\pi}\right)^2 \int\limits_{\psi=-\pi}^{\pi} \int\limits_{\xi=-\infty}^{\infty} \begin{pmatrix} \cdot \\ \cdot \\ \cdot \\ \cdot \end{pmatrix} \exp\left[j\hat{\omega}\xi\left(\rho'\sin\psi' - \rho\sin\psi\right)\right] \exp(-j\ell\psi)\, d\xi d\psi,
$$

$$
(4.68)
$$

where the dots represent the vector elements in either Eq. (4.64) or Eq. (4.65) for $\rho_s > \rho_s'$ and $\rho_s < \rho_s'$, respectively.

The integration over ψ is performed by a Gauss-Legendre quadrature rule, whereas the one over ξ is performed by a 20-41 points Gauss-Kronrod rule. Further, note that the modified Bessel functions of large complex order and argument, which are evaluated by a Gauss-Kronrod quadrature rule as well, occur in the inner integrand. Their numerical computation is discussed in Appendix C. As a result, the total computation consists of a triple integral and is therefore time-consuming. Fortunately, we can accelerate the computation to make computation times reasonable by a proper choice of the location of the ring sources and a deformation of the integration path.

Acceleration of the numerical computation

To evaluate the integral over ξ, we deform the integration path in the complex ξ-plane in such a way that convergence is exponential, as shown in Figure 4.10. The location
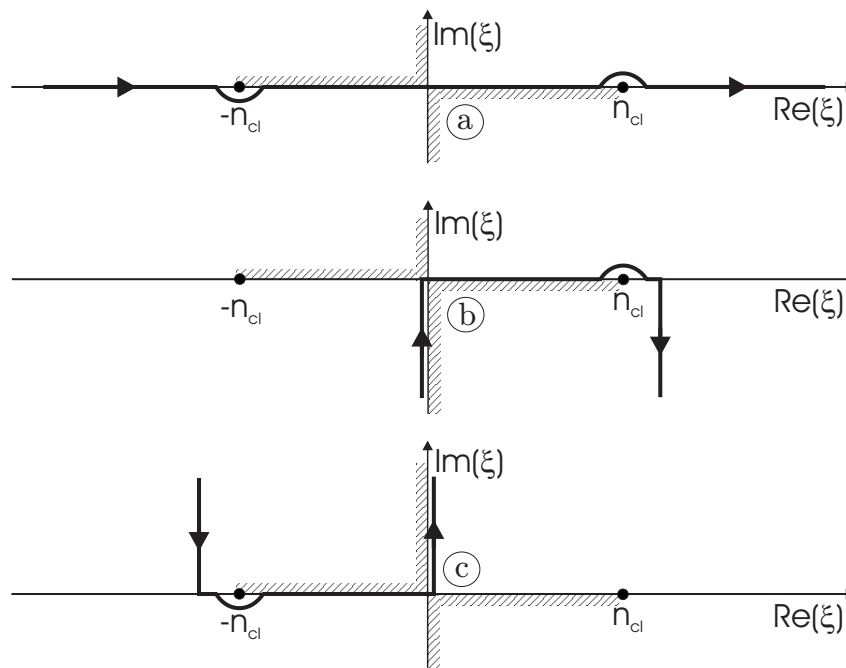
Figure 4.10: *Deformed integration paths in the complex ξ-plane.*

of the branch points at $\xi = \pm n_{\rm cl}$, and the branch cuts, which are rendered as hatched lines, follow directly from the square root definition of γ in Eq. (4.45) [23]. However, computation times depend highly on the difference between ρ and ρ', as the pertaining tails of the integral increase as the difference decreases. This becomes clear if we take a closer look at the product of modified Bessel functions in the four-dimensional vector and the exponential containing the integration variable ξ in Eq. (4.68). For large arguments,

the product of Bessel functions for $\rho_s > \rho'_s$ behaves as [1]

$$I_\nu(x') K_\nu(x) \sim \exp[-\hat{\omega}\gamma(\rho\cos\psi - \rho'\cos\psi')] \, (4xx')^{-1/2} \,, \qquad (4.69)$$

which implies that we have a considerable exponential decay if we integrate along path ⓐ in Figure 4.10, as long as $(\rho'\cos\psi' - \rho\cos\psi)$ is not too small. A similar line of reasoning holds for $(\rho\sin\psi - \rho'\sin\psi')$, where we integrate along one of the deformed paths ⓑ or ⓒ, for $(\rho\sin\psi - \rho'\sin\psi') \gtrless 0$, respectively.

Now, how do we define too small? To give an answer to this question, we have to look at the bigger picture, i.e. to which accuracy do we wish to acquire the propagation coefficient ζ. Obviously, for large radii of curvature the imaginary part of ζ is many orders of magnitude smaller than the real part, which requires a high relative precision in the quadrature. As we start our search in the complex ζ-plane from the analytically known propagation coefficients of the straight fibre, which are real-valued, and gradually proceed into the plane, we opt for a relative precision of at least 10^{-8}. This implies that the outer integral over ψ in Eq. (4.68) should at least be computed to that accuracy. Consequently, the inner integrals are to be computed with an even higher accuracy. For smaller radii of curvature, we may slightly relax the required accuracy in all quadratures.

To limit the length of the tails to about $|\xi| = 6n_{\mathrm{cl}}$, the decay of the integrand has to be at least in the same order of magnitude as the required precision at the tail ends. We integrate along path ⓑ or ⓒ if $|\rho\sin\psi - \rho'\sin\psi'| > 0.2$, otherwise path ⓐ is used.

Integration along the steepest-descent path will probably reduce computation time. However, that contour of integration would partially be located on the lower Riemann sheet in the complex ξ-plane. On this sheet, the computation of the product of modified Bessel function through their integral representations are fraught with difficulties which we sought to avoid.

A further acceleration is achieved by making use of the symmetry in the integral along ψ. Note that a change in the integration variables $\psi \to -\psi$ and $\xi \to -\xi$, results in the same integrand, though supplemented with a minus sign for the first and third field vector elements. This implies that we only need to evaluate the inner integrals for the region $0 \le \psi \le \pi$.

Field solutions for a magnetic ring source

Until now we have obtained $2M + 1$ independent field solutions. Since we need $2(2M + 1)$ solutions to realise the interconnection at the fibre surface, we employ an array of magnetic ring sources as well. A similar derivation has been performed as for the electric case. The components of the four-dimensional vector in Eq. (4.68) are related to those for the

magnetic case via

$$[\mathbf{f}(1), \mathbf{f}(2), \mathbf{f}(3), \mathbf{f}(4)]^T_{\mathrm{magn}} = jZ_0^{-1} \left[-\mathbf{f}(4), \mathbf{f}(3), n_{\mathrm{cl}}^2 \mathbf{f}(2), -n_{\mathrm{cl}}^2 \mathbf{f}(1) \right]^T_{\mathrm{elec}}. \qquad (4.70)$$

This leads to an additional set of $2M + 1$ independent field solutions.

Modulation of an array of ring sources

To generate a wavefield which is rich enough to give us $2M + 1$ independent field solutions, we have to employ at least $2M + 1$ ring sources. More ring sources may reduce the susceptibility to aliasing of the wavefield (cf. Appendix D). We have employed an array of N' ring sources, located on a circle about the core centre with a radius ρ' and evenly distributed at angles $\psi' = 2\pi n'/N'$, where $n' = 0, 1, ..., N' - 1$, as shown in Figure 4.8. Further, we modulate each ring source by factors $(N')^{-1} \exp(jm'\psi')$, with $m' = \{-M, ..., M\}$, through the amplitude factor $A(\psi')$ in Eq. (4.68). These considerations hold for both types of sources.

4.5 The bent optical fibre: scalar analysis versus full-wave analysis

Our method is valid for arbitrary refractive-index profiles. However, to provide a validation with results available in literature, we have carried out computations for a weakly-guiding step-index and parabolic-index single-mode fibre.

Step-index profile

The respective refractive indices in the step-index optical fibre of the core and cladding are $n_{\mathrm{co}} = 1.45$ and $n_{\mathrm{cl}} = 1.447$. Our comparison consists of the computation of the bending-loss for various radii of curvature R, at a representative wavelength of $\lambda = 1.3\,\mu\mathrm{m}$. For this configuration, the results of our vectorial full-wave (VFW) method are compared with the ones obtained by Eq. (4.22) and Eq. (4.23). This is shown in Figure 4.11(a).

Obviously, Eq. (4.23) overestimates the bending losses for all radii of curvature. On the other hand, the losses computed by Eq. (4.22) are in quite good agreement with the full-vectorial results for radii of curvature $R > 4\,\mathrm{mm}$. The somewhat chaotic behaviour for $R < 4\,\mathrm{mm}$, is caused by the fact that for certain ζ the denominator in the integrand in Eq. (4.22) vanishes, due to the presence of the Airy function $\mathrm{Bi}\left[\chi(a, \zeta)\right]$. For bending radii below $4\,\mathrm{mm}$, both approximate formulae overestimate, rather than underestimate the losses, which is good news from a design point of view.
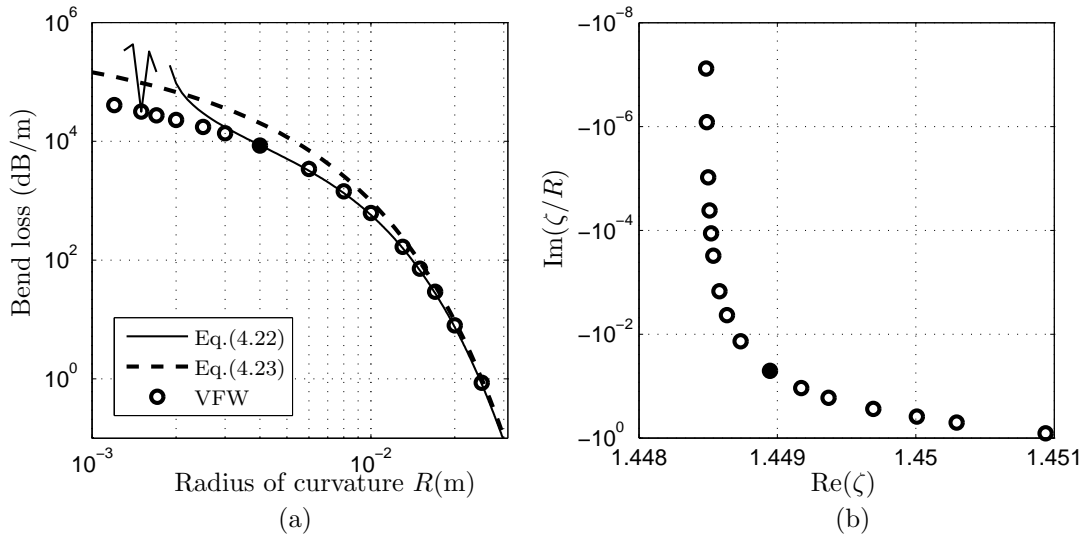
Figure 4.11: *(a) Bending losses in a step-index fibre as a function of the radius of curvature.
The approximations of Eq. (4.22) and Eq. (4.23) are set against the full-vectorial results. (b)
The location of the propagation coefficient ζ in the complex plane. The solid disc indicates the
result for $R = 4\,mm$.*

Only the imaginary part of the propagation coefficient ζ is needed to obtain the bend-
ing loss. All information regarding the real part of ζ is lost in the approximate bending-
loss formulae. To give an indication, we have plotted the location of the propagation
coefficients for different values of the radius of curvature in the complex ζ-plane in Fig-
ure 4.11(b). Observe the gradual change of the propagation coefficients for a gradually
decreasing radius of curvature.

Since the field solutions of the exterior domain involve triple integrals, which have to be
computed to at least eight significant digits to obtain meaningful results, the computation
of a converged value of ζ takes two to three days on a Pentium IV, 2.6 GHz. To limit
computation times, the truncation of the Fourier series in ψ has to be as tight as possible.
For $\rho_s = 0.58$ and $R \geq 2\,mm$, $M = 6$ suffices for an acceptable convergence, i.e ζ remains
unchanged for larger values of M. Obviously, for smaller radii of curvature, M should be
increased and computation time will increase accordingly.

As discussed in Section 4.4.1, the initial estimate for ζ, used in Muller's method,
has to be as close to the actual one as possible. For large radii of curvature, we use the
approximate bending-loss formulae to obtain an accurate initial estimate, but as the radius
decreases, extrapolation of previous values of ζ proves to be more precise. Evidently, if
we use the VFW method to compute the loss of higher-order modes, the number of zeros
in the complex ζ-plane will increase accordingly, and an accurate initial guess has to be
obtained via a cautious extrapolation from the exact straight-fibre propagation coefficient.
Altogether, it has taken about five weeks to perform the computations of all full-vectorial
results shown in Figure 4.11. Thus, although the proposed method provides reliable insight

into which of the numerous bending-loss formulae to use, it is in its present implementation not suitable for design purposes.

In Figure 4.12, the intensity patterns for a cross section of a straight fibre $(R = \infty)$ and a bent fibre with $R = 1\,\mathrm{cm}$ are shown. Observe the centrifugal shift of the peak amplitude.

Figure 4.12: *Intensity patterns for a cross section of the fibre with $R = \infty$ (left) and $R = 1\,cm$ (right). The white circle denotes the core/cladding interface.*

Parabolic-index profile

Next, we compute the bending losses in a parabolic-index single-mode fibre. We consider a parabolic refractive-index profile in the core region, which is given by Eq. (2.1) as

$$n(r) = n_{\mathrm{co}}\sqrt{1 - 2\Delta\rho^2}, \tag{4.71}$$

where $n_{\mathrm{co}} = 1.45$, $n_{\mathrm{cl}} = 1.447$, and therefore $\Delta \approx 0.2\,\%$, at $\lambda = 1.3\,\mathrm{\mu m}$. The results are compared with the ones obtained by the scalar approximation of Eq. (4.21), which holds for arbitrary refractive-index profiles in the core and are shown in Figure 4.13.

Further, we have computed the bending loss for the equivalent step-index (ESI) fibre by Eq. (4.22), where n_{co} is varied such that we obtain the same propagation coefficient as the one for the parabolic-index fibre, i.e. $\zeta \approx 1.44763$. This yields for the ESI fibre the values $n_{\mathrm{co}} \approx 1.44887$ and $n_{\mathrm{cl}} = 1.447$. The ESI losses are plotted in Figure 4.13 as well.

In comparison to the case of the step-index fibre of Figure 4.11, the bending losses are much higher. This is a result of the parabolic refractive-index profile, which provides a weaker confinement of the modal field in the core region. As a consequence, the fibre loses its power more easily through radiation. Note that the solid disc, which indicates the point at which the approximation deviates from the VFW results, is now located at about $R = 8\,\mathrm{mm}$. The power loss at this point is about equal to loss in the step-index

(a)   (b)
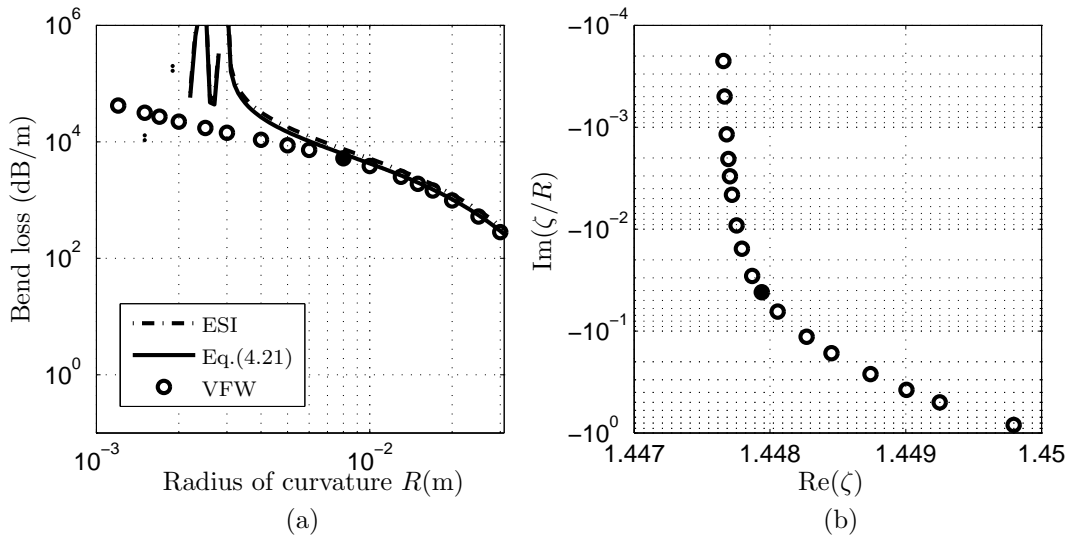
Figure 4.13: *(a) Bending losses in a parabolic-index fibre as a function of the radius of curvature. The approximation of Eq. (4.21) and the ESI computed by Eq. (4.22) are set against the full-vectorial results. (b) The location of the propagation coefficient ζ in the complex plane. The solid disc indicates the result for $R = 8\,mm$.*

fibre, i.e. $\text{Im}(\nu) \approx -5 \cdot 10^{-1}$. The bending losses computed for the simplified ESI fibre slightly overestimate the actual losses.

In Figure 4.14, intensity patterns for the parabolic-index fibre are plotted for a straight and a curved fibre with $R = 1\,\text{cm}$. We observe that, in comparison to the step-index fibre case in Figure 4.12, the power loss for the parabolic-index is indeed higher. Again, we observe the centrifugal shift of the peak amplitude.

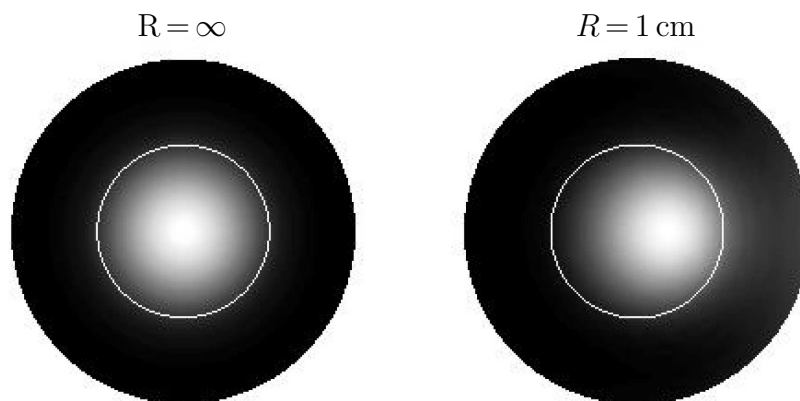$R = \infty$ $R = 1\,\text{cm}$
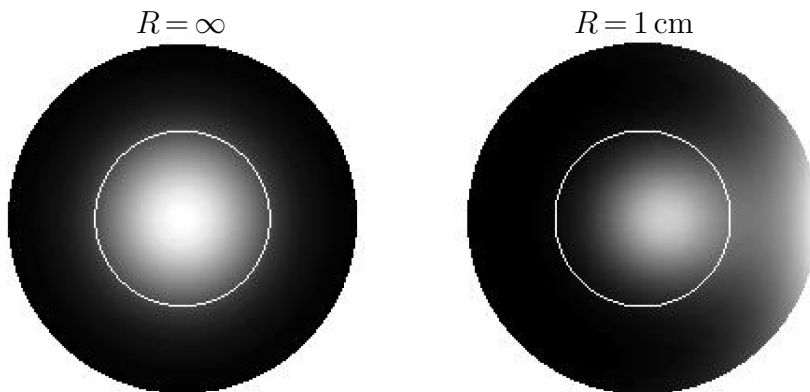
Figure 4.14: *Intensity patterns for a cross section of a parabolic-index fibre with $R = \infty$ (left) and $R = 1\,cm$ (right). The white circle denotes the core/cladding interface.*

4.6   Validation of the effective cut-off wavelength

The validation of the computation of the effective cut-off wavelength, discussed in Section 3.1.6, is not an as trivial a task as it might seem. Reference papers are available, although only one of those [46] uses the standardised bending method, and gives proper fibre characteristics, viz. a complete *specification* of the refractive-index profile. Moreover, the core radius and the numerical aperture (NA) supplied by the manufacturer can be off by a few percent due to manufacturing inaccuracies.

For a step-index York SM600 fibre, fabricated by York Technology (nowadays Fibercore Ltd.), an effective cut-off wavelength of $\lambda_{ce} = 568\,\text{nm}$ has been measured by the bending method by Kaur et al. [46]. Also, accurately measured values for the core radius and the NA are given. In Table 4.1, we have distinguished between these measured values (meas) and the ones supplied by the manufacturer (man). For both we have computed λ_{ce} at the effective radius of curvature $R_{\text{eff}} = 18.2\,\text{cm}$.

Table 4.1: *Cut-off wavelengths for various specification of the step-index York SM600 fibre [46] that has a measured effective cut-off wavelength of $\lambda_{ce} = 568\,\text{nm}$. Supplied values by the manufacturer and measured ones are denoted by the abbreviations (man) and (meas), respectively.*

Core radius (µm)	NA at 633 nm	λ_{ce}
2.45 (man)	0.09 (meas)	538.8
2.45 (man)	0.10 (man)	597.8
2.6 (meas)	0.09 (meas)	567.5
2.6 (meas)	0.10 (man)	630.5

Evidently, a relatively small difference in core radius and NA causes a significant difference in λ_{ce}. Hence, the importance of a meticulous specification of the refractive-index profile to properly compare simulation results with measurements. With pleasure, we observe that simulations on the basis of measured values for the core radius and NA give an effective cut-off wavelength that is very close to the measured value of $\lambda_{ce} = 568\,\text{nm}$ (to less than 0.1 %). Therefore, we may conclude that the proposed computation of λ_{ce} provides us with a good estimate of the actual effective cut-off wavelength.

Chapter 5

Profile optimisation

Often, desired optical fibre properties are conflicting, e.g. minimum dispersion and dispersion slope are at odds with minimum bending losses. In addition, one would like to keep the mode-field diameter fixed. From a design point of view, it is a challenging task to adapt the refractive-index profile of an optical fibre to meet the specific demands. Fortunately, computer-based optimisation schemes can speed up this design step considerably. In other fields of research such schemes often lead to counter-intuitive designs that could not have been contrived otherwise [88].

Usually, an optimisation problem is formulated in terms of the minimisation of a cost function. In our case, this function is expressed in terms of the fibre quantities introduced in Chapter 3. The specific form of the cost function is important, since it not only determines the relative importance of the individual fibre quantities, but it also influences the rate of convergence to a minimum. Likewise, the choice and the number of optimisation parameters, viz. the parameters that define the refractive-index profile, influence the efficiency and the result of the search substantially. Although many algorithms are available to perform the optimisation, by and large, they can be subdivided into two categories, viz. global stochastic techniques and local deterministic methods based on gradient information.

Deterministic gradient-based optimisers, e.g. Newton algorithms [25, 31], are usually much more efficient than stochastic ones. However, a careful initial (refractive-index profile) guess is of vital importance as the minimisation process may otherwise end up in a local minimum instead of in the desired global one. Further, we have to compute the gradients of the objective function with respect to all optimisation parameters at each iteration step in an efficient way. These gradients can be estimated by means of a finite-difference approximation, although the optimisation is faster if the actual gradients in terms of Fréchet derivatives are used.

Stochastically oriented optimisation techniques, on the other hand, are generally geared

towards finding the global minimum and only require cost-function evaluations. A major drawback forms the computation time, which can be extremely long, and therefore severely hampers a flexible design process. Also the initialisation of these routines is delicate, as various control parameters have to be set carefully. Genetic algorithms, particle swarm techniques, differential evolution (DE) methods and simulated annealing (SA) are typical examples that belong to this class of optimisers [34, 50, 92].

We have performed profile optimisations with two deterministic gradient-based optimisers viz. a modified-Newton (MN) algorithm E04KDF [71] and a quasi-Newton (QN) algorithm [24, 25], and two global ones, viz. the DE [63] scheme and SA [34] scheme. The choice of the latter two schemes is adopted from two articles by Mishra [62, 63], which give benchmark results for stochastic optimisation routines for a large number of test functions. There, the DE scheme comes out best, whereas the SA scheme performs only moderately well. Nevertheless, these benchmark results strongly depend on the employed test function, and there is no guarantee that one optimisation routine will perform better than the other for our cost function. Therefore, and for reasons of comparison, we have chosen to employ both schemes.

The greater part of this chapter deals with an efficient numerical computation of the gradients for the Newton algorithms, derived in terms of Fréchet derivatives. It is only in Section 5.4 that the stochastic optimisers come into play when we initialise them and perform a comparison with the optimised profiles obtained by the gradient-based optimisation schemes. For manufacturing purposes, the sensitivity of some of the obtained optimised profiles has been analysed in Section 5.5.4.

Finally, we wish to emphasise that it has not been our intent to write an optimisation routine that performs the refractive-index profile optimisation ourselves. This choice was especially influenced by the circumstance that available optimisation routines are quite sophisticated and yield satisfactory solutions.

5.1 Optimisation parameters and cost function

An essential step in any optimisation scheme is the identification of proper optimisation parameters. As it is our desire to optimise the refractive-index profile of an optical fibre to realise a set design goal, we want to retain an optimum flexibility as to its shape. For the discretisation of the profile in the core region, we have chosen a continuous concatenation of piecewise-linear segments. The endpoints of these linear segments serve as the free optimisation parameters. This restriction is sensible, since in practice, piecewise-linear profiles are relatively easy to manufacture.

At each sample point we allow for a horizontal and a vertical variation except for

the on-axis one where we allow for a vertical variation only. This implies that the total number of optimisation parameters, N, is odd. Each possible variation is denoted by an optimisation parameter x_n, with $n = 1, \ldots, N$. Since upward and downward refractive index variations are achieved by adding Germanium and Fluor to the Silica, respectively (see Section 3.1.2), each dopant can, in principle, be seen as an optimisation parameter. To keep the total number of parameters limited, we consider the Fluor concentration, X^{F}, to be constant between two adjacent sample points. Of course, this constant value sets the maximum possible depth of a trench in the refractive-index profile. Hence, for vertical variations, solely the Germanium concentration, X^{Ge}, at a sample point is considered as an optimisation parameter. In Figure 5.1(a), we have plotted an arbitrary Germanium concentration profile with four sample points as a function of the normalised radial coordinate $\rho = r/a$, where a is the core radius. The sample points are denoted by solid dots, which correspond to seven optimisation parameters.
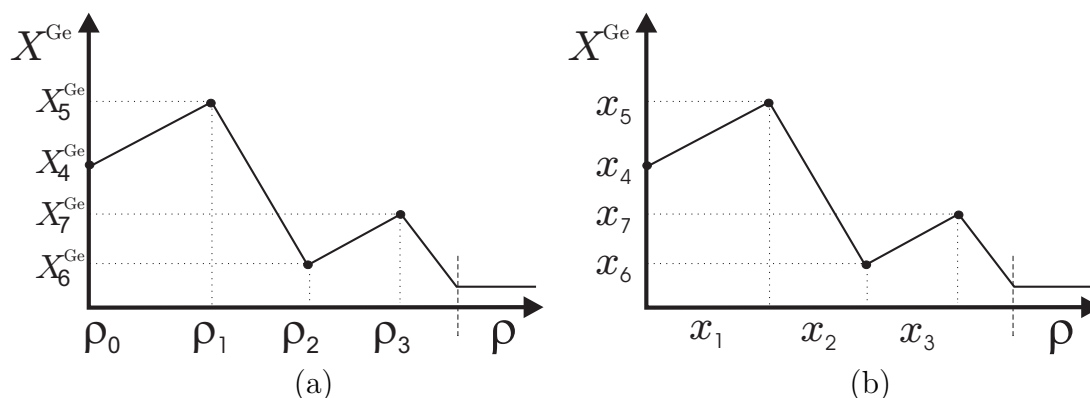
Figure 5.1: *Optimisation parameters x_n (b) and their relation to the Germanium concentration profile defining variables (a).*

Another possibility is to regard the permittivity as the vertical optimisation parameter, instead of its dopant building blocks. Recall that both physical quantities are (mildly non-linearly) related through the Sellmeier equation of Eq. (3.8). By choosing for the permittivity, we are not restricted to the dopants that are currently used, thus generalising the overall optimisation. Moreover, in the literature, the refractive-index profile, which is the square root of the permittivity profile, is the standard. On the other hand, if one uses different dopants to create the same permittivity profile, this profile is only valid for the pertaining wavelength, since the parameters in the Sellmeier equation change and consequently the frequency characteristics of the fibre change as well. Moreover, since the permittivity profile is defined at a wavelength of $\lambda = 632.8\,\mathrm{nm}$ (see Section 2.1), and designed with linear segments at that specific wavelength, the conversion to the desired optimisation wavelength requires additional computation time since we have to acquire the dopant concentrations first. Therefore, we prefer the profile optimisation of a dopant,

which is in our case the Germanium concentration profile. To underpin this preference, we have implemented both cases, i.e. profile optimisation of the Germanium concentration profile and the permittivity profile, and compare their performance in Section 5.3.1.

In view of our numerical integration scheme, it is necessary to limit the radial range in which to optimise the profile. This limit is set by the core/cladding transition. The optimisation parameters are chosen as follows

$$x_n = \rho_n - \rho_{n-1}, \quad \text{for } n = \{1, ..., (N-1)/2\}, \tag{5.1a}$$

$$x_n = X_n^{\text{Ge}}, \qquad \text{for } n = \{(N+1)/2, ..., N\}, \tag{5.1b}$$

and are shown explicitly in Figure 5.1(b). To exclude physically impossible profiles and limit the parameter space, we set simple bounds for all the optimisation parameters

$$\epsilon \leq x_n \leq 1 - \epsilon, \quad \text{for } n = \{1, ..., (N-1)/2\}, \tag{5.2a}$$

$$0 \leq x_n \leq 0.5, \quad \text{for } n = \{(N+1)/2, ..., N\}, \tag{5.2b}$$

and a single constraint for the horizontal parameters

$$\sum_{n=1}^{(N-1)/2} x_n \leq 1 - \epsilon. \tag{5.3}$$

The small number ϵ is introduced to prevent very steep slopes in the profile, which could lead to numerical difficulties in the gradient computations. The upper bound $X_n^{\text{Ge}} = 0.5$ corresponds to a refractive-index difference of about $\Delta \approx 3.5\%$, which we deem large enough for practical applications.

Unfortunately, the modified-Newton algorithm available to us cannot be supplemented with constraints. For this algorithm, the bounds are chosen in such a way that the constraint of Eq. (5.3) cannot be violated, which inevitably reduces the parameter space according to

$$\epsilon \leq x_n \leq 2\,(1-\epsilon)\,/\,(N-1), \quad \text{for } n = \{1, ..., (N-1)/2\}, \tag{5.4a}$$

$$0 \leq x_n \leq 0.5, \qquad \text{for } n = \{(N+1)/2, ..., N\}. \tag{5.4b}$$

Now that we have defined proper optimisation parameters, we translate the design goal into a cost function (CF). It is this function that we will minimise to obtain an optimal refractive-index profile. The fibre quantities v_q that have been discussed in Chapter 3, characterise the optical fibre, and may be used to construct the CF. Since these are physical quantities, they are all real-valued. We express the CF as a sum of squared errors, i.e.

$$\text{CF} = \sum_{q=1}^{Q} w_q \left[v_q(x_n) - v_q^{\text{ref}} \right]^2, \tag{5.5}$$

where Q denotes the number of fibre quantities. The desired value for a fibre quantity is denoted by the superscript 'ref'. Weighting coefficients w_q are included to scale the pertaining quantities to the same order of magnitude, or to stress the importance of a certain quantity above others.

Optimisation with a stochastic technique carries out repeated evaluations of the CF of Eq. (5.5). For the gradient-based algorithms, gradients of the CF with respect to the optimisation parameters are required as well. The computation of these gradients is treated in the next section.

5.2 Gradient-based optimisation

The gradient-based optimisation is performed by commercially available routines. We have used a modified-Newton algorithm from the NAG library (E04KDF) [71], and a quasi-Newton solver named FILTER, developed by Fletcher and Leyffer [25]. In both routines, gradient information accelerates the search for the minimum of the CF by providing steepest-descent directions. Hence, the first derivatives of the CF with respect to the optimisation parameters x_n need to be computed, i.e.

$$\partial_{x_n}\mathrm{CF} = 2 \sum_{q=1}^{Q} w_q \left[v_q(x_n) - v_q^{\mathrm{ref}} \right] \partial_{x_n} v_q. \tag{5.6}$$

The more accurate these gradients are computed, the faster the convergence to a minimum will be. The fibre quantities v_q are not simple functions of the optimisation parameters, and therefore, inevitably, we have to carry out part of the computation of $\partial_{x_n} v_q$ numerically. From Eq. (5.1) and Figure 5.1, we infer that

$$\partial_{x_n}F = \sum_{i=n}^{(N-1)/2} \partial_{\rho_i}F, \quad \text{for } n = \{1, ..., (N-1)/2\}, \tag{5.7a}$$

$$\partial_{x_n}F = \partial_{X_n^{\mathrm{Ge}}}F, \qquad \text{for } n = \{(N+1)/2, ..., N\}, \tag{5.7b}$$

where, for the sake of simplicity, we have introduced the functional $F : D \to \mathbb{R}$, which corresponds to a single fibre quantity v_q [61]. To obtain the directional derivatives on the right-hand side of Eq. (5.7), we have applied two approaches, i.e. the finite-difference approximation and the Fréchet derivative. To elucidate both procedures, we have redrawn the arbitrary profile of Figure 5.1 in Figure 5.2.

The finite-difference approximation is, wherever physically possible, carried out with a central-difference scheme, i.e.

$$\left\{ \partial_{\rho_i}, \partial_{X_n^{\mathrm{Ge}}} \right\} F(X^{\mathrm{Ge}}, \delta X^{\mathrm{Ge}}) \approx \frac{1}{2h} \left[F\left(X^{\mathrm{Ge}} + h\delta X^{\mathrm{Ge}} \right) - F\left(X^{\mathrm{Ge}} - h\delta X^{\mathrm{Ge}} \right) \right] = \Delta F_{n,\mathrm{central}}, \tag{5.8}$$
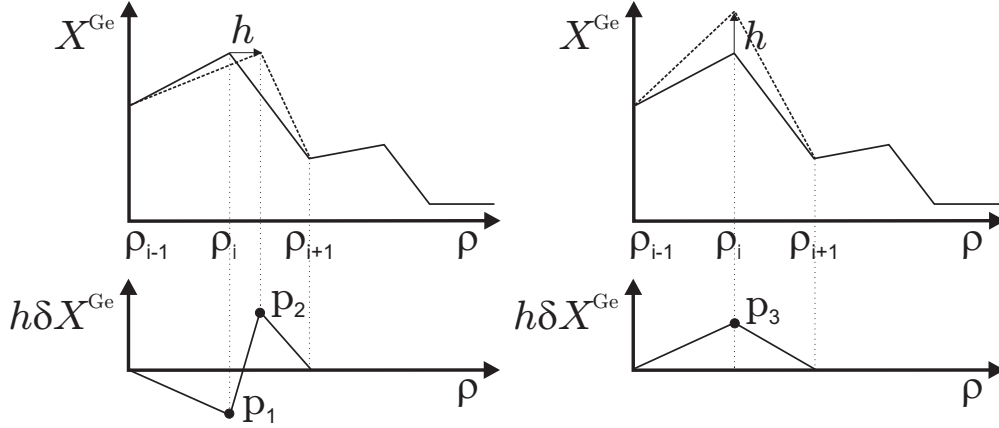
Figure 5.2: *Horizontal and vertical profile variations and the corresponding profile variation functions $h\delta X^{Ge}$.*

where h is a small value by which the profile is altered at a specific sample point. The corresponding profile variation function $h\delta X^{\text{Ge}}$ about this sample point is shown in Figure 5.2, and is defined by the points p_i, with $i \in \{1, 2, 3\}$, as follows

$$\text{p}_1 = h \left[\frac{X^{\text{Ge}}(\rho_{i-1}) - X^{\text{Ge}}(\rho_i)}{\rho_i + h - \rho_{i-1}} \right], \ \text{p}_2 = h \left[\frac{X^{\text{Ge}}(\rho_i) - X^{\text{Ge}}(\rho_{i+1})}{\rho_{i+1} - \rho_i} \right], \ \text{p}_3 = h. \qquad (5.9)$$

A horizontal variation of the profile corresponds to the directional derivative $\partial_{\rho_i} F$, whereas a vertical one corresponds to $\partial_{X_n^{\text{Ge}}} F$. As a result, three evaluations of F are required in our optimisation scheme for each CF evaluation, namely two for the finite-difference scheme and one for the unperturbed profile to obtain the actual values of v_q. Additionally, the value of the step-size h has to be determined carefully to avoid loss of accuracy. The accuracy of the finite-difference approximation in Eq. (5.8) depends on the accuracy to which the functional F can be computed, since the subtraction reduces the number of correct digits.

The Fréchet derivative, which denotes a directional derivative of the functional F in the direction of a test function $\delta X^{\text{Ge}} \in D$, is defined as follows [61]

$$\left\{ \partial_{\rho_i}, \partial_{X_n^{\text{Ge}}} \right\} F(X^{Ge}, \delta X^{\text{Ge}}) = \lim_{h \to 0} \frac{1}{h} \left[F(X^{\text{Ge}} + h\delta X^{\text{Ge}}) - F(X^{\text{Ge}}) \right] = \delta F_n, \qquad (5.10)$$

where the δ is also known as the first variation of F_n. The test functions δX^{Ge}, which differ for a horizontal and a vertical variation, are obtained by performing the limiting process in Eq. (5.10) on the profile variations in Figure 5.2. This limiting process will be elucidated in the next section.

Once the test functions δX^{Ge} are known, we determine the first variation of the propagation coefficient $\delta \zeta$, and subsequently, the first variation of the fibre quantities v_q. An accuracy and time comparison between the finite-difference approximation and the exact Fréchet derivative is performed in Section 5.2.4.

5.2.1   Gradient computation of the refractive-index profile

We perform the limiting process in Eq. (5.10) on the profile variations in Figure 5.2. The resulting first variations δX^{Ge} are shown in Figure 5.3, where expressions for the linear
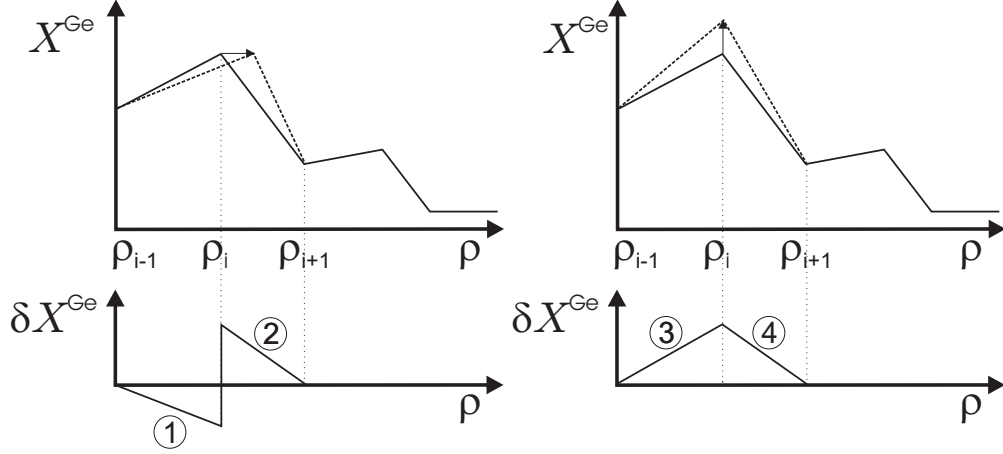

Figure 5.3: *Horizontal and vertical profile variations and the corresponding profile variation functions δX^{Ge}, which are obtained through Eq. (5.10).*

flanks are, with the aid of Eq. (5.9), readily given by

$$\text{①}: \delta X^{\mathrm{Ge}} = \left[X^{\mathrm{Ge}}(\rho_{i-1}) - X^{\mathrm{Ge}}(\rho_i)\right] \frac{\rho - \rho_{i-1}}{(\rho_i - \rho_{i-1})^2}, \quad \text{③}: \delta X^{\mathrm{Ge}} = \frac{\rho - \rho_{i-1}}{\rho_i - \rho_{i-1}},$$
$$\text{②}: \delta X^{\mathrm{Ge}} = \left[X^{\mathrm{Ge}}(\rho_i) - X^{\mathrm{Ge}}(\rho_{i+1})\right] \frac{\rho_{i+1} - \rho}{(\rho_{i+1} - \rho_i)^2}, \quad \text{④}: \delta X^{\mathrm{Ge}} = \frac{\rho_{i+1} - \rho}{\rho_{i+1} - \rho_i}. \tag{5.11}$$

Through the Sellmeier equation, given by Eq. (3.8), we obtain the first variation of the permittivity $\delta\varepsilon_r$

$$\delta\varepsilon_r(\rho) = \sum_{i=1}^{3} \delta X^{\mathrm{Ge}} \hat{\omega}_i^2 \upsilon^{-1} \left[db_i^{\mathrm{Ge}} + b_i d\lambda_i^{\mathrm{Ge}} \hat{\omega}^2 \hat{\omega}_i \left(\pi a \upsilon\right)^{-1}\right]. \tag{5.12}$$

Consequently, the derivative with respect to ρ of $\delta\varepsilon_r$ is given by

$$\partial_\rho \delta\varepsilon_r = \sum_{i=1}^{3} \hat{\omega}_i^2 \upsilon^{-1} \Big\{ \partial_\rho \delta X^{\mathrm{Ge}} \left[db_i^{\mathrm{Ge}} + b_i d\lambda_i^{\mathrm{Ge}} \hat{\omega}^2 \hat{\omega}_i \left(\pi a \upsilon\right)^{-1}\right]$$
$$+ \frac{\hat{\omega}_i \hat{\omega}^2 \delta X^{\mathrm{Ge}} d\lambda_i^{\mathrm{Ge}} \partial_\rho X^{\mathrm{Ge}}}{2 \left(\pi a \upsilon\right)^2} \left[4\pi a db_i^{\mathrm{Ge}} \upsilon^{-1} + b_i \hat{\omega}_i d\lambda_i^{\mathrm{Ge}} \left(3\hat{\omega}^2 + \hat{\omega}_i^2\right)\right] \Big\}, \tag{5.13}$$

where

$$\text{①}: \partial_\rho \delta X^{\mathrm{Ge}} = \frac{X^{\mathrm{Ge}}(\rho_{i-1}) - X^{\mathrm{Ge}}(\rho_i)}{(\rho_i - \rho_{i-1})^2}, \quad \text{③}: \partial_\rho \delta X^{\mathrm{Ge}} = (\rho_i - \rho_{i-1})^{-1},$$
$$\text{②}: \partial_\rho \delta X^{\mathrm{Ge}} = \frac{X^{\mathrm{Ge}}(\rho_{i+1}) - X^{\mathrm{Ge}}(\rho_i)}{(\rho_i - \rho_{i-1})^2}, \quad \text{④}: \partial_\rho \delta X^{\mathrm{Ge}} = (\rho_i - \rho_{i+1}), \tag{5.14}$$

for the pertaining flanks, and a delta function is introduced due to the step between flank ① and ②. These delta functions only occur in the computation of the first variation of the MFD d_{II} as we will show in Section 5.2.3, and similar to the discussion for the MFD d_{II} in Section 3.1.4, we neglect them during the pertaining computations.

5.2.2   Gradient computation of the propagation coefficient

The propagation coefficient ζ forms the cornerstone in the computation of all fibre quantities v_q (see Chapter 3). To compute the directional derivative of the fibre quantities, $\partial_{x_n} v_q$, it is therefore evident that we first have to determine the gradients $\partial_{x_n} \zeta$ by employing the definition from Eq. (5.10). Further, we will frequently refer to Section 2.3 where we have elaborated on the computation of ζ.

First of all, we expand all variables that are required to compute ζ, and that depend on the Germanium concentration X^{Ge} and its variation δX^{Ge}, in terms of their first variation

$$
\begin{cases}
\varepsilon_r(X^{\mathrm{Ge}}) & \to \quad \varepsilon_r + h\delta\varepsilon_r, \\
\zeta(X^{\mathrm{Ge}}) & \to \quad \zeta + h\delta\zeta,
\end{cases}
\qquad
\begin{cases}
\mathbf{f}(X^{\mathrm{Ge}}) & \to \quad \mathbf{f} + h\delta\mathbf{f}, \\
\mathsf{A}(X^{\mathrm{Ge}}) & \to \quad \mathsf{A} + h\delta\mathsf{A}.
\end{cases}
\tag{5.15}
$$

The propagation coefficient ζ is obtained from the characteristic equation $\mathsf{C}(\zeta)$ of Eq. (2.42). Upon substituting the expansion of the field vector $\mathbf{f}$ in $\mathsf{C}(\zeta)$, an expression for the first variation $\delta\zeta$ is readily obtained, i.e.

$$
\begin{aligned}
\delta\mathsf{C}(\zeta, \delta\zeta)|_{\rho=1} \; = \; 0 \; = \quad & \det\left[\delta\mathbf{f}_1 \; \mathbf{f}_2 \; \mathbf{f}_3 \; \mathbf{f}_4\right]\big|_{\rho=1} + \det\left[\mathbf{f}_1 \; \delta\mathbf{f}_2 \; \mathbf{f}_3 \; \mathbf{f}_4\right]\big|_{\rho=1} + \\
& \det\left[\mathbf{f}_1 \; \mathbf{f}_2 \; \delta\mathbf{f}_3 \; \mathbf{f}_4\right]\big|_{\rho=1} + \det\left[\mathbf{f}_1 \; \mathbf{f}_2 \; \mathbf{f}_3 \; \delta\mathbf{f}_4\right]\big|_{\rho=1}.
\end{aligned}
\tag{5.16}
$$

For the core region, the first variations $\delta\mathbf{f}_1$ and $\delta\mathbf{f}_2$ are obtained by an expansion of the system of differential equations of Eq. (2.29) in the following way

$$
d_\rho \begin{pmatrix} \mathbf{f} \\ \delta\mathbf{f} \end{pmatrix} = \rho^{-1} \begin{pmatrix} \mathsf{A}(\rho) & 0 \\ \delta\mathsf{A}(\rho) & \mathsf{A}(\rho) \end{pmatrix} \begin{pmatrix} \mathbf{f} \\ \delta\mathbf{f} \end{pmatrix},
\tag{5.17}
$$

with

$$
\delta\mathsf{A}(\rho) = \begin{pmatrix}
0 & \dfrac{\hat{\omega}\zeta}{\varepsilon_r^2}\left(2\varepsilon_r\delta\zeta - \zeta\delta\varepsilon_r\right) & \dfrac{m}{\varepsilon_r^2}\left(\varepsilon_r\delta\zeta - \zeta\delta\varepsilon_r\right) & 0 \\
\hat{\omega}\rho^2\delta\varepsilon_r & 0 & 0 & -m\delta\zeta \\
m\delta\zeta & 0 & 0 & \hat{\omega}\left(2\zeta\delta\zeta - \delta\varepsilon_r\right) \\
0 & -\dfrac{m}{\varepsilon_r^2}\left(\varepsilon_r\delta\zeta - \zeta\delta\varepsilon_r\right) & \dfrac{m^2\delta\varepsilon_r}{\hat{\omega}\varepsilon_r^2} & 0
\end{pmatrix}.
\tag{5.18}
$$

Above, $\mathsf{A}(\rho)$ and $\delta\varepsilon_r$ are given by Eq. (2.30) and Eq. (5.12), respectively. The initial field vectors, which are needed for the numerical integration of the system of Eq. (5.17), consist

of the two 4-vectors given by Eq. (2.34) and their first variations, i.e.

$$(\delta\mathbf{f}_1, \delta\mathbf{f}_2) = \begin{pmatrix} 0 & \delta\zeta \\ 0 & 0 \\ \delta\zeta & \delta\varepsilon_{r,0} \\ 0 & 0 \end{pmatrix}, \quad (\delta\mathbf{f}'_1, \delta\mathbf{f}'_2) = V \begin{pmatrix} 0 & \delta\zeta + \zeta W \\ 0 & 0 \\ 0 & -\delta\varepsilon_{r,0} - \varepsilon_{r,0}W \\ 0 & -m\hat{\omega}^{-1}W \end{pmatrix}, \quad (5.19)$$

where V is given by Eq. (2.35) and where

$$W = \partial_\rho \delta\varepsilon_{r,0} \left(\partial_\rho \varepsilon_{r,0}\right)^{-1} - \delta\varepsilon_{r,0} \left(\varepsilon_{r,0}\right)^{-1}. \quad (5.20)$$

The derivative $\partial_\rho \delta\varepsilon_{r,0}$ at the fibre axis is given by Eq. (5.13).

For the invariant cladding region, where analytical expressions for the field vectors are available, the first variations are given by

$$[\delta\mathbf{f}_3(\rho), \delta\mathbf{f}_4(\rho)] = \frac{\hat{\omega}\delta\zeta}{w^2\gamma^2} \begin{pmatrix} 0 & 0 \\ \zeta\varepsilon_{r,\text{cl}}\left[2 + w^2\rho^2\left(1 - \tau^2\right)\right] & m\left(\zeta^2 + \varepsilon_{r,\text{cl}}\right) \\ 0 & 0 \\ m\left(\zeta^2 + \varepsilon_{r,\text{cl}}\right) & \zeta\left[2 + w^2\rho^2\left(1 - \tau^2\right)\right] \end{pmatrix}, \quad (5.21)$$

where $\tau = K'_{|m|}(w\rho)/K_{|m|}(w\rho)$, in which the prime denotes a derivative with respect to the argument.

Now that all field vectors and their first variations are known, we employ a Van Wijngaarden–Dekker–Brent root-finding scheme [78] to perform the search for the variation $\delta\zeta$ in Eq. (5.16). This search involves on average about eight function evaluations to obtain a high precision. However, at the cost of a larger system of differential equations, we will now present a more efficient alternative, which merely requires a single evaluation.

Alternative gradient computation of the propagation coefficient

Let us regard the propagation coefficient ζ as an independent variable. Since $\delta\mathsf{C}(\zeta) = 0$ holds for all profile variations δX^{Ge} (see Eq. (5.16)), its derivative with respect to δX^{Ge} results in

$$\frac{\delta\mathsf{C}}{\delta X^{\text{Ge}}} = 0 = \partial_\zeta\mathsf{C}\frac{\delta\zeta}{\delta X^{\text{Ge}}} + \frac{\delta\mathsf{C}}{\delta X^{\text{Ge}}}\bigg|_{\zeta=\text{cst.}} \quad \Rightarrow \quad \delta\zeta = -\frac{\delta\mathsf{C}}{\partial_\zeta\mathsf{C}}. \quad (5.22)$$

Hence, to determine $\delta\zeta$, we need, in addition to $\delta\mathsf{C}$, also $\partial_\zeta\mathsf{C}$. The computation of the latter variation has already been discussed in Section 3.1.1. As ζ is considered an independent variable, field solutions for both core and cladding regions have to be derived anew.

Let us start with the core region by expanding the system of Eq. (2.29) as follows

$$d_\rho \begin{pmatrix} \mathbf{f} \\ \delta\mathbf{f} \\ \partial_\zeta\mathbf{f} \end{pmatrix} = \rho^{-1} \begin{pmatrix} \mathsf{A}(\rho) & 0 & 0 \\ \delta\mathsf{A}_1(\rho) & \mathsf{A}(\rho) & 0 \\ \partial_\zeta\mathsf{A}(\rho) & 0 & \mathsf{A}(\rho) \end{pmatrix} \begin{pmatrix} \mathbf{f} \\ \delta\mathbf{f} \\ \partial_\zeta\mathbf{f} \end{pmatrix}, \quad (5.23)$$

where

$$
\delta\mathsf{A}_1(\rho) = \delta\varepsilon_r
\begin{pmatrix}
0 & -\dfrac{\hat{\omega}\zeta^2}{\varepsilon_r^2} & -\dfrac{m\zeta}{\varepsilon_r^2} & 0 \\
\hat{\omega}\rho^2 & 0 & 0 & 0 \\
0 & 0 & 0 & -\hat{\omega} \\
0 & \dfrac{m\zeta}{\varepsilon_r^2} & \dfrac{m^2}{\hat{\omega}\varepsilon_r^2} & 0
\end{pmatrix},
\quad
\partial_\zeta\mathsf{A}(\rho) =
\begin{pmatrix}
0 & \dfrac{2\hat{\omega}\zeta}{\varepsilon_r} & \dfrac{m}{\varepsilon_r} & 0 \\
0 & 0 & 0 & -m \\
m & 0 & 0 & 2\hat{\omega}\zeta \\
0 & -\dfrac{m}{\varepsilon_r} & 0 & 0
\end{pmatrix}.
\quad (5.24)
$$

The initial vectors, and their gradients, which follow from Eq. (2.34), read

$$
(\delta\mathbf{f}_1, \delta\mathbf{f}_2) =
\begin{pmatrix}
0 & 0 \\
0 & 0 \\
0 & \delta\varepsilon_{r,0} \\
0 & 0
\end{pmatrix},
\quad
(\delta\mathbf{f}_1', \delta\mathbf{f}_2') = -V
\begin{pmatrix}
0 & -\zeta W \\
0 & 0 \\
0 & \delta\varepsilon_{r,0} + \varepsilon_{r,0}W \\
0 & m\hat{\omega}^{-1}W
\end{pmatrix},
$$

$$(5.25)$$

$$
(\partial_\zeta\mathbf{f}_1, \partial_\zeta\mathbf{f}_2) =
\begin{pmatrix}
0 & 1 \\
0 & 0 \\
1 & 0 \\
0 & 0
\end{pmatrix},
\quad
(\partial_\zeta\mathbf{f}_1', \partial_\zeta\mathbf{f}_2') = V
\begin{pmatrix}
0 & 1 \\
0 & 0 \\
0 & 0 \\
0 & 0
\end{pmatrix},
$$

where W is given by Eq. (5.20). In the cladding region, the pertaining derivatives of the two independent solutions are, with the aid of Eq. (2.38), found as

$$
[\partial_\zeta\mathbf{f}_3(\rho), \partial_\zeta\mathbf{f}_4(\rho)] =
\begin{pmatrix}
0 & 0 \\
\partial_\zeta v_1 \varepsilon_{r,\mathrm{cl}} & \partial_\zeta v_2 \\
0 & 0 \\
\partial_\zeta v_2 & \partial_\zeta v_1
\end{pmatrix},
\quad
(\delta\mathbf{f}_3, \delta\mathbf{f}_4) = \mathbf{0}
\quad (5.26)
$$

where

$$
\partial_\zeta v_1 = v_1\zeta\hat{\omega}^2 w^{-2}\left[\hat{\omega}\rho\left(\sigma - \tau\right) - 1\right], \quad \partial_\zeta v_2 = m\hat{\omega}^2(\zeta^2 + \varepsilon_{r,\mathrm{cl}})w^{-4},
\quad (5.27)
$$

with $\sigma = K_{|m|}''(w\rho)/K_{|m|}'(w\rho)$ and $\tau = K_{|m|}'(w\rho)/K_{|m|}(w\rho)$. Again, the primes denote derivatives with respect to the argument of the Bessel function. Now, we have determined all the ingredients to tackle Eq. (5.22). The alternative gradient computation has been used for the computation of $\delta\zeta$ as it is about five times more efficient.

Finally, we point out that for the weakly guiding case of Section 2.5, an equivalent derivation can be performed, although the sizes of the systems of differential equations are reduced by a factor of two.

5.2.3   Gradient computation of the fibre quantities

To determine the directional derivatives of the fibre quantities $\partial_{x_n} v_q$ that are required to compute the gradient of the cost function in Eq. (5.6), the propagation coefficient and

the refractive-index profile as well as their gradients prove essential. In the following, we address all the quantities of the single-mode fibre that have been introduced in Chapter 3 and give expressions of their first variations.

Dispersion

The dispersion is defined by Eq. (3.3). Upon employing the limiting process in Eq. (5.10) in combination with the expansion of Eq. (5.15), its first variation reads

$$\delta D = -\frac{\hat{\omega}^2}{2\pi a c_0}\left(2\frac{d\delta\zeta}{d\hat{\omega}} + \hat{\omega}\frac{d^2\delta\zeta}{d\hat{\omega}^2}\right).$$ (5.28)

The derivative of $\delta\zeta$ with respect to $\hat{\omega}$ is, with the aid of Eq. (3.4) and Eq. (3.7), determined from

$$\frac{d\ \delta\mathsf{C}(\zeta,\delta\zeta)}{d\hat{\omega}} \equiv 0 \quad \Rightarrow \quad \frac{d\delta\zeta}{d\hat{\omega}} = -\frac{\partial_{\hat{\omega}}\delta\mathsf{C}}{\partial_{\delta\zeta}\delta\mathsf{C}} - \frac{\partial_{\zeta}\delta\mathsf{C}}{\partial_{\delta\zeta}\delta\mathsf{C}}\left(\frac{d\zeta}{d\hat{\omega}}\right),$$ (5.29)

$$\begin{aligned}\frac{d^2\delta\zeta}{d\hat{\omega}^2} = &-(\partial_{\delta\zeta}\delta\mathsf{C})^{-1}\left\{\partial_{\hat{\omega}}^2\delta\mathsf{C} + \left(\frac{d\zeta}{d\hat{\omega}}\right)\left[\partial_{\zeta}^2\delta\mathsf{C}\left(\frac{d\zeta}{d\hat{\omega}}\right) + 2\partial_{\hat{\omega}\zeta}^2\delta\mathsf{C} + \partial_{\zeta\delta\zeta}^2\delta\mathsf{C}\left(\frac{d\delta\zeta}{d\hat{\omega}}\right)\right]\right.\\ &\left.+ \left(\frac{d^2\zeta}{d\hat{\omega}^2}\right)\partial_{\zeta}\delta\mathsf{C} + \left(\frac{d\delta\zeta}{d\hat{\omega}}\right)\left[\partial_{\delta\zeta}^2\delta\mathsf{C}\left(\frac{d\delta\zeta}{d\hat{\omega}}\right) + 2\partial_{\hat{\omega}\delta\zeta}^2\delta\mathsf{C} + \partial_{\zeta\delta\zeta}^2\delta\mathsf{C}\left(\frac{d\zeta}{d\hat{\omega}}\right)\right]\right\}.\end{aligned}$$ (5.30)

The derivation of the various first-order and second-order derivatives of $\delta\mathsf{C}$, which is given by Eq. (5.16), requires a considerable amount of bookkeeping, although it is quite straightforward. As an example, we give the first-order derivative for $\alpha \in \{\zeta, \delta\zeta, \hat{\omega}\}$

$$\begin{aligned}\partial_\alpha\delta\mathsf{C} =&|\partial_\alpha\delta\mathbf{f}_1\ \mathbf{f}_2\ \mathbf{f}_3\ \mathbf{f}_4| + |\partial_\alpha\mathbf{f}_1\ \delta\mathbf{f}_2\ \mathbf{f}_3\ \mathbf{f}_4| + |\partial_\alpha\mathbf{f}_1\ \mathbf{f}_2\ \delta\mathbf{f}_3\ \mathbf{f}_4| + |\partial_\alpha\mathbf{f}_1\ \mathbf{f}_2\ \mathbf{f}_3\ \delta\mathbf{f}_4|\\ &+|\delta\mathbf{f}_1\ \partial_\alpha\mathbf{f}_2\ \mathbf{f}_3\ \mathbf{f}_4| + |\mathbf{f}_1\ \partial_\alpha\delta\mathbf{f}_2\ \mathbf{f}_3\ \mathbf{f}_4| + |\mathbf{f}_1\ \partial_\alpha\mathbf{f}_2\ \delta\mathbf{f}_3\ \mathbf{f}_4| + |\mathbf{f}_1\ \partial_\alpha\mathbf{f}_2\ \mathbf{f}_3\ \delta\mathbf{f}_4|\\ &+|\delta\mathbf{f}_1\ \mathbf{f}_2\ \partial_\alpha\mathbf{f}_3\ \mathbf{f}_4| + |\mathbf{f}_1\ \delta\mathbf{f}_2\ \partial_\alpha\mathbf{f}_3\ \mathbf{f}_4| + |\mathbf{f}_1\ \mathbf{f}_2\ \partial_\alpha\delta\mathbf{f}_3\ \mathbf{f}_4| + |\mathbf{f}_1\ \mathbf{f}_2\ \partial_\alpha\mathbf{f}_3\ \delta\mathbf{f}_4|\\ &+|\delta\mathbf{f}_1\ \mathbf{f}_2\ \mathbf{f}_3\ \partial_\alpha\mathbf{f}_4| + |\mathbf{f}_1\ \delta\mathbf{f}_2\ \mathbf{f}_3\ \partial_\alpha\mathbf{f}_4| + |\mathbf{f}_1\ \mathbf{f}_2\ \delta\mathbf{f}_3\ \partial_\alpha\mathbf{f}_4| + |\mathbf{f}_1\ \mathbf{f}_2\ \mathbf{f}_3\ \partial_\alpha\delta\mathbf{f}_4|,\end{aligned}$$ (5.31)

where we have used the notation $\det(\mathsf{A}) = |\mathsf{A}|$ and have assumed that all determinants are evaluated at $\rho = 1$. In the core region, the pertaining field vectors are again obtained by expanding the system of differential equations in Eq. (5.17), i.e.

$$d_\rho\begin{pmatrix}\mathbf{f}\\\partial_\alpha\mathbf{f}\\\delta\mathbf{f}\\\partial_\alpha\delta\mathbf{f}\end{pmatrix} = \rho^{-1}\begin{pmatrix}\mathsf{A}(\rho) & 0 & 0 & 0\\\partial_\alpha\mathsf{A}(\rho) & \mathsf{A}(\rho) & 0 & 0\\\delta\mathsf{A}_1(\rho) & 0 & \mathsf{A}(\rho) & 0\\\partial_\alpha\delta\mathsf{A}_1(\rho) & \delta\mathsf{A}_1(\rho) & \partial_\alpha\mathsf{A}(\rho) & \mathsf{A}(\rho)\end{pmatrix}\begin{pmatrix}\mathbf{f}\\\partial_\alpha\mathbf{f}\\\delta\mathbf{f}\\\partial_\alpha\delta\mathbf{f}\end{pmatrix}.$$ (5.32)

For the cladding region, the derivatives of the field vectors and their first variations follow from Eq. (2.38) and Eq. (5.26), respectively. This provides us with all the components required to compute the first variation of the dispersion in Eq. (5.28).

Dispersion slope

The first variation of the dispersion slope is, with the aid of Eq. (3.11), obtained as

$$\delta S = \frac{\hat{\omega}^3}{(2\pi a)^2 c_0} \left(4 \frac{d\delta\zeta}{d\hat{\omega}} + 5\hat{\omega} \frac{d^2\delta\zeta}{d\hat{\omega}^2} + \hat{\omega}^2 \frac{d^3\delta\zeta}{d\hat{\omega}^3} \right), \tag{5.33}$$

where the first two derivatives on the right-hand side are given by Eqs. (5.29) and (5.30), respectively. The third-order derivative reads

$$
\begin{aligned}
\frac{d^3\delta\zeta}{d\hat{\omega}^3} = &- (\partial_{\delta\zeta}\delta\mathsf{C})^{-1} \left\{ \partial_{\hat{\omega}}^3 \delta\mathsf{C} + \partial_\zeta^3 \mathsf{C} \left(\frac{d\zeta}{d\hat{\omega}} \right)^3 + \partial_{\delta\zeta}^3 \mathsf{C} \left(\frac{d\delta\zeta}{d\hat{\omega}} \right)^3 + \partial_\zeta \mathsf{C} \left(\frac{d^3\zeta}{d\hat{\omega}^3} \right) \right. \\
&+ 3 \left(\frac{d\zeta}{d\hat{\omega}} \right) \left[\partial_{\hat{\omega}^2\zeta}^3 \delta\mathsf{C} + \partial_{\hat{\omega}\zeta^2}^3 \delta\mathsf{C} \left(\frac{d\zeta}{d\hat{\omega}} \right) + \partial_\zeta^2 \delta\mathsf{C} \left(\frac{d^2\zeta}{d\hat{\omega}^2} \right) \right. \\
&\left. + \partial_{\zeta^2\delta\zeta}^3 \mathsf{C} \left(\frac{d\zeta}{d\hat{\omega}} \right) \left(\frac{d\delta\zeta}{d\hat{\omega}} \right) + \partial_{\hat{\omega}\zeta\delta\zeta}^3 \mathsf{C} \left(\frac{d\delta\zeta}{d\hat{\omega}} \right) + \partial_{\zeta\delta\zeta}^2 \mathsf{C} \left(\frac{d^2\delta\zeta}{d\hat{\omega}^2} \right) \right] \\
&+ 3 \left(\frac{d\delta\zeta}{d\hat{\omega}} \right) \left[\partial_{\hat{\omega}^2\delta\zeta}^3 \delta\mathsf{C} + \partial_{\hat{\omega}\delta\zeta^2}^3 \delta\mathsf{C} \left(\frac{d\delta\zeta}{d\hat{\omega}} \right) + \partial_{\delta\zeta}^2 \delta\mathsf{C} \left(\frac{d^2\delta\zeta}{d\hat{\omega}^2} \right) \right. \\
&\left. + \partial_{\zeta\delta\zeta^2}^3 \mathsf{C} \left(\frac{d\zeta}{d\hat{\omega}} \right) \left(\frac{d\delta\zeta}{d\hat{\omega}} \right) + \partial_{\hat{\omega}\zeta\delta\zeta}^3 \mathsf{C} \left(\frac{d\zeta}{d\hat{\omega}} \right) + \partial_{\zeta\delta\zeta}^2 \mathsf{C} \left(\frac{d^2\zeta}{d\hat{\omega}^2} \right) \right] \\
&\left. + 3\partial_{\hat{\omega}\zeta}^2 \mathsf{C} \left(\frac{d^2\zeta}{d\hat{\omega}^2} \right) + 3\partial_{\hat{\omega}\delta\zeta}^2 \mathsf{C} \left(\frac{d^2\delta\zeta}{d\hat{\omega}^2} \right) \right\}.
\end{aligned}
\tag{5.34}
$$

Obviously, third-order derivatives of the fields vectors with their variations are needed. Hence, the by now familiar system of differential equations must be expanded such that it yields all desired field vectors in the core region. Also in the cladding region, the third-order derivatives of the field vectors must be derived. Although these derivations constitute a precise and time-consuming exercise, they are straightforward, while stating the resulting expressions would amount to a notable number of pages containing matrices and vectors. Therefore, we omit these expressions here.

Mode-field diameter and effective area

The main building block in the computation of the mode-field diameter and effective area is the complex Poynting vector defined in Eq. (3.14). Its first variation is given by

$$\delta S(\rho) = E_r \delta H_\psi^* + \delta E_r H_\psi^* - H_r^* \delta E_\psi - \delta H_r^* E_\psi. \tag{5.35}$$

The computation of the transverse field components has been discussed in Section 3.1.4. Once the proper variations of the modal amplitudes are obtained, the variations of the transverse field components follow via the scaling of Eq. (2.28) and the variations in the

core and cladding field vectors in Eqs. (5.17) and (5.21), respectively. The variation in the radial components follows from Eq. (2.39)

$$
\begin{aligned}
\delta E_r &= (\hat{\omega}\varepsilon_r)^{-1} Z_0 \left[\rho^{-1} m \left(\delta H_z - H_z \delta\varepsilon_r \varepsilon_r^{-1} \right) + \hat{\omega} \left(\delta\zeta H_\psi - \zeta\delta H_\psi - \zeta H_\psi \delta\varepsilon_r\varepsilon_r^{-1} \right) \right], \\
\delta H_r &= -(\hat{\omega}Z_0)^{-1} \left[\rho^{-1} m \delta E_z + \hat{\omega} \left(\delta\zeta E_\psi + \zeta\delta E_\psi \right) \right].
\end{aligned}
\tag{5.36}
$$

To determine the variations of the modal amplitudes, we recall the matrix-vector product of Eq. (2.41) and write it in a generic way,

$$
\mathsf{F}\mathbf{a}\big|_{\rho=1} = \mathbf{0},
\tag{5.37}
$$

where $\mathsf{F} = [\mathbf{f}_1(\rho)\ \mathbf{f}_2(\rho)\ \mathbf{f}_3(\rho)\ \mathbf{f}_4(\rho)]$ and where the vector $\mathbf{a}$ contains the modal amplitudes of the field vectors for the pertaining propagation coefficient ζ. The first variation at $\rho = 1$ follows from

$$
\mathsf{F}\delta\mathbf{a} = -\delta\mathsf{F}\mathbf{a},
\tag{5.38}
$$

where $\delta\mathsf{F} = [\delta\mathbf{f}_1(\rho)\ \delta\mathbf{f}_2(\rho)\ \delta\mathbf{f}_3(\rho)\ \delta\mathbf{f}_4(\rho)]$, with vectors given by Eqs. (5.17) and (5.21), and where $\delta\mathbf{a}$ is the desired variation vector of the modal amplitudes. The evaluation of $\delta\mathbf{a}$ is complicated by the fact that the matrix F is singular through Eq. (5.37). In [78], a solution procedure is described, based on the singular-value decomposition of the matrix $\mathsf{F} = \mathsf{U}\left[\mathrm{diag}(\sigma_j)\right]\mathsf{V}$, which circumvents this problem. This is achieved by replacing the inverse of the singular value σ_j that is (nearly) zero by zero itself. In other words, the vector $\delta\mathbf{a}$ is given by

$$
\delta\mathbf{a} = \mathsf{V}\left[\mathrm{diag}(1/\sigma_j)\right]\mathsf{U}^T\delta\mathsf{F}\mathbf{a},
\tag{5.39}
$$

where $(1/\sigma_j) = 0$ if σ_j becomes too small. The apparent ambiguity with the null-space of F is due to the fact that the modulus of the vector of modal amplitudes is arbitrary (cf. Eq. (5.37)).

Once $\delta S(\rho)$ has been computed, the first variation of the Petermann-1 (d_I) and the Petermann-2 (d_{II}) definitions of the mode-field diameter follow from

$$
\delta d_I = \frac{4a^2}{d_I} \frac{\displaystyle\int_{\rho=0}^{\infty} \delta S \rho^3 d\rho \int_{\rho=0}^{\infty} S\rho d\rho - \int_{\rho=0}^{\infty} S\rho^3 d\rho \int_{\rho=0}^{\infty} \delta S \rho d\rho}{\left(\displaystyle\int_{\rho=0}^{\infty} S\rho d\rho\right)^2},
$$

$$
\delta d_{II} = \frac{16a^2}{d_{II}} \frac{\displaystyle\int_{\rho=0}^{\infty} \delta S\rho d\rho \int_{\rho=0}^{\infty} \frac{(d_\rho S)^2}{S}\rho d\rho - \int_{\rho=0}^{\infty} S\rho d\rho \int_{\rho=0}^{\infty} \frac{d_\rho S}{S^2}\left(2S d_\rho \delta S - \delta S d_\rho S\right)\rho d\rho}{\left(\displaystyle\int_{\rho=0}^{\infty} \frac{(d_\rho S)^2}{S}\rho d\rho\right)^2},
$$

$$
\tag{5.40}
$$

where we already have performed the integration over ψ and have omitted the ρ-dependence of the complex Poynting vector. For the effective area, we obtain the following expression

$$\delta\mathrm{A}_{\mathrm{eff}} = 4\pi a^2 \frac{\int_{\rho=0}^{\infty} S\rho d\rho \left(\int_{\rho=0}^{\infty} \delta S\rho d\rho \int_{\rho=0}^{\infty} S^2 \rho d\rho - \int_{\rho=0}^{\infty} S\rho d\rho \int_{\rho=0}^{\infty} S\delta S\rho d\rho \right)}{\left(\int_{\rho=0}^{\infty} S^2 \rho d\rho \right)^2}. \qquad (5.41)$$

The integration over the core and cladding regions is performed with fixed quadrature rules or, where possible, analytically (see Appendix F.3). The delta functions that occur in δd_{II}, and originate from possible refractive-index profile jumps and jumps due to vertical variations (see Figure 5.11), are neglected.

Macrobending loss

In Chapter 4, we have shown that Faustini's approximation [22] is most suitable to compute the bending losses in an optical fibre with a step-index and parabolic-index profile for radii of curvature $R > 8\,\mathrm{mm}$. That is, if one does not wish to resort to a vectorial full-wave approach. Since a fast computation of an optimised profile is essential, and the fibre specifications given by manufacturers are defined for $R \geq 10\,\mathrm{mm}$, we will use this approximation, which is given by Eq. (4.21), to compute the bending losses. For the fundamental LP_{01}-mode ($\ell = 0$), the first variation reads

$$\begin{aligned}\delta\alpha = {}& 2\left(P_0\zeta_{str}\right)^{-1} \int_{\xi=0}^{\infty} \left(\delta S_0 \mathrm{AiBi}^{-1} + S_0\mathrm{Bi}^{-2}\left[\mathrm{Ai}'\mathrm{Bi}\delta\chi_a - \mathrm{AiBi}'\delta\chi_b\right]\right) d\xi \\ & - 2\left(\delta P_0 \zeta_{str} + P_0\delta\zeta_{str}\right)\left(P_0\zeta_{str}\right)^{-2}\int_{\xi=0}^{\infty} S_0\mathrm{AiBi}^{-1}d\xi,\end{aligned} \qquad (5.42)$$

where the prime indicates a derivative of the Airy function with respect to the whole argument, $S_0 = S_0(\xi)$, $\mathrm{Ai} = \mathrm{Ai}\left(\chi_a\right)$, $\mathrm{Bi} = \mathrm{Bi}\left(\chi_b\right)$, with $\chi_a = \chi\left(0,\xi\right)$ and $\chi_b = \chi\left(1,\xi\right)$, and

$$\begin{aligned}\delta P_0 = {}& 4a^2\pi \Bigg\{ K_0^2(w)\int_{\rho=0}^{1}\left[\frac{\psi(\rho)\delta\psi(\rho)\psi(1) - \delta\psi(1)\psi^2(\rho)}{\psi^3(1)}\right]\rho d\rho \\ & - \frac{\zeta\delta\zeta}{2\gamma^2}K_1^2(w) - K_0(w)K_1(w)\hat{\omega}\zeta\delta\zeta\gamma^{-1}\int_{\rho=0}^{1}\left[\frac{\psi(\rho)}{\psi(1)}\right]^2\rho d\rho\Bigg\},\end{aligned} \qquad (5.43)$$

$$\delta S_0 = -a\pi\delta\gamma\left(1 + \hat{\omega}\gamma\right)\left(\hat{\omega}\gamma^2\right)^{-1}\exp\left(-\hat{\omega}\gamma\right),$$

$$\delta\chi(X,\xi) = \left(4\hat{\omega}\zeta\rho_c\right)^{2/3}\frac{\delta\zeta}{\zeta}\left[\frac{1}{2} - \frac{1}{3}\left(\frac{\gamma^2}{\zeta^2} + \frac{X}{\rho_c}\right)\right].$$

The variation $\delta\psi$ is the weak-guidance equivalent of the variation in the field vectors $\delta\mathbf{f}$.

Profile optimisation for the MAC-value has not been implemented in the optimisation process, as it takes about ten seconds to perform the search for the effective cut-off

wavelength (see Section 3.1.6). This would lead to a considerable increase of the overall optimisation time. Moreover, a proper choice for the bending loss and the mode-field diameter usually implicitly results in an acceptable MAC-value.

5.2.4 Gradient approximation by finite differences

To check the accuracy (and correctness) of the computed gradients, we have performed a comparison with the finite-difference approximation. In addition, this comparison provides us with an optimal value for the step size h. The finite-difference approximation is performed with the central finite-difference scheme, which is given by Eq. (5.8). For horizontal profile variations, we recall from Eq. (5.2) that the difference between two subsequent ρ_n points is at least ϵ. This imposes an upper limit on the step size, viz. $h \leq \epsilon$. Experimentally, we have obtained a relative value of $\epsilon = 0.004$ with respect to the normalised unit core radius.

In case of a vertical profile variation, the Germanium concentration X^{Ge} may not become negative if we add a variation to the profile. If this is about to happen, we employ a forward finite-difference scheme, i.e.

$$\partial_{x_n} F(X^{\mathrm{Ge}}, \delta X^{\mathrm{Ge}}) \approx \frac{1}{h} \left[F\left(X^{\mathrm{Ge}} + h\delta X^{\mathrm{Ge}}\right) - F\left(X^{\mathrm{Ge}}\right) \right] = \Delta F_{n,\mathrm{forward}}. \qquad (5.44)$$

For evaluation purposes, we have constructed a Germanium concentration profile, with a core radius $a = 5\,\mu\mathrm{m}$, which is shown in Figure 5.4. The solid dots indicate the optimisa-
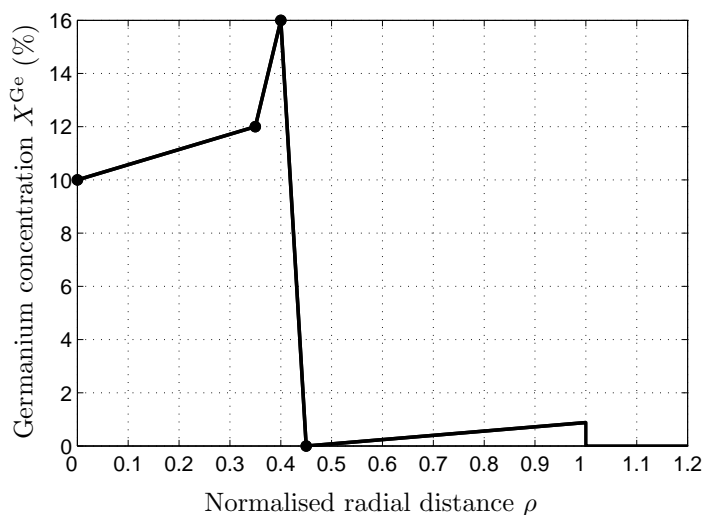

Figure 5.4: *Germanium concentration profile with $X_{co}^F = 0.27\,\%$ and $X_{cl}^F = 0$.*

tion points, which correspond to "three" horizontal and "four" vertical parameters. The

horizontal step size h is clearly limited near $\rho = 0.425$, whereas the vertical one is unidirectional at $\rho = 0.45$, and hence Eq. (5.44) is used. Further, we have assumed a background concentration of Fluor, $X_{\mathrm{co}}^{\mathrm{F}} = 0.27\,\%$, in the core region. The jump in the Germanium concentration profile at $\rho = 1$ is such that the permittivity profile is continuous throughout at $\lambda = 632.8\,\mathrm{nm}$.

First of all, we validate our gradients $\partial_{x_n}\zeta$ by comparing the Fréchet derivatives δF_n in Eq. (5.10) with the finite-difference approximations ΔF_n given by the Eqs. (5.8) and (5.44) for a central and a forward difference scheme, respectively. The relative error between both results, which we define as

$$\text{Rel. error} = \left| 1 - \frac{\Delta F_{n,\text{central or forward}}}{\delta F_n} \right|, \tag{5.45}$$

is shown as a function of the step size h in Figure 5.5. The step size h is taken as an unscaled quantity. In particular, it is the variation of the radial coordinate r in micrometres and of the Germanium concentration X^{Ge} in mole fractions. The results for horizontal profile variations are plotted in Figure 5.5(a), whereas the vertical ones are shown in (b).
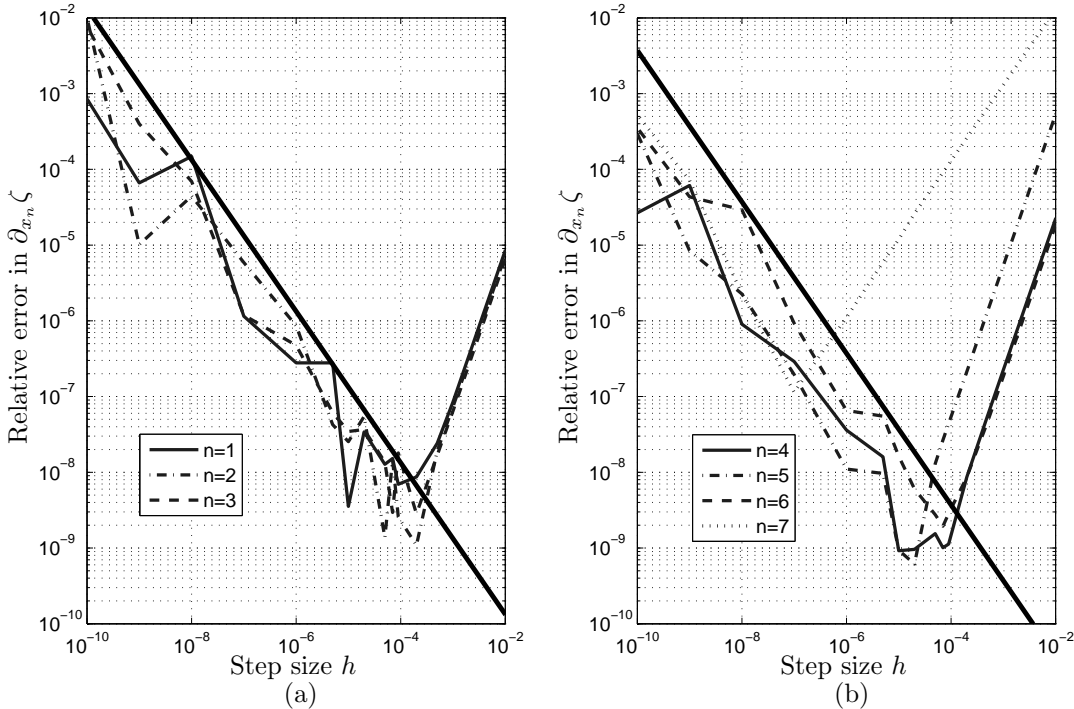
Figure 5.5: *The relative error in $\partial_{x_n}\zeta$, $n = 1, ..., 7$, obtained by Eq. (5.45) as a function of the absolute step size h. Horizontal profile variations in (a) and vertical ones in (b). The straight line corresponds to the estimated error after applying the finite-difference subtraction. For $n = 7$, a forward finite-difference scheme has been used.*

In the core region, the field vectors and their first variation are computed up to a relative accuracy of 10^{-12}. In the cladding region, solutions are available up to machine
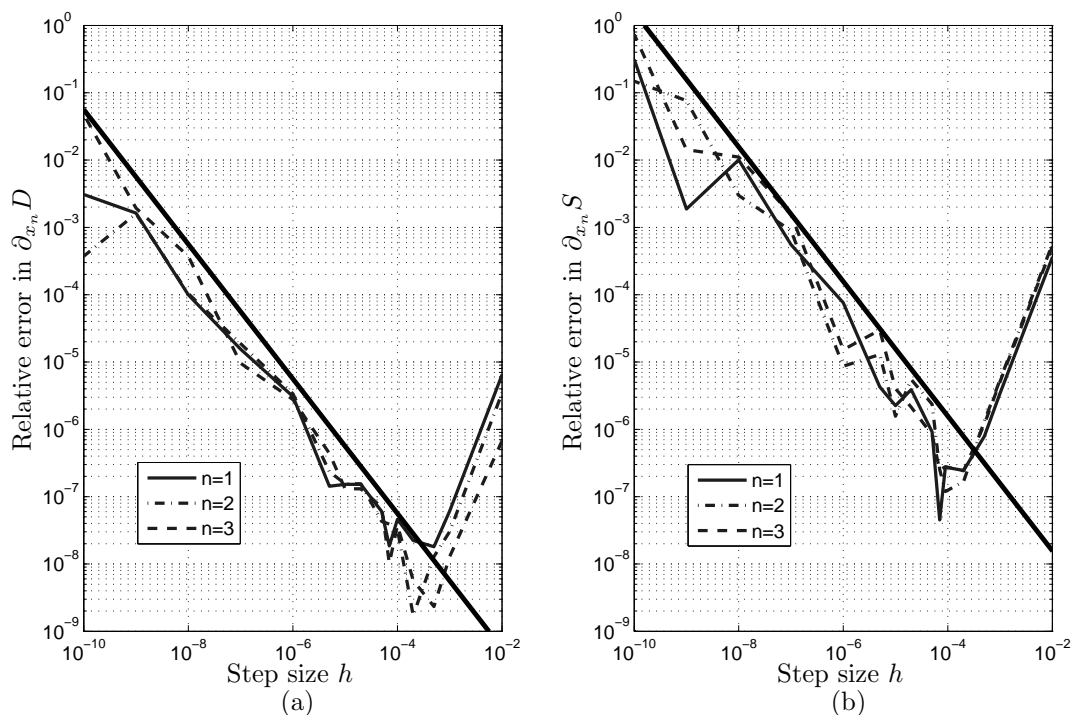
Figure 5.6: *The relative error in $\partial_{x_n} D$ (a) and $\partial_{x_n} S$ (b) obtained by Eq. (5.45) as a function of the absolute step size h for horizontal variations. The straight line corresponds to the estimated error after applying the finite-difference subtraction.*

precision. The variation $\delta\zeta$ is computed to the same order of precision. However, when we compute the gradient with the finite-difference approximation, we lose significant digits due to the subtraction in the numerator. The upper limit of "trusted" digits is denoted by the straight lines in Figure 5.5. Below this line we find ourselves in the noise regime.

For $n = 7$ we had to employ the forward-difference scheme of Eq. (5.44). As a consequence, the relative error is several orders of magnitude higher and a step size of about $h = 6 \cdot 10^{-7}$ seems best to guarantee 6 correct digits. For $n \in \{1, 2, 3\}$ and $n \in \{4, 5, 6\}$, we have chosen absolute step sizes of $h = 5 \cdot 10^{-4}$ and $h = 5 \cdot 10^{-5}$, which will leave about 8 correct digits for $\partial_{x_n} \zeta$.

The dispersion and dispersion slope, respectively given by Eq. (3.3) and Eq. (3.12), constitute the most tedious computations, due to the presence of several partial derivatives with respect to ζ, which introduce cancellations in the final assembly of the expressions. Therefore, we have computed the relative error between the finite-difference method and the gradient method for both $\partial_{x_n} D$ and $\partial_{x_n} S$. For convenience, we have only plotted the elements $n \in \{1, 2, 3\}$ in Figure 5.6. In comparison to the propagation coefficient in Figure 5.5(a), we lose little accuracy in the computation of the dispersion. For the dispersion slope, on the other hand, we lose two digits. The previously chosen finite-difference step size of $h = 5 \cdot 10^{-4}$ remains about the optimal one. Also for the vertical

variations, we have obtained the same best absolute step size of about $h = 5 \cdot 10^{-5}$. For the mode-field diameter, the effective area, and the bending loss similar comparisons have been performed with comparable results.

From this comparison, we infer that the exact gradient computation works fine. Moreover, as we will discuss in Section 5.3.2, computation times favour the pertaining method considerably. Conversely, the effort of deriving the gradients by hand is a time-consuming and tedious job.

5.3 Increasing the optimisation efficiency of the deterministic gradient-based schemes

To make the profile optimisation with the gradient-based algorithms as efficient as possible, we first determine whether the Germanium concentration or the permittivity is the better vertical optimisation parameter. In Section 5.1, we have already elaborated on the advantages and disadvantages of each vertical optimisation parameter. Subsequently, we use the thus acquired vertical parameter to compare a profile optimisation using the finite-difference approximation with a profile optimisation using Fréchet derivatives.

Practical values for the fibre quantities v_q depend on the utilisation of the optical fibre. For the purpose of illustration, we have chosen all weighting coefficients w_q in the cost function (CF) of Eq. (5.5) to be equal to one. Further, we have added a test in the optimisation loop, which checks whether the fibre is still in its single-mode regime. Although the effective cut-off wavelength would be the appropriate quantity for this check, it is too time consuming inside the optimisation loop (see Section 3.1.6). Therefore, we have employed a mode-counting scheme that is based on the theoretical cut-off wavelength [17, 18] which is much faster, and safely, overestimates the cut-off wavelengths of the higher-order modes. If there exists more than one mode, a penalty is added to the CF. Finally, we note that all computations have been performed on a Pentium IV, 2.6 GHz computer.

5.3.1   The best vertical optimisation parameter

To determine whether the Germanium concentration or the permittivity is the better vertical optimisation parameter, we have used the modified-Newton algorithm to perform profile optimisations for both profiles. The relation between the Germanium concentration and the permittivity, given by the Sellmeier equation in Eq. (3.8), is in practice almost but not completely linear. Moreover, the Germanium concentration does not depend on the wavelength, whereas the permittivity does.

We start the permittivity profile optimisation with a simple arbitrarily chosen initial permittivity profile, which consists of linear segments at a wavelength of 632.8 nm and is continuous as a function of radius. The corresponding Germanium concentration profile, with mildly non-linear segments, and the piecewise constant Fluor concentration profile are shown in Figure 5.7. The core radius is assumed to be $a = 5\,\mu m$. The
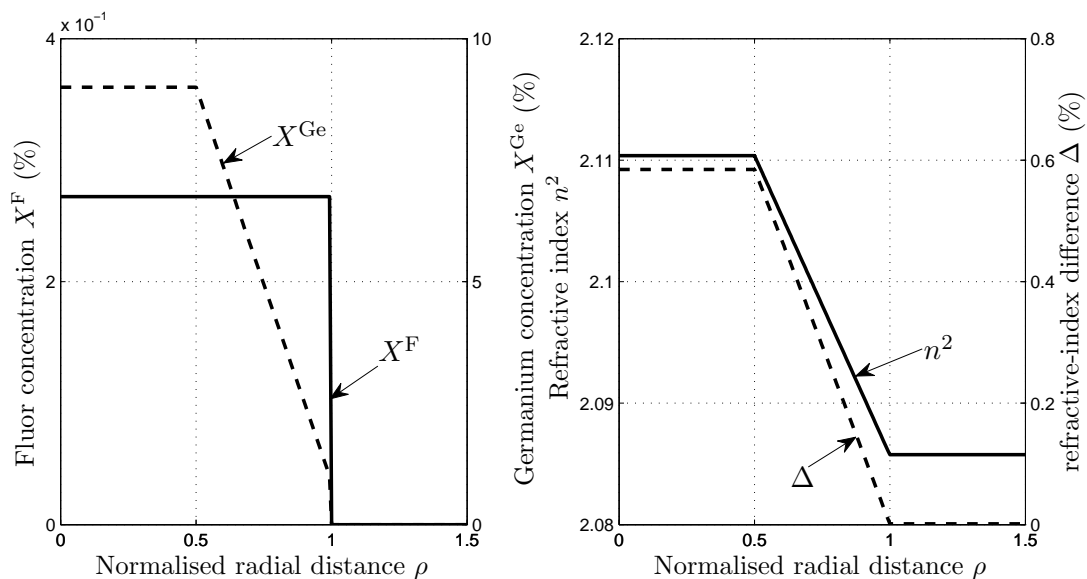

Figure 5.7: *Doping concentrations (X^F, X^{Ge}) with the corresponding mildly non-linear refractive-index profile $n^2(\rho)$ at 1550 nm and the refractive-index difference Δ given at the wavelength of 632.8 nm. The radius of the fibre is $a = 5\,\mu m$.*

refractive-index difference at $\lambda = 632.8$ nm is plotted as well. Since the permittivity profile is plotted at $\lambda = 1550$ nm, it is slightly non-linear, although this is hardly visible. Due to the presence of Fluor in the core region, the Germanium concentration is discontinuous at the core/cladding transition at $\rho = 1$ to achieve a continuous permittivity profile at $\lambda = 632.8$ nm.

For the optimisation of the Germanium concentration profile, we employ linear segments as well. Also here we consider a continuous profile as a function of radius. Consequently, the permittivity profile is now mildly non-linear and is discontinuous at the core/cladding interface.

We point out that the initial profile differs for both profile optimisation runs, i.e. there is a discontinuity at $\rho = 1$ in either the Germanium concentration or the permittivity. Consequently, the resulting optimised profiles may differ somewhat as well as the value of the end value of the cost function (CF_e). Therefore, we choose the computation time per iteration as the primary selection criterium for the best vertical and not the CF_e.

We have performed two profile optimisation runs, at the typical wavelength of 1550 nm,

for various weighting coefficients w_q in the CF. The results are summarised in Table 5.1,

Table 5.1: *Results for the optimisation of a permittivity (Perm) and Germanium (Germ) profile with various weighting coefficients w_q at $\lambda = 1550\,nm$.*

	v_q^{ref}	w_q	v_q^{Germ}	v_q^{Perm}	w_q	v_q^{Germ}	v_q^{Perm}
D (ps/km/nm)	13	1	13.97	13.88	1	13.00	13.00
S (ps/km/nm^2)	0	1	5.86E-2	6.03E-2	0	5.97E-2	6.12E-2
MFD d_{II} (µm)	10	1	10.30	10.40	1	10.00	10.00
Bend. loss (dB/turn)	0	1	0.92	0.98	0	0.49	0.34
Eff. Area (µm^2)	80	1	79.77	79.73	0	73.52	73.37
Comp. time per iter. (s)	-	-	0.58	0.89	-	0.54	0.82
Number of iter.	-	-	26	28	-	16	16
CF$_{\text{e}}$	-	-	1.94	1.98	-	$<$ 1E-6	$<$ 1E-6

where the superscripts "Germ" and "Perm" denote optimisation with respect to the Germanium concentration profile and the permittivity profile, respectively. The desired values of the fibre quantities are given by v_q^{ref}. The bending loss is computed by Eq. (4.21). In accordance with typical optical specifications, we have chosen a mandrel diameter of $32\,\text{mm}$ and a single wind of the optical fibre. Further, we have applied the stress-induced correction factor of $R_{\text{eff}} = 1.3R = 20.8\,\text{mm}$, as discussed in Section 3.1.6.

Note that the number of iterations as well as the value of CF$_{\text{e}}$ between both vertical optimisation parameters are about the same. However, since the Germanium concentration is wavelength-independent, the profile optimisation is about a factor of 1.5 faster. Moreover, from a manufacturing point of view, information of the dopant concentration as a function of the radial coordinate is more convenient. Therefore, we will regard the Germanium concentration as the vertical optimisation parameter of choice.

5.3.2   Finite-difference versus exact-gradient computation

The computation of the gradient by a finite-difference scheme has been discussed extensively in Section 5.2.4. There, it was shown that, with a proper choice for the step-size h, a fair estimate of the gradient can be obtained. Now, how does this finite-difference approximation affect the optimisation process in comparison to its exact counterpart? To answer this question, we start a profile optimisation from the Germanium concentration profile as given in Figure 5.7, consisting of linear segments and being continuous as a function of radius. For simplicity, we optimise three fibre quantities, i.e. the dispersion

(D), the dispersion slope (S) and the mode-field diameter (MFD) d_{II}, at a wavelength of $\lambda = 1550\,\text{nm}$.

We have performed three optimisation runs with the modified-Newton (MN) algorithm optimising to a single fibre quantity at a time. The set reference values of these quantities with their pertaining weighting coefficients are given in Table 5.2. If the reference value cannot be reached, the run is terminated as soon as the relative difference between the exact (ex) and finite-difference (fd) value for that quantity is smaller than 10^{-6}. Otherwise, the relative difference between the reference value and the computed ex-value or fd-value should be smaller than 10^{-6} to stop the optimisation run. Further, we have added the number of iterations and the used computation time.

Table 5.2: *Results for the MN optimisation scheme of a Germanium concentration profile with the finite-difference (fd) approximation or by the exact (ex) gradient for various weighting coefficients w_q at $\lambda = 1550\,nm$.*

	v_q^{ref}	w_q	v_q^{ex}	v_q^{fd}	w_q	v_q^{ex}	v_q^{fd}	w_q	v_q^{ex}	v_q^{fd}
D	13	1	13.00	13.00	0	15.56	15.56	0	15.66	15.64
S ($\times$1E-2)	0	0	5.87	5.87	1	5.69	5.69	0	5.77	5.77
MFD d_{II}	10	0	8.83	8.83	0	8.50	8.50	1	10.00	10.00
Comp. time (s)	-	-	9	20	-	13	48	-	11	24
No. of iter.	-	-	16	20	-	22	48	-	19	24

The profile optimisation with respect to the dispersion slope, employing the finite-difference scheme, proves to be the most strenuous one. From the discussion in Section 5.2.4, this was to be expected as several digits are lost during the computation of this quantity, due to cancellation. For the dispersion and mode-field diameter, the differences in the number of iterations are marginal.

The latter observation is important if we recall that in the first variation of the MFD d_{II} delta functions occur through Eq. (5.13) for piecewise-linear continuous profiles, which we have neglected in the exact-gradient computations. In the finite-difference scheme, these delta functions are absent and therefore the profile optimisation might yield better results in a shorter period of time. However, this does not follow from the optimisation results in Table 5.2, and hence, it seems fair to employ the exact-gradient computations also for the MFD d_{II} while neglecting the presence of any delta functions.

The difference in computation time between the finite-difference approximation and the exact-gradient computation is nearly a factor of two, and, hence, the analytic derivation of all gradients seems worthwhile. Moreover, if we increase the number of optimisation parameters, the difference in computation time becomes even more pronounced. This is

shown in Figure 5.8, where we have plotted the computation time of a single CF evaluation versus the number of optimisation parameters for both schemes.
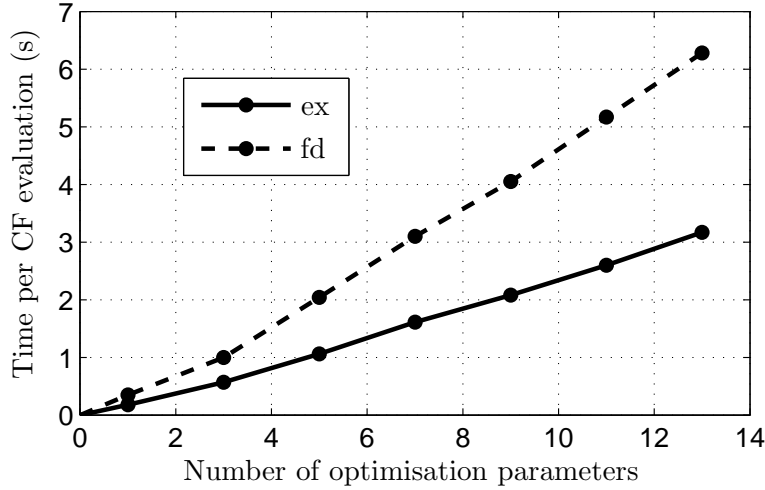

Figure 5.8: *Computation time per CF evaluation set against the number of optimisation parameters with the exact (ex) and finite-difference (fd) gradient computations.*

5.4   Initialisation of the profile optimisation

As the input control parameters of the optimisation algorithms severely influence the outcome of the optimised profile, they have to be chosen carefully. Especially, for the stochastic optimisation schemes, this initialisation is of importance. For the deterministic gradient-based schemes, the error in the Karush-Kuhn-Tucker conditions, which we will discuss in Section 5.5.4, and the relative step size towards the minimum, serve as the only controllable parameters that can be set to achieve somewhat lower end values of the cost function (CF$_e$). We have set both parameters to a tolerance of 10^{-6}. In addition, the Quasi-Newton algorithm also terminates when the trust-region radius gets smaller than the set tolerance [25]. Therefore, we solely touch upon the initialisation of the stochastic optimisation schemes. Further, the choice of the initial Germanium concentration profile is essential, as the minima found with the gradient-based schemes strongly depend on this choice. We introduce a selection of various Germanium concentration profiles to initiate the profile optimisation with.

5.4.1   Initialisation of the stochastic optimisation schemes

Although the global search algorithms lay claims to finding the global minimum, independent of the initial profile choice, the fine-tuning of the control parameters in the algorithms proves to be rather delicate.

For the simulated annealing (SA) scheme, the choice of the initial temperature T_0 should be such that the entire parameter space is searched. The reduction coefficient r_T, the factor by which the temperature decreases, and the number of function evaluations N_T after which this reduction takes place, determine the overall computation time. We have followed the recommendations given in [14] to initialise the SA minimisation, and started the profile optimisation with $T_0 = 10^{13}$, $r_T = 0.85$, and $N_T = 100$. Obviously, these values may be modified to decrease the computation time, and the employed bounds on the optimisation parameters may be adapted on the basis of the obtained local minima to reduce the parameter space [34]. However, although smaller values for N_T and r_T decrease the computation time considerably, the found minimum is not guaranteed to be the global one, and several additional runs are required to verify this. Moreover, this tailoring process of the SA algorithm strongly depends on the employed cost function. Since our cost function may differ, e.g. with the inclusion of more optimisation parameters, different weighting coefficients, or different reference values for the fibre quantities, this process has to be repeated each time a new cost function is used. In our opinion, the effort of finding the optimum values for each individual case is too time-consuming. Therefore, we have chosen the initial control parameters such that the whole parameter space is searched for and sufficient function evaluations are performed before a reduction step is taken. Adaptive simulated annealing [41] has been developed to perform the r_T reduction process adaptively, reducing the number of function evaluations.

For the differential evolution (DE) scheme, the main control parameters are the population size NP, the amplification factor F, and the crossover constant CR. Although intervals for these parameters are clearly defined, their optimum values depend on the cost function and the number of optimisation parameters N. Experimentally, and with reference to [92], we have chosen $NP = 8N$, $F = 0.6$, and $CR = 0.9$.

5.4.2 The initial Germanium concentration profile

Before we start the profile optimisation, the initial profile needs to be chosen. Especially for the deterministic gradient-based schemes, this choice is critical, as we may end up in a local minimum instead of the desired global one. We introduce a selection of various Germanium concentration profiles to initiate the profile optimisation. For an optimisation with five optimisation parameters, we distinguish between seven different initial profiles that are shown in Figure 5.9. At each equally spaced radial point $\rho = \{0, \frac{1}{3}, \frac{2}{3}\}$ we can choose between two Germanium concentration values, namely $X^{\text{Ge}} = 0\,\%$ or $X^{\text{Ge}} = 7\,\%$. Hence, each profile consists of three successive solid dots, which indicate the values of the optimisation variables. For simplicity, we introduce a binary notation where 0 corresponds to $X^{\text{Ge}} = 0\,\%$ and 1 to $X^{\text{Ge}} = 7\,\%$. The maximum value of $X^{\text{Ge}} = 7\,\%$ is the highest integer
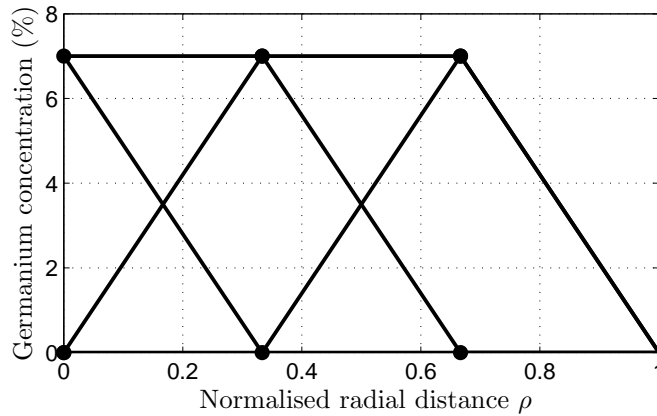
Figure 5.9: *Seven possible initial X^{Ge} profiles with $X^F = 0.27\%$. The dots denote the optimisation parameters in the X^{Ge} profile. The radius of the fibre is $a = 5\,\mu m$.*

value for which the fibre with profile $(1,1,1)$ is still in its (theoretical) single-mode regime. This implies that for an increasing number of optimisation parameters the maximum value of X^{Ge} decreases and approaches that of a step-index fibre (assuming that X^F is constant throughout the core region).

As discussed in Section 5.3.1, we consider the Germanium concentration to be continuous as a function of radius. Consequently, the permittivity profile has a discontinuous core/cladding transition.

Now that we have initialised the employed optimisation algorithms and have introduced a procedure to select initial profiles, it is time to perform the actual refractive-index profile optimisation.

5.5   Optimised profile results

We distinguish between profile optimisation using variations in both horizontal and vertical directions at each solid dot, except for the on-axis one where only a vertical variation is allowed, and profile optimisation with variations in the vertical direction only. Obviously, the latter search has less freedom, although it turns out that it is much less sensitive to the initial profile than the Newton algorithms. The choice of the initial profile and its influence on the number of iterations and the overall computation time are shown for both the stochastic optimisation schemes and the deterministic gradient-based schemes. Further, we have performed a sensitivity analysis on the resulting optimised refractive-index profiles to provide the manufacturer with information on how accurate the profile has to be made.

5.5.1 Profile variations in both horizontal and vertical directions

First, we consider profile variations in both horizontal and vertical directions at each point, with the exception of the fibre axis where only a variation in the vertical direction is allowed. We start with optimisation runs consisting of five optimisation parameters. Next, profile optimisations with seven optimisation parameters will be performed. Finally, we will give a brief overview of the end values of the cost function for profiles with nine, eleven, thirteen and fifteen optimisation parameters.

Five optimisation parameters

We have performed optimisation runs at $\lambda = 1550$ nm with the simulated annealing (SA) and differential evolution (DE) schemes and with both Newton algorithms, viz. the modified-Newton (MN) algorithm and quasi-Newton (QN) algorithm. We have restricted ourselves to five optimisation parameters. The initial profiles are chosen as discussed in Section 5.4.2. The same weighting coefficients w_q and reference values of the fibre quantities v_q^{ref} have been used as the ones in Table 5.1. For simplicity, we have not optimised the profile with respect to the effective area. The start (CF_{s}) and end values (CF_{e}) of the CF for the profiles under consideration are shown in Table 5.3. The lowest value for CF_{e} obtained by each optimisation algorithm is highlighted by a bold typeface. The computation time and the number of iterations are specified as well. Here, we distinguish between the computation of the CF only (F) and of the CF and its gradient (F&G). For profile (1,0,0)

Table 5.3: *Start values (CF_s) and end values (CF_e) of the CF for various initial profiles, containing five optimisation parameters, optimised with the MN, QN, SA and DE algorithms, or combinations of them. The computation time and the number of iterations of the CF (F) and the CF with its gradient (F&G) for the best profile are shown as well.*

Profile	CF_{s}	$\text{CF}_{\text{e}}^{\text{MN}}$	$\text{CF}_{\text{e}}^{\text{QN}}$	$\text{CF}_{\text{e}}^{\text{MN}\to\text{QN}}$	$\text{CF}_{\text{e}}^{\text{SA}}$	$\text{CF}_{\text{e}}^{\text{DE}}$
(1,1,1)	23.6	5.44E-3	**5.49E-3**	5.40E-3	**5.09E-3**	**5.09E-3**
(1,1,0)	426	**5.39E-3**	5.54E-3	**5.39E-3**	5.09E-3	5.09E-3
(1,0,1)	211	9.12E-2	1.11E+1	3.21E-2	5.09E-3	5.09E-3
(1,0,0)	-	-	-	-	5.09E-3	5.09E-3
(0,1,1)	23.9	9.89E-2	5.10E-2	9.89E-1	5.09E-3	5.09E-3
(0,1,0)	3.1E4	9.83E-2	4.98E-2	9.88E-2	5.09E-3	5.09E-3
(0,0,1)	2.2E3	9.42E-2	4.35	9.42E-2	5.09E-3	5.09E-3
F/F&G		0/329	403/210	50/24	2640000/0	660000/0
Comp. time		5.8 min.	5.3 min.	37 sec.	7.0 days	42.2 hrs.

no guided mode was found, which implies that the fundamental mode extends far into the cladding, and that optimisation becomes problematic at best. Likewise, the fundamental mode would cease to exist altogether for profile (0,0,0).

We observe that all schemes find values for CF_e that are substantially lower than their starting values CF_s. Further, we note that the stochastic optimisation methods outperform the gradient-based ones when it comes down to the lowest value of CF_e. Moreover, they are independent of the initial-profile choice. The SA technique attains the same global minimum as the DE scheme although at the expense of about four times as many function evaluations.

Neither of the Newton algorithms converge to the global minimum. However, they arrive at local minima that are about 6 % to 8 % higher than the global one. An additional optimisation with QN after the MN optimisation does not yield substantially lower values of the CF, and is therefore no longer considered. For the SA and DE schemes, there is no improvement upon making an additional QN run, and hence the resulting minima in this parameter space are proper ones. A sensitivity analysis in Section 5.5.4 confirms this. The overall computation times are definitely in favour of the gradient-based routines. The QN algorithm is a little bit faster than the MN scheme, although the latter algorithm reaches, in general, somewhat lower minima.

For the best values of CF_e, obtained by each optimisation algorithm, the fibre quantities v_q and their set reference values v_q^{ref} are given in Table 5.4. Owing to the choice of

Table 5.4: *Values of the fibre quantities v_q with the pertaining weighting coefficients w_q at $\lambda = 1550\,nm$ for which the profile, with five optimisation parameters, has been optimised.*

	v_q^{ref}	w_q	v_q^{MN}	v_q^{QN}	v_q^{SA}	v_q^{DE}
D (ps/km/nm)	13	1	13.00	13.00	13.00	13.00
S (ps/km/nm²)	0	1	7.20E-2	7.27E-2	7.01E-2	7.01E-2
MFD d_{II} (µm)	10	1	10.00	10.00	10.00	10.00
Bend. loss (dB/turn)	0	1	1.43E-2	1.41E-2	1.35E-2	1.34E-2

the weighting coefficients w_q, it is not surprising that the values for the dispersion D and mode-field diameter d_{II}, which are about three orders of magnitude larger than the dispersion slope S and the bending loss, correspond to the desired values. The subsequent "competition" between the dispersion slope and the bending loss determines the final minimum. One may adapt the weighting coefficients to reduce the importance of D and MFD d_{II} such that their end values are within a tolerable region about the desired value, and may arrive at somewhat lower values for the slope and bending loss. Obviously, this requires a fine tuning of the weighting coefficients, a process for which the Newton

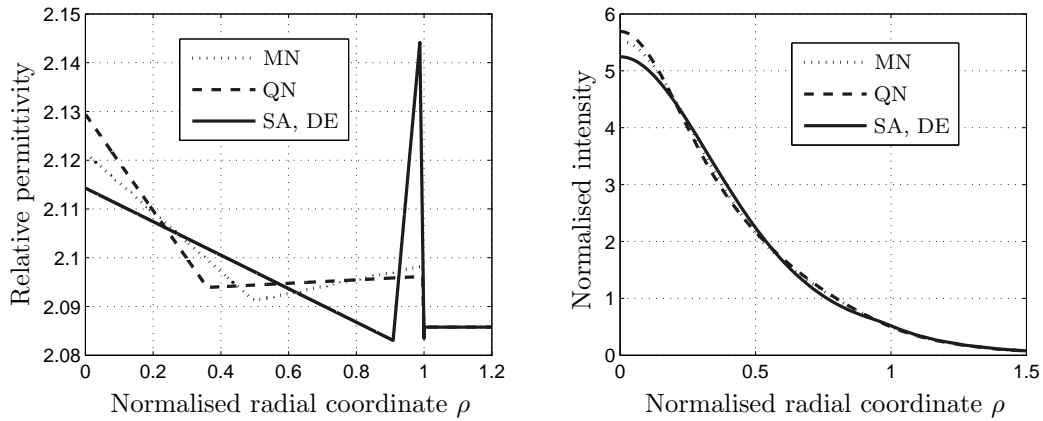algorithms, with their short computation times, are extremely well suited.

Figure 5.10: *Best optimised profiles at $\lambda = 1550\,nm$ (a) and corresponding intensity patterns (b) obtained by optimisation runs with five optimisation parameters.*
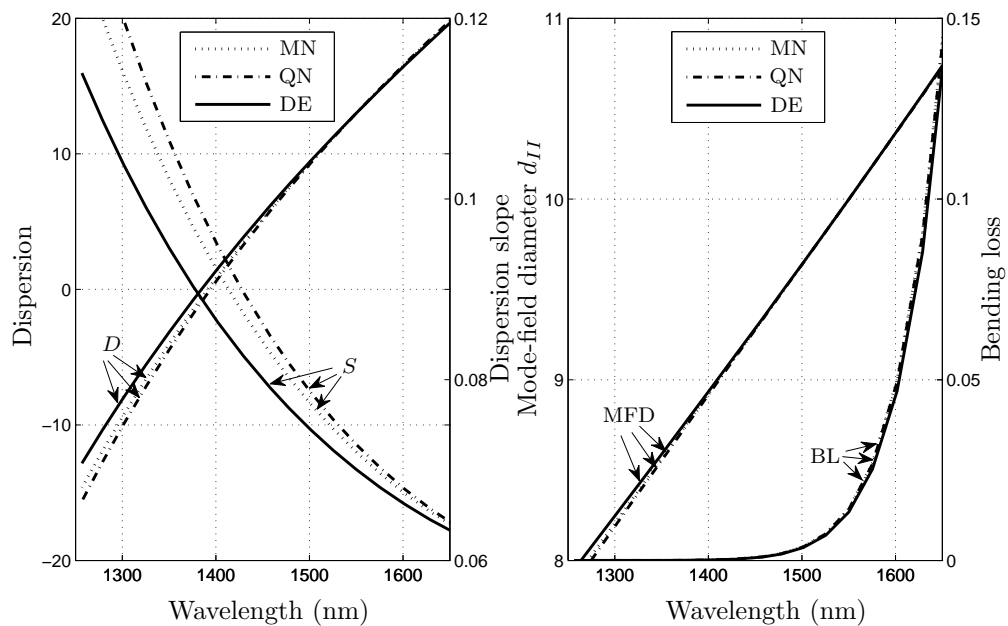

Figure 5.11: *Dispersion (D), dispersion slope (S), MFD d_{II} and bending loss (BL) as a function of wavelength for the best profile obtained by the MN, QN and DE schemes.*

The corresponding optimised profiles and their intensity patterns $S(\rho)$ normalised to the total power carried by the propagating mode are plotted in Figure 5.10 at a wavelength of $\lambda = 1550\,nm$. The Newton algorithms are not able to generate the sharp profile peak near the core/cladding transition. This is due to the circumstance that in their search, they are encountering the multi-mode regime limitation. The peak causes the value of the

dispersion slope to lower, which can be seen in Figure 5.11, where we have performed a wavelength sweep on the four fibre quantities for the best profiles obtained through the MN, QN and DE schemes.

Seven optimisation parameters

We have also performed optimisation runs with seven optimisation parameters, which are given in Table 5.5. Based on the observations in Table 5.3, we have made a selection in the choice of initial profiles, in particular, profiles starting at $X^{\mathrm{Ge}} = 0\,\%$ do not yield good results and are no longer considered. Further, we have only shown the results of those profiles that contain one transition from $X^{\mathrm{Ge}} = 7\,\%$ to $0\,\%$.

Table 5.5: *Start values (CF_s) and end values (CF_e) of the CF for various initial profiles, containing seven optimisation parameters, optimised with the MN, QN, SA and DE algorithms. The computation time and the number of iterations of the CF (F) and the CF with its gradient (F&G) for the best profile are shown as well.*

Profile	CF_s	CF_e^{MN}	CF_e^{QN}	CF_e^{SA}	CF_e^{DE}
(1,1,1,1)	34.5	5.78E-3	5.66E-3	5.09E-3	5.09E-3
(1,1,1,0)	4.1	**5.12E-3**	**5.16E-3**	**5.09E-3**	**5.09E-3**
(1,1,0,0)	8.1E6	5.12E-3	5.16E-3	5.09E-3	5.09E-3
F/F&G		0/436	239/153	3878000/0	952000/0
Comp. time		7.7 min.	5.2 min.	11.7 days	2.9 days

Again, we observe that optimisation results obtained by the Newton algorithms strongly depend on the choice of the initial profile, whereas the DE and SA scheme do not. Differences between the lowest values of the CF for the various schemes (bold typeface) are marginal (within $1.0\,\%$). Computation times are unequivocally much better for the Newton algorithms.

The SA scheme performs marginally better than the DE scheme, but at the expense of a four times longer computation time. The differences are shown in Table 5.6, where we have listed the computed fibre quantities that correspond to the best optimised profiles.

Although the differences in the computed fibre quantities between the various schemes are small, the corresponding optimised profiles, which are plotted in Figure 5.12(a), are rather different. The corresponding intensity patterns $S(\rho)$ normalised to the total power carried by the propagating mode are plotted in Figure 5.12(b). In Section 5.5.4, we will present a sensitivity analysis of these optimised profiles, which will give more insight in the influence of each optimisation parameter on the value of the CF.

Table 5.6: *Values of the fibre quantities v_q with the pertaining weighting coefficients w_q at $\lambda = 1550\,nm$ for which the profile, with seven optimisation parameters, has been optimised. The maximum deviation for each quantity v_q is given in the last column.*

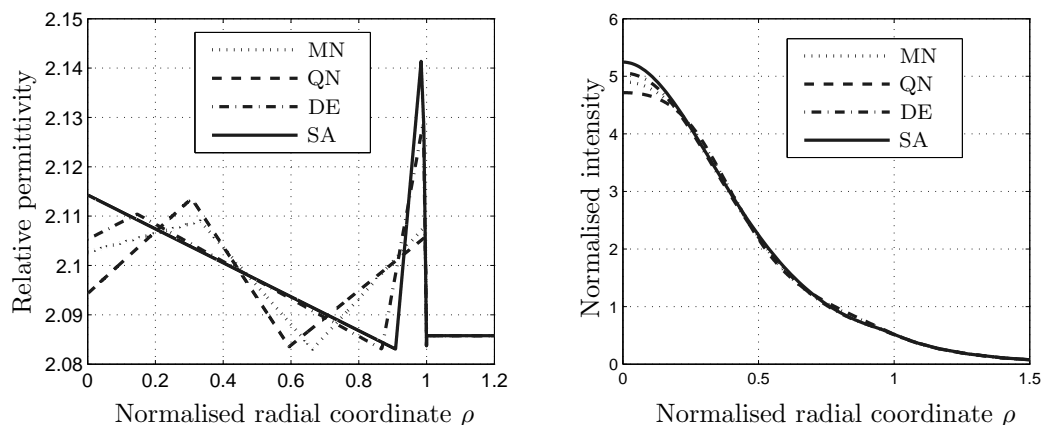|	v_q^{ref}	w_q	v_q^{MN}	v_q^{QN}	v_q^{SA}	v_q^{DE}	Max. dev.
D (ps/km/nm)	13	1	13.00	13.00	13.00	13.00	8.3E-5
S (ps/km/nm^2)	0	1	7.02E-2	7.02E-2	7.01E-2	7.01E-2	1.2E-4
MFD d_{II} (µm)	10	1	10.00	10.00	10.00	10.00	3.7E-4
Bend. loss (dB/turn)	0	1	1.41E-2	1.44E-2	1.33E-2	1.35E-2	1.0E-3

Figure 5.12: *Best optimised profiles at $\lambda = 1550\,nm$ (a) and corresponding intensity patterns (b) obtained by the MN and SA algorithms with seven optimisation parameters.*

More than seven optimisation parameters

For completeness, we have carried out similar optimisation runs with nine, eleven, thirteen and fifteen optimisation parameters. To limit the number of initial profiles, we have used the same selection procedure as in the case of the run with seven optimisation parameters. The lowest value of the CF for each parameter run with the various schemes are given in Table 5.7. We point out that in order to achieve such low minima for the DE scheme, we have had to change the control parameter NP to 200. With the initial recommended $NP = 8N$, the attained minimum values of the CF were increasing for an increasing number of optimisation parameters. As a result of these changes, the computation time increases drastically though.

For all algorithms, the value of $\mathrm{CF_e}$ gradually decreases for an increasing number of optimisation parameters, which is good from an optimisation point of view. Still, one has to contemplate on whether this relatively large number of parameters is practical as the fabrication process is more involved when the profile consists of more kinks. Profile

Table 5.7: *The end values of the CF (CF$_e$) for the best profiles, containing nine, eleven, thirteen and fifteen optimisation parameters.*

Algorithm	CF$_e$ (9 p)	CF$_e$ (11 p)	CF$_e$ (13 p)	CF$_e$ (15 p)	Comp. times
MN	5.09E-3	4.96E-3	4.96E-3	4.91E-3	21/31/54/86 min.
QN	5.11E-3	5.06E-3	5.02E-3	5.00E-3	7/12/13/15 min.
DE	4.79E-3	4.72E-3	4.71E-3	4.69E-3	12/62/83/96 days
SA	5.09E-3	4.98E-3	4.97E-3	4.81E-3	17/25/31/40 days

optimisation with the permittivity as the vertical parameter yields similar results for the cases considered in this section.

A hybrid method that first uses a stochastic optimisation scheme to locate the valley that harbours the global minimum and thereafter a fast Newton one to find it, might prove worthwhile if the computation time of a single CF iteration can be accelerated. For a kick-start using the DE scheme, an acceleration by at least a factor of 80 is required to arrive at an overall computation time that is within the hour for seven optimisation parameters. As discussed in Appendix E, a direct numerical integration of our system under the weak-guidance approximation can lessen the required acceleration factor by a factor of 1.5, which is not nearly enough.

As a last remark, we mention that there are faster computers commercially available. However, the inevitable reduction of overall computation time is still insufficient.

5.5.2 Profile variations in vertical directions only

Next, let us consider profile variations in the vertical direction only. This curtails the size of the parameter space drastically. It turns out that the MN algorithm is most suited since the pertaining computation times are short as compared to the global optimisers. Further, the results using the MN algorithm turn out to depend less on the initial profile choice than those obtained using the QN algorithm. In about 70 % of the possible initial profiles, selected by the procedure that is shown in Figure 5.9, the MN algorithm is able to find the global minimum, which has been verified with the DE scheme for up to nine optimisation parameters. In Table 5.8, the value of CF$_e$ is given for an increasing number of vertical parameters.

Also here, we observe a steady decrease in the value of the CF$_e$, which goes hand in hand with an increase in computation time. A further optimisation with the QN algorithm, while dropping the restriction on the horizontal parameters and thus considering a much larger parameter space, did not yield significantly lower minima. On the whole, the

Table 5.8: *End values of the CF (CF$_e$) with vertical optimisation parameters only, optimised with the MN algorithm.*

Opt. Parameters	CF$_e$	Comp. time	# of iterations
3	5.96E-3	43 sec.	76
5	5.40E-3	6 min.	328
7	5.16E-3	11 min.	428
9	5.05E-3	23 min.	664
11	4.94E-3	36 min.	828
22	4.71E-3	82 min.	905

large number of kinks, when optimising for many vertical parameters, renders the method impractical.

5.5.3   Comparison with commercially available fibres

To see if we can design refractive-index profiles such that they meet the specifications of single-mode fibres on today's market, we have downloaded the data-sheets of two leading optical fibre companies, Draka Communications [20] and Corning [15]. We have assumed a core radius of $a = 5\,\mu$m, and have extracted the values of those fibre quantities that we are able to optimise to from the data-sheets. In Table 5.9, these values are listed for several optical fibres, Corning's SMF-28e^{XB}, Draka Communications' Enhanced single-mode optical fibre (ESMF), and Draka Communications' BendBright^{XS} single-mode optical fibre (BB^{XS}).

To start our profile optimisation, we have to set the desired values of the fibre quantities at a specific wavelength in our CF. In view of the values given in the table, we have chosen for a wavelength of $\lambda = 1550$ nm. As the dispersion and dispersion slope are specified in the data-sheets in terms of inequality constraints, we have used the following rational expression [15]

$$D(\lambda) \approx \frac{S(\lambda_D)}{4}\left(\lambda - \frac{\lambda_D^4}{\lambda^3}\right) \quad \text{for } 1200\,\text{nm} \leq \lambda \leq 1625\,\text{nm}, \tag{5.46}$$

to arrive at an estimate for D to optimise for. For the zero-dispersion wavelength λ_D, we have used the centre value of the pertaining range, and for the dispersion slope, the maximum allowed value is chosen. Hence, for the ESMF we have found that $D = 17$ ps/km/nm, for the BB^{XS}, $D = 17.3$ ps/km/nm, and for the SMF-28e^{XB}, $D = 16.8$ ps/km/nm, respectively. For the mode-field diameter d_{II} of the BB^{XS}, we have chosen the centre value of the given range, i.e. MFD $d_{II} = 9.9\,\mu$m. The desired values of the dispersion slope S and

Table 5.9: *Specifications of Corning's SMF-28e^{XB} (issued 05/07), and Draka Communications' ESMF and BB^{XS} (issued 11/07). Our optimised results are given in the columns denoted by "Opt" next to each fibre.*

Optical fibre	ESMF	Opt	BB^{XS}	Opt	SMF-28e^{XB}	Opt
D (1550 nm)	≤18	17	-	17.3	≤18	16.8
D (1625 nm)	≤22	21.2	-	21.7	≤22	21.1
λ_D	1300-1322	1311	1300-1324	1313	1302-1322	1313
S (λ_D)	≤0.090	0.088	≤0.092	0.090	≤0.089	0.087
MFD d_{II} (1310 nm)	9.0	8.9	8.5-9.3	8.7	8.6	8.6
MFD d_{II} (1550 nm)	10.1	10.1	9.4-10.4	9.9	9.8	9.8
Bend. loss						
-R=25 mm, 100 turns	≤0.05	**1.1E-4**	-	-	-	-
-R=10 mm, 1 turn	-	-	≤0.10	**0.06**	≤0.50	**0.11**

the bending loss are set to zero to obtain optimal results. Further, we have made sure that the fibre is still in the single-mode regime for $\lambda_{ce} > 1300$ nm by tweaking the theoretical cut-off frequency in the mode-counting scheme [17, 18].

After some manual fine-tuning of the weighting coefficients w_q in the CF, we have been able to meet the specifications of current day's commercially available optical fibres, as is shown in the columns in Table 5.9 denoted by "Opt". To achieve these results, we have employed nine optimisation parameters and have used both Newton algorithms to optimise with, which is essential in the design process as computation times of the global optimisation schemes are prohibitive. Although the BB^{XS} and SMF-28e^{XB} have especially been designed to achieve a low macrobending sensitivity, there still appears to be room for improvement as can be seen from the values highlighted by a bold typeface.

5.5.4 Sensitivity analysis of the optimised profiles

For the optical-fibre manufacturer, the sensitivity of the fibre quantities, or more specifically of the CF, to small variations in the optimised refractive-index profile is of great importance. The less sensitive a profile is, the more robust the manufacturing process will be. To get an idea of the landscape in which the best profiles are located, we have defined distances from the best value of the CF in terms of percentages, i.e 1 %, 5 % and 10 %. Subsequently, we repeated the optimisation with the pertaining best optimiser and saved those vectors x_n that yield a value of the CF which is within one of these percentage regions. Upon recalling the refractive-index profiles of Figure 5.10 and 5.12, the DE scheme

performed best for five optimisation parameters and the SA scheme for seven, and hence, we have employed these schemes to determine the regions. This is shown in Figure 5.13, where we have shaded, next to the best optimised profile, from dark to light grey the areas that correspond to the 1 %, 5 % and 10 % deviations from this profile, respectively.
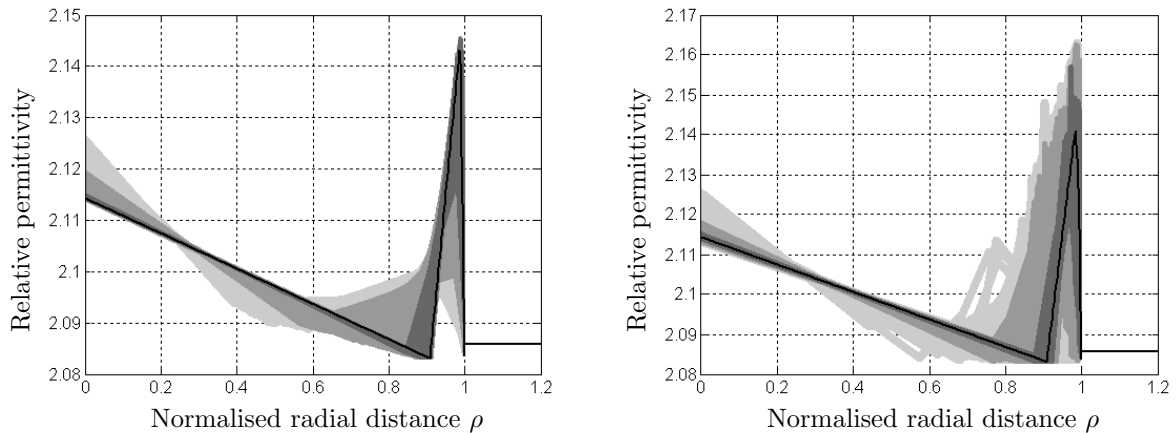

Figure 5.13: *Best optimised profiles (solid line) obtained by the DE and SA schemes for five (left) and seven (right) parameters, respectively. The dark grey and light grey area denote deviations in the CF from the best profile by 1 %, 5 % and 10 %, respectively.*

Although the sensitivity of the profiles can be readily determined from these plots, they require a full additional run to be generated, as knowledge of the minimum is required. An alternative would be to save all values of the CF with the corresponding vector x_n during the first run, but this requires too much memory to be efficient.

Sensitivity information can also be extracted from the deterministic methods using the gradient vector and the Hessian matrix. Since the MN algorithm provides both on exit, we have employed this scheme to demonstrate the principle. We recall from Section 5.1 that the MN algorithm is supplemented with simple bounds and that no additional constraints on the optimisation parameters can be added. An adaption of these simple bounds is required if one wishes to perform the sensitivity analysis on the profiles obtained by the other schemes in Figure 5.13, since the parameters of these profiles are generally outside the pertaining simple bounds. Then the simple bounds are modified such that the pertaining optimisation parameter is included, but almost fixed.

For convenience, we employ the simple bounds as defined by Eq. (5.4), which results in the optimised MN profiles determined in Section 5.5.1. Due to these bounds, the search for the minimum is generally obstructed and the optimisation may end there. If such a bound c_i is actively obstructing the search, the pertaining non-negative Lagrange multiplier λ_i in the Karush-Kuhn-Tucker conditions tells us how sensitive the CF is to a change in such a bound [70], i.e. the larger λ_i, the harder the CF is "pushing" or "pulling" against the

particular bound. In that case, the following relation holds

$$\partial_{x_n} \mathrm{CF}(x_n)\big|_{x_n = x_n^*} = \sum_{i \in \mathcal{A}(x_n^*)} \lambda_i \partial_{x_n} c_i(x_n^*), \tag{5.47}$$

where the optimisation parameters x_n^* correspond to the optimal profile, and $\mathcal{A}(x_n^*)$ denotes the set of active bounds or constraints. For example, for the optimisation with seven parameters, the pertaining relation results in

$$\begin{pmatrix} -8.9 \\ -8.8 \\ -9.0 \\ 0 \\ 0 \\ 7.8 \\ 0 \end{pmatrix} \times 10^{-3} = -\lambda_1 \begin{pmatrix} 1 \\ 0 \\ 0 \\ 0 \\ 0 \\ 0 \\ 0 \end{pmatrix} - \lambda_2 \begin{pmatrix} 0 \\ 1 \\ 0 \\ 0 \\ 0 \\ 0 \\ 0 \end{pmatrix} - \lambda_3 \begin{pmatrix} 0 \\ 0 \\ 1 \\ 0 \\ 0 \\ 0 \\ 0 \end{pmatrix} + \lambda_4 \begin{pmatrix} 0 \\ 0 \\ 0 \\ 0 \\ 0 \\ 1 \\ 0 \end{pmatrix}, \tag{5.48}$$

with the following set of active bounds

$$\begin{aligned} c_1: \quad & x_1 \le (1-\epsilon)/3, & c_2: \quad & x_2 \le (1-\epsilon)/3, \\ c_3: \quad & x_3 \le (1-\epsilon)/3, & c_4: \quad & x_6 \ge \epsilon. \end{aligned} \tag{5.49}$$

Since Eq. (5.47) is satisfied and all λ_i are greater than zero, we have found the lowest possible point. The best optimised profile obtained by the optimisation run with five parameters also satisfies the Karush-Kuhn-Tucker conditions.

Now that we have ascertained that x_n^* corresponds to the lowest point, we can obtain sensitivity information from the available gradient vector and Hessian matrix H. A Taylor series expansion of the CF about this point gives us

$$\mathrm{CF}(x_n) = \mathrm{CF}(x_n^*) + (\Delta x_n)^T \partial_{x_n} \mathrm{CF} + (\Delta x_n)^T \mathsf{H} (\Delta x_n) + O\left[(\Delta x_n)^3\right], \tag{5.50}$$

where $\Delta x_n = x_n - x_n^*$. Neglecting the third-order derivatives, we obtain for any requested absolute error in the value of CF a quadratic equation in terms of Δx_n. If a bound or constraint is encountered for a certain parameter, a first-order equation suffices as long as the requested absolute error is small. In Table 5.10, we have shown the deviations in Δx_n corresponding to an error of 1% in the value of the CF for the optimised MN profile with seven optimisation parameters

Apparently, deviations in the optimisation parameter x_5, which is the first vertical optimisation parameter away from the fibre axis, prove most stringent, and consequently manufacturing precision is most important there. As we have assumed first-order equations for those parameters that encounter a bound, the deviations Δx_1, Δx_2, Δx_3, and Δx_6 are inversely proportional to the Lagrange multipliers in Eq. (5.48).

Table 5.10: *Deviations Δx_n from the minimum x_n^* to achieve an absolute error of 1% in the value of the CF for the optimised MN profile with seven optimisation parameters*

n	1	2	3	4	5	6	7
x_n^*	3.32E-1	3.32E-1	3.32E-1	6.47E-2	8.55E-2	0	8.21E-2
Δx_n	-5.78E-3	-5.84E-3	-5.72E-3	$\pm$6.27E-5	$\pm$3.42E-5	6.56E-3	$\pm$4.31E-5

5.6   Short summary

We can imagine that after all these results it is hard to see the wood for the trees. Therefore, we summarise the most important findings of this chapter in bullet form:

- profile optimisation of the Germanium concentration profile is more than two times faster than optimisation of the permittivity profile and is more convenient from a manufacturing point of view;

- profile optimisation with an exact gradient computation is about twice as efficient than using a finite-difference approximation;

- profile optimisation with a Newton algorithm is at least 300 times faster than optimisation with the DE scheme, which in turn is the fastest among the tested stochastic algorithms for a limited number of parameters;

- profile optimisation with the stochastic schemes leads to minima that are comparable or better than the ones found with the Newton algorithms. By a systematic selection of the initial profiles for the deterministic schemes the number of optimisation runs are limited and minima are found within a margin of error of 6 %;

- profile optimisation in vertical directions only is more stable from an initial profile point of view. However, to the method's detriment the attained minima differ too much from the ones found with a profile optimisation in both horizontal an vertical directions;

- profile optimisation with the stochastic schemes requires a considerable amount of fine-tuning, whereas the Newton algorithms require an extensive analytical gradient calculation;

- a sensitivity analysis of the profile provides us with information on the shape of the valley in the cost function, which is of importance for the accuracy of the manufacturing process;

- the Hessian matrix, the gradient vector and the set of constraints determine whether the obtained minimum is the lowest point in the valley and sensitivity information can be retrieved from their values;

- there still appears to be room for improvement in the design of the refractive-index profiles of commercially available fibres.

The optimisation method of preference depends on the designer who has to contemplate on the necessity to find the global minimum instead of a local one with a 6 % error, the maximum number of optimisation parameters, and the available time to find an optimised profile. Both Newton algorithms, but in particular the quasi-Newton algorithm, are recommended in the design process when fine-tuning the weighting coefficients in the CF.

Chapter 6

Wave propagation in MMF links

The multi-mode fibre (MMF) has long been the preferred means of transmission in short-range data communication networks, e.g. campus and in-building networks, as it offers a cheap easy-to-install alternative to the single-mode fibre (SMF). In particular, the MMF consisting of a graded-index (GI) power-law profile, i.e. a power-law profile with a finite power-law exponent g, is favourable for its differential mode delay (DMD) qualities, as discussed in Section 3.2.1. Typical wavelengths of operation are 850 nm and 1300 nm.

Next to the silica-based MMF, the polymer optical fibre (POF) is gaining ground rapidly [43, 44]. Owing to its large core diameter ($120 \sim 1000\,\mu\text{m}$), it offers a larger ductility than its silica counterpart, improving the ease of installation even further and thus reducing the installation costs. Modal-dispersion management is key, as thousands of modes propagate along the POF. Due to the polymer, the attenuation per unit length is considerably higher than that of silica. However, since production technology improves, a steady decrease in the loss is attained, increasing its range of usage ($100 \sim 300\,\text{m}$). To analyse such fibres, more suitable solution techniques exist than an extensive vectorial full-wave computation, like, for example, the ray approach [90]. We concentrate on the silica-based MMF.

As already indicated, the transmission rate of a GI-MMF is primarily limited by DMD. Much research is conducted into methods by which the information capacity of optical fibres may be increased. These methods consist primarily of multiplexing techniques, i.e. the simultaneous transmission of a number of signals along the optical fibre. An overview of these techniques can be found in [48]. We mention the most frequently employed, namely wavelength division multiplexing, time division multiplexing, subcarrier multiplexing, and mode group diversity multiplexing (MGDM). The latter technique, which we will concentrate on in this chapter, is only applicable in MMF links.

In Section 6.1, we will demonstrate the MGDM technique on the basis of measurements and simulations of the intensity patterns at the receiver's end of the MMF. The

measurements have been performed by the electro-optical communication group at the Eindhoven University of Technology [101]. For the simulations, we use the model that has been introduced in Section 3.2.1 to compute the DMD properties of the fibre. However, for large propagation distances the intensity patterns simulated at the fibre's end begin to deviate from the measured ones. To compensate for these differences, we have included mode coupling and differential mode attenuation (DMA) in our model in Section 6.2. In Section 6.3, we have investigated a new technique called mode-selective spatial filtering (MSSF) to increase the spatial diversity of the MGDM link by employing a lens between the fibre end and the photodetector that captures the light [102]. We have compared the available MSSF measurements with our simulations.

As a side step, we have examined the effect of small deviations in the refractive-index profile on the intensity pattern. A statistical analysis of these profile defects was first investigated by Webster [114], and was later on expanded upon by the IEEE 802.3aq committee [40], which resulted in the "108-fiber model".

6.1   Mode group diversity multiplexing

Mode group diversity multiplexing (MGDM) is a technique that is used to increase the information rate in an MMF by creating parallel independent communication channels [53]. Each independent channel carries only a subset of all guided modes in the MMF. To create one such a channel, we excite the GI-MMF by a single single-mode fibre (SMF) pigtail with a possible radial offset. Since excitations at different radial offsets result in different intensity patterns at the fibre end, an optimal radial offset can be determined such that the overall DMD is minimised. Bandwidth gains up to a factor of 4 have been achieved in this way [79].

Employing several SMF pigtails at different offset positions enables the possibility to launch different signals in different channels (see Figure 3.8). By placing a properly tuned photodetector at the fibre end, it is possible to retrieve the transmitted signals via a matrix inversion implemented in adaptive electronics, thus creating a multiple-input multiple-output (MIMO) system. Inevitably, optical cross talk among the pertaining channels and noise is introduced, which limits the possible number of channels. With every group of modes, we can associate certain helical ray paths. By adjusting the angular tilt of the pigtail according to its radial offset, a more selective excitation of the mode groups can be achieved [89]. As a result, the optical cross talk among the channels can be reduced.

To numerically model an MGDM link, we recall the discussions in Section 3.2 and Appendix F.2, where we have introduced differential mode attenuation, mode coupling, and selective launching. In the following sections, these concepts will be used in the

simulation of a stable MGDM link.

6.1.1   Excitation with a radial offset

It has been demonstrated experimentally that a 3×3 MIMO system, consisting of three transmitters and three receivers, can be achieved with the MGDM technique [103]. That system has been proven stable and robust over time. The setup is shown in Figure 6.1. The end faces of the three transmitters, i.e. the SMF pigtails, are denoted by T_i, with
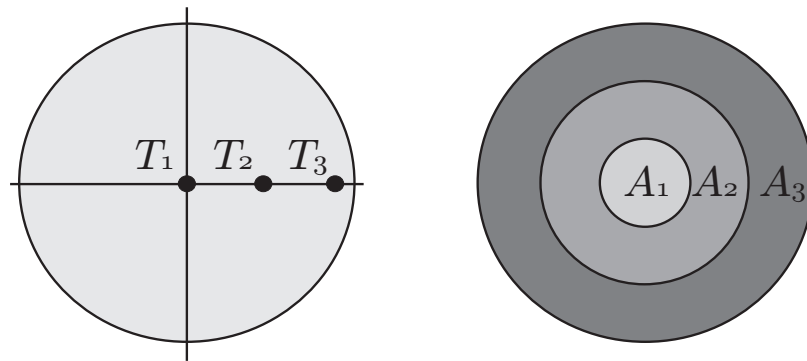

Figure 6.1: *A 3×3 MIMO system consisting of three transmitters T at the launch (left) and three annular regions A corresponding to the receiving areas of the photodetector (right).*

$i = \{1, 2, 3\}$. At the receiving end of the MMF, three annular regions A_i, with $i = \{1, 2, 3\}$, are defined. From the power captured within each region, the corresponding transmitted signal T_i can be retrieved, provided that the cross talk among the three channels is limited. To this end, a proper choice of the radii of the pigtail offsets and the annular regions is essential.

Regarding the annular regions, it is convenient to employ a multi-segment photodetector to collect the light [76]. The total power within an annular region is obtained by integration. Mathematically, the MGDM link can be cast in the form [6, 101]

$$\mathbf{s}_{A_i} = \mathsf{H}\, \mathbf{s}_{T_i} + \mathbf{n}_i, \quad \Rightarrow \quad \mathbf{s}_{T_i} = \mathsf{H}^{-1}\, \mathbf{s}_{A_i} + \mathsf{H}^{-1}\mathbf{n}_i, \tag{6.1}$$

where $\mathbf{s}_{A_i}$ denotes the power that arrives at each segment A_i and $\mathbf{s}_{T_i}$ is the transmitted power launched at T_i. Since we employ a coherent source in our simulations and the propagating modes are mutually orthogonal, we may add the modal powers to arrive at the total power vectors $\mathbf{s}_{A_i}$ and $\mathbf{s}_{T_i}$. The real-valued transmission matrix H, which characterises the MGDM link, must vary much slower with time than the vectors $\mathbf{s}_{A_i}$ and $\mathbf{s}_{T_i}$ to recover the transmitted signal. Further, we have added the term $\mathbf{n}_i$ to account for the noise of the channel and the electronic processing unit. Note that signal recovery depends on the condition number of the transmission matrix as its inverse is required. Moreover,

since the matrix inversion is carried out by adaptive electronics, the eigenvalues of the pertaining matrix may vary over time due to temperature changes and noise. According to Gershgorin's circle theorem [93], the inverse exists for diagonally dominant matrices and the influence of varying eigenvalues is easily recognised. Hence, ideally $\mathsf{H} = \mathsf{I}$, where I denotes the identity matrix. Under this condition, there is no optical cross talk, and consequently, no demultiplexing processing would be required to separate the channels. As a result, noise would not be amplified during this step. The Frobenius norm for an ideal $N \times N$ MIMO system equals N. It is this ideal transmission matrix behaviour that we aim to achieve.

To verify our simulation results and demonstrate the MGDM principle, we have performed measurements for a 3×3 MGDM link. The employed GI-MMF has a core radius of $a = 31.25\,\mu\text{m}$ and an $\text{NA} = 0.275$ [20]. Its refractive-index profile has been designed for operation at either $\lambda = 850\,\text{nm}$ or $\lambda = 1300\,\text{nm}$. The linewidth of the employed laser is 85 kHz with a central wavelength of 1310 nm. The laser is pigtailed to a 1 m standard SMF with a mode-field diameter d_{II} of 9.3 µm at $\lambda = 1310\,\text{nm}$. To control the level of the optical power, a variable optical attenuator with SMF pigtails is used. The radial offset of the SMF axis from the GI-MMF axis is set by means of computer-controlled translational stages. A microscope with a $50\times$ magnification and an $\text{NA} = 0.75$ projects the intensity pattern at the fibre end onto an infra-red vidicon camera. Thereupon, an image is grabbed with video processing software. The SMF pigtails are positioned at three distinct radial offsets, i.e at $r_0 = 0\,\mu\text{m}$, 13 µm and 26 µm. In Figure 6.2, the measured intensity patterns are shown for fibre lengths of $z = 1\,\text{m}$, 75 m and 1 km. These distances are typical fibre
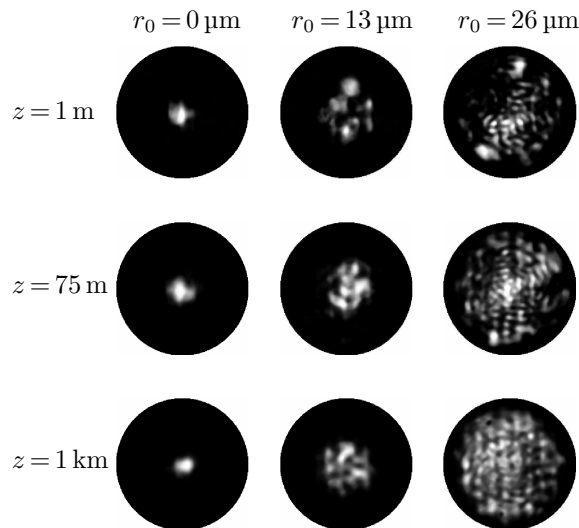

Figure 6.2: *Measured intensity patterns at $\lambda = 1310\,nm$ for various distances z from the launch end and radial offsets of $r_0 = 0\,\mu m$, $13\,\mu m$ and $26\,\mu m$, at $\lambda = 1310\,nm$. The profile of the GI-MMF is designed for either $\lambda = 850\,nm$ or $\lambda = 1300\,nm$.*

lengths in computer-router connections, in-building connections and campus connections, respectively.

We observe that the radial offset position is an indication for the shape of the intensity pattern, i.e. the power remains confined to an imaginary disc of about $r = r_0$, independent of the fibre length. This is a result of the optimised power-law profile, which guides the propagating modes towards the centre in a controlled fashion. In MGDM links, this confinement is exploited as the multi-segment photodetector can recover the three simultaneously transmitted signals from the retrieved power provided that the cross talk among the channels is limited.

The speckles in the patterns are caused by the constructive and destructive interference among the propagating modes, which have different group velocities. Moreover, it is demonstrated in [16, 36, 52] that for a coherent source the speckle contrast is maximal. The broader the emission spectrum of the source and the longer the fibre, the less pronounced the speckle contrast will be. Additionally, mode coupling reduces the speckle contrast by introducing an overall blur to the pattern. For small wavelengths, the chance of power exchange among the propagating modes increases owing to the large number of modes. Since the employed laser has a small linewidth and the employed wavelength is large, the speckles remain clearly visible even for larger distances z.

Next, we have performed simulations on a similar GI-MMF, viz. the core radius equals $a = 31.25 \, \mu m$ and NA $= 0.275$. In Section 3.2.1, we have optimised the power-law profile of this particular GI-MMF to achieve a good DMD behaviour at $\lambda = 850 \, nm$, resulting in a power-law exponent $g = 2.06$. As the current measurements have been performed at $\lambda = 1310 \, nm$, DMD simulations have been performed at this wavelength, yielding an optimal value of $g = 1.97$. The dimension and refractive index of the step-index SMF pigtail have been adjusted such that for its MFD we have $d_{II} = 9.3 \, \mu m$ at $\lambda = 1310 \, nm$. In Figure 6.3, the simulated intensity patterns for both $g = 1.97$ and $g = 2.06$ are shown for various lengths of the GI-MMF. For reasons of clarity, we have not yet taken mode coupling and differential mode attenuation into account in the simulations. These phenomena will be included to our model in Section 6.2.

A closer look at the patterns for $r = 0 \, \mu m$ indeed reveals that for $g = 1.97$, which is the optimal g at this wavelength, the power remains confined to the core centre, whereas the power for $g = 2.06$ exhibits a gradual spread as the distance increases. On the other hand, if we excite the GI-MMF with a radial offset, the distinction between the spreading effects disappears. The power remains confined to the imaginary disc of about $r = r_0$. Since the source in the simulations is monochromatic and mode coupling has not been taken into account, the speckle contrast is maximal. The symmetry in the patterns reflects the polarisation of the excitation probe, which is chosen along the horizontal axis. As
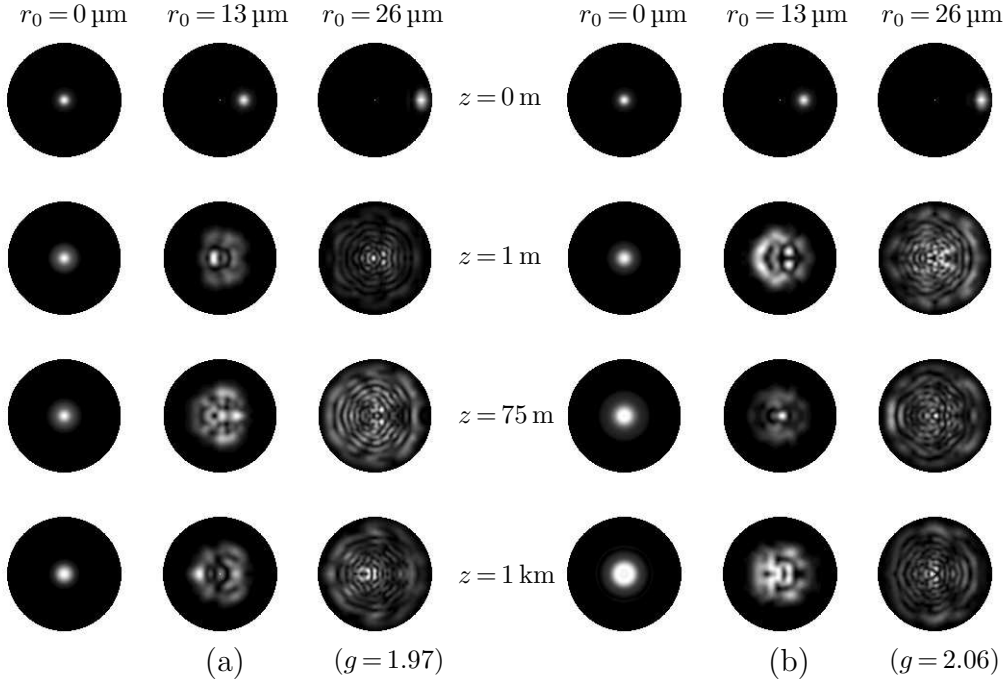
Figure 6.3: *Simulated intensity patterns at various distances z from the launch end and radial offsets of $r_0 = 0\,\mu m$, $13\,\mu m$ and $26\,\mu m$, at $\lambda = 1310\,nm$. For (a) g = 1.97 and for (b) g = 2.06.*

a consequence, only half of the intensity pattern has to be computed, which leads to a reduction in computation time.

When the SMF pigtail approaches the core/cladding transition, the overlap efficiency reduces as more power is leaking into the cladding region of the GI-MMF. To acquire the same amount of power at the fibre end for all offsets, either the laser has to deliver more power to offsets close to the core/cladding transition, or the power collected at the outer segments of the photodetector needs to be amplified. Inevitably, this introduces constraints on the power budget. To give an unbiased comparison, we choose to operate the laser at a fixed power for all offset positions and amplify all output signals equally. For our model, this implies that we normalise the output power with respect to the power transferred into the GI-MMF at $z = 0\,m$ for a cental launch, which in turn is normalised to its maximum amplitude. In Figure 6.4, we have plotted the power, after integrating over a single period of the angular coordinate ψ at the launch $z = 0\,m$ for the three radial offsets. The GI-MMF with $g = 1.97$ is used. A subsequent integration over the radial coordinate reveals that the total cross-sectional power for $r_0 = 26\,\mu m$ is about $80\,\%$ of that for $r_0 = 0\,\mu m$, whereas that for $r_0 = 13\,\mu m$ is still about $100\,\%$.

Figure 6.5 shows the spread in power at a distance of $z = 75\,m$. In view of the intersection of the various lines, the radii R_i of the corresponding annular regions A_i of the
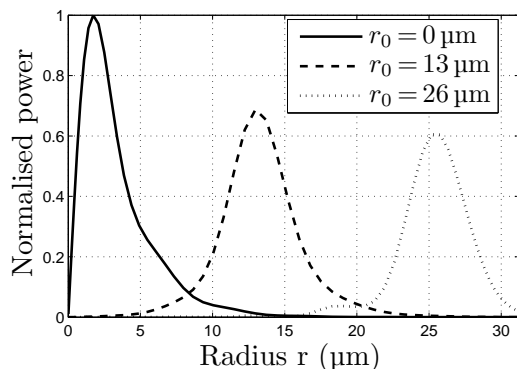
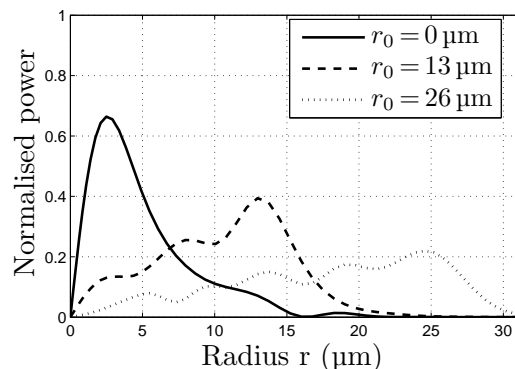Figure 6.4: *Normalised power at $z = 0\,m$ for various radial offset.*

Figure 6.5: *Normalised power at $z = 75\,m$ for various radial offset.*

photodetector (see Figure 6.1), are best given by

$$0\,\mu m \leq R_1 \leq 7\,\mu m \leq R_2 \leq 17\,\mu m \leq R_3 \leq 31.25\,\mu m, \qquad (6.2)$$

to minimise the optical cross talk. This is in close agreement with the annular regions found experimentally by Tsekrekos et al. [103] for an excitation of the same GI-MMF at $\lambda = 660\,$nm by an SMF pigtail with an MFD d_{II} of 4.2 μm at the operating wavelength, which resulted in a stable 3×3 link. As a consequence, it appears that the proposed MGDM technique is not restricted to a confined wavelength range when defining optimal radii R_i but only to distance and to differences in power amplifications of the various signals at the transmitter and receiver end. A stable 4×4 link based on the MGDM technique has not been achieved in practice due to the power penalty introduced by thermal and shot noise [2, 101].

Next, let us determine the transmission matrix H in Eq. (6.1), as it is a measure for the optical cross talk between the channels, and thus for the maximum number of possible channels. For the three received signals j at $z = 75\,$m, the elements $h_{i,j}$ building the transmission matrix H at the receiver's end (rec) are obtained by

$$h_{i,j}^{\mathrm{rec}} = \iint_{A_i} S_j(\rho, \psi)\rho d\rho d\psi \bigg/ \sum_{j=1}^{3} \iint_{A_i} S_j(\rho, \psi)\rho d\rho d\psi, \qquad (6.3)$$

where $\rho = r/a$, which results in the following transmission matrix

$$\mathsf{H} = \begin{pmatrix} 0.72 & 0.21 & 0.07 \\ 0.18 & 0.58 & 0.24 \\ 0.01 & 0.12 & 0.87 \end{pmatrix}. \qquad (6.4)$$

Consequently, from

$$\mathrm{OC}(A_i) = 10 \log_{10} \left(\sum_{j \neq i} h_{i,j} \bigg/ h_{i,i} \right), \qquad (6.5)$$

the total optical cross talk (OC) in the regions A_1, A_2 and A_3 are given by -4.1 dB, -1.4 dB and -8.3 dB, respectively. The diagonally dominant transmission matrix has a Frobenius norm condition number of 3.9. In [103], the transmission matrix elements are determined from a transmitter side of view, which also results in a diagonally dominant matrix and a Frobenius norm condition number equal to 3.9.

6.1.2   Excitation with both a radial offset and an angular tilt

In addition to the radial offset, we employ an angular tilt to the SMF pigtails in the 3×3 MGDM link [10, 106]. Since the propagating modes tend to follow helical-shaped paths, the addition of an angular tilt under an optimal angle $\theta'' = \theta_0$ matching the trajectory of these paths is expected to yield steeper power peaks in Figure 6.5. As a result, a better reception of the signals may become feasible as optical cross talk is reduced and the possibility to increase the number of independent channels arises.

To determine the angle θ_0 for the radial offset of $r_0 = 13\,\mu\mathrm{m}$ (T_2), we gradually increase the angle θ'' starting from $\theta'' = 0$. We define the optimal angle as the angle at which the power within annular region A_2 attains a maximum at a distance of $z = 75\,\mathrm{m}$. After numerous simulations, we have found that $\theta_0 \approx 4.0°$ is best to a resolution of 0.1°. For a radial offset of $r_0 = 26\,\mu\mathrm{m}$ (T_3), we have maximised the power within annular region A_3 and obtained an optimal angle of $\theta_0 \approx 1.5°$. Theoretically, the sharpest peak in the pertaining interval occurs for $\theta_0 \approx 9.1°$, although the intensity at the output is very low, due to an increased leakage into the cladding at the launch. To retain enough confinement, the optimal angle θ_0 has to remain small.

In Figure 6.6(a), we have plotted the "optimised" equivalent of Figure 6.5. We observe that the power is indeed more confined to the preset annular regions than for the case of Figure 6.3(a). The irrevocable conclusion is thus that the cross talk can be reduced with an angular tilt added to possible radial offset. This confinedness is clearly visible in the intensity patterns that are plotted in Figure 6.6(b) for the radial offset $r_0 = 13\,\mu\mathrm{m}$ at several distances z from the launch end.

The transmission matrix H of this MGDM link for $z = 75\,\mathrm{m}$ is given by

$$\mathsf{H} = \begin{pmatrix} 0.80 & 0.13 & 0.07 \\ 0.17 & 0.60 & 0.23 \\ 0.01 & 0.18 & 0.81 \end{pmatrix}, \tag{6.6}$$

which yields an optical cross talk in the regions A_1, A_2, and A_3 of -6.0 dB, -1.8 dB, and -6.3 dB, respectively. The Frobenius norm condition number of H equals 3.7 and its inverse exists owing to diagonal dominance.
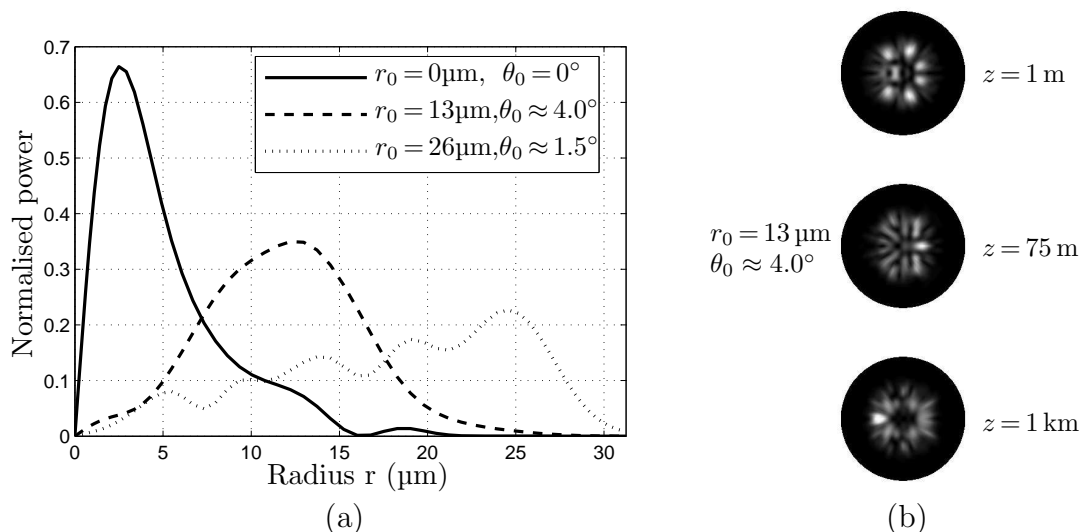
Figure 6.6: *The GI-MMF (g = 1.97) is excited by an SMF pigtail at $\lambda = 1310\,nm$ with an offset of $r = r_0$ and $\theta'' = \theta_0$. (a) Normalised power in an annular region of the GI-MMF as a function of radius optimised for $z = 75\,m$. (b) Corresponding intensity patterns for $r_0 = 13\,\mu m$ at various distances z.*

This might look promising as this condition number is slightly closer to the ideal value of 3 than the condition number of 3.9 obtained from the matrix of Eq. (6.4) for radial offset excitation only. However, in practice, there are two major drawbacks to an excitation with an angular tilt. First of all, the SMF pigtail and the GI-MMF should be connected properly, which is more difficult with an additional tilt angle. Moreover, more light is reflected at the pertaining transition, and as a result, the coupling efficiency reduces. Secondly, the length of the GI-MMF will affect the intensity pattern, as the finite linewidth of the source and/or the presence of mode coupling will cause a gradual fill of the disk-shaped ring. An example of this filling is shown in the rightmost column of Figure 6.7. Hence, in practice, the inclusion of an additional angular tilt next to the radial offset does not lead to a sufficient improvement.

6.2 The effect of mode coupling and DMA

Thus far we have neglected the influence of mode coupling and differential mode attenuation (DMA) in the computation of the intensity patterns. These phenomena, and their numerical evaluation, have been discussed in detail in Section 3.2. To validate our simulation results, we have performed measurements with the same GI-MMF as introduced in Section 6.1, although this time at a wavelength of $\lambda = 660\,nm$. Consequently, about a thousand modes propagate at nearly identical group velocities, which increases the likelihood of power mixing. To exclude an overall fill due to a wide linewidth, we have used

a continuous-wave Fabry-Pérot laser, which has a very narrow linewidth when operated above threshold [100]. At the operating wavelength, the employed 1 m SMF pigtail has an MFD $d_{II} = 4.2\,\mu m$ and a numerical aperture NA $= 0.12$. The measured intensity patterns are shown in Figure 6.7.
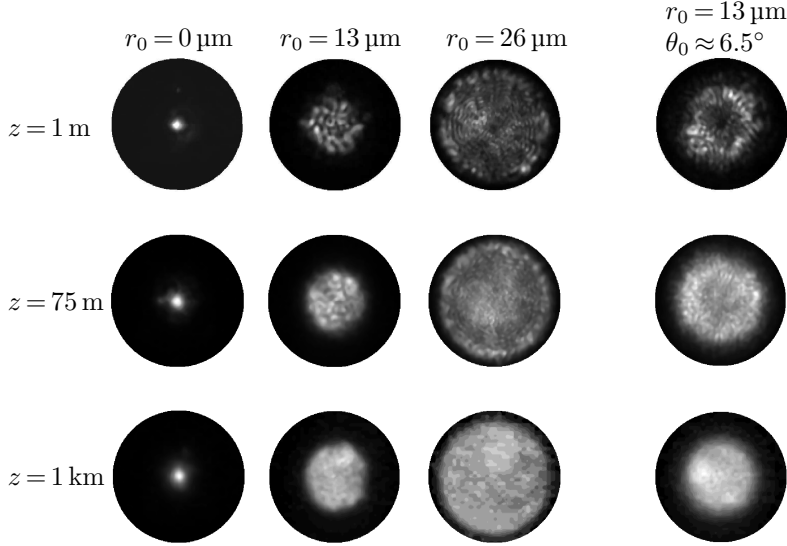

Figure 6.7: *Measured intensity patterns at various distances z from the launch end and radial offsets of $r_0 = 0\,\mu m$, $13\,\mu m$ and $26\,\mu m$, at $\lambda = 660\,nm$. For $r_0 = 13\,\mu m$, an additional measurement is performed with $\theta_0 \approx 6.5°$. The profile of the GI-MMF is, according to the manufacturer, designed for operation at either $\lambda = 850\,nm$ or $\lambda = 1300\,nm$.*

Mode coupling is visible as the power gradually spreads for increasing distances from a few hot spots into a more overall fill. Already at an intermediate distance of $z = 75\,m$, mode coupling is well under way. For $z = 1\,km$, the coupling seems complete. From an MGDM point of view, it is again good to see that the power remains within an imaginary disc of about $r = r_0$. Employing an angular tilt of $\theta_0 \approx 6.5°$ at $r_0 = 13\,\mu m$ shows a ring in the intensity pattern for small distances. As a result of mode coupling, the ring is completely indistinguishable at $z = 1\,km$. Note that the angular tilt causes the imaginary disc to have a slightly larger radius [104].

All simulations performed up until now do not show this overall filling. To investigate its origin, we have taken intra-group mode coupling into account for the distances $z = 75\,m$ and $z = 1\,km$. At the operating wavelength of $\lambda = 660\,nm$ extended precision arithmetic has been used for our numerical scheme (see Section 2.4). Since the GI-MMF is, according to the manufacturer, designed for operation at either $\lambda = 850\,nm$ or $\lambda = 1300\,nm$, we have assumed the power-law exponent $g = 2.06$, corresponding to the lower wavelength. The computed intensity patterns are shown in Figure 6.8(a). Note that the speckle pattern turns into a more gradual fill when mode coupling is included, similar to the measurements. The annular ring, on the other hand, observed for excitation with an angular
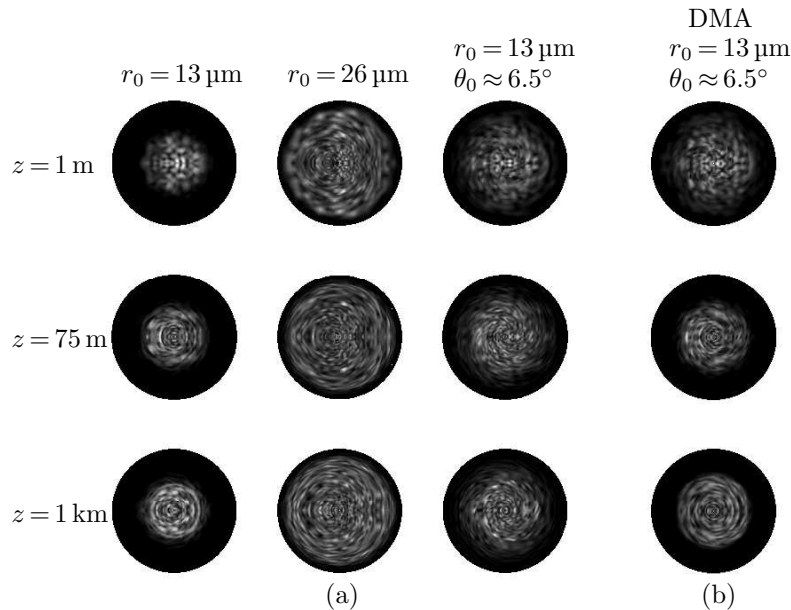
Figure 6.8: *Simulated intensity patterns at various distances z from the launch end with radial offsets and angular tilts of $r_0 = 13\,\mu m$, $r_0 = 26\,\mu m$ and $\theta_0 \approx 6.5°$, at $\lambda = 660\,nm$. Intra-group mode coupling is included for $z = 75\,m$ and $z = 1\,km$ (a). The effect of including DMA is shown in (b).*

tilt of $\theta_0 \approx 6.5°$, cannot be reproduced. Already at $z = 1\,\mathrm{m}$, the ring seems to be absent, although an integration of the pertaining power still yields a steep peak at about $r = r_0$. In addition, we observe that the power is more spread in comparison to the measurements for this type of offset. The inclusion of DMA mitigates this spreading effect, as is shown in Figure 6.8(b). Although the spreading is not noticeable for non-angular excitations, inclusion of DMA for large z does not alter the intensity patterns either.

We must admit that the measurements do not fully coincide with the simulations for angular tilts, and that the speckle contrast is still discernible even if mode coupling is included. The inclusion of inter-group mode coupling and the finite linewidth of the laser might lead to a closer match.

6.3 Mode-selective spatial filtering

The mode-selective spatial filtering (MSSF) technique was first introduced in [102], as a means to reduce the optical cross talk in an MGDM system, while maintaining its ease of realisation. This is achieved by placing a properly chosen lens between the output of the GI-MMF and the multi-segment photodetector, as is schematically shown in Figure 6.9. Light rays departing from the GI-MMF exit at an angle $\theta = \theta_{\mathrm{out}}$, which is determined by the abrupt change in refractive index at the MMF-air transition and the local wavenumber. If this angle of departure is within the cone with angle θ_{lens}, the light is captured by the
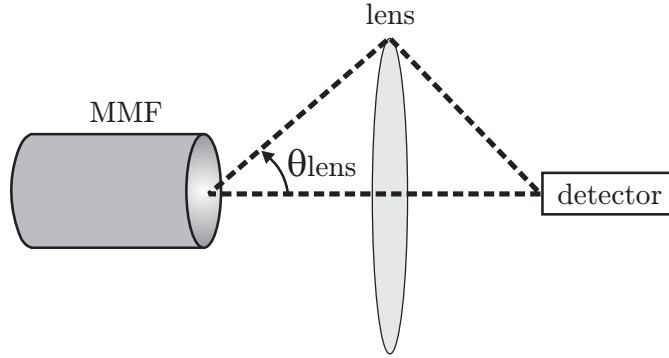
Figure 6.9: *Configuration used for MSSF. A lens projects light from the output of the GI-MMF onto the multi-segment photodetector.*

detector. The angle θ_{lens} is given by

$$\text{NA}_{\text{lens}} = n_{\text{sur}} \sin \theta_{\text{lens}}, \tag{6.7}$$

where NA_{lens} is the numerical aperture of the lens, and n_{sur} denotes the refractive index of the medium surrounding the lens, which in our case is air, i.e. $n_{\text{sur}} = 1$.

To determine the angle θ_{out} at the MMF-air transition, we regard each mode as a plane wave, with a normalised longitudinal propagation coefficient ζ, incident on the transition, and neglect any reflected waves. Although this may seem a crude approximation, it proves to be a rather effective and efficient one, as it avoids the time-consuming computational solution of the total scattering problem. We will demonstrate that the attained intensity patterns are in close agreement with measurements available in the literature.

As an initial impetus, we consider two regions that are separated by the MMF-air transition. In each region, the dispersion relation must hold for each propagating mode i, i.e. [83]

$$\begin{aligned} \xi_1^2(\rho) + \zeta_{i,1}^2 &= n^2(\rho) \quad \text{in region 1 (MMF)}, \\ \xi_2^2(\rho) + \zeta_{i,2}^2(\rho) &= 1 \qquad \text{in region 2 (air)}, \end{aligned} \tag{6.8}$$

where ξ denotes the normalised transverse wavenumber. The angle θ_{out} is given by

$$\tan \theta_{\text{out}} = \xi_2(\rho)/\zeta_{i,2}(\rho). \tag{6.9}$$

At the MMF-air transition, continuity of the transverse wavenumber yields $\xi_1 = \xi_2$. Since we have expressions for all the electromagnetic field components of every mode at each sample point ρ_j at our disposal, we set those portions of the field components to zero that are not captured by the lens, i.e. for which

$$\left[n^2(\rho_j) - \zeta_{i,1}^2 \right] > \left[1 - n^2(\rho_j) + \zeta_{i,1}^2 \right] \tan^2 \theta_{\text{lens}}. \tag{6.10}$$

Inevitably, the power radiating into free space is lost. With the MSSF technique, it is possible to create a stable 5×5 MGDM link, whereas without the pertaining technique,

we have only been able to establish a stable 3×3 MGDM link (see Section 6.1.1). In the next section, we will construct this 5×5 MGDM link with MSSF and compute intensity patterns for an excitation of the MMF with SMF pigtails at five different radial offsets. In addition, we demonstrate the effectiveness of this technique by comparing the transmission matrices H of this link with and without the inclusion of the MSSF technique.

6.3.1   A stable 5×5 MGDM link with MSSF

According to [101], a 5×5 MGDM link is possible through the construction of a stable transmission matrix H by using the following radial offset positions for the SMF pigtails: $r_0 = 0$, 10, 15, 21, and 26 μm. At the employed excitation wavelength of $\lambda = 635$ nm, the pigtails are characterised by MFD $d_{II} = 4.2$ μm, and NA $= 0.12$. We employ the same GI-MMF as introduced in Section 6.1, viz. $a = 31.25$ μm, NA $= 0.275$ and $g = 2.06$, optimised at $\lambda = 850$ nm. For the lens, we take NA$_{\text{lens}} = 0.10$. The simulated intensity patterns for this configuration are shown in Figure 6.10 for $z = 1$ m and $z = 1$ km.
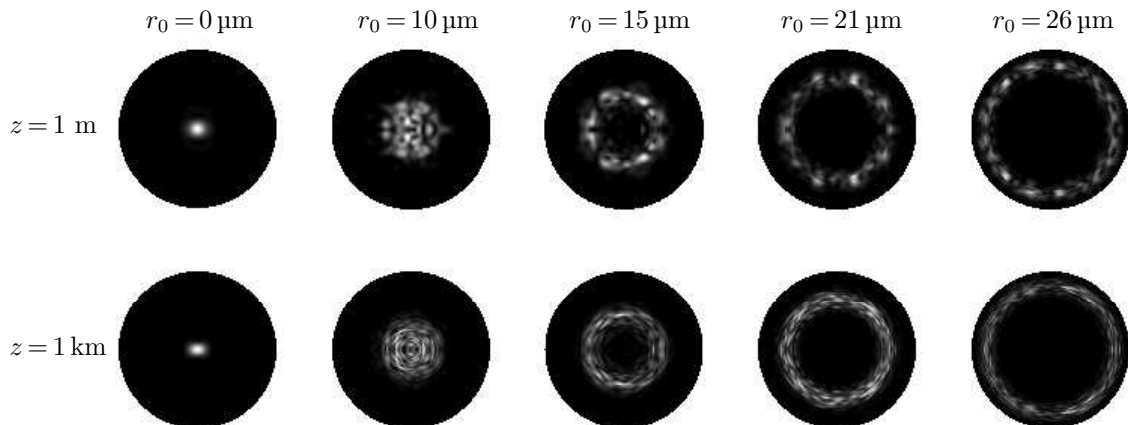

Figure 6.10: *Simulated intensity patterns with MSSF and an $NA_{lens} = 0.10$ at $z = 1$ m and $z = 1$ km from the launch end with radial offsets of $r_0 = 0$ μm, 10 μm, 15 μm, 21 μm, and 26 μm at $\lambda = 635$ nm. Mode coupling and DMA are included for $z = 1$ km.*

The inclusion of the lens clearly introduces annular rings in the intensity pattern because the power at the centre leaves the end face of the fibre at quite an acute angle, especially for the radial offsets $r_0 = 15$ μm, 21 μm, and 26 μm, respectively. For $r_0 = 0$ μm the presence of the lens does not change the intensity pattern and for $r_0 = 10$ μm the hole at the centre has not yet formed. Further, we observe that the rings are more pronounced at $z = 1$ km than at $z = 1$ m, indicating that the power is more equally spread owing to intra-group mode coupling. This is in agreement with the measurements in [101].

To examine the optical cross talk of the 5×5 MIMO system, we have determined the

transmission matrix at $z = 1\,\text{km}$ with and without the inclusion of MSSF, i.e.

$$\mathsf{H}_{\text{MSSF}} = \begin{pmatrix} 0.839 & 0.159 & 0.002 & 0.000 & 0.000 \\ 0.050 & 0.851 & 0.098 & 0.000 & 0.000 \\ 0.000 & 0.216 & 0.730 & 0.055 & 0.000 \\ 0.000 & 0.036 & 0.068 & 0.786 & 0.109 \\ 0.000 & 0.004 & 0.009 & 0.065 & 0.921 \end{pmatrix},$$

(6.11)

$$\mathsf{H}_{\text{NO\_MSSF}} = \begin{pmatrix} 0.746 & 0.124 & 0.069 & 0.037 & 0.023 \\ 0.020 & 0.451 & 0.285 & 0.157 & 0.087 \\ 0.000 & 0.140 & 0.435 & 0.264 & 0.161 \\ 0.000 & 0.018 & 0.110 & 0.524 & 0.348 \\ 0.000 & 0.006 & 0.013 & 0.157 & 0.824 \end{pmatrix},$$

respectively. For $\mathsf{H}_{\text{NO\_MSSF}}$, the radii R_i of the corresponding annular regions A_i of the photodetector, with $i = \{1, 2, 3, 4, 5\}$, are set as follows

$$0\,\mu\text{m} \leq R_1 \leq 5\,\mu\text{m} \leq R_2 \leq 11\,\mu\text{m} \leq R_3 \leq 16\,\mu\text{m} \leq R_4 \leq 22\,\mu\text{m} \leq R_5 \leq 31.25\,\mu\text{m}.$$

(6.12)

The optical cross talk in the annular regions A_1 until A_5 is with the aid of Eq. (6.5) given by -4.7 dB, 0.9 dB, 1.1 dB, -0.4 dB, and -6.7 dB, respectively. Since the matrix is no longer diagonally dominant, the inverse transmission matrix may become singular and signal recovery is no longer guaranteed. The transmission matrix Frobenius norm condition number equals 9.2.

For the transmission matrix H_{MSSF}, on the other hand, the radii R_i, corresponding to the annular regions A_i, are set as follows

$$0\,\mu\text{m} \leq R_1 \leq 5\,\mu\text{m} \leq R_2 \leq 12\,\mu\text{m} \leq R_3 \leq 18\,\mu\text{m} \leq R_4 \leq 24\,\mu\text{m} \leq R_5 \leq 31.25\,\mu\text{m}.$$

(6.13)

The optical cross talk in the regions A_1 until A_5 are -7.2 dB, -7.6 dB, -4.5 dB, -5.7 dB, and -10.7 dB, respectively, and the Frobenius norm condition number equals 5.4.

The MSSF techniques ensures that the optical cross talk between the channels becomes small, which results in a nearly ideal identity matrix, and thus diagonal dominance guaranteeing a stable MGDM link. However, this advantage comes at a price, since the power that is not captured by the photodetector is inevitably lost. Upon comparing the case with MSSF to the one without, we have found the loss for increasing radial offset positions to be 0 dB, 0 dB, 3.7 dB, 6.2 dB, and 7.8 dB, respectively. Fortunately, the power penalty introduced by shot and thermal noise is low for near-ideal transmission matrices and thus signal recovery is possible [101].

We have performed similar runs for a lens with $NA_{lens} = 0.09$ and $NA_{lens} = 0.50$, resulting in, respectively, thinner rings at the expense of more power loss, and in no rings at all, i.e. an overall fill with less power loss. Further, at $\lambda = 1300\,\mathrm{nm}$, there exists less coupling as fewer modes propagate and therefore there exists a clear hole in the intensity pattern for $r_0 = 10\,\mathrm{\mu m}$.

We conclude that the number of independent channels in an MGDM link with MSSF is higher than a link without. Since the choice of the lens determines the thickness of the annular rings, the number of channels might still be increased somewhat, although this will inevitably introduce more loss of power.

6.4   Refractive-index profile defects

A statistical analysis of defects in the refractive index power-law profile for the MMF was first investigated by Webster [114] and was later expanded upon by the IEEE 802.3aq committee [40]. The analysis is exclusively concerned with MMFs that are operated at $\lambda = 1300\,\mathrm{nm}$ and have a core radius of $a = 31.25\,\mathrm{\mu m}$. At the pertaining wavelength, the unperturbed refractive index $n(\rho)$ has a numerical aperture of $NA = 0.28$ and a power-law exponent of $g = 1.97$. The set consists of 108 fibres with one or more defects, which are considered to represent the 5% of "worst case" fibres that are likely to be installed. The following defects are included in this set

- different values for the power-law exponent g in the regions $0 < \rho < 0.5$ and $0.5 < \rho < 1$, varying between 1.89 and 2.05. The continuity of the refractive profile n_{res} is retained by defining it as follows (see also Eq. (2.1))

$$n_{res}(\rho) = \begin{cases} n_1(\rho) = n_{co}\sqrt{1 - 2\Delta_1\rho^{g_1}} & \text{for } 0 \leq \rho < 0.5, \\ n_2(\rho) = n_{h}\sqrt{1 - 2\Delta_2\rho^{g_2}} & \text{for } 0.5 \leq \rho < 1, \end{cases} \qquad (6.14)$$

where $\Delta_1 = \Delta$, given by Eq. (2.2) and $\Delta_2 = (n_h^2 - n_{cl}^2)/(2n_h^2)$ with

$$n_h^2 = \left\{[n_1(0.5)]^2 - (0.5)^{g_2}\, n_{cl}^2\right\} / \left[1 - (0.5)^{g_2}\right]. \qquad (6.15)$$

Conversion to the permittivity profile is achieved by $\varepsilon_r(\rho) = n_{res}^2(\rho)$;

- an on-axis dip or peak. To the unperturbed refractive index $n_{unp}(\rho)$ a contribution $n_{axis}(\rho)$ is added, which accounts for the perturbation at the axis, i.e.

$$n_{axis}(\rho) = A \exp\left[-4\ln(2)\rho^2/\rho_{FWHM}^2\right], \qquad (6.16)$$

where the subscript FWHM denotes the full width at half maximum of the pertaining dip or peak and $\rho_{FWHM} = FWHM/a$. In the standard, one has chosen $A = -0.004$

for a dip and $A = 0.002$ for a peak. Further, FWHM $= 3 \, \mu\text{m}$. Consequently, the permittivity profile is given by $\varepsilon_r(\rho) = [n(\rho) + n_{\text{axis}}(\rho)]^2$;

- an exponential, instead of an abrupt, core/cladding transition for $\rho > \rho_e = 0.896$. The thus constructed refractive index profile is given by

$$n_{\text{exp}}(\rho) = \begin{cases} n(\rho) & \text{for } \rho < \rho_e, \\ n_{\text{cl}} + [n(\rho_e) - n_{\text{cl}}] \exp\left[-b\left(\rho - \rho_e\right)\right] & \text{for } \rho \geq \rho_e, \end{cases} \qquad (6.17)$$

where $b = 9.5178 \text{m}^{-1}$. The corresponding permittivity profile reads $\varepsilon_r(\rho) = n_{\text{exp}}^2(\rho)$;

- a kink perturbation at $\rho = \rho_k$. The kink is defined as an additive perturbation to the refractive-index difference Δ according to

$$\delta\Delta = a_k \left[\exp\left(-b_k|\rho - \rho_k|\right) - \exp\left(-b_k|1 - \rho_k|\right)\right]\Delta, \qquad (6.18)$$

where $a_k = 0.03$ and $b_k = 3.2$. This results in the following addition to permittivity profile $\varepsilon_r(\rho)$

$$\delta\varepsilon_r(\rho) = 2\Delta n_{\text{co}}^2 a_k \left[\exp\left(-b_k|\rho - \rho_k|\right) - \exp\left(-b_k|1 - \rho_k|\right)\right]. \qquad (6.19)$$

The set of 108 near-ideal power-law profiles is representative for the imperfections found in installed-base MMFs. Based on these profiles, a statistical assessment can be given of important fibre quantities, like DMD. We have selected the most pronounced profiles occurring in the set to compute their intensity patterns. The fibres are specified via the parameters in Table 6.1. The permittivity profiles of fibre no. 26, fibre no. 78,

Table 6.1: *Specifications of several fibres out of the "108 fiber model".*

Fibre no.	g_1	g_2	On axis	Kink at ρ_k
26	1.89	2.05	Dip	0.864
30	1.89	2.05	Peak	0.672
74	2.05	1.89	Dip	0.480
78	2.05	1.89	Peak	0.544

and the unperturbed fibre are plotted in Figure 6.11(a). The difference in the refractive index between the unperturbed fibre and the perturbed ones is plotted in (b).

The MMF is excited by an SMF pigtail at the prescribed wavelength of $\lambda = 1300 \, \text{nm}$ at three radial offsets, i.e. $r_0 = 0 \, \mu\text{m}$, $13 \, \mu\text{m}$ and $26 \, \mu\text{m}$, respectively. In Figure 6.12(a), the intensity patterns of the various fibres are shown for $z = 75 \, \text{m}$. Since an exponential core/cladding transition only affects the intensity pattern if we excite the MMF at a radial
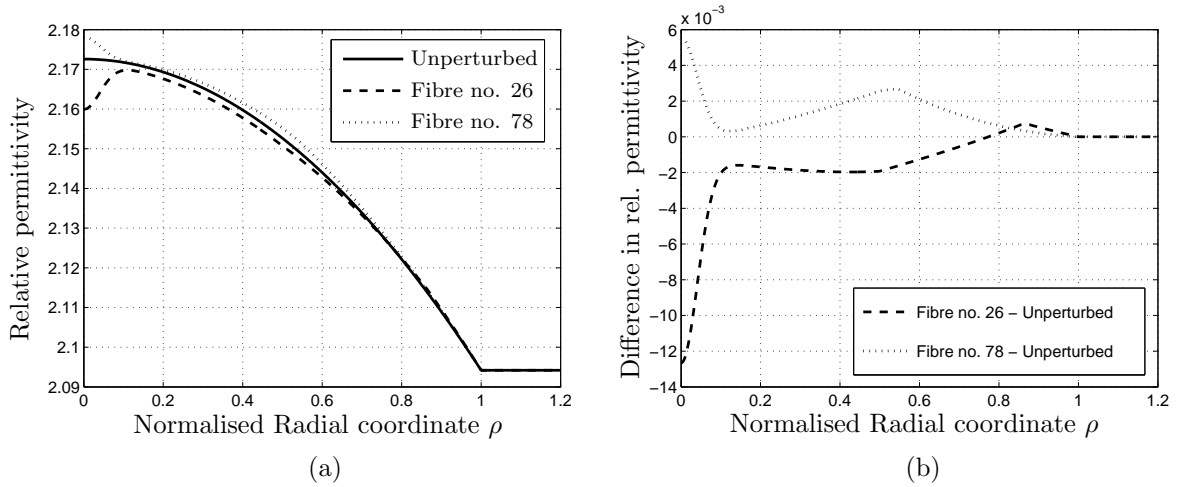
(a)   (b)

Figure 6.11: *(a) Relative permittivity profiles for the unperturbed fibre with g = 1.97, fibre no. 26 and fibre no. 78. (b) Absolute difference in the relative permittivity profiles between the perturbed fibres and the unperturbed one.*
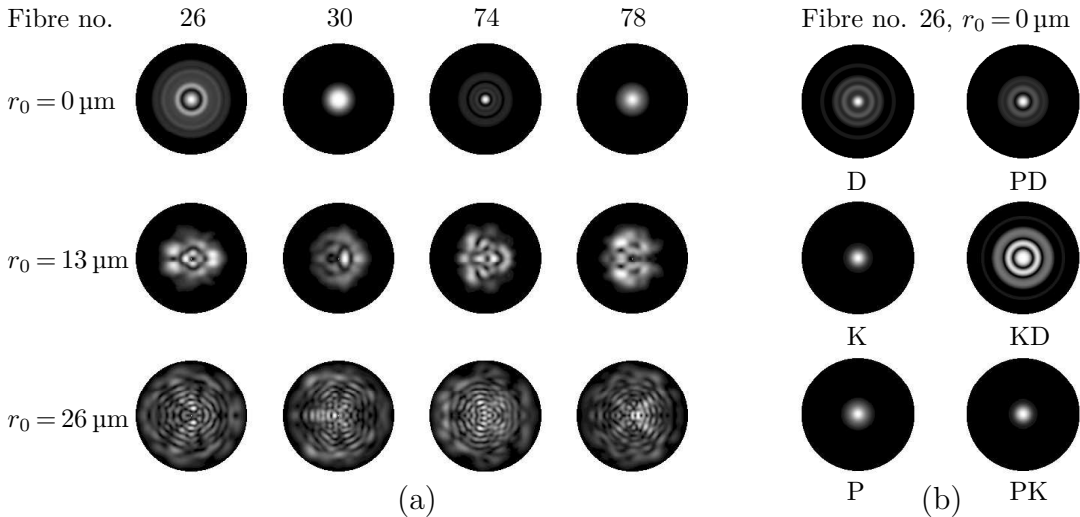

(a)   (b)

Figure 6.12: *Intensity patterns at z = 75 m (a) for the fibres in Table 6.1, (b) for fibre no. 26 at $r_0 = 0\,\mu m$ with the inclusion of a dip (D), a kink (K), and/or different g-values (P).*

offset of $r_0 > 28\mu m$ [6, 114], we have not included this case in our selection of fibres in Table 6.1. Although intra-group mode coupling and DMA could influence the patterns at this distance, as discussed in Section 6.2, we have switched these features off for the sake of clarity. The presence of mode coupling would introduce an additional blur to the patterns.

For $r_0 = 0\,\mu m$, fibre no. 26 immediately attracts our attention as power spreads outwards. For fibre no. 74, we see several ripples appear, although they are not as pronounced as the ones for fibre no. 26. On the basis of fibre no. 26, we specify the impact of each of the aforementioned profile defects separately. The results are shown in Figure 6.12(b).

The capitals D, K and P, corresponds to the inclusion of a dip, a kink, and/or a change of g at $\rho = 0.5$, respectively. Apparently, a dip in the refractive-index profile, possibly in combination with a kink or a change of g, introduces an unwanted spread of power. A kink, a change of g or a combination of them are not as severe. For fibre no. 74, we have performed the same analysis and have arrived at the same conclusions. However, already a minor change in the propagated distance z causes fibre no. 74 to have more pronounced ripples in its intensity profile than the ones in fibre no. 26. This confirms our observation that a dip at the fibre axis is the worst profile defect among the ones investigated.

Chapter 7

Conclusions and recommendations

In view of the broad range of applications in which the optical fibre can be employed, and the ever-increasing demands to improve current day's commercially available fibres, simulations have become an indispensable part in the design process. On the basis of an optical fibre model, including radial inhomogeneity, we have implemented a robust and modular vectorial numerical scheme to perform these simulations. This scheme uses the Marcuvitz-Schwinger equations as its keystone and consists of a coupled system of four differential equations. Since the numerical integration of the scheme is limited in the radial direction, we have tweaked its performance to tackle multi-mode fibres with large core radii, or equivalently operation at short wavelengths, by introducing extended precision arithmetic. Obviously, this extension should be used with care as the computation time, which depends on the used compiler and computer, may increase drastically.

The thus implemented numerical scheme enables us to compute a set of important fibre quantities that characterise the optical fibre. For the single-mode fibre, we can compute the quantities dispersion, dispersion slope, mode-field diameter, effective area, bending loss, effective and theoretical cut-off wavelength and MAC-value, whereas for the multi-mode fibre, we have focused on differential mode delay, differential mode attenuation and (intra-group) mode coupling. The inclusion of polarisation-mode dispersion is still a recommended improvement, especially since it is regarded as an effect that should receive extra attention in the coming years according to the International Telecommunication Union [42]. To model polarisation-mode dispersion, a coupled system of two stochastic differential equations must be solved, which is a non-trivial task. However, one may define a perturbation to the effective modal dielectric matrix, which links the dopant profile to the polarisation-mode dispersion. Then, one must set manufacturing tolerances for the maximum deviations in the fibre geometry, which, via the perturbation to the effective modal dielectric matrix leads to an estimate for the expected differential group delay [7].

The scalar equivalent of our vectorial full-wave scheme, which is referred to as the

weak-guidance approximation, has been implemented as well. A comparison between both schemes showed that the computation time decreases at the expense of accuracy when the approximation is used. For weakly guiding single-mode fibres, the loss of accuracy in the fibre quantities is marginal. However, for an increasing refractive-index difference, the accuracy becomes a non-negligible issue. As computation times merely differ by a factor of 1.5, we prefer exact computations over approximate ones, even in an optimisation scheme.

We have performed a vectorial full-wave analysis of a single-mode bent fibre to compute the macrobending loss. To introduce the bottleneck in this bending problem, viz. the computation of a product of Bessel functions of large complex order and argument to a high accuracy, we have first analysed the bent slab configuration, its two dimensional equivalent. Due to a triple integral involving these Bessel functions in the 3-D case, computations times are excessive and a full-wave analysis is therefore inappropriate in an optimisation scheme. On the basis of a step-index and parabolic-index profile, we have determined the best of many approximate modelling techniques that estimate the bending loss rapidly, and have used the full-wave analysis as a reference [86]. It is shown that the approximation of Faustini and Martini gives good bending loss results for radii of curvature $R > 8\,\mathrm{mm}$ for these two profiles. We have extended this approximation to compute the bending loss of the higher-order modes to determine the effective cut-off wavelength and as a result the MAC-value. Computations have been compared with measurements and the results are in good agreement.

The extension to higher-order modes may form the first step towards computing the bending losses in a multi-mode fibre. Owing to its larger refractive-index contrast, the bending losses for a multi-mode fibre are less significant than the ones for a single-mode fibre. Still, the higher-order modes loose their power already for the slightest bends or imperfections in the fibre. This will put, for example, a limit on a mode group diversity multiplexing link, which may use the higher-order modes to create an independent channel. Moreover, in extreme bends that may occur during the in-building installation process, mode coupling must be taken into account in the model as well. Reliable modelling techniques for simulating bending effects in multi-mode fibres are not yet available in the literature.

To aid in the design of single-mode optical fibres, we have implemented and performed a numerical optimisation of the refractive-index profile. The fibre quantities have been used to set a design goal in terms of a cost function. The refractive-index profile, or more specifically one of its dopant building blocks, viz. the Germanium concentration profile, has been discretised in continuous piecewise-linear segments, whose endpoints serve as the free parameters in the optimisation scheme. We have employed two statistically oriented optimisers, viz. differential evolution and simulated annealing, and two gradient based

ones, namely a modified-Newton and a quasi-Newton algorithm. We have discussed their effectiveness in finding the global minimum of a cost function. While the latter algorithms are fast (minutes), and therefore preferable in a design tool, in particular the quasi-Newton scheme, they frequently end up in a local minimum, depending on the initial profile guess. The statistically oriented optimisers, on the other hand, find the global minimum at the expense of sometimes excessive computation times (days to months).

A hybrid method that determines the right "valley" with a stochastic optimisation scheme, and the minimum of the pertaining "valley" with a gradient-based scheme, may be an effective alternative. For acceptable computation times, this implies that one should accelerate the computation of a single cost function evaluation by a factor of 80. A finite-element method under the condition of weak guidance with basis functions that are defined over a whole or finite support of the unknown field, e.g. Laguerre-Gauss functions, may give solace as long as the approximation does not alter the location of the valleys too much.

Further, we have performed a sensitivity analysis of the optimised profiles to verify whether the attained minima are really the lowest points in the landscape and to provide the manufacturer with information on how accurate the profile has to be made. We have demonstrated that there still appears to be room for improvement in the design of the refractive index profile of commercially available fibres.

Since, in practice, it is more convenient to fabricate quadratic profiles, one may consider this profile shape instead of the piecewise-linear segment profile which has been implemented now. It is already possible to change the Flour concentration, albeit piecewise constant, to establish more degrees of freedom.

For the multi-mode fibre, we have investigated the effects of differential mode delay, differential mode attenuation and mode coupling on short (in-house) multi-mode fibre links. Once the power-law exponent g in the multi-mode power-law fibre had been optimised to minimise its differential mode delay, we have used this fibre in a mode group diversity multiplexing link. This is a multiplexing technique that creates multiple independent channels by exciting mode groups in the fibre with singe-mode fibre pigtails at different radial offsets and/or angular tilts. The intensity patterns, primarily created by constructive and destructive interference among the propagating modes, have been generated for distances up to a kilometre. The inclusion of differential mode attenuation and mode coupling to our model via an empirical formula and a set of coupled power equations, respectively, reduces the differences between experiments and simulations.

The maximum possible number of independent transmission channels is determined from the transmission matrix, which relates the input signals to the signals retrieved at the fibre's end. The condition number of this matrix is a measure for robustness of the link.

A 3×3 mode group diversity multiplexing link has been established through an excitation with radial offsets only and a photodetector with proper defined annular regions at the receiver end. Further, we have shown that a link with five independent channels is possible if we employ the mode-selective spatial filtering technique. Also here measurements have been set against simulations and are in good agreement.

Additionally, we have shown the influence of possible manufacturing defects in the fibre's refractive-index profile by analysing the most pronounced fibres in the set of the "108-fiber model". It turns out that an on-axis dip in the refractive-index profile, possibly in combination with a kink or a change of the power-law index, introduces an unwanted spread of power for a central launch at the fibre's end. A kink, a change of the power-law index or a combination of them are not as severe.

The multi-mode fibre effects are thus far only simulated for silica-based fibres. Since the (graded-index) polymer optical fibre is gaining ground rapidly, as difficulties regarding its attenuation proved bridgeable, simulations for this type of fibre become increasingly important. Moreover, the possibility to construct arbitrary profiles is being improved as we speak, which may make profile optimisation a desirable feature in the future. Owing to its large core diameter this type of fibre is even more flexible than the silica-based multi-mode fibre, and thus installation costs are reduced. On the other hand, thousands of modes will propagate along the fibre, and hence, mode coupling becomes a significant factor, which limits its application to short-range networks. Obviously, this poses new challenges to the employed model and the solution procedure to obtain the propagation characteristics. The ray approach may prove a suitable procedure [90].

Appendix A

List of abbreviations

BB	BendBright
BDF	Backward differentiation formula
CF	Cost function
CF_e	End value of cost function
CF_s	Start value of cost function
CSF	Conventional single-mode fibre
DCF	Dispersion compensating fibre
DE	Differential evolution
DMA	Differential mode attenuation
DMD	Differential mode delay
DMG	Degenerate mode group
DSF	Dispersion-shifted fibre
ESI	Equivalent step-index
ESMF	Enhanced single-mode fibre
FWHM	Full width at half maximum
GI-MMF	Graded-index multi-mode fibre
ITU	International telecommunication union
LAN	Local area network
LPS	Linear path segment
MFD	Mode-field diameter
MGDM	Mode group diversity multiplexing
MIMO	Multiple-input multiple-output
MMF	Multi-mode fibre
MN	Modified Newton
MSSF	Mode-selective spatial filtering

NA	Numerical aperture
OC	Optical cross talk
PCVD	Plasma-activated chemical vapour deposition
PMD	Polarisation mode dispersion
PMG	Principle mode group
POF	Polymer optical fibre
QN	Quasi Newton
SA	Simulated annealing
SDP	Steepest-descent path
SMF	Single-mode fibre
TE	Transverse electric
TM	Transverse magnetic
TEM	Transverse electromagnetic
VFW	Vectorial full-wave
WGA	Weak-guidance approximation

Appendix B

The Marcuvitz-Schwinger equations in an orthogonal coordinate system

The aim of this appendix is to give the Maxwell equations of Eq. (2.6) in terms of the well-known scale factors h_i [3], without utilising tensor notation. Although this approach might be more familiar, it is only valid for orthogonal coordinate systems. In an orthogonal coordinate system, the metric g_{ij} of Eq. (2.9) diagonalises. Its elements are given in terms of the scale factors by $g_{ii} = h_i^2$, where $i \in \{1, 2, 3\}$. These scale factors are related to the differential arc length $d\mathbf{r}$ through an inner product

$$\langle d\mathbf{r}, d\mathbf{r} \rangle = h_1^2 dx_1^2 + h_2^2 dx_2^2 + h_3^2 dx_3^2, \tag{B.1}$$

where $\{x_1, x_2, x_3\}$ denote curvilinear coordinates and dx_i is an infinitesimal scalar displacement along the directions $\mathbf{u}_i(\mathbf{r}(x_i))$, which form a right-handed set of unit vectors normal to the surfaces of constant x_i.

Although all differential vector operators may be expressed in terms of the scale factors, we are particularly interested, in view of Eq. (2.6), in the curl of a vector field $\mathbf{v}$, i.e.

$$\nabla \times \mathbf{v} = \nabla \times (v_i \mathbf{u}_i) = \mathcal{H}^{-1} \epsilon_{ijk} h_i \partial_{x_j} (h_k v_k) \mathbf{u}_i, \tag{B.2}$$

where lowercase Roman subscripts take the values $1, 2, 3$, ϵ_{ijk} denotes the Levi-Civita symbol and $\mathcal{H} = h_1 h_2 h_3$. Consequently, Maxwell's equations can be written as

$$\mathcal{H}^{-1} \epsilon_{ijk} h_i \partial_{x_j} (h_k E_k) + j\omega\mu H_i = -K_i, \tag{B.3a}$$

$$-\mathcal{H}^{-1} \epsilon_{\ell mn} h_\ell \partial_{x_m} (h_n H_n) + j\omega\varepsilon E_\ell = -J_\ell. \tag{B.3b}$$

To express the transverse electric field components in terms of the magnetic ones, we wish to eliminate the longitudinal component of the electric field in Eq. (B.3a). We regard $\mathbf{u}_3$ as the longitudinal direction. Consequently, it follows from Eq. (B.3b) that

$$E_3 = (j\omega\varepsilon)^{-1} \left[\mathcal{H}^{-1} \epsilon_{3\mu\nu} h_3 \partial_{x_\mu} (h_\nu H_\nu) - J_3 \right], \tag{B.4}$$

where Greek subscripts take the values $1, 2$. Upon substituting Eq. (B.4) in Eq. (B.3a), and after some rearranging, we arrive at the following differential equation for the transverse field components

$$-\partial_{x_3}(h_\kappa E_\kappa) = j\omega\mu \left[h_\sigma^{-2}\mathcal{H}\epsilon_{\kappa\sigma3} + k^{-2}\varepsilon\partial_{x_\kappa}\left(h_3^2\mathcal{H}^{-1}\varepsilon^{-1}\partial_{x_\mu}\epsilon_{\mu\sigma3} \right) \right](h_\sigma H_\sigma) + \epsilon_{\kappa\sigma3}K_\sigma^{\mathrm{eff}}, \quad \text{(B.5)}$$

where

$$K_\sigma^{\mathrm{eff}} = h_\sigma^{-1}\mathcal{H}K_\sigma + (j\omega)^{-1}\epsilon_{\kappa\sigma3}\partial_{x_\kappa}\left(\varepsilon^{-1}h_3 J_3 \right). \quad \text{(B.6)}$$

Invoking duality, we may replace $\{E_k, H_k, \varepsilon, \mu, J_k, K_k\}$ by $\{H_k, -E_k, \mu, \varepsilon, K_k, -J_k\}$, which leads to

$$-\partial_{x_3}(h_\lambda H_\lambda) = j\omega\varepsilon \left[h_\tau^{-2}\mathcal{H}\epsilon_{\lambda3\tau} + k^{-2}\mu\partial_{x_\lambda}\left(h_3^2\mathcal{H}^{-1}\mu^{-1}\partial_{x_\nu}\epsilon_{\nu3\tau} \right) \right](h_\tau E_\tau) + \epsilon_{\lambda3\tau}J_\tau^{\mathrm{eff}}, \quad \text{(B.7)}$$

where

$$J_\tau^{\mathrm{eff}} = h_\tau^{-1}\mathcal{H}J_\tau - (j\omega)^{-1}\epsilon_{\lambda\tau3}\partial_{x_\lambda}\left[\mu^{-1}h_3 K_3 \right]. \quad \text{(B.8)}$$

In matrix form, we see that we have obtained the Marcuvitz-Schwinger equations of Eq. (2.18) for an orthogonal coordinate system

$$-\partial_{x_3}\begin{pmatrix} h_\kappa E_\kappa \\ h_\lambda H_\lambda \end{pmatrix} = \begin{pmatrix} 0 & j\omega\mu\left[\mathcal{U}_\kappa + \mathcal{T}_{\kappa\mu}\left(\varepsilon\right)\right] \\ j\omega\varepsilon\left[\mathcal{U}_\lambda + \mathcal{T}_{\lambda\nu}\left(\mu\right)\right] & 0 \end{pmatrix}\begin{pmatrix} h_\tau E_\tau \\ h_\sigma H_\sigma \end{pmatrix}$$
$$+ \begin{pmatrix} \epsilon^{\kappa\sigma3}K_\sigma^{\mathrm{eff}} \\ \epsilon^{\lambda3\tau}J_\tau^{\mathrm{eff}} \end{pmatrix}, \quad \text{(B.9)}$$

where

$$\mathcal{U}_\kappa = h_\sigma^{-2}\mathcal{H}\epsilon_{\kappa\sigma3}, \quad \text{and} \quad \mathcal{T}_{\kappa\mu}(x) = k^{-2}x\partial_{x_\kappa}h_3^2\mathcal{H}^{-1}x^{-1}\partial_{x_\mu}\epsilon_{\mu\sigma3}. \quad \text{(B.10)}$$

The longitudinal components E_3 and H_3 are, with reference to Eq. (B.4), given by

$$E_3 = (j\omega\varepsilon)^{-1}\left[\mathcal{H}^{-1}\epsilon_{3\mu\nu}h_3\partial_{x_\mu}\left(h_\nu H_\nu \right) - J_3 \right],$$
$$H_3 = (j\omega\mu)^{-1}\left[\mathcal{H}^{-1}\epsilon_{\mu3\nu}h_3\partial_{x_\mu}\left(h_\nu E_\nu \right) - K_3 \right]. \quad \text{(B.11)}$$

Appendix C

Bessel functions with large complex order and argument

In this appendix, we discuss the numerical computation of Bessel functions with large complex order and argument [87]. For common ranges of order and argument, it is well known how to evaluate the Bessel functions numerically, and many routines are available to perform the actual computation. However, the available (double precision) routines fail when it comes to computing a product of Bessel functions with large complex order and argument, especially when a high relative precision (10^{-11}) is required [99, 111, 117]. With radiation problems in mind, we have developed a method and a computer code in which a high accuracy can be attained, even up to machine precision, for orders, ν, that vary over the entire range of $1 < \mathrm{Re}(\nu) < 10^6$.

Since asymptotic expansion techniques cannot be guaranteed to provide sufficient accuracy over the total range of ν [77], we take standard integral representations of the Bessel functions as our starting point [1, 98]

$$\mathrm{J}_\nu(x) = \frac{1}{2\pi j} \int\limits_{-\infty-\pi j}^{-\infty+\pi j} e^{-x\sinh t + \nu t} dt,$$

$$\mathrm{H}_\nu^{(1)}(x) = \frac{1}{\pi j} \int\limits_{-\infty-\pi j}^{\infty} e^{-x\sinh t + \nu t} dt; \quad \mathrm{H}_\nu^{(2)}(x) = \frac{1}{\pi j} \int\limits_{\infty}^{-\infty+\pi j} e^{-x\sinh t + \nu t} dt,$$

(C.1)

where $\{\nu, x\} \in \mathbb{C}$ and $|\arg(x)| < \pi/2$. This region of validity can be extended via analytic continuation. Note that modified Bessel functions are covered as well, as the argument of the Bessel function may be complex, i.e. [1]

$$\mathrm{I}_\nu(\xi) = e^{-\frac{1}{2}\nu\pi j} \mathrm{J}_\nu\left(\xi e^{\frac{1}{2}\pi j}\right) \qquad \text{for} \quad -\pi < \arg(\xi) \leq \pi/2,$$

$$\mathrm{K}_\nu(\xi) = \frac{\pi j}{2} e^{\frac{1}{2}\nu\pi j} \mathrm{H}_\nu^{(1)}\left(\xi e^{\frac{1}{2}\pi j}\right) \quad \text{for} \quad -\pi < \arg(\xi) \leq \pi/2.$$

(C.2)

Since the integral representations have the same integrand, we will only consider $J_\nu(x)$ for the moment, to perform some mathematical manipulations.

Since both $|\nu|$ and $|x|$ can be large, we introduce the variable $x = \nu z$, which renders a more suitable exponent in the integrand, i.e. $\exp[w(t)]$, where $w(t) = -\nu(z \sinh t - t)$. Since the integration is performed in the complex t-plane, we adopt $t = \sigma + j\tau$, where $\{\sigma, \tau\} \in \mathbb{R}$. In general, the integrand is a highly oscillating function for large complex orders, and consequently numerical integration becomes slow. To avoid this oscillatory behaviour, we deform the current integration path into the steepest-descent path (SDP).

C.1   Steepest-descent paths

It is well-known that along an SDP, which passes through a saddle-point, the integrand decays most rapidly and the exponential function no longer oscillates. The locations of the saddle points $t_0^\pm$, which follow from $w'(t_0^\pm) = 0$, are given by

$$t_0^\pm = \ln\left(\frac{1 \pm \sqrt{1 - z^2}}{z}\right) + 2n\pi j, \tag{C.3}$$

where $n \in \mathbb{Z}$. We consider the principal branches, i.e. $-\pi < \mathrm{Im}(t_0^\pm) \le \pi$. The SDPs in the complex t-plane follow from the root locus of

$$w(t) - w(t_0^\pm) = -s^2, \quad \text{with} \quad s \ge 0, \tag{C.4}$$

and consequently, the asymptotes, obtained by letting $s \to \infty$, are given by

$$\tau = -\arg(x) \quad \text{for} \quad \sigma \to \infty, \tag{C.5a}$$

$$\tau = \arg(x) \pm \pi \quad \text{for} \quad \sigma \to -\infty. \tag{C.5b}$$

For ν and x complex, no analytical solutions to Eq. (C.4) exist (except for specific combinations of imaginary and real orders and arguments, e.g. [28]). Hence, we have to search for the SDPs numerically. To give an impression of their location in the complex plane, we have sketched some typical steepest ascent and descent paths in Figure C.1 that are frequently encountered in problems involving small losses. For the various kinds of Bessel functions in Eq. (C.1), the limits of the integrals determine the appropriate asymptotes.

A transition stage, like the one depicted in Figure C.1(b), is important for our numerical integration scheme, as it clearly demarcates parameter regions associated with integration along fundamentally different SDPs. Watson [113] derives an expression for this transition stage. However, upon close observation, the integrands along his "SDPs", although decaying exponentially, still oscillate for $x \in \mathbb{C}$. To arrive at non-oscillatory integrands, we have to take the corresponding phase term of x into account as well, as
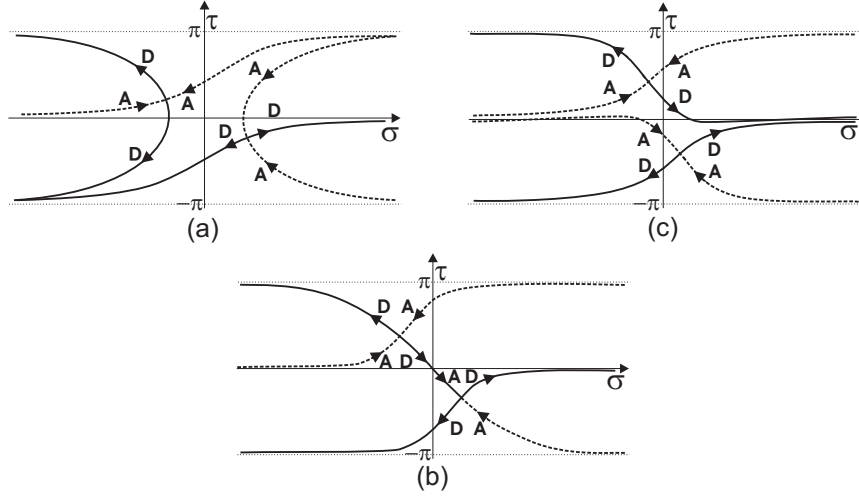
Figure C.1: *Impression of the steepest ascent (A) and descent (D) paths in the complex t-plane for Bessel functions with complex order and argument for a case in which Im(ν) < 0, Re(ν) > 0, Im(ν) < Re(ν) and x ∈ ℝ⁺. Upon increasing x, we obtain the plots (a) → (c), where stage (b) is defined by γ = 0 (see Eq. (C.6)).*

remarked by Felsen [23]. Upon defining the saddle-points as $t_0^\pm = \pm(\alpha + j\beta)$, such that $0 < \beta \leq \pi$, the condition of the transition stage for the SDPs becomes unique and reads $\gamma = 0$, with

$$\begin{aligned} \gamma = &\mathrm{Im}(x) \left[(\sinh\alpha - \alpha\cosh\alpha)\cos\beta + \beta\sinh\alpha\sin\beta \right] + \\ &\mathrm{Re}(x) \left[(\cosh\alpha - \alpha\sinh\alpha)\sin\beta - \beta\cosh\alpha\cos\beta \right]. \end{aligned} \tag{C.6}$$

The condition $\gamma = 0$ amounts to $w(t_0^\pm) \in \mathbb{R}$ in Eq. C.4. To gain more insight in, and to show the importance of the variable γ, we have plotted the contours $\gamma = 0$ in Figure C.2 for three successive cases regarding the argument of $x = |x|\exp(j\phi)$, viz. $\phi = \{0, \pi/4, \pi/2\}$. The shaded areas represent those areas for which $\gamma > 0$. A counter-clockwise rotation occurs for a decreasing phase term. Not only the saddle-points are opposites, the SDPs in opposite regions are symmetric with respect to the origin of the complex t-plane as well. Hence, it suffices to compute the Bessel functions in those regions for which $0 < \beta \leq \pi$.

The transition encountered in Figure C.1 corresponds to the case $\mathrm{Im}(x) = 0$ in Figure C.2. In particular, Figure C.1(a) corresponds to a value of γ in region III, and C.1(c) denotes a value of γ in region II. Further, we infer from Figure C.1(a) that in region III the SDPs that approach the proper asymptotes are associated with $J_\nu(x)$ and $H_\nu^{(1)}(x)$, whereas the SDP for $H_\nu^{(2)}(x)$ is a composition of the former two. In region II, on the other hand, the topology of the SDPs indicate that the integral representations for $H_\nu^{(1)}(x)$ and $H_\nu^{(2)}(x)$ should be used to calculate $J_\nu(x)$ through addition. In Table C.1, we have denoted for all regions, which combination of Bessel functions is readily evaluated. Note that since the SDPs in opposite regions are similar, the same combinations of paths must be used.
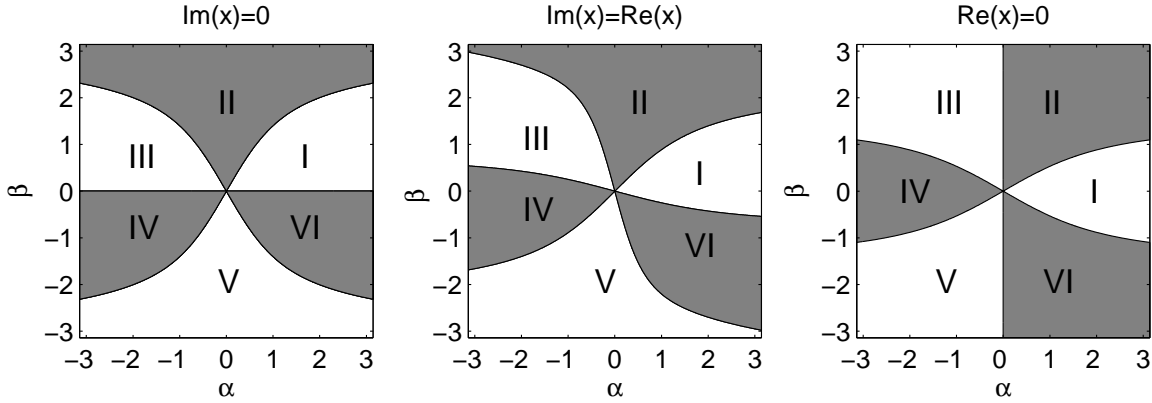
Figure C.2: *Contour plots of Eq. (C.6) for different arguments of $x = |x| \exp(j\phi)$, i.e. from left to right $\phi = \{0, \pi/4, \pi/2\}$. Shaded areas correspond to $\gamma > 0$ and unshaded ones to $\gamma < 0$ under the condition that that α is chosen for which $0 < \beta \leq \pi$.*

Table C.1: *The Bessel functions $J_\nu(x)$, $H_\nu^{(1)}(x)$, or $H_\nu^{(2)}(x)$ that are computed in each region. A combination of the two renders the third one.*

Region	I	II	III	IV	V	VI
	J_ν, $H_\nu^{(2)}$	$H_\nu^{(1)}$, $H_\nu^{(2)}$	J_ν, $H_\nu^{(1)}$	J_ν, $H_\nu^{(2)}$	$H_\nu^{(1)}$, $H_\nu^{(2)}$	J_ν, $H_\nu^{(1)}$

We have employed a Van Wijngaarden–Dekker–Brent root-finding scheme [78] to obtain the location of the SDP via Eq. (C.4), while the numerical integration was performed through an adaptive $30 - 61$ point Gauss-Kronrod rule, which can be set to a required accuracy [65]. We would like to integrate with respect to τ, since this would amount to an integral over a domain of bounded support [29]. However, if the path of integration becomes locally horizontal, like the upper SDP in Figure C.1(c), the integration variable needs to be changed to avoid singularities. This complicates the search considerably and therefore leads to an increase in the time required to evaluate the integral.

To avoid overflow and underflow, we scale the Bessel functions with respect to the value of the integrand at the saddle point [30]. For the products of Bessel functions under consideration, both saddle points are involved. If both have the same order and argument, the saddle points are opposites and the scaling factors cancel. Otherwise, the different orders as well as the arguments have to be commensurate to guarantee stability.

After some extensive testing, it turned out that integration along well-chosen piecewise-linear path segments (LPSs) is not only much easier but also much faster. The exception forms the SDP for $J_\nu(x)$ in Figure C.1(a), which for real order and argument can be derived analytically [29]. For complex argument, the asymptotes of the SDP for $J_\nu(x)$

are shifted by $\arg(x)$ (see Eq. (C.5b)). However, the shape of the SDP does not change significantly. Therefore, a simple translation of the analytical SDP through the pertaining saddle point suffices to attain accurate results.

C.2 Piecewise-linear path segments

Especially for large orders and arguments, the integrand oscillates rapidly if we stray too far away from the SDPs. However, if we choose piecewise-linear integration paths, through the saddle-points and tangent to the descent paths, the residual oscillations pose no difficulties whatsoever. The application of a Taylor expansion about the saddle point up to second order yields an expression for the angle θ between a line parallel to the real axis and the tangents of the paths crossing in the saddle point, i.e.

$$\theta_n = -\arg(\nu)/2 - \arg\left(1 - z^2\right)/4 + n\pi/2, \tag{C.7}$$

where $n \in \{0, 1, 2, 3\}$ and $\arg(\nu)$ denotes the argument of ν. Note that the crossing of the paths in the saddle point are perpendicular, since the saddle points under consideration are isolated ones for $\nu \neq x$. In Figure C.3, we have plotted the employed LPSs for the situations in Figure C.1, and have indicated the angle $\theta = \theta_0$ in Figure C.3(b), explicitly. If a LPS passes through the saddle point at the angle θ, the integrand will hardly oscillate
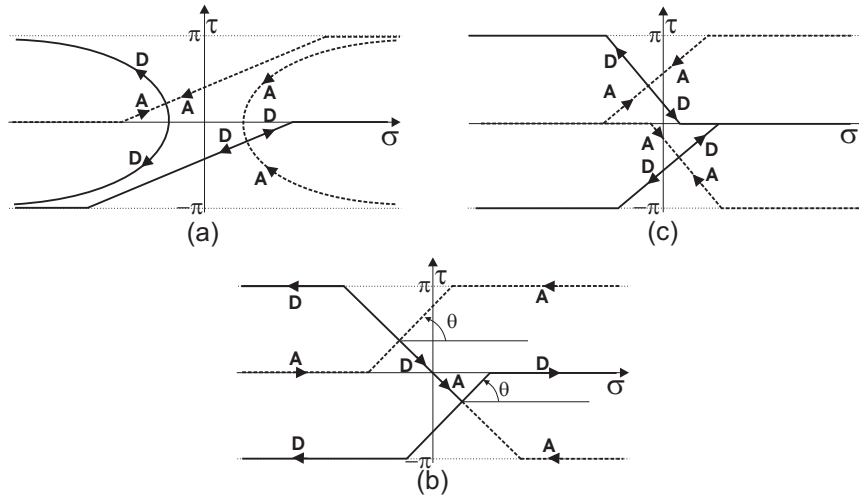

Figure C.3: *Replacement of the SDPs in Figure C.1 by LPSs.*

in the vicinity of the saddle point. Moreover, for large orders, decay along an SDP is exceptionally fast and therefore oscillations that might occur at a greater distance are negligible. We connect this segment to other segments that run towards infinity along the appropriate asymptotes defined in Eq. (C.5).

C.3   Numerical results

We have developed a numerical code to compute results for a product of (modified) Bessel functions. The modified Bessel functions are directly related to the Bessel functions by Eq. (C.2). We are not aware of a single mathematical package which can be used as a reference to validate our results over the entire range of complex orders $1 < \mathrm{Re}(\nu) < 10^6$ and arguments that occur in practice. For validation purposes, we have computed the absolute value of the product $I_\nu(\xi)K_\nu(\xi)$ and settled for a relatively small constant complex order $\nu = 1200 - 10j$. The real part of the complex argument ξ has been varied, with $\mathrm{Im}(\xi) = -800$ fixed. Mathematica$^{\mathrm{TM}}$ [117] has been used to verify our results, as is shown in Figure C.4. In Table C.2, the numerical results for various complex orders and arguments are given.
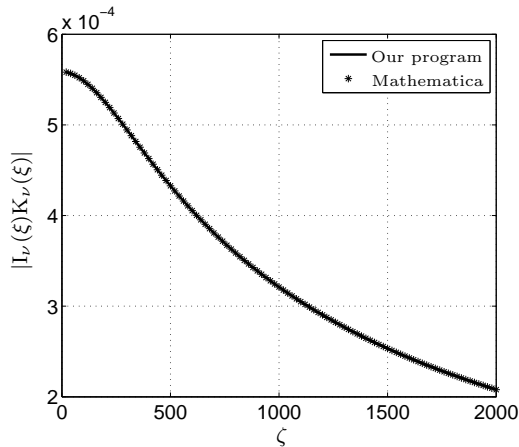

Figure C.4: *Product of the modified Bessel functions* $|I_\nu(\xi)K_\nu(\xi)|$, *where* $\xi = \zeta - 800j$ *and* $\nu = 1200 - 10j$.
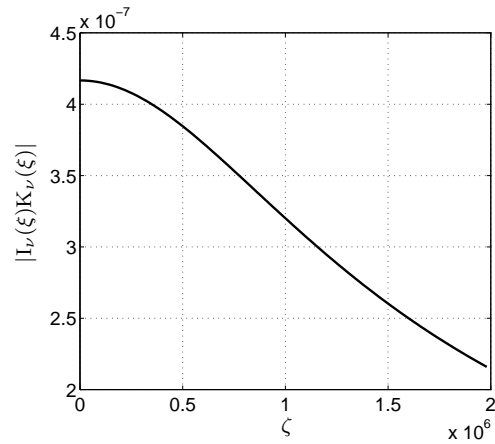
Figure C.5: *Product of the modified Bessel functions* $|I_\nu(\xi)K_\nu(\xi)|$, *where* $\xi = \zeta - 800j$ *and* $\nu = 1.2 \cdot 10^6 - 10j$.

Mathematica$^{\mathrm{TM}}$ failed to produce results for some of the values of ζ in Figure C.4. Oddly enough, we have had to request a "60-digit precision" to obtain results for all values. If we set the real part of the order to $\mathrm{Re}(\nu) = 1.2 \cdot 10^6$, Mathematica$^{\mathrm{TM}}$ aborts due to overflows, while our program still functions properly, as is shown in Figure C.5. The set relative accuracy of 10^{-11} has been checked via the Wronskian relation given in [1], i.e. $I_{\nu+1}(\xi)K_\nu(\xi) + I_\nu(\xi)K_{\nu+1}(\xi) = \xi^{-1}$.

In Table C.2, we have given some typical values that occur in the problem of a bent optical fibre [86] and some values with small complex orders and arguments to show the range of applicability. We have underlined the digits that differ between the obtained results and computed the relative error. Note that all are well within the set relative accuracy of 10^{-11}.

A comparison of computation times between integration along the paths of Figure C.1

Table C.2: *Comparison of the accuracy for the results of a product of modified Bessel functions* $|I_\nu(\xi)K_\nu(\xi)|$ *between Mathematica^{TM} and integration along the paths of Figure C.3.*

ν	ξ	Mathematica^{TM}	Our program	Rel.error
2+j	-6j	1.02079122908986422	1.02079122908986442	2.2E-16
35-j	1-j	1.4279211363517527E-2	1.4279211363517530E-2	2.4E-16
1+35j	1	1.4288396754169612E-2	1.4288396754169647E-2	2.5E-15
$1.2 \cdot 10^3$-10j	10-8j	4.16646605857194E-4	4.16646605857148E-4	1.1E-13
$1.2 \cdot 10^3$-10j	10^5-8j	4.99964004697354E-6	4.99964004696312E-6	2.1E-12
$2 \cdot 10^5$-0.2j	10^3j	2.50003125058470E-6	2.50003125058207E-6	1.1E-12
$1.2 \cdot 10^6$-10j	10-$5 \cdot 10^3$j	4.1667028360457E-7	4.1667028360156E-7	7.2E-12
$1.2 \cdot 10^6$-10j	10^5-$5 \cdot 10^3$j	NAN	4.15230927117101E-7	-

and the paths of Figure C.3 for the same products of Bessel functions of Table C.2 is shown in Table C.3. Further, we have added the computation times of Mathematica^{TM}

Table C.3: *Comparison of computation times between integration along the paths of Figure C.1, the paths of Figure C.3, and by Mathematica^{TM} for a product of modified Bessel functions* $|I_\nu(\xi)K_\nu(\xi)|$ *using a Pentium IV, 2.6 GHz computer.*

ν	ξ	Fig. 1	Fig. 2	Mathematica^{TM}	Region
2+j	-6j	2.9s	0.9ms	15.6ms	I
35-j	1-j	3.5s	1.4ms	15.6ms	III
1+35j	1	3.4s	1.6ms	15.6ms	IV
1200-10j	10-8j	3.4s	2.4ms	15.6ms	III
1200-10j	10^5-8j	7.9s	3.6ms	15.6ms	II
$2 \cdot 10^5$-0.2j	10^3j	6.8s	4.0ms	75s	III
$1.2 \cdot 10^6$-10j	10-5000j	3.5s	4.6ms	1692s	III
$1.2 \cdot 10^6$-10j	10^5-5000j	3.7s	4.6ms	NAN	III

and the region in Figure C.2 to show which combination of Bessel functions in Table C.1 has been used. As the order and argument increase, Mathematica^{TM} becomes much slower and eventually fails, whereas computation times for our routine are only marginally influenced by a change in order or argument. Since a numerical path search is not required, integration along the paths in Figure C.3 is, by as much as three orders of magnitude, faster than integration along the SDPs in Figure C.1. Especially for the fourth and fifth case

in Table C.3, integration along the SDPs takes much longer. This is due to the extensive search to locate the upper SDP numerically, which is needed to compute $J_\nu(\xi)$. Since this path contains a minimum, where the integrand is not negligible yet, the integration variables have to be changed to perform the numerical evaluation.

In the product of Bessel functions, one of the constituents of the product may be recessive, while the other may be dominant. If that recessive constituent were calculated as a linear combination of two dominant solutions, the accuracy of the product would be swamped [30]. The fact that this does not happen indicates that the combinations of Bessel functions in Table C.1 are the right ones.

Appendix D

Wavefields generated by a bundle of phased line sources

The scalar wavefield, ϕ, generated by a phased line source with an $\exp(j\omega t)$ time factor and a longitudinal phase factor $\exp(-jk_0\zeta z)$, satisfies

$$-\left(\partial_x^2 + \partial_y^2 - k_0^2 n_{\mathrm{cl}}^2\right)\phi = \delta(x)\delta(y)\exp(-jk_0\zeta z). \tag{D.1}$$

The substitution $\phi = \exp(-jk_0\zeta z)\, G(x,y)$ leads to the modified Helmholtz equation for a two-dimensional Green's function

$$-\left(\partial_x^2 + \partial_y^2 - \kappa^2\right) G = \delta(x)\delta(y), \tag{D.2}$$

where $\kappa = k_0\sqrt{\zeta^2 - n_{\mathrm{cl}}^2}$. For a source and point of observation, respectively located on concentric circles at $\{x', y'\} = \{\varrho\cos\chi, \varrho\sin\chi\}$ and $\{x, y\} = \{r\cos\theta, r\sin\theta\}$, with $\varrho \leq r$, the solution reads

$$G = \frac{1}{2\pi}K_0(\kappa R) = \frac{1}{2\pi}\sum_{i=-\infty}^{\infty} I_i(\kappa\varrho)K_i(\kappa r)e^{ji(\theta-\chi)}, \tag{D.3}$$

with $R = \sqrt{(x-x')^2 + (y-y')^2}$.

To determine the modes of propagation of a straight open waveguide with circularly cylindrical symmetry, one aims at connecting the interior field solutions that remain bounded in the core region to exterior field solutions that remain bounded in the homogeneous region outside the core. In this case the angular harmonics decouple, and the Cartesian components of the exterior field solutions for the mth angular harmonic are proportional to combinations of $K_m(\kappa r)$ and its derivative. For bent optical fibres, analytical solutions for the exterior fields on a toroidal coordinate system are not available. As has been explained in Section 4.4, such bounded exterior fields can be generated with

the aid of auxiliary ring sources located inside the imaginary core region of an auxiliary homogeneous configuration.

To assess the validity of that approach, we investigate the ramifications of using auxiliary sources for straight open waveguides. To this end, suppose that instead of a single source, we have an array of N' sources, located on a circle about the origin with radius ϱ and polar angles $\chi_{n'} = 2\pi n'/N'$, $n' = 0, 1, \ldots, N'-1$. The sources are modulated by factors $(N')^{-1} \exp(jm'\chi_{n'})$, with $m' \in \{-M, \ldots, M\}$. The corresponding field is given by

$$g_{m'}(\theta) = \frac{1}{2\pi} \sum_{l'=-\infty}^{\infty} I_{m'+l'N'}(\kappa\varrho) K_{m'+l'N'}(\kappa r) e^{j(m'+l'N')\theta}. \tag{D.4}$$

To extract a single angular harmonic, one would like to evaluate

$$g_{m,m'} = \int_{\theta=0}^{2\pi} e^{-jm\theta} g_{m'} \, \mathrm{d}\theta = \begin{cases} I_m(\kappa\varrho) K_m(\kappa r), & m - m' = 0 \bmod N', \\ 0, & \text{otherwise.} \end{cases} \tag{D.5}$$

Hence, although the array of line sources produces higher-order angular harmonics, selecting $m \in \{-M, \ldots, M\}$ will result in angular harmonics that correspond to the array phase factor, provided that $N' \geq 2M + 1$.

In the case of a bent fibre, the computational burden of evaluating the integrands is very high. Hence, the numerical quadrature rule mesh for the full range of angular harmonics ($m, m' \in \{-M, M\}$) should be as coarse as possible. If we choose $N = N' \geq 2M + 1$ equally spaced samples, the discrete counterpart of Eq. (D.5) reads

$$\bar{g}_{m,m'} = \frac{2\pi}{N} \sum_{n=0}^{N-1} e^{-2\pi jmn/N} g_{m'}(2\pi n/N) = \sum_{\ell=-\infty}^{\infty} I_{m+\ell N}(\kappa\varrho) K_{m+\ell N}(\kappa r) \delta_{m,m'}, \tag{D.6}$$

for $m, m' \in \{-M, \ldots, M\}$. In Eq. (D.6) aliasing is manifest in the terms with $\ell \neq 0$. However, owing to the asymptotically exponential decay $I_n(\kappa\varrho) K_n(\kappa r) \simeq (2n)^{-1}(\varrho/r)^n$ for large orders with respect to the arguments, the unwanted higher-order harmonics may be suppressed, by choosing N and $\rho_s = \varrho/r$ large and small enough, respectively. In the case of bent optical fibres, the actual dominant modes have large amplitudes for m small, and rapidly decaying ones for higher m, which has a mitigating effect on the aliasing error. In our experience, taking $N = N' = 2M + 2$ (just above the minimum $N = N' = 2M + 1$) turns out to be adequate since aliasing mainly affects the high-m constituents.

It would seem that by choosing ρ_s very small, aliasing may be eliminated altogether, since the field excited through the source modulation factors associated with azimuthal index m may always be scaled back to unity, while the higher order angular harmonics decay more rapidly. However, let us assume that the field amplitudes of the required $2M + 1$ independent angular harmonics are arranged on the diagonal of a matrix A, and

that each harmonic is contaminated by noise, represented through the off-diagonal components of A (for simplicity, we have taken all off-diagonal entries equal). If ρ_s is chosen too small, the noise constituents with m small will decay at a much smaller rate than the diagonal components of A for large m. As a consequence, the original $2M+1$ independent harmonic constituents will almost become dependent. For the straight fibre, this can be quantified through the condition number of $A^T A$. It turns out that for $\rho_s = \varrho/r = 0.2$, $M = 9$ and a 10^{-5} noise level, the condition number becomes prohibitive ($> 5 \times 10^6$), while for $\rho_s = 0.58$ and $M = 9$, a 10^{-3} noise level poses no problems whatsoever ($\mathrm{cond} A^T A < 5$). The observation that regarding the location of the auxiliary sources, one should steer clear of both the boundary of the circular cylinder of radius r and its centre is in agreement with results reported on the scattering from dielectric cylinders using a multifilament current mode [56]. Although the analysis above pertains the scalar-wave straight-fibre case, we have reached similar conclusions empirically for the much more complicated, full-vectorial bent-optical fibre case.

Appendix E

Comparison of the vectorial full-wave computation with the weak-guidance approximation

The accuracy of the weak-guidance approximation (WGA) is investigated by a comparison with exact vectorial full-wave (VFW) results for the normalised propagation coefficient ζ, the group slowness per meter $p_g = 1/v_g$, the dispersion D, and the dispersion slope S. Their computation has been discussed in Chapter 3. From the results we have extracted validity regions for the use of the WGA. Further, we have recorded the computation times to compute these quantities with both methods.

Accuracy check

We have examined the accuracy of the WGA on the basis of several refractive-index profiles, viz. step, parabolic, and arbitrary. The latter is shown in Figure E.1. The fibres
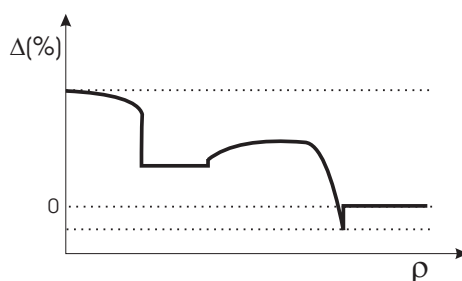

Figure E.1: *Arbitrary refractive-index profile.*

are weakly guiding, as we have assumed a refractive-index difference with a maximum Δ of $0.27\,\%$ at $\lambda = 632.8\,\text{nm}$. The core radius, $a = 4.1\,\mu\text{m}$, is similar to that of the CSF in

Table 3.1.

To perform the actual accuracy check, we define a relative error between a fibre quantity v_q, either computed via the WGA or the VFW analysis, as

$$\text{Rel. err. } v_q(\%) = \left| 1 - \frac{v_q^{\text{WGA}}}{v_q^{\text{VFW}}} \right| \times 100\,\%. \tag{E.1}$$

In Figure E.2, the relative error is plotted for p_g, D and S as a function of wavelength. A wavelength sweep is performed about the centre wavelength, $\lambda = 1550\,\text{nm}$. Observe that

(a) Relative error in the group slowness p_g

(b) Relative error in the dispersion D

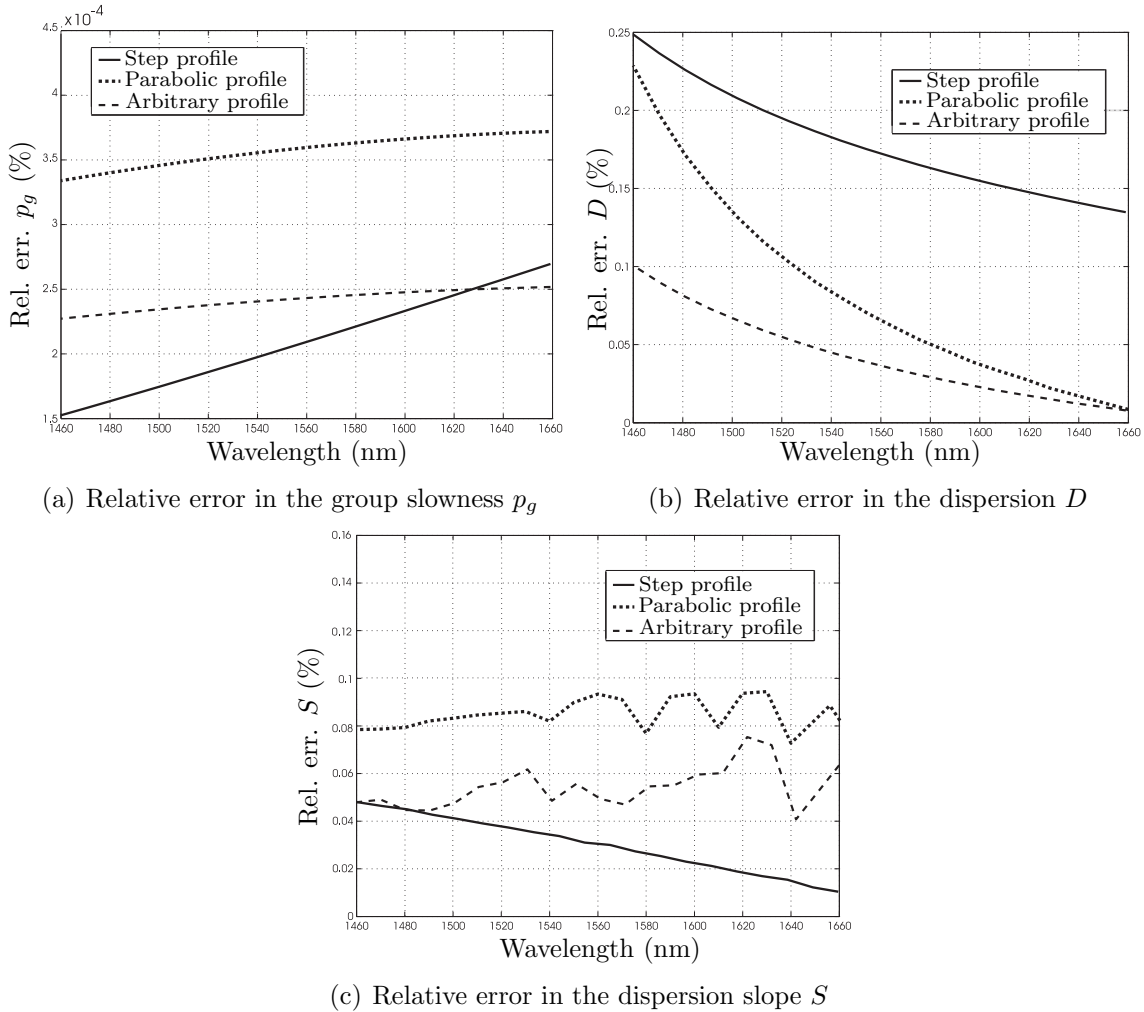(c) Relative error in the dispersion slope S

Figure E.2: *The relative error is set against the wavelength for various profiles with a maximum $\Delta = 0.27\,\%$ and a core radius of $a = 4.1\,\mu m$.*

the relative error is small, but whether it is negligible depends on the application. For example, let us regard a 10 Gbit/s bit stream. According to Figure E.2(a), the relative error for all profiles is of $O(10^{-6})$, which implies that for distances $z > 10\,\text{km}$ the pulses are no

longer distinguishable. As we are constantly pursuing higher bit rates, the aforementioned distance will inevitably decrease. Although the assumed values are (rough) estimates, it gives an idea of the limitations of the WGA.

Further, we note that the relative error in the dispersion slope, the third derivative of ζ with respect to $\hat{\omega}$, approaches the noise level as the wavelength increases. This is due to cancellations in its numerical computation in Eq. (3.12).

Next, we have examined the influence of an increasing Δ, which renders the fibre less weakly guiding. Again, the relative error is our measure. To give a fair comparison, we aim to keep the normalised frequency V, given by Eq. (2.43), constant at $V = 2.4$, such that we are still operating in the single-mode regime. This is achieved by a proper adjustment of the core radius for a fixed wavelength at $\lambda = 632.8\,\text{nm}$. In Figure E.3, the relative error

(a) Relative error in the group slowness p_g

(b) Relative error in the dispersion D
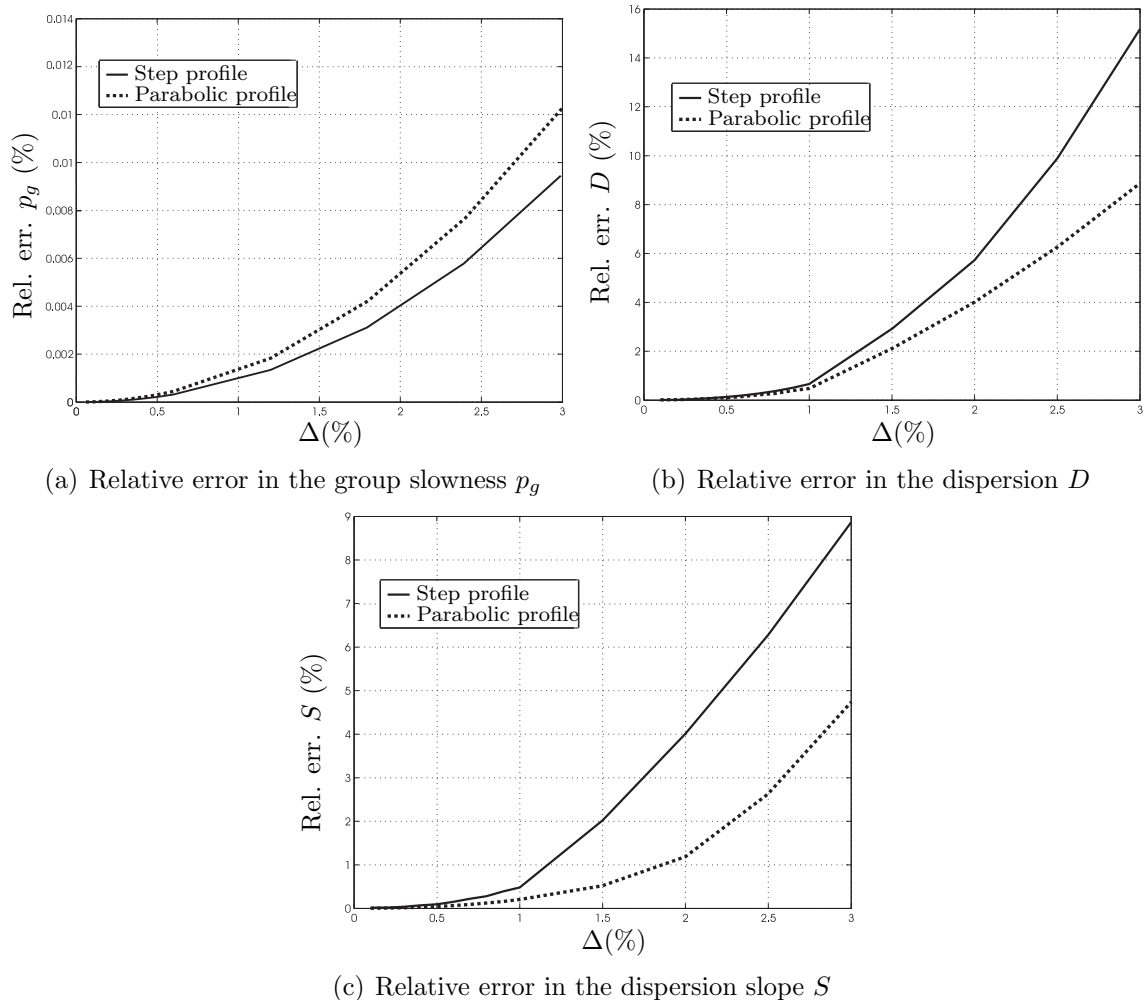
(c) Relative error in the dispersion slope S

Figure E.3: *The relative error of various fibre quantities set against the refractive-index difference Δ for a constant normalised frequency of $V = 2.4$.*

for the fibre quantities under consideration is plotted as a function of Δ at $\lambda = 632.8\,\text{nm}$ for the step-index and parabolic-index profile. As expected, we observe a steady increase of the error for higher contrasts. Whether the error is still acceptable depends on the application. However, in the synthesis problem, one would like to design a fibre profile with specified or optimum fibre properties. In that case a higher accuracy allows one to obtain sharper estimates for the pertaining quantities.

Time comparison

Under the WGA, the dimension of the system of differential equations expressed in terms of the number of field vectors, is halved. Consequently, less computation time is needed to perform the numerical integration of the system in the core region. The comparison is made for a parabolic-index weakly-guiding fibre with $\Delta = 0.3\,\%$ and $a = 5\,\mu\text{m}$, at a wavelength, $\lambda = 1550\,\text{nm}$. In Table E.1, the computation times for both the WGA and VFW analyses are shown. A Pentium IV, 2.4 GHz computer has been used to perform the computation. In addition, we have given the values for the propagation coefficient ζ, the group slowness p_g, the dispersion D, and the dispersion slope S computed by both methods. To keep the value of p_g tractable, we have multiplied it with the speed of light in vacuum c_0.

Table E.1: *Values for the propagation coefficient ζ and the fibre quantities p_g, D and S at $\lambda = 1550\,nm$ and the overall computation time for a single-mode fibre of radius $a = 5\,\mu m$ with a parabolic-index profile of $\Delta = 0.3\,\%$.*

Method	ζ	$c_0 p_g$	D	S	Time
VFW	1.4450879	1.4660822	14.853122	0.0620421	0.12 s
WGA	1.4450901	1.4660847	14.875426	0.0620389	0.08 s

Owing to the smaller system in the WGA case, the numerical computation of the various fibre quantities is about 1.5 times faster than with the VFW. It is this (marginal) gain in time that one has to weigh against the induced error in the computation of the pertaining quantities. In our opinion, accuracy prevails over computation time, as we do not want to limit ourselves to weakly guiding fibres. In particular, during the optimisation process of the refractive-index profile discussed in Chapter 5, this limitation may prove an impediment.

Appendix F

Transverse integrals for bent pipes, and single- and multi-mode fibres

F.1   The curved pipe

The integrals that arise on the right-side of Eq. (4.28) follow directly from the Marcuvitz-Schwinger equations of Eq. (2.18). Eventually, they form the elements of the tensor B in Eq. (4.29). They are given by

$$
I_1 = \frac{1}{2\pi} \int\limits_{\psi=-\pi}^{\pi} \frac{\rho_c + \rho \cos \psi}{\rho} \exp[-j(m-\ell)\psi]d\psi,
$$
$$
I_2 = \frac{1}{2\pi} \int\limits_{\psi=-\pi}^{\pi} \frac{\rho}{\rho_c + \rho \cos \psi} \exp[-j(m-\ell)\psi]d\psi.
$$

(F.1)

The integral I_1 occurs in the term B_{12} of Eq. (4.29), and only yields a non-vanishing solution for certain combinations of m and ℓ, i.e.

$$
I_1 = \frac{\rho_c}{\rho}\delta_{\ell,m} + \frac{1}{2}(\delta_{\ell+1,m} + \delta_{\ell,m+1}).
$$

(F.2)

To evaluate I_2, we introduce the variable $\xi = \exp(j\psi)$, which gives for $\ell \geq m$

$$
I_2 = \frac{1}{2\pi j} \oint \frac{2\xi^{\ell-m}}{\xi_+ - \xi_-} \left(\frac{1}{\xi - \xi_+} - \frac{1}{\xi - \xi_-} \right) d\xi,
$$

(F.3)

where

$$
\xi_\pm = -\rho^{-1} \left(\rho_c \mp \sqrt{\rho_c^2 - \rho^2} \right) = -\rho \left(\rho_c \pm \sqrt{\rho_c^2 - \rho^2} \right)^{-1}.
$$

(F.4)

Note that ξ_+ is located inside the unit circle in the complex ξ-plane, whereas ξ_- lies outside. Upon employing the residue theorem, we readily obtain

$$
I_2 = \rho \xi_+^{\ell-m} \left(\rho_c^2 - \rho^2 \right)^{-1/2}, \quad \text{for} \quad \ell \geq m.
$$

(F.5)

A similar derivation holds for $\ell \leq m$. If we compose both solutions, we arrive at

$$I_2 = \rho \xi_+^{|\ell-m|} \left(\rho_c^2 - \rho^2 \right)^{-1/2} = \rho G, \tag{F.6}$$

where G is given by Eq. (4.29).

F.2   The overlap integral

The aim of this section is to perform the numerical computation of Eq. (3.27), which we repeat here for convenience

$$A_{mn} = \frac{1}{2} \int\limits_{\rho=0}^{\infty} \int\limits_{\psi=0}^{2\pi} \mathrm{Re} \left[\mathbf{E}_i \left(\rho'', \psi'' \right) \times \mathbf{H}_{mn}^* \left(\rho, \psi \right) \right] \cdot \mathbf{u}_z a_{\mathrm{M}}^2 \rho \, d\psi \, d\rho, \tag{F.7}$$

where the integral over a cross section of the fibre is to be performed at the plane $z = 0$. The electric field $\mathbf{E}_i$ of the step-index SMF pigtail is expressed in a cylindrical coordinate system $\{\rho'', \psi'', z''\}$, with the by now familiar normalised radial coordinate $\rho'' = r''/a_{\mathrm{S}}$ where a_{S} denotes the pertaining core radius. The magnetic field $\mathbf{H}_{mn}$ in the MMF is expressed in a cylindrical coordinate system $\{\rho, \psi, z\}$, where $\rho = r/a_{\mathrm{M}}$ with a_{M} the core radius of the MMF. The configuration is shown in Figure 3.10. The unit vectors of both coordinate systems are related via

$$\begin{bmatrix} \mathbf{u}_{\rho''} \\ \mathbf{u}_{\psi''} \\ \mathbf{u}_{z''} \end{bmatrix} = \begin{bmatrix} s_\psi s_{\psi''} c_{\theta''} + c_\psi c_{\psi''} & c_\psi s_{\psi''} c_{\theta''} - s_\psi c_{\psi''} & s_{\psi''} s_{\theta''} \\ s_\psi c_{\psi''} c_{\theta''} - c_\psi s_{\psi''} & c_\psi c_{\psi''} c_{\theta''} - s_\psi s_{\psi''} & c_{\psi''} s_{\theta''} \\ -s_\psi s_{\theta''} & -c_\psi s_{\theta''} & c_{\theta''} \end{bmatrix} \begin{bmatrix} \mathbf{u}_\rho \\ \mathbf{u}_\psi \\ \mathbf{u}_z \end{bmatrix}, \tag{F.8}$$

where s_ξ and c_ξ, with $\xi \in \{\psi, \psi'', \theta''\}$, denote $\sin \xi$ and $\cos \xi$, respectively. The angle θ'' corresponds to the angular tilt of the SMF pigtail. The cross-products between the unit vectors of the various field components of $\mathbf{E}_i$ and $\mathbf{H}_{mn}$ are now readily derived. The field components of a step-index SMF are available analytically in terms of Bessel functions [27]. For the MMF, the field components are obtained via the method proposed in Chapter 2.

If we assume that the fibre axis of the SMF is located at $\rho = \rho_0$, the following relations hold between a point $P(\rho, \psi, 0)$ and $P(\rho'', \psi'', z'')$

$$\begin{aligned} t_{\psi''} &= t_{\psi'} c_{\theta''} = \rho s_\psi c_{\theta''} \left(\rho c_\psi - \rho_0 \right)^{-1}, \quad z'' = \rho a s_\psi s_{\theta''} \\ \rho'' c_{\psi''} &= \rho' c_{\psi'} = \rho' \left(\rho c_\psi - \rho_0 \right) = \left(\rho^2 + \rho_0^2 - 2\rho\rho_0 c_\psi \right)^{1/2} \left(\rho c_\psi - \rho_0 \right), \end{aligned} \tag{F.9}$$

where t_ξ denotes $\tan \xi$. This conversion enables us to perform the actual numerical integration over the cross section of the MMF. First, we perform the numerical integration over ψ. As is shown in Figure F.1, we can identify three regions of integration, depending on the radial offset and angular tilt, i.e.
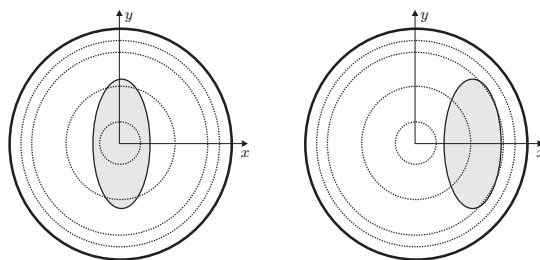
Figure F.1: *Various angular integration paths parameterised by ψ are given by dots. The gray ellipse denotes to the overlap of the SMF with the MMF for a radial offset and an angular tilt.*

1. integration is completely in the SMF core

$$\rho_0 \leq a_S \wedge 0 \leq \rho \leq a_{SMF} - \rho_0, \tag{F.10}$$

2. integration is completely in the SMF cladding

$$\begin{aligned} \rho \geq \rho_0 + a_S \quad &\vee \quad \rho_0 > a_S \wedge 0 \leq \rho \leq \rho_0 - a_S, \ \text{if } \theta'' = 0, \\ \rho \geq \sqrt{(\rho_0/s_{\theta''})^2 + (a_S/c_{\theta''})^2} \quad &\vee \quad \rho_0 > a_S \wedge 0 \leq \rho \leq \rho_0 - a_S, \ \text{elsewhere,} \end{aligned} \tag{F.11}$$

3. integration is partially in the SMF core and partially in the cladding

$$\left. \begin{aligned} & \rho_0 \geq a_S \wedge \rho_0 - a_S \leq \rho \leq \rho_0 + a_S, \\ & \rho_0 < a_S \wedge a_S - \rho_0 \leq \rho \leq \rho_0 + a_S, \end{aligned} \right\} \ \text{if } \theta'' = 0, \\ \left. \begin{aligned} & \rho_0 \geq a_S \wedge \rho_0 - a_S \leq \rho \leq \sqrt{(\rho_0/s_{\theta''})^2 + (a_S/c_{\theta''})^2}, \\ & \rho_0 < a_S \wedge a_S - \rho_0 \leq \rho \leq \sqrt{(\rho_0/s_{\theta''})^2 + (a_S/c_{\theta''})^2}, \end{aligned} \right\} \ \text{otherwise.} \tag{F.12}$$

The integration limits of the ψ integral are defined by the angle $\psi_b(\rho)$, which denotes an intersection between the circle and the ellipse, i.e.

$$\begin{aligned} \cos \psi_b &= \left(\rho^2 + \rho_0^2 - a_S^2 \right) / \left(2\rho\rho_0 \right), & \text{if } \theta'' = 0, \\ \cos \psi_b &= \left(\rho_0 \pm \sqrt{\rho_0^2 c_{\theta''}^2 - s_{\theta''}^2 \left(\rho^2 c_{\theta''}^2 - a_S^2 \right)} \right) / \left(\rho s_{\theta''}^2 \right), & \text{elsewhere.} \end{aligned} \tag{F.13}$$

For simplicity, we have assumed that the ellipse does not cross the core/cladding interface of the MMF at any point. The subsequent numerical integration over ρ is performed by a Gauss-Laguerre quadrature rule over a semi-infinite interval. The decay as $\rho \to \infty$ is exponential, i.e. $\exp(-b\rho)$, with $b = w_S + w_M$, where w is given by Eq. (2.36), and the subscript indicates whether the SMF propagation coefficient or an MMF one is used, respectively. Further, to include a polarisation angle ψ_i to the incident field, the ψ-dependence of the pertaining electromagnetic field components has to be changed into $\exp\left[-jm\left(\psi + \psi_i\right)\right]$.

F.3   Integrals in closed form for the MFD in the cladding region

This section deals with the analytical integration over the cladding region of the numerators of the MFD and A_{eff} in Eq. (3.13) and Eq. (3.15). Note that the denominator of the MFD d_I is implicitly addressed as well, since it is the numerator of the MFD d_{II}. The pertaining integrals are given by

$$\int_{A_\infty} S(\rho)\rho d\rho d\psi, \quad \text{and} \quad \int_{A_\infty} S(\rho)\rho^3 d\rho d\psi, \tag{F.14}$$

where A_∞ denotes the infinite cross section of the fibre and the complex Poynting vector $S(\rho)$ is given by Eq. (3.14). The Poynting vector depends solely on the radial coordinate, and hence we are left with the following integrals that are derived analytically

$$\int_{\rho=1}^{\infty} K_{|m|}(w\rho)K'_{|m|}(w\rho)d\rho = w^{-1}\int_{x=w}^{\infty} K_{|m|}(x)K'_{|m|}(x)dx = -\frac{1}{2w}K_{|m|}^2(w), \tag{F.15}$$

$$\int_{\rho=1}^{\infty} \rho^2 K_{|m|}(w\rho)K'_{|m|}(w\rho)d\rho = w^{-3}\int_{x=w}^{\infty} x^2 K_{|m|}(x)K'_{|m|}(x)dx$$
$$= \frac{1}{2w^3}\left[m^2 K_{|m|}^2(w) - w^2 K_{|m|}'^2(w)\right], \tag{F.16}$$

$$\int_{\rho=1}^{\infty}\left[m^2\rho^{-1}K_{|m|}^2(w\rho) + \rho w^2 K_{|m|}'^2(w\rho)\right]d\rho = \int_{x=w}^{\infty}\left[m^2 x^{-1}K_{|m|}^2(x) + x K_{|m|}'^2(x)\right]dx$$
$$= \frac{1}{2}K_{|m|}^2(w)\left[(m^2+w^2) - 2w\frac{K'_{|m|}(w)}{K_{|m|}(w)} - \left(w\frac{K'_{|m|}(w)}{K_{|m|}(w)}\right)^2\right], \tag{F.17}$$

$$\int_{\rho=1}^{\infty}\left[m^2\rho K_{|m|}^2(w\rho) + \rho^3 w^2 K_{|m|}'^2(w\rho)\right]d\rho = w^{-2}\int_{x=w}^{\infty}\left[m^2 x K_{|m|}^2(x) + x^3 K_{|m|}'^2(x)\right]dx$$
$$= \frac{2}{3}K_{|m|}^2(w)\left\{1 - w\frac{K'_{|m|}(w)}{K_{|m|}(w)} + \frac{(4+2m^2-w^2)}{4}\left[\left(\frac{K'_{|m|}(w)}{K_{|m|}(w)}\right)^2 - \frac{m^2+w^2}{w^2}\right]\right\}. \tag{F.18}$$

A prime indicates the derivative of the modified Bessel function with respect to its argument.

Bibliography

[1] M. Abramowitz and I. A. Stegun. *Handbook of Mathematical Functions with Formulas, Graphs, and Mathematical Tables.* New York: Dover, 1965.

[2] G. P. Agrawal. *Nonlinear Fiber Optics.* Academic Press, Inc, 1989.

[3] G. B. Arfken and H. Weber. *Mathematical Methods for Physicists.* Amsterdam: Elsevier, 6th edition, 2005.

[4] H. Bach and N. Neuroth. *The Properties of Optical Glass.* Springer, 1995.

[5] N. H. G. Baken, M. B. J. Diemeer, J.M. van Splunter, and H. Blok. Computational modeling of diffused channel waveguides using a domain integral equation. *J. Lightwave Techn.*, 8(4):576–586, 1990.

[6] K. Balemarthy. *Electronic Equalization of High-Speed Multi-mode Fiber Links.* PhD thesis, School of Electrical and Computer Engineering, Georgia Institute of Technology, 2007.

[7] W. Bardyszewski and D. Yevick. Spectral density matrix description of polarization mode dispersion. *J. Opt. Soc. Am. A*, 22(6):1158–1162, 2005.

[8] M. Bingle and B. P. de Hon. Differential mode delay – full wave modelling and various levels of approximations. In *Proceedings of the General XXVIIth Assembly of the International Union of Radio Science*, page paper 2060, 2002.

[9] M. Bingle, B. P. de Hon, and M. J. N. van Stralen. Electromagnetic modelling and optimisation for the design of single-mode optical fibres. In *2001 URSI International Symposium of Electromagnetic Theory, Victoria, CA*, volume 307.2/MN06.20, pages 515–517, 13-17 May 2001.

[10] M. Calzavara, R. Caponi, and F. Cisternino. Selective excitation of annular zones in graded index multimode fiber. *J. Opt. Commun.*, 5(3):82–86, 1984.

[11] K. S. Chiang. Review of numerical and approximate methods for the modal analysis of general optical dielectric waveguides. *Opt. Quant. Electron.*, 26:S113–S134, 1994.

[12] S. Chung. Macrobend loss of 1300 nm optimized single mode fibre at 1550 nm. In *IWCS*, pages 704–709, 1988.

[13] P. J. B. Clarricoats and K. B. Chan. Electromagnetic-wave propagation along radially inhomogeneous dielectric cylinders. *Electron. Lett.*, 6(22):694–695, 1970.

[14] A. Corana, M. Marchesi, C. Martini, and S. Ridella. Minimizing multimodal functions of continuous variables with the simulated annealing algorithm. *ACM Trans. Math. Softw.*, 13(3):262–280, 1987.

[15] Corning. Available at URL: http://www.corning.com/opticalfiber/.

[16] R. Dändliker, A. Bertholds, and F. Maystre. How modal noise in multimode fibers depends on source spectrum and fiber dispersion. *J. Lightwave Technol.*, 3(1):7–12, 1985.

[17] B. P. de Hon. A modal impedance-angle formalism: Rigorous proofs for optical fiber mode counting and bracketing. *Radio Sci.*, 38(2):14–1, 2003.

[18] B. P. de Hon and M. Bingle. A modal impedance-angle formalism: Schemes for accurate graded-index bent-slab calculations and optical fiber mode counting. *Radio Sci*, 38:13–1, 2003.

[19] J. G. Dil and H. Blok. Propagation of electromagnetic surface waves in a radially inhomogeneous optical waveguide. *Opt. Quant. Electron.*, 5:415–428, 1973.

[20] Draka Communications. Available at URL: http://www.drakafibre.com/.

[21] EXFO. Optical fiber analyzer nr-9200/nr-9200hr, spnr9200hr.11an, 2006.

[22] L. Faustini and G. Martini. Bend loss in single-mode fibers. *J. Lightwave Technol.*, 15(4):671–679, 1997.

[23] L.B. Felsen and N. Marcuvitz. *Radiation and Scattering of Waves*. Prentice-Hall, 1994.

[24] R. Fletcher. *IFIP International Federation for Information Processing, System Modeling and Optimization*, volume 199/2006, chapter A New Low Rank Quasi-Newton Update Scheme for Nonlinear Programming, pages 275–293. Springer Boston, 2006.

[25] R. Fletcher and S. Leyffer. User manual for FilterSQP. *University of Dundee Numerical Analysis Report NA/181*, April 1998, version1, June 1998, updated March 1999.

[26] T. Fujisawa, K. Saitoh, K. Wada, and M. Koshiba. Chromatic dispersion profile optimization of dual-concentric-core photonic crystal fibers for broadband dispersion compensation. *Opt. Express*, 14(2):893–900, 2006.

[27] A. Ghatak and K. Thyagarajan. *Introduction to Fiber Optics*. Cambridge University Press, 1998.

[28] A. Gil, J. Segura, and N. M. Temme. Evaluation of the modified Bessel function of the third kind of imaginary orders. *J. Comput. Phys.*, 175(2):398–411, 2002.

[29] A. Gil, J. Segura, and N. M. Temme. Computing special functions by using quadrature rules. *Numer. Algorithms*, 33:265–275, 2003.

[30] A. Gil, J. Segura, and N. M. Temme. *Numerical Methods for Special Functions*. Philidelphia, PA SIAM, 2007.

[31] P. E. Gill and W. Murray. *Numerical Methods for Constrained Optimisation*. Academic Press, London, 1974.

[32] N. Gisin, R. Passy, and B. Perny. Optical fiber characterization by simultaneous measurement of the transmitted and refracted near field. *J. Lightwave Technol.*, 11(11):1875–1883, 1993.

[33] D. Gloge. Weakly guiding fibers. *Appl. Opt.*, 10(10):2252–2258, 1971.

[34] W.L. Goffe, G.D. Ferrier, and J. Rogers. Global optimization of statistical functions with simulated annealing. *J. Econometrics*, 60(1/2):65–100, 1994.

[35] J. P. Gordon and H. Kogelnik. PMD fundamentals: Polarization mode dispersion in optical fibers. *Proc. Nat. Acad. Sci. 97*, 97(9):4541–4550, 2000.

[36] J. Gowar. *Optical Communication Systems*. Prentice Hall International, Inc., London, 1984.

[37] G. Hall and J.M. Watt. *Modern Numerical Methods for Ordinary Differential Equations*. Oxford University Press, 1976.

[38] W. Hermann and D. U. Wiechert. Refractive index of doped and undoped PCVD bulk silica. *Mat. Res. Bull.*, 24(9):1083–1097, 1989.

[39] K. R. Hiremath, M. Hammer, R. Stoffer, L. Prkna, and J. Čtyrok. Analytic approach to dielectric optical bent slab waveguides. *Opt. Quant. Electron.*, 37(1-3):37–61, 2005.

[40] IEEE. P802.3aq, 10gbase-lrm task force tools, output of 108 fiber model. Available at URL: http://www.ieee802.org/3/aq/public/tools/.

[41] L. Ingber. Adaptive simulated annealing (asa), global optimization C-code, caltech alumni association, pasadena, california. Available at URL: http://www.ingber.com/#ASA-CODE, 1993.

[42] International Telecommunication Union. ITU-T Recommendations, G. series, G650-G659. Available at URL: http://www.itu.int/net/home/index.aspx.

[43] T. Ishigure, E. Nihei, and Y. Koike. Optimum refractive-index profile of the graded-index polymer optical fiber, toward gigabit data links. *Appl. Opt.*, 35(12):2048–2053, 1996.

[44] T. Ishigure, K. Ohdoko, Y. Ishiyama, and Y. Koike. Mode-coupling control and new index profile of GI-POF for restricted-launch condition in very-short-reach networks. *J. Lightwave Technol.*, 23(12):4155–4168, 2005.

[45] D.I. Kaklamani and H.T. Anastassiu. Aspects of the method of auxiliary sources (MAS) in computational electromagnetics. *IEEE Antennas Propagat. Mag.*, 44(3):48–64, 2002.

[46] J. Kaur, K. Thyagarajan, and B. P. Pal. Estimation of cut-off wavelength of rare earth doped single-mode fibers. *Opt. Comm.*, 170:355–359, 1999.

[47] S. Kawakami and H. Tanji. Evolution of power distribution in graded-index fibres. *Electr. lett.*, 19(3):100–102, 1983.

[48] G. Keiser. *Optical Fiber Communications*. McGraw-Hill Companies, third edition, 2000.

[49] E. Kerrinckx, L. Bigot, M. Douay, and Y. Quiquempois. Photonic crystal fiber design by means of a genetic algorithm. *Opt. Express*, 12(9):1990–1995, 2004.

[50] S. Kirkpatrick, C. D. Gelatt, and M. P. Vecchi. Optimization by Simulated Annealing. *Science*, 220(4598):671–680, 1983.

[51] K. Y. Kolossovski and R. A. Sammut. Three-step design optimization for multi-channel fibre Bragg gratings. *Opt. Express*, 11(9):1029–1038, 2003.

[52] A. M. J. Koonen. Bit-error-rate degradation in a multimode fiber optic transmission link due to modal noise. *IEEE J. Sel. Areas Commun.*, SAC-4(9):1515–1522, 1986.

[53] T. Koonen, H. van den Boom, A. Ng'oma, L. Bakker, I. Tafur Monroy, and G. D. Khoe. Recent development in broadband service delivery techniques for short-range networks. In *Proc. 9th European Conference on Networks and Optical Communications (NOC 2004)*, pages 86–93, 2004.

[54] R. de L. Kronig and H.A. Kramers. Zur theorie der absorption und dispersion in den rntgenspektren. *Z. Phys.*, 48:174–179, 1928.

[55] G. Kuyt, P. Matthijsseand, L. Gasca, L. de Montmorillon, A. Berkers, M. Doorn, K. Nothofer, and Alexander Weiss. Perfecting fiber for FTTH deployments. *Broadband Properties Magazine*, pages 64–67, February 2008.

[56] Y. Leviatan and A. Boag. Analysis of electromagnetic scattering from dielectric cylinders using a multifilament current model. *IEEE Trans. Antennas Propag.*, 35:1119–1127, 1987.

[57] L. Lewin, D. C. Chang, and E. F. Kuester. *Electromagnetic Waves and Curved Structures.* Peter peregrinus LTD., 1977.

[58] D. Marcuse. Curvature loss formula for optical fibers. *J. Opt. Soc. Am.*, 66(3):216–220, 1976.

[59] D. Marcuse. *Light Transmission Optics.* Van Nostrand Rheingold, New York, 1982.

[60] N. Marcuvitz and J. Schwinger. On the representation of electric and magnetic felds produced by currents and discontinuities in wave guides. *J. Appl. Phys.*, 22(6):806–820, 1951.

[61] K. Meyberg and P. Vachenauer. *Höhere Mathematik.* Springer, 1991.

[62] S. K. Mishra. Performance of the barter, the differential evolution and the simulated annealing methods of global optimization on some new and some old test functions. Available at URL: http://www.ssrn.com/abstract=941630, November 1, 2006.

[63] S. K. Mishra. Global optimization by differential evolution and particle swarm methods: Evaluation on some benchmark functions. Available at URL: http://www.ssrn.com/abstract=933827, September 30, 2006.

[64] W. Mohammed, X. Gu, and P. W. E. Smith. Full vectorial modal analysis of specialty fibers and their Bragg grating characterization. *Appl. Opt.*, 45:3307–3316, 2006.

[65] G. Monegato. An overview of the computational aspects of Kronrod quadrature rules. *Numer. Algorithms*, 26:173–196, 2001.

[66] Y. Murakami, A. Kawana, and H. Tsuchiya. Cut-off wavelength measurements for single-mode optical fibers. *Appl. Opt.*, 18(7):1101–1104, 1979.

[67] K. Nagano, S. Kawakami, and S. Nishida. Change of the refractive index in an optical fiber due to external forces. *Appl. Opt.*, 17(13):2080–2085, 1978.

[68] Y. Namihira. Relationship between nonlinear effective area and modefield diameter for dispersion shifted fibres. *Electronics Letters*, 30(3):262–264, 1994.

[69] E.G. Neumann. *Single-Mode Fibers.* Springer-Verlag, 1988.

[70] J. Nocedal and S. J. Wright. *Numerical Optimization.* Springer-Verlag New York, 1999.

[71] Numerical Algorithms Group Ltd. NAG Fortran library Mark 20. Available at URL: http://www.nag.co.uk/, 2001.

[72] K. Okamoto and T. Okoshi. Vectorial wave analysis of inhomogeneous optical fibers using finite element method. *IEEE Trans. Microwave Theory Techn.*, MTT-26(2):109–114, 1978.

[73] T. Okoshi. *Optical Fibers.* Academic Press, 1982.

[74] R. Olshansky. Effect of the cladding on pulse broadening in graded-index optical waveguides. *Appl. Opt.*, 16(8), 1977.

[75] R. Orta and B. P. de Hon. Electromagnetic theory of waveguides. Lecture notes for the course 5MH20, 2005.

[76] K.M. Patel and S.E. Ralph. Enhanced multimode fiber link performance using a spatiallyresolved receiver. *IEEE Photon. Technol. Lett.*, 14(3):393–395, 2002.

[77] E.C.M. Pennings. *Bends in Optical Ridge Waveguides : Modeling and Experiments.* Ph.D. Thesis, University of Delft, 1990.

[78] W. H. Press, S. A. Teukolsky, and W. T. Vetterling. *Numerical Recipes in Fortran 77: The Art of Scientific Computing*. Cambridge University Press., second edition, 1994.

[79] L. Raddatz, I. H. White, D. G. Cunningham, and M. C. Nowell. An experimental and theoretical study of the offset launch technique for the enhancement of the bandwidth of multimode fiber links. *J. Lightwave Technol.*, 16:324–331, 1998.

[80] K. W. Raine, J. G. Baines, and R. J. King. Comparison of refractive index measurements of optical fibres by three methods. *IEE Proc. J*, 135(3):190–195, 1988.

[81] S. S. Rao. *The Finite Element Method in Engineering*. Amsterdam : Elsevier Butterworth Heinemann, 4 edition, 2005.

[82] H. Renner. Bending losses of coated single-mode fibers: A simple approach. *J. Lightwave Technol.*, 10(5):544–551, 1992.

[83] E. J. Rothwell and M. J. Cloud. *Electromagnetics*. London: CRC Press, 2001.

[84] E. Schweig and W. B. Bridges. Computer analysis of dielectric waveguides: A finite-difference method. *IEEE Trans. Microwave Theory Tech.*, MTT-32(5):531–541, 1984.

[85] P. P. Silvester and G. Pelosi. *Finite Elements for Wave Electromagnetics: Methods and Techniques*. New York : IEEE Press, 1994.

[86] R. W. Smink, B. P. de Hon, and A. G. Tijhuis. Bending loss in optical fibers – a full-wave approach. *J. Opt. Soc. Am. B*, 24(10):2610–2618, 2007.

[87] R. W. Smink, B. P. de Hon, and A. G. Tijhuis. Fast and accurate computation of Bessel functions with (large) complex order and argument. *Appl. Math. Comput.*, 207(5):442–447, 2009.

[88] R. W. Smink, B. P. de Hon, and A. G. Tijhuis. Refractive index profile optimisation for the design of optical fibres. *Opt. Quant. Electron.*, Accepted for publication, 2009.

[89] A. W. Snyder and J. D. Love. *Optical Waveguide Theory*. London: Chapman and Hall, 1977.

[90] A. W. Snyder and W. R. Young. Modes of optical waveguides. *J. Opt. Soc. Am.*, 68(3):297–309, 1978.

[91] A.W. Snyder. Asymptotic expressions for eigenfunctions and eigenvalues of a dielectric or optical waveguide. *IEEE Trans. Microwave Theory Techn.*, MTT-17(12):1130–1138, 1969.

[92] R. Storn and K. Price. Differential Evolution A simple and efficient heuristic for global optimization over continuous spaces. *J. Global Optim.*, 11(4):341–359, 1997.

[93] G. Strang. *Linear Algebra and Its Applications.* Academic Press, Inc., New York, second edition, 1976.

[94] H. R. Sunak. Single-mode fiber measurements. *IEEE Trans. Instrum. Meas*, 37(4):557–560, Dec. 1988.

[95] B. J. Sung, J. H. Moon, and M. S. Kim. Checking the influence of numerically induced chaos in the computational study of intramolecular dynamics using trajectory equivalence. *Chem. Phys. Lett.*, 432(5-6):610–616, 2001.

[96] J. L. Synge and A. Schild. *Tensor Calculus.* University of Toronto Press, Toronto, Canada, 1956.

[97] Telecommunications Industry Association (TIA). Differential mode delay measurement of multimode fiber in the time domain. FOTP 220, TIA/EIA-455220, 2001.

[98] N. M. Temme. *Special Functions: an Introduction to the Classical Functions of Mathematical Physics.* Chichester: Wiley-Interscience, 1996.

[99] I. J. Thompson and A. R. Barnett. Coulomb and Bessel functions of complex arguments and order. *J. Comput. Phys.*, 64(2):490–509, 1986.

[100] Thorlabs. Pigtailed laser system diodes, lps-3224-660fc. Available at URL: http://www.thorlabs.com/.

[101] C. P. Tsekrekos. *Mode group diversity multiplexing in multimode fiber transmission systems.* PhD thesis, Eindhoven University of Technology, 2008.

[102] C. P. Tsekrekos and A. M. J. Koonen. Mode-selective spatial filtering for increased robustness in a mode group diversity multiplexing link. *Opt. Lett.*, 32(9):1041–1043, 2007.

[103] C. P. Tsekrekos, A. Martinez, F.M. Huijskens, and A. M. J. Koonen. Design considerations for a transparent mode group diversity multiplexing link. *IEEE photon. Technol. Lett.*, 18(22):2359–2361, 2006.

[104] C. P. Tsekrekos, R. W. Smink, B. P. de Hon, A. G. Tijhuis, and A. M. J. Koonen. Near field intensity pattern at the output of silica-based graded-index multimode fibers under selective excitation with a single-mode fibe. *Opt. Express*, 17(7):3656–3664, 2007.

[105] C. Unger and W. Stöcklein. Characterization of the bending sensitivity of fibers by the MAC-value. *Opt. Commun.*, 107:361–364, 1994.

[106] H. P. A. van den Boom, A. M. J. Koonen, F. M. Huijskens, and W. van Gils. Angular mode group diversity multiplexing for multi-channel communication in a single step-index plastic optical fibre. In *Proc. IEEE/LEOS Symposium Benelux Chapt.*, pages 121–124, 2004.

[107] C. Vassallo. Perturbation of a LP mode of an optical fibre by a quasi-degenerate field: a simple formula. *Opt. Quant. Electron.*, 17:201–205, 1985.

[108] C. Vassallo. Scalar-field theory and 2-D ray theory for bent single-mode weakly guiding optical fibers. *J. Lightwave Technol.*, LT-3(2):416–423, 1985.

[109] C. Vassallo. *Optical Waveguide Concepts*. Elsevier Science Publishers B.V., 1991.

[110] M. O. Vassell. Calculation of propagating modes in a graded-index optical fibre. *Opt. Quant. Electron.*, 6(4):271–286, 1974.

[111] J. Molina Vazquez, R. W. Smink, B. P. de Hon, A. G. Tijhuis, G. D. Khoe, and H. J. S. Dorren. Size limitations of quantum dot microdisc lasers. *Proc. Symp. IEEE/LEOS Benelux Chapt.*, pages 33–36, 2006.

[112] Q. Wang, G. Farrell, and T. Freir. Theoretical and experimental investigations of macro-bend losses for standard single mode fibers. *Opt. Express*, 13(12):4476–4484, 2005.

[113] G. N. Watson. *A Treatise on the Theory of Bessel Functions*. Cambridge: Cambridge University Press, second edition, 1966.

[114] M. Webster, L. Raddatz, I. H. White, and D. G. Cunningham. A statistical analysis of conditioned launch for gigabit ethernet links using multimode fiber. *J. Lightwave Technol.*, 17:1532–1541, 1999.

[115] I. A. White. Radiation from bends in optical waveguides: the volume-current method. *IEE J. Microwaves Opt. Acoustics*, 3:186–188, 1979.

[116] K. I. White. Practical application of the refracted near-field technique for the measurement of optical fibre refractive index profiles. *Opt. Quant. Elect.*, 11(2):185–196, 1979.

[117] Wolfram. *Mathematica*. Wolfram Research Inc., Champaign, Illinois, version 5.1 edition, 2004.

[118] G. Yabre. Comprehensive theory of dispersion in graded-index optical fibers. *J. Lightwave Technol.*, 18(2):166–177, 2000.

[119] Z. Zhu and T. G. Brown. Full-vectorial finite-difference analysis of microstructured optical fibers. *Opt. Express*, 10(17):853–864, 2002.

Samenvatting

Al enkele tientallen jaren worden op silicium gebaseerde glasvezels gebruikt voor telecommunicatie en sensor toepassingen. In netwerken waarbij grote afstanden moeten worden overbrugd worden vaak monomode glasvezels gebruikt. Bij kortere afstanden, bijvoorbeeld in een thuisnetwerk, heeft de multimode glasvezel de voorkeur. Door de enorme bandbreedte van de glasvezels in vergelijking met hun elektronische draadloze of op koper gebaseerde tegenhangers, blijft de vraag naar glasvezels stijgen. In een concurrende markt, zullen glasvezelfabrikanten betere vezels moeten produceren die niet alleen goedkoop maar ook eenvoudig te installeren zijn.

Omdat het onderzoek, de ontwikkeling en het fabricageproces van glasvezels al een volwassen discipline is, kunnen verbeteringen in de huidige generatie van vezels alleen bewerkstelligd worden door het constueren van robuuste, nauwkeurige en effciënte numerieke modellen. Met behulp van deze modellen kunnen we de grootheden berekenen welke het gedrag van de vezel bepalen. We hebben een modulair computerprogramma geschreven, gebaseerd op de vergelijkingen van Maxwell, om deze grootheden te berekenen voor zowel monomode als multi-mode glasvezels. Essentieel hierbij is het brekings-index profiel, of meer specifieker het doping profiel, welke de glasvezel volledig karakteriseert. Voor de monomode glasvezel hebben we ons geconcentreerd op de volgende grootheden: de dispersie, de afgeleide van de dispersie naar frequentie, de modale veld diameter, het effectieve gebied, de effectieve afsnijfrequentie en de buigingsverliezen. Voor de multimode glasvezel zijn de differentiële modale vertraging en de buigingsverliezen essentiële grootheden.

Voor de numerieke berekening van de buigingsverliezen van een monomode glasvezel, welke we uitgebreid behandeld hebben, bestaan enkele benaderende uitdrukkingen in de literatuur. Echter zij geven verschillende resultaten. Om duidelijkheid te verschaffen hebben we een volledig vectoriële analyse van de gebogen glasvezel uitgevoerd. Hierbij komen drievoudige integralen voor waarin de binnenste integrand bestaat uit producten van Bessel functies met een grote, complexe orde en argument. Deze producten dienen met een hoge nauwkeurigheid berekend te worden omdat cijfers in de betreffende integrand elkaar kunnen opheffen. Dit heeft tot gevolg dat de berekening van de buigingsverliezen als functie van de kromtestraal weken kan duren op een hedendaagse computer. De berek-

ende resultaten zijn als referentie gebruikt om de meest accurate benaderingsmethode te selecteren. Vervolgens is die benaderingsmethode gebruikt om de buigingsverliezen van hogere orde modi te berekenen, omdat de effectieve afsnijfrequentie afhangt van het buigingsverlies van de eerste hogere orde mode.

Daar de eigenschappen van een glasvezel vaak tegenstrijdig zijn, blijft het een uitdaging om een juist doping profiel te ontwerpen dusdanig dat de gewenste ontwerpdoeleinden (zo goed mogelijk) worden gehaald. Een ontwerpdoel bestaat uit een set van gewenste waarden voor enkele typische glasvezel grootheden, welke wiskundig kunnen worden gegoten in een kostenfunctie. Het minimaliseren van deze kostenfunctie levert het optimale doping profiel. Voor de monomode glasvezel hebben we voor stuksgewijs lineaire doping profielen deze optimalisatie uitgevoerd, waarbij we gebruik hebben gemaakt van globale en op gradient informatie gebaseerde routines om het ontwerpproces aanzienlijk te kunnen versnellen. Vaak leiden deze optimalisatie routines tot tegen intuïtieve doping profielen. We hebben een weloverwogen keuze gemaakt en de uitkomsten van de verschillende routines met elkaar vergeleken voor de monomode glasvezel. De belangrijkste conclusie is misschien wel dat er nog steeds ruimte is voor verbetering in de doping profielen van de huidige generatie van glasvezels.

Voor multimode glasvezels is profiel optimalisatie te tijdrovend. Een handmatige afstemming van het populaire geleidelijk veranderende brekings-index profiel in de radiële richting is wel mogelijk om de differentiële modale vertraging te minimaliseren. Daarnaast hebben we differentiële modale verzwakking en modale overspraak tussen de propagerende modi gesimuleerd om resultaten te verkrijgen die overeenstemmen met de metingen. Tevens hebben we de invloed bekeken op het intensiteitspatroon voor kleine imperfecties in de glasvezel, zoals bijvoorbeeld de aanwezigheid van een kink in het profiel.

Een selectieve excitatie van verschillende mode groepen in de multimode glasvezel biedt de mogelijkheid om onafhankelijk kanalen te creëren, en daardoor de informatie capaciteit te vergroten. Kort geleden is de haalbaarheid van deze zogenaamde mode groep diversiteits multiplexing techniek aangetoond. Numerieke simulaties zijn een middel om de werking van deze techniek beter te begrijpen en om de methode wellicht te verbeteren. De scheiding van de kanalen kan worden vergroot door een lens te plaatsen tussen de uitgang van de glasvezel en de detector. Deze techniek heet modale selectieve spatiële filtering en is geïmplementeerd in onze programmatuur. Onze metingen aan mode groep diversiteits multiplexing links, met en zonder toepassing van de mode groep diversiteits multiplexing techniek, onderbouwen de simulaties.

De ontwikkelde programmatuur heeft een brede inzetbaarheid. Mede door zijn modulaire opbouw zijn uitbreidingen, zoals het toevoegen van meerdere grootheden of andere profiel materialen, rechtlijnig.

Curriculum vitae

Rutger W. Smink was born in Wijnandsrade, The Netherlands, on July 3, 1980. He received his M.Sc. degree in electrical engineering (*Cum Laude*) in 2004 from the Eindhoven University of Technology (EUT), The Netherlands. In 2002 he performed an internship at the Dutch research institute TNO in The Hague, where he developed a program to connect a cascade of different-sized waveguides by their impedance matrices for filter and antenna applications. At the same institute, he realised his M.Sc. study under the supervision of dr. G. Gerini and dr. A. Neto from TNO, and dr. M.C. van Beurden and prof. A.G. Tijhuis from the Electromagnetics group at the EUT. The study concerned the acceleration of a frequently occurring integral to compute the radiation pattern of a phased-array antenna.

In 2004 he started working toward a Ph.D. degree in electrical engineering in the Electromagnetics group at the EUT under the supervision of dr. B.P. de Hon and prof. A.G. Tijhuis. Refractive-index profile optimisation of single-mode optical fibres, the vectorial full-wave computation of macrobending losses, and the numerical modelling of contemporary multi-mode fibre links have been his main research topics. In addition, he collaborated with the Electro-Optical Communications group at the EUT to model a quantum-dot microdisc laser. Further, he had the supervision of a master student and instructed undergraduate students. In 2008 he started working as an RF and Circuits & Design Engineer at Tyco Electronics in 's-Hertogenbosch, the Netherlands.

Acknowledgements

During my Ph.D. period, I had the privilege of working and meeting with many researchers in the field of electromagnetics and I owe lots of thanks to many of them. First of all, I would like to thank my daily supervisor dr. Bastiaan de Hon for his continuing enthusiasm, for enlightening discussions on all kind of things, and for being an excellent guide through the amazing field of fibre optics. Also Prof. Anton Tijhuis deserves my utmost gratitude for his insights and critical comments on drafts of journal papers and this thesis. Further, I owe thanks to the members of the committee for struggling through more than 60 figures and nearly 270 equations, definitions and formulae.

In addition, I would like to thank my colleagues from the Electromagnetics group for broadening my vision to other aspects in this fascinating electrotechnical discipline. In particular, I owe special thanks to Jean-Pierre Vaessen and Tom Gierstberg for being a sometimes much needed way of release. Further, I would like to thank Christos Tsekrekos, former member of the Electro-Optical Communication group at the university, for performing the measurements of the intensity patterns in Chapter 6. From the same group, I owe special thanks to Javier Molina Vázquez, Karen Solís Trápala and Prof. Harm Dorren for introducing me to the physical aspects of the micro-disk quantum-dot laser.

Finally, I would like to thank my friends and my family. My mother for her loving care and her perseverance. You will always live in our hearts. My father for his advisory role and different perspective on everyday things. My brother for designing the cover of this thesis and granting me the title of "uncle" twice. And last but definitely not least, my wife Sandra for her everlasting support and for being the frequently needed reset button on my harddisk. Thanks to all of you and my apologies to any I might have missed.